Additively Manufactured High Pressure High Temperature Heat Exchangers for Solar Thermal Applications

By

INES-NOELLY TAKUA TANO
DISSERTATION

Submitted in partial satisfaction of the requirements for the degree of

DOCTOR OF PHILOSOPHY

in

Mechanical and Aerospace Engineering

in the

OFFICE OF GRADUATE STUDIES

of the

UNIVERSITY OF CALIFORNIA

DAVIS

Approved:

Vinod Narayanan, Chair

Paul A. Erickson

Barbara Linke

Committee in Charge

2024

To Nanan, Maman and Papa

Acknowledgements

This research is the result of the effort and support of several people. I wish to express my heartfelt thanks to my PI, Professor Narayanan, for his unwavering support and invaluable guidance. His positive attitude and confidence in my abilities have been crucial in me reaching this point in my PhD. I am also very grateful to my professional mentor Dr. Rasouli for his encouragements, availability, and priceless experimental expertise. His can-do yet practical attitude and lightheartedness helped me tremendously. I am very grateful to Professor Erickson and Professor Linke for their guidance throughout my PhD, especially during the preliminary and qualifying exams. The expertise and relentless efforts of our partner teams at Carnegie Mellon University, University of Michigan, Colorado School of Mines has been a sine qua non to the progress and completion of this work, my sincere gratitude goes to Professor Rollett, Professor Vaishnav, Professor Hildreth, Junwon, Dino, Tracey, Subbarao, Nick, and Srujana. Thanks for the fruitful, cheerful, and solution-oriented interactions. Many thanks to Aref, whose help in the lab has been key to the success of my experiments. Special thanks to my labmates (Emily, Valentina, Ramuel, Antash, Shubhankar) whose warmth and support helped me throughout grad school from helping me locate TB207, to the productive discussions, fun lunches and running 5k races together.

Thanks to Meliane, Liliane and Christelle who patiently listened to me rant about pressure transducers and continuity residuals and to my friends who inquired on the state of my sanity throughout this journey (Corine, Diego, Ting, Keivan, Laura). Nanan, uncle Aggrey, mom, dad, Jean-Philippe, Yohan, Melie, Akouavi and Ahoukan have been the best lifeline (or lifenet) I could have wished for. My gratitude for their love, unconditional support (despite not knowing exactly what I have been up to since 2018) and infectious high spirits, is ineffable.

Last but definitely not the least, I am thankful for the financial support of the U.S. Department of Energy's (DOE) Solar Energy Technology Office (SETO) [grant DE-EE0008536] and the computational resources (located at the National Renewable Energy Laboratory) sponsored by the Department of Energy's Office of Energy Efficiency and Renewable Energy.

Abstract

Design, fabrication and experimental characterization of the performance of a molten salt (MS)-to-supercritical carbon dioxide (sCO_2) heat exchanger (HE) for concentrating solar power (CSP) applications using laser powder bed fusion (L-PBF) additive manufacturing (AM) of nickel-based superalloys is presented in this work. The hypothesis is that such additively manufactured HEs will result in a monolithic, compact, low-pressure drop HE that is durable under cyclic operation at high temperature and high pressure in a corrosive salt environment, making them suitable to withstand the stringent operating conditions of the US Department of Energy's Generation 3 technologies roadmap for concentrating solar power systems.

The primary heat exchanger (PHE) is designed to handle temperatures up to 720 °C on the MS side and an internal pressure of 200 bar on the sCO_2 side. Two designs (generation 1 and 2) of the heat exchanger were developed by a co-design effort considering mechanical stresses, thermal and fluidic performance, and AM fabrication constraints such as overhangs, powder removal, and build dimensions. Additional design considerations included creep, fatigue, and thermal stresses. Two Nickel-based superalloys were originally considered to manufacture the PHE- Haynes 230 (H230: 57% Nickel, 22% Chromium, 14% Tungsten, 2% Molybdenum) and Haynes 282 (H282: 57% Nickel, 20% Chromium, 10% Cobalt, 8.5% Molybdenum, 2% Titanium). Ultimately, Haynes 282 was down selected for the HE fabrication based on its better dimensional tolerance, better corrosion resistance to chloride salt, and higher creep strength.

An experimentally-validated, correlation-based sectional PHE core thermofluidic model is developed to study the impact of flow and geometrical parameters on the PHE performance, with varied parameters including the mass flow rate, surface roughness, and PHE dimensions. The model results show that a heat exchanger with a power density of 16 MW/m^3 (including sCO_2 header volume) and effectiveness of 0.93 can be achieved at a heat capacity rate ratio of 0.83.

To experimentally demonstrate the performance of the HE, a 20 pair unit was built and characterized using heated air as a surrogate to the chloride salt on the hot side and sCO_2 in the 100-200 bar range was used on the cold side. The results of exit temperatures and heat transfer rate were compared against the model. The model was able to predict experimental results within 1.00% percent for heat transfer rate, 1.26% percent for exit sCO_2 temperature, and 1.01% percent for exit air temperature. The validated HE model was used to determine the performance of a scaled-up design. With a 20 cm tall build that covers 24 cm x 24 cm of the build plate, a 167.5 kW HE can be built in a single laser machine with a bed size of 25 cm x 25 cm. The impact of system-level variations in inlet temperature on the performance of this HE was established.

Contents

List of Figures

List of Tables

Nomenclature

A_{cr}	Footprint of cross-flow region, $= L_{cr}H$ (m^2)
A_{min}	minimum flow area within the pin array (m^2)
A_{pin}	Pin half surface area, $= 0.5\pi D_{pin} H_{pin}$ (m^2)
A_{surf}	Pin array footprint area (m^2)
A_w	Wall surface area not including the pins (m^2)
AM	Additive-manufacturing
C	Heat capacity rate (W/K)
c_p	Specific heat capacity (J/kg-K)
C_r	Heat capacity rate ratio
CT	Computed tomography
D_{Amin}	Heat sink hydraulic diameter based on A_{min} and P_{min} (m)
D_h	Hydraulic diameter based on pin fin size (m)
D_{pin}	Pin fin diameter (m)
f	Darcy friction factor
h	Average heat transfer coefficient (W/m^2-K)
H	Height (m)
H282	Haynes 282
HS	Heat sink
HX	Heat Exchanger
IN740H	Inconel 740H
k_w	Wall conductivity (W/m-K)
L	Length (m)
$\dot{m}$	Mass flow rate (kg/s)
MS	Molten salt
N_{pin}	Number of pin fins in the array

N_{plates}	Number of plates in the heat exchanger
N_{row}	Number of pin fins rows in the flow direction
NTU	Number of Transfer Units
Nu_{Amin}	Average Nusselt number based on D_{Amin}
Nu_{Dh}	Average Nusselt number based on hydraulic diameter
P_{min}	wetted perimeter associated to A_{min} (m)
PCHE	Printed Circuit Heat Exchanger
PHE	Primary Heat Exchanger
Pr	Prandtl number
Q	Thermal rating (W)
R”	Thermal resistance (K-m^2/W)
R_z	Peak to valley roughness (μm)
Re_{Amin}	Reynolds number based on D_{Amin}
Re_{Dh}	Reynolds number based on hydraulic diameter
S_L	Longitudinal pitch (mm)
S_T	Transverse pitch (mm)
sCO_2	Supercritical carbon dioxide
t	Thickness (m)
UA	Overall heat transfer conductance (W/K)
VS	Vortex shedding
W_{max}	Overall width of heat exchanger core (m)

Greek symbols

α	Aspect ratio, $= H_{pin}/D_{pin}$
β	Pitch ratio, $= S_{L/T}/D_{pin}$
ε	Heat exchanger effectiveness
η_{pin}	Fin efficiency

Subscripts

c	Cold
co	Cold outlet
cr	Cross-flow
h	Hot
ho	Hot outlet
vs	Vortex shedding
w	wall

Chapter 1 Introduction, literature review, and objectives

1.1. Introduction

Solar energy has the potential to offer a cleaner and reliable way to meet the energy needs while offsetting CO_2 emissions. Advances in technology and reductions of cost associated with solar systems have allowed the US solar capacity to increase over the years. There are essentially two ways to harness solar energy: photovoltaics (PV) systems which directly convert solar radiation to electricity through the agency of semi-conducting materials or concentrated solar power (CSP) systems that focus the sun's irradiance to generate heat which can subsequently be used to produce electricity. Although the former medium is more prevalent nowadays, a key advantage of the latter lies in its thermal storage ability. Recent focus on solar thermal electric power generation has been on operating at higher receiver temperatures and using supercritical carbon dioxide (sCO_2) in the power cycle. The potential for thermal storage, as opposed to the more expensive battery storage of associated utility scale photovoltaic systems, is often presented as a key advantage of the solar thermal power generation route. Based on their respective receiver designs, three pathways are being investigated to couple the power cycle and the solar field paired with storage. Of the three pathways considered (liquid, gas, solid particles medium) the liquid one involving the use of molten salt (MS) solar thermal systems, is mature and is based on the industry's experience with nitrate-based salts [1]. Another noteworthy advantage is the fact it has been successfully commercialized over three decades with examples including the Andasol 1 plant in Spain, the Noor I Ourzazate CSP power station in Morrocco and the Shouhang Dunhuang 100 MW plant in China [2].

However, higher temperature salts, such as chloride salt mixtures are needed to obtain desired turbine inlet temperatures of 700 °C. As per the US Department of energy's Generation 3 technologies roadmap for concentrating solar power systems, the MS-to-sCO_2 primary heat exchanger (PHE), which transfers heat from the stored salt in the hot tank to the working fluid of the power generation cycle (sCO_2), is a key component that needs to be developed to facilitate the molten salt pathway to solar thermal power generation [1]. The operating conditions of this PHE are demanding – with surface temperatures of up to 720°C on the MS side, pressure of 200 bar on the sCO_2 side, 1 bar on the MS side and potential for corrosion by the salt. The work presented in this dissertation addresses the design and development of this component of the solar thermal plant.

1.2. Literature review

1.2.1. sCO_2 for power generation

A fluid is said to be supercritical when it is at a state defined by a temperature and pressure higher than the critical values of the substance of interest. In this state, it is not possible to distinguish whether the fluid is in its gas or liquid state, as the properties of a supercritical substance look like an amalgamation of liquid and gas properties [3]. A supercritical fluid can be thought of as a hybrid substance that would expand like a gas despite having a density much closer to that of a liquid. A supercritical fluid is characterized by a relatively higher thermal conductivity and heat capacity, as well as a high thermal diffusivity. Comparing this peculiar substance to the liquid state, the diffusion coefficient and compressibility factor of a supercritical fluid are higher while the viscosity and solubility parameters are lower [3]. This association of properties provides supercritical fluids with unique features and the capacity to enhance a wide range of thermal and chemical processes ranging from caffeine extraction to applications in concentrated solar power systems. Among the fluids typically used in their supercritical state, carbon dioxide has gained significant attention these past years. One of the first known uses of supercritical CO_2 in turbomachinery is traced back to the Sulzer Brothers and their patent of a partial condensation CO_2 Brayton cycle in 1948. Further research was performed, and a turning point was reached with the work of Feher: in 1967, this researcher trying to overcome the limitations of the Rankine and Brayton cycles, designed a cycle with a working fluid at a pressure higher than the critical pressure throughout the loop [4]. Even though there was no constraint on the choice of fluid, Feher decided to use CO_2 because of its low critical pressure compared to water, inertness, high availability and the vast documentation on CO_2 properties that could hence provide solid grounds for his investigation. He concluded that besides a high efficiency and low volume to power ratio, this supercritical cycle had the advantages of avoiding turbine blades erosion and cavitation in the pump [4]. Another important benefit was that this cycle required a smaller number of stages to achieve the desired compression and expansion. Nevertheless, the author pointed out that to make the cycle efficient, it was necessary to recuperate the heat at the turbine outlet and reuse it to preheat the compressor effluent before it entered the combustor. This recuperation process was made more complex due to the sharp variation in properties near the critical point. Today's use of sCO_2 in the power generation industry spans a wide spectrum of applications including nuclear, fossil fuel, geothermal, solar thermal plants [5] for the increase in efficiency and the low footprint which can be achieved with this working fluid. In the CSP industry in particular, the US Department of Energy identified the sCO_2 Brayton cycle as the best candidate to optimize the efficiency of solar thermal power plants and make them cost-competitive with other energy systems [1]. This new generation of CSP systems are characterized by high receiver and fluid temperatures (exceeding 700 °C), required to increase the efficiency, reduce the cost of solar thermal electricity, and help achieve the 2030 Department of Energy (DOE) target of 5¢ per kWh for a baseload CSP. Three pathways (molten salt, falling particles, gas) towards that objective are being investigated but in all three cases, the temperatures and the fluids involved present design challenges in terms of material selection, manufacturing techniques and durability.

1.2.2. Heat exchangers (HE) for high pressure high temperature applications (PCHEs, brazed plates)

Three potential conceptual designs were identified for MS-sCO_2 PHE in the DOE report [2] a shell and tube design, a printed circuit heat exchanger (PCHE) design, and a shell and tube serpentine design. However, details of design, modeling and performance were not reported. Table 1.1 shows a summary of PCHE literature review. It includes salient characteristics of the PCHE geometry, the fluid considered as well as the operating conditions in terms of temperature and pressure. Table 1.1 also specifies whether the heat exchanger was studied in the context of a numerical or analytical work. A typical architecture for a compact metallic PHE for this application is that of microchannel (printed circuit/micro-lamination) heat exchangers, for their compactness and high effectiveness. The key stages in the fabrication process include chemical etching of multiple metallic shims to create flow geometries and diffusion bonding/brazing a stack of shims to create a heat exchanger. Headers need to be designed and brazed or welded to the stack. Such heat exchangers have been proposed for recuperators in the sCO_2 cycle by many groups. Variants on the design include changes to the patterns etched in the shims that form channels such as straight, zig-zag channels or pin arrays [6-13].

Table 1.1. PCHE literature review summary.

HE Geometry - Ref	Method	Fluids (hot-cold)	Operating conditions
Straight, zigzag channels PCHE Pandey et al. [6]	Numerical and modelling	CO_2 - CO_2	T = 110-427 °C P = 7.6-21 MPa
Zigzag channels PCHE – Zhang et al. [7]	Numerical	CO_2 - CO_2	T = 295.15-390.15 K P = 8.5-21 MPa
Sinusoidal fins PCHE – Saeed et al. [8]	Numerical	CO_2 - CO_2	T = 108-280 °C P = 2.5-8.3 MPa
Multi flow path PCHE with arc ribs – Jing et al. [9]	Numerical	CO_2 - CO_2	T = 423-593 K P = 8-13 MPa
PCHE with airfoil fins – Wang et al. [10]	Experimental	Ternary salt (hot side) – synthetic oil (cold)	T = 81–254 °C [-]

Rectangular microchannels PCHE – Khalesi et al. [11]	Numerical	Liquid sodium – CO_2	T = 300-366 K P_h = 1 bar P_c = 8, 10, 30 MPa
Airfoil-fin PCHE – Shi et al. [12]	Numerical	Molten salt - CO_2	T = 873-1073 K P_c = 20 MPa
Cambered airfoil fins PCHE – Chu et al. [13]	Numerical	CO_2 (single fluid with temperature applied as BC)	T_initial = 473.15 K P_initial = 8 MPa T_plate = 313 K
Zigzag PCHE – Katz et al. [14]	Experimental	He-CO_2	T_h = 20-550 °C P_h = 4 MPa T_c = 20-350 °C P_c = 20 MPa
Airfoil-fin PCHE – Wang et al. [15]	Experimental	Molten salt-synthetic oil	T_h = 198-254 °C T_c = 80-165 °C
Straight channel PCHE – Kruizenga et al. [16]	Experimental and numerical	CO_2-H_2O	T = 29-65 °C and P = 7.5-10.2 MPa
Straight channel PCHE – Ren et al. [17]	Numerical	CO_2-H_2O	T_h = 40-100 °C P_h = 7.5-8.1 MPa T_c = 10-50 °C P_c = 0.1013 MPa
Zigzag channel PCHE – Jin et al. [18]	Experimental	CO_2-H_2O	T_h = 45-87 °C T_c = 20-30 °C P = 7.5-9 MPa
Zigzag channel PCHE – Safari et al. [19]	Numerical	CO_2-CO_2	T = 400-630 K P_h = 8.5 MPa P_c = 23 MPa
Straight channel PCHE – Su et al. [20]	Numerical	Lead bismuth eutectic-CO_2	T_hi = 623.15-773 K P_ho = 0.1 MPa T_ci = 423.15-573 K P_co = 15 MPa
Straight channel PCHE – Liu et al. [21]	Experimental	CO_2-H_2O	T_h = 26-122 °C P_h = 7.5-11.97 MPa T_c = 23-61 °C P_c = 0.14-0.18 MPa
Zigzag channel PCHE – Cheng et al. [22]	Experimental	CO_2-H_2O	T_h = 363 – 383 K P_hi = 8.07-8.6 MPa T_c = 293 – 300 K P_ci = 0.16-0.20 MPa
Straight channel PCHE – Chai and Tassou. [23]	Numerical	CO_2-CO_2	T_i = 100-400 °C P_i = 75-150 bar
Straight channel PCHE – Chu et al. [24]	Experimental	CO_2-H_2O	T = 310-375 K P = 8, 9.5,11 MPa
Straight channel PCHE – Han et al. [25]	Experimental and numerical	CO_2-H_2O	T_h = 60-100 °C P_h = 7.6-9.1 MPa

			T_c = 20-50 °C P_c = 0.1-0.24 MPa
Zigzag channel PCHE – Jin et al. [26]	Numerical	CO_2-H_2O	T = 290 - 370 K
Zigzag channel PCHE – Liu et al. [27]	Numerical	CO_2-H_2O	T_h = 101-83 °C P_h = 7.96-11.8 MPa T_c = 25-27 °C P_c = 0.15-0.14 MPa
Zigzag channel PCHE – Wang et al. [28]	Numerical	CO_2-CO_2	T = 651-385 K P = 90.6-148.5 bar
Airfoil-fin PCHE – Han et al. [29]	Experimental and numerical	CO_2-H_2O	T_h = 324-366 K P_h = 7.6-8.8 MPa T_c = 296.15 K P_c = 0.13 MPa
Airfoil-fin PCHE – Wu et al. [30]	Numerical	CO_2-CO_2	T = 381-553 K P_co = 8.28 MPa P_ho = 2.52 MPa
Airfoil-fin PCHE – Han et al. [31]	Numerical	CO_2-H_2O	T = 16.4-155 °C P_h = 8.35 MPa P_c = 0.147 MPa
Airfoil-fin PCHE – Zhang et al. [32]	Experimental and numerical	CO_2-H_2O	T_h = 70-110 °C P_h = 7.6-9 MPa T_c =16-25 °C P_c = 0.1 MPa
Airfoil-fin PCHE – Chang et al. [33]	Experimental	CO_2-H_2O	T_h = 30-60 °C P_h = 8-10 MPa T_c = 20-40 °C P_c = 0.15-0.26 MPa

These studies have typically considered lower temperature applications for which the hot side inlet temperature is lower than 600 °C. These temperatures permit the use of stainless steel or Inconel for which etching and diffusion bonding schemes are well established.

Katz et al. [14] experimentally studied a 17-plate photochemically etched and diffusion bonded PCHE with zigzag channels. Their experiments used Helium and sCO_2 at temperatures up to 550 °C and 350 °C, respectively. The primary goal of the study was to assess the thermofluidic performance of commercially available architectures by pressure drop and heat transfer experiments and develop correlations. In addition to this main objective, the study also provided some valuable insight regarding the contribution of the headers: while 10% of the total heat transfer happens in the headers, a sizable fraction of the pressure losses was associated with the headers (28-34%) [14], hence the need for a thorough header design was noted.

Wang et al. [15] experimentally studied the performance of a 316L stainless steel PCHE with airfoil fins on the hot side and rectangular microchannels on the cold side. The two fluids used were a ternary salt (Hitec) and a synthetic oil, with temperatures varying from 198 to 254 °C and 81.5 to 165.2 °C for the hot and cold side, respectively. This PCHE shows a better performance compared to straight and zigzag channels. In a numerical study [12] following up this experimental work, a 3D numerical model was designed and compared against the experimental results for validation. In the numerical work, the hot side with the airfoil geometry, the $MgCl_2$-KCl salt temperature varied from 534 to 800 °C and the cold side had a straight rectangular microchannel geometry where sCO_2 flowed at temperatures between 506 and 800 °C. The comparison revealed a maximum deviation of +/- 12% between experimental and numerical results and an improved performance evaluation indicator compared to a zigzag channel.

In summary, several studies have been conducted to assess how to improve the performance of heat exchangers for CO_2 applications by modifications such as variations on the channel design with straight [16, 17, 20, 21, 23, 24, 25], zigzag/wavy channels [18, 19, 22, 26, 27, 28] and the use of airfoil fins [29, 30, 31, 32, 33].

Two noteworthy limitations of PCHEs are inherent to the way they are manufactured. The first one is the lack of flexibility in the design: because of the diffusion bonding procedure in the fabrication of PCHEs, the design window is typically narrowed down to using patterns which are very similar, on both the hot and cold sides in order to establish and maintain a uniform stress across the stack of plates undergoing the diffusion bonding process.

In addition to this first constraint, another disadvantage has to do with the reduced strength of diffusion bonded heat exchangers which are prone to failure at a diffusion bond location. Kapoor et al. [34] studied the tensile strength of diffusion bonded H230 specimens and compared their findings against the strength of the base material. It was determined that the diffusion bonded H230 specimens systematically exhibit lower strengths than the original base material. At 750 °C, the yield strength of the Nickel-plated and non-Nickel-plated H230 specimen were 76% and 82% of the base sheet material. Additionally, the study found evidence of ductile failure (cup-and-cone) at the diffusion bond, thus reinforcing existing concerns regarding the durability of diffusion-bonded heat exchangers, especially in applications calling for high temperatures and pressures.

1.2.3. Additively manufactured heat exchangers

To address the aforementioned limitations of PCHEs, this research focuses on the mechanical and thermofluidic design of a compact additively manufactured (AM) chloride MS-sCO_2 primary heat exchanger. Table 1.2 shows a summary of AM heat exchangers with several applications for high temperature systems. Heat transfer and thermal management using additively manufactured components has been on the rise in recent years, with applications in both macro and micro scales [35-41]. These studies exemplify one of the most note-worthy advantages of AM techniques compared with other more conventional manufacturing methods: design flexibility. Pilagatti et al. [35] manufactured heat sink geometries resulting from thermal optimization, and Cormier et al. [36] and Dupuis et al. [37] investigated the performance of pyramidal fins heat sinks. Aside from the unparalleled level of design versatility afforded by AM, another note-worthy advantage considering the observations made by Kapoor et al. [34] is the monolith nature of additively manufactured builds. This feature makes AM a more reliable manufacturing technique especially compared with fabrication techniques that involve welding or brazing.

Table 1.2. AM Heat exchangers literature review summary

HE Geometry - Ref	Method	Material and manufacturing method	Working fluid and operating conditions
Thermally optimized heat sinks -	Numerical and experimental	CL 31 AL Aluminium alloy	Air [-]

Pilagatti et al. [35]		L-PBF	
Pyramidal pin fins array – Cormier et al. [36]	Numerical and experimental	Aluminium Cold gas dynamic spraying (CGDS)	Air [-]
Pyramidal pin fins array – Dupuis et al. [37]	Numerical and experimental	Aluminium Cold gas dynamic spraying (CGDS)	Fluorescent-particles-doped water T_pyramid_base = 360 K
Manifold-microchannel heat sinks - Kong et al. [38]	Numerical and experimental	AlSi10Mg L-PBF	Water T_in = 17.2-20.1 °C P_in = 1.15-1.2 bar
Heat sinks with rectangular fins – Schleifer and Regev [39]	Experimental	Polymer-based composite material with vat photopolymerization (VPP)	[-] Heat sink placed on top of a hot plate kept at 50 °C
Staggered, straight, zigzag heat sinks – Lad et al. [40]	Numerical and experimental	Aluminium and Copper SLS (selective laser sintering)	Water (experimental), Water, WEG50, NOVEC 7300 (numerical) T_max = ~110 °C T_in_coolant = 30 °C
Heat pipes with a rectangular cross section – Yun et al. [41]	Numerical and experimental	Aluminium Selective laser melting	Acetone T = 15-70 °C
Inter-layer channel heat exchanger – Greiciunas et al. [42]	Numerical and experimental	Pure titanium Selective laser melting	Water T_wall = 318 K T_inlet = 293 K
Inter-layer channel heat exchanger – Greiciunas et al. [43]	Numerical and experimental	Pure titanium Selective laser melting	Air T_h = 363 K T_c = 290 K
Compact plate-fin HX with 1) twisted fins, 2) improved rectangular fins and 3) conventional rectangular fins – Ning et al. [44]	Experimental and numerical	316L stainless steel L-PBF	Water T_h = 353 K T_c = 298 K
Cylindrical, triangular, star, dimpled-sphere pin fin arrays – Ferster et al. [45]	Experimental	Inconel 718 Direct metal laser sintering (DMLS)	Air [-]
Gyroid and Schwarz-D structures HX –	Numerical	[-]	CO_2 T_hi = 553 K

Li et al. [46]			T_ci = 494 K P_hi = 2.545 MPa P_ci = 8.283 MPa
Schwarz-D HX cells – Kelly et al. [47]	Experimental	ZrB2 zirconium diboride Binder jet additive manufacturing	[-]
Gyroid and primitive – Alteneiji et al. [48]	Numerical	[-]	Water T_h = 355 K T_c = 300 K
Semi-elliptical channel modular HX – Singh et al. [49]	Numerical	Ceramic [-]	Molten salt – CO_2 T_h = 750 °C P_h = 0.1013 MPa T_c = 540 °C P_c = 20 MPa
Semi-elliptical channel modular HX Du et al. [50]	Experimental and numerical	Silicon carbide Binder jetting	Air T_hi = 249.8 °C T_ci = 42.5 °C
Manifold heat exchanger – Zhang et al. [51]	Experimental	Inconel 718 Direct Metal Laser Sintering	N_2-Air T_hi = 600 °C Tci = 38 °C
Circular channels – Zilio et al. [52]	Numerical and experimental	Stainless steel 316L Selective laser melting	Integrity tests up to 700 bar

Studies have demonstrated the possibility to use AM as a fabrication process able to enhance the performance of heat exchangers at both the larger scale (overall shape) and smaller scale (subsection/fins) of the design.

Greiciunas et al. [42] fabricated an inter-layer heat exchanger using selective laser melting (SLM). It was made up of a stack of plates including slanted conduits that allow communication between plates on one side, while acting as pins and promoting mixing on the other. The numerical study demonstrated that the inter-layer configuration rendered possible by AM could enhance the heat exchanger performance while reducing flow maldistribution. In a follow-on study [43] the authors validated the numerical findings by conducting experiments on an inter-layer channel heat exchanger manufactured out of commercially pure titanium. Ning et al. [44] both numerically and experimentally studied the heat transfer and pressure drop in compact plate-fin HX with twisted fins, improved rectangular fins and conventional rectangular fins. They concluded that due to its ability to generate more vorticity in the channels, the twisted fins model has the best thermal performance, followed by the improved rectangular channel. One caveat was that these non-conventional geometries come at the price of higher pressure losses. Ferster et al. [45] experimentally investigated the performance of triangles, stars and dimpled-sphere arrays manufactured using direct metal laser sintering and reported that the geometry had a greater impact on heat transfer and pressure drop compared to the spacing in the array. Other examples including Li et al. [46], Kelly et al. [47] and Alteneiji et al. [48] studied heat transfer in triply periodic minimal surfaces (TPMS) and noted an improvement in performance using these geometries. In their studies, Li et al. [46] noted that by inducing more turbulent mixing, the Gyroid and Schwarz-D structures were able to achieve a flow configuration yielding a higher Nusselt number. Although the criterion used to evaluate performance showed an improvement varying from 17 to 100% compared to the zigzag PCHE over the range of Reynolds number considered, it should be noted that a more pronounced enhancement was typically observed at lower Reynolds numbers.

In addition to harnessing the flexibility of AM, several works have used this manufacturing method to tackle applications with stringent requirements dictated by operational conditions such as CSP.

Singh et al. [49] designed a ceramic heat exchanger for CSP applications. The use of ceramics for this application was justified by their superior physical properties and corrosion/oxidation resistance that make them desirable candidates for surviving applications involving corrosive fluids at high temperatures (up to 750 °C). The final geometry is a result of an optimization of thermal performance but also a design that factors in the stress constraints established by the high pressure and temperature requirements for CSP. In a subsequent work, [50] the group printed silicon carbide heat exchangers samples, characterized their properties and experimentally validated the thermal performance using streams of cold and hot air at temperatures varying from 42 to 250 °C. Zhang et al. [51] experimentally validated a compact manifold heat exchanger additively manufactured for high temperature applications. The printed model was made from Inconel 718 and was tested using nitrogen and air at 600 and 38 °C inlet temperatures, respectively. The authors observed not only a good agreement between numerical and experimental results, but they also highlighted a 25% enhancement in heat transfer density compared to an optimal plate fin heat exchanger of the same coefficient of performance. Caccia et al. [53] Established the validity of a ZrC/W cermet PCHE for sCO_2. The fabricated heat exchangers have a good corrosion resistance at 800 °C and 20 MPa. Based on operating conditions from 600 to 800 °C at 200 bar on the sCO_2 side and 1 bar on the molten salt side, it was determined that the cermet PCHE could withstand a stress of 125 MPa, thus yielding a factor of safety of 3 against the flexure strength of the material of 370 MPa. Zilio et al. [52] experimentally and numerically studied the mechanical strength of AM heat exchanger cores with circular channels. A hydrostatic test bench was used to ramp the pressure stepwise all the way to 700 bar and ambient temperature. The study confirmed that the manufactured units could withstand pressures up to 700 bar. The difference in stress between experimental and numerical results varied between 0.6 and 17% difference and the investigators also assessed the influence of heat treatment on the samples. A 15 % difference in stress at 350 MPa before and after heat treatment was observed.

Altogether, while existing literature emphasizes the advantages of using additive manufacturing for heat exchanger design, especially considering improvements in terms of thermofluidic performance, there is not much work addressing the structural aspect of additively manufactured heat exchanger (with and without postprocessing) for CSP application and the impact on this fabrication methodology on the thermofluidic performance of pin fin arrays.

1.3. Motivation and objectives

Literature on high temperature MS-sCO_2 PHE is scarce; the studies mentioned in the previous section highlight the state of the art of AM heat exchangers but, with the exception of Caccia et al. [53], all PHE designs are for lower temperature salts. While AM has been used for heat exchanger and heat sink fabrication, literature on use of metal AM for high pressure and high temperature applications is extremely limited and important questions such as the durability of the heat exchanger or the impact of the AM-introduced roughness on the thermofluidic performance are left unanswered. The objective of the present study is to introduce the design of a compact additively manufactured chloride MS-sCO_2 PHE for solar thermal applications. The mechanical design will include consideration for creep and fatigue for 100,000-hr life of operation. The thermofluidic component of the design includes CFD simulations but also the development of a simplified correlation-based model to evaluate the PHE performance and its sensitivity to a set of relevant geometrical and flow parameters. Experiments are performed on heat sinks, smaller scale versions of the final heat exchanger, to corroborate the numerical predictions of the performance or probe the reasons for potential discrepancies. Another objective of the experimental work is to study the effect of dimensional tolerance of AM fabrication on pressure drop and heat transfer to develop correlations for friction factor and Nusselt number and investigate methods of surface roughness modelling for pin arrays. Finally, the full-scale heat exchanger will be experimentally tested using air and sCO_2.

In summary the aforementioned goals can be defined as:

Objective 1: Design of high temperatures and pressure molten salt to sCO_2 heat exchanger with mechanical considerations,

Objective 2: Assessment of the impact of additive manufacturing on the pressure drop and heat transfer in the heat exchanger core,

Objective 3: Study of the impact of surface chemical smoothing on pressure drop, heat transfer and mechanical stresses,

Objective 4: Experimental validation of the heat exchanger functionality through testing with air and sCO_2, The sections of this work are as follows: Chapter 2 introduces the architecture of the two heat exchangers created in the context of this study, focusing on their salient features and motivations behind the design decisions made. Since these heat exchangers are to be made through AM (specifically L-PBF), it is anticipated that the final thermofluidic and mechanical performances will be impacted by the fabrication technique. The objective of Chapter 3 is therefore to assess how much design and printed HXs differ from each other in terms of performance and understand the underlying mechanisms behind the differences observed. The following section focuses on characterizing heat transfer and pressure drop for sCO_2 in additively manufactured heat sinks. While various correlations for flow through pin arrays exist in the literature, these correlations were derived for arrays fabricated using other manufacturing techniques and resulted from experiments run with different fluids. Chapter 4 aims at selecting appropriate correlations in preparation for the design modeling effort of the following two sections. The first complete iteration of a working HX for the application considered is discussed in Chapter 5 with detailed mechanical and thermofluidic design. CFD and FEA simulations are carried out to ensure that the performance goals for the HX are met in terms of structural soundness and thermofluidic requirements. A simplified thermofluidic model is developed to assess the HX performance over a range of multiple design parameters. In light of the limitations and area of improvements observed at the end of this first iteration, a revised HX design is presented in Chapter 6 and experiments are carried out to evaluate the mechanical integrity of a prototype printed on a lower scale. A full-scale prototype is finally tested in Chapter 7 using air as a surrogate for Molten Salt and the experimental performance at pressure and temperature is compared to the prediction of the thermofluidic model. Concluding remarks and suggestions for future work are presented in Chapter 8.

Chapter 2 Overview of the first- and second-generation PHE design

The objective of this research is to design and experimentally validate the performance of a molten salt to supercritical carbon dioxide heat exchanger for concentrating solar power application using additive manufacturing of nickel superalloys. The motivation behind the geometry and manufacturing processes was to obtain heat exchangers that will yield a compact low-pressure drop design that is reliable under cyclic operation at high temperatures and pressures in a corrosive environment. The heat exchanger is expected to operate at 200 bar and atmospheric pressure on the sCO_2 and molten salt sides, respectively. The inlet temperatures of the molten salt and sCO_2 are 720 °C and 500 °C, respectively, with thermal gradients set up along the HE length and expected permanent deformation in terms of creep. Additional constraints pertaining to manufacturing (overhanging structures, minimum wall thickness, pin array density) will also be taken into consideration in the design process. In this Chapter, two generations of the HE design are presented. These designs build on established performance results of heat exchangers (e.g. higher effectiveness of counterflow HE) and incorporate constraints dictated by the expected operating conditions of the HE. The design choices and comparison between the designs is provided. Details of the simulations that support these designs are provided in Chapters 5 and 6.

2.1. First generation (Gen 1) HE design

The first generation HE design is shown in Figure 2.1. As depicted in the cut-away view in Figure 2.1(b) and (c), the core of the PHE is made up of several "cold plates" within which sCO_2 flows through microscale pin arrays, while MS flows around and in between the plates in parallel channels.

The PHE cold plates are connected to an inlet header that distributes the sCO_2 between the plates and collector header on the other end of the core where the sCO_2 exits the HX unit (Figure 2.1(a)). A staggered pin array architecture (see detail in Figure 2.1(d)) is used for the microscale regions since it leads to higher heat transfer rate and better flow distribution than parallel microchannels.

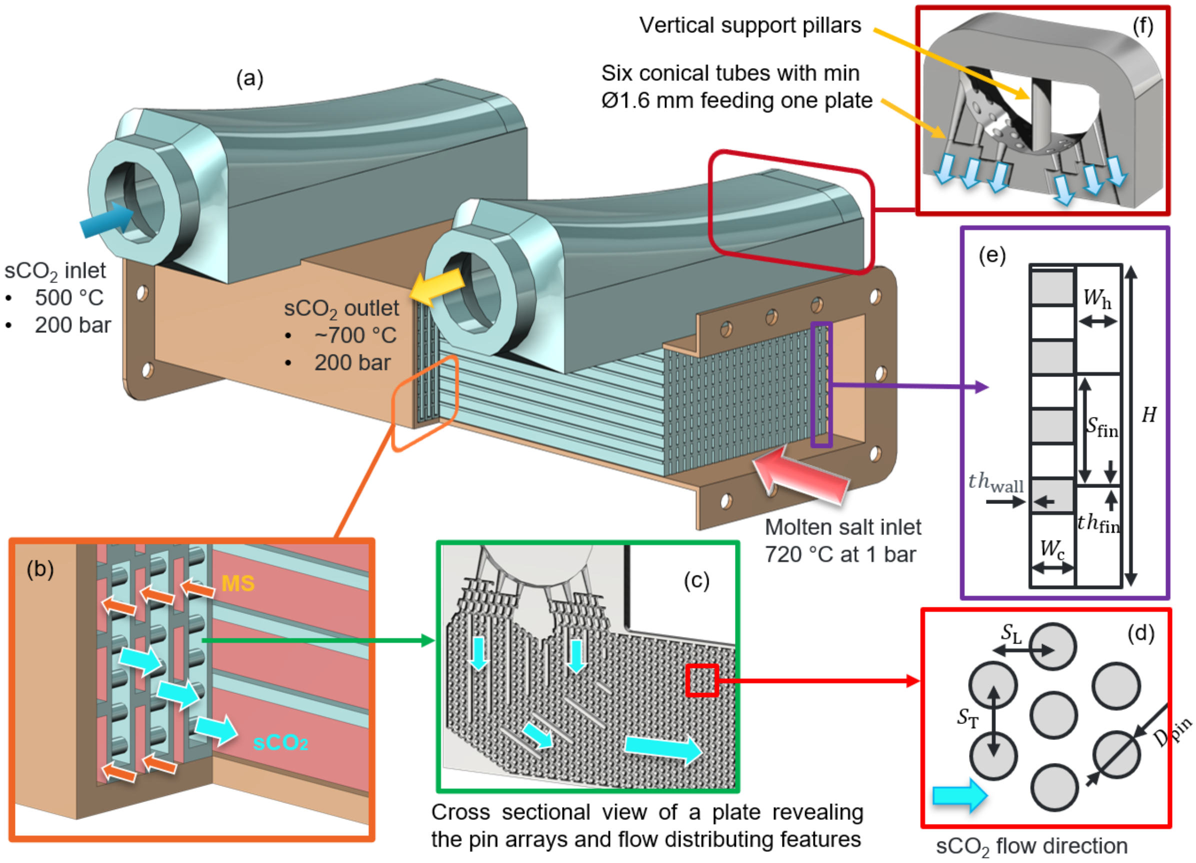

Figure 2.1. Proposed concept for AM PHE. (a) solid model of the PHE with a cut-away view of the core architecture, (b) cut-away view of the core showing the sCO_2 and MS passages, (c) view of the pin arrays and distributing features, (d) top view schematic of the pin array, (e) schematic of the cross-sectional view of a cold plate and adjacent hot side, (f) details of the header design with vertical support pillars and distributor tubes to direct the flow into the plates.

The sCO_2 headers are located on the top side of the duct, the sCO_2 stream enters through the inlet header and is distributed into plates as shown in Figure 2.1(c). Within each plate, sCO_2 enters a cross flow section, followed by a counter-flow section and a second cross flow region before the fluid exits the unit. Considering sCO_2 and molten salt flow directions, the sCO_2

entrance region is partially in a cross-flow configuration. Although fully counter-flow design is favorable for optimal heat exchange, headers are located outside the MS flow; such a placement of headers is typical of plate heat exchangers. Straight fins are located on the MS side to enhance heat transfer area while facilitating ease of drainage by gravity (when oriented vertically) during idle conditions. The AM PHE design alleviates limitations imposed by the microlamination approach to designing the conventional PCHE by allowing for independent variations in aspect and pitch ratio of the pin array on the sCO_2 side and for variations between the MS and sCO_2 flow passage designs. Furthermore, the headers can be directly integrated and printed with the core as a monolithic unit to reduce failure locations. Scale-up of this design can be achieved by increasing the number of sCO_2 plates in the core and proportionally increasing the header depth. Additional scale-up can be achieved through modularity, by connecting multiple such PHE units. A PHE of dimensions that could be fabricated in the available L-PBF machine (EOS M290, with a build area of 25 cm × 25 cm) is discussed as a baseline.

Details of the design for this Gen 1 PHE are provided in Chapter 5. The design of the PHE was divided into the core (pin array) and header sections. A key consideration in the design of the PHE is the large mechanical stresses imposed on the structure by the 200-bar pressure on the pin array by sCO_2. For each section, iterative mechanical integrity and CFD simulations will be performed to ensure that the final design is structurally sound and able to withstand the imposed stresses, while optimizing the usage of fabrication material and demonstrating desirable flow uniformity. The mechanical integrity and CFD simulations of the PHE were performed using ANSYS Mechanical and Fluent 2021R1, respectively. The detailed design of the Gen 1 HE and associated parametric study will be presented in Chapter 5.

2.2. Second generation (Gen 2) HE design

The second-generation heat exchanger was devised to address the shortcomings identified in the Gen 1 model, namely the low heat transfer rate on the MS side, which hinders compactness of the PHE, and the absence of scalability of the design in the vertical build direction, which is critical for system requiring a higher thermal rating. These changes will also help to reduce the cost of the HE. The large headers of the Gen 1 HE lower its power density, increase the amount of powder required for a given build as well as the printing time for each unit, which ultimately compound into a more expensive HE. It was also found that the flow rates on the MS side limited the heat transfer of that side of the HE.

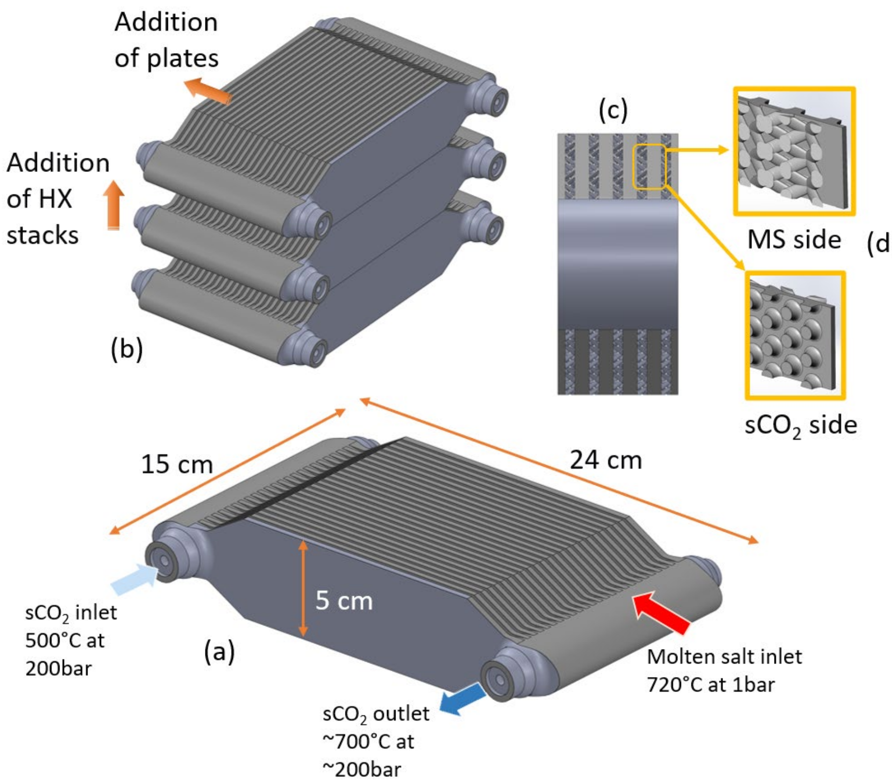

Figure 2.2. Proposed concept for Gen 2 AM PHE (a) overall dimensions and operational conditions, (b) vertical and horizontal scalability of Gen 2 HX, (c) HX view in the direction of the MS flow, (d) cross-sectional view of MS and sCO_2 arrays.

As shown in Figure 2.2, the first significant change effected in the design is with respect to the shape and location of the headers. As illustrated in Figure 2.2(a), the new sCO_2 headers are aerodynamically shaped and integrated into the MS flow passages. Integration of the headers in the flow path allows for scalability of the unit and makes for a near counter-flow design by eliminating the large cross-flow sections in Gen 1 PHE (Figure 2.1(c)). The Gen 1 design can only be scaled up by adding more plates in the depth (horizontal scalability) but as shown in Figure 2.2(b) with the Gen 2 architecture, it is now possible to achieve vertical scalability by building the stacks one on top of the other. The overall length of a single Gen 2 stack, which conforms to the dimensions of the EOS M290 build plate, is 24 cm, including the headers. The sCO_2 pin array plates are 18 cm in total length and include 2.3 cm long diverging and converging sections near the headers followed by a 13.4 cm long rectangular section that is 5 cm tall. Twenty-six such pin array plates are assembled in the width to make up the stack with a nominal rating of 20.7 kW under the current design conditions listed in Table 2.1. The second major change to the design is depicted in Figure 2.2(c) and (d) showing a side view of the Gen 2 HE and cross-sectional view of the pin array of the sCO_2 and MS plates. Unlike the Gen 1 version, the MS side is such that no clear path exist from inlet to outlet on the MS side, thus preventing the fluid from rapidly covering the whole length of the HE.

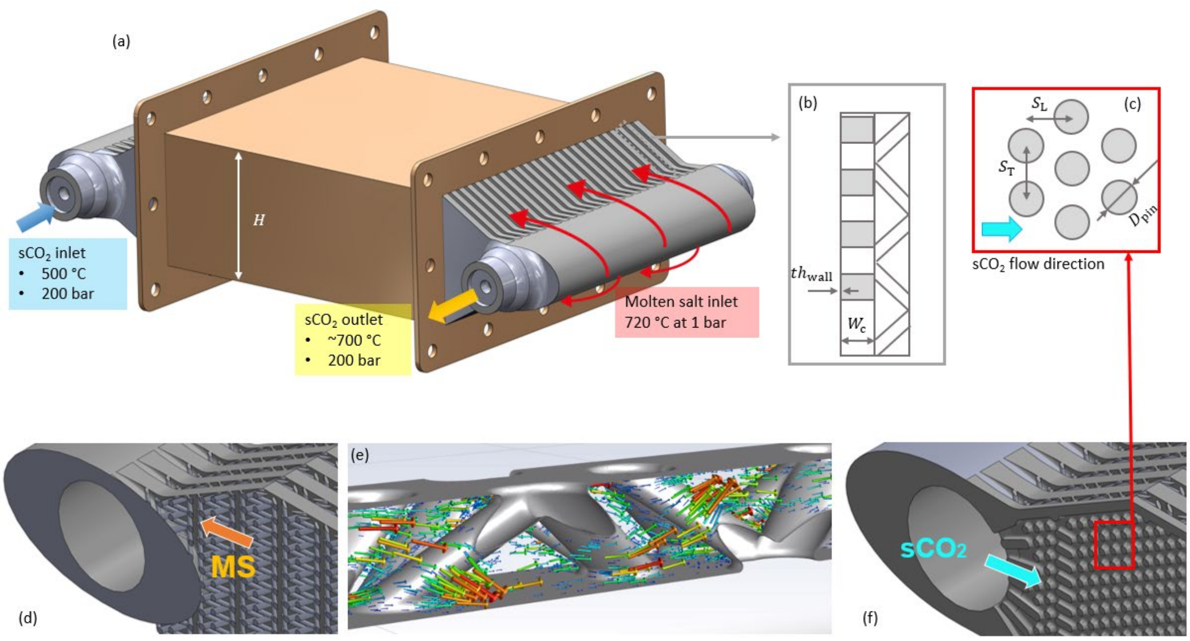

Figure 2.3.(a) Gen 2 PHE concept and expected operating conditions, (b) schematic of the cross-sectional view of a cold plate and adjacent hot channel with 3D lattice of slanted pins, (c) schematic of the top view of the pin array, (d) MS flow in 3D lattice, (e) velocity vectors illustrating flow path in the MS lattice, (f) cross view of sCO_2 flow passages.

Figure 2.3 shows the Gen 2 design and provides a detailed view of the MS and sCO_2 plates (b-d, f), along with a close-up view on the flow path in the lattice of pins on the salt side (e). By comparing Figure 2.1(c) with Figure 2.3(f), the less efficient cross flow zones observed in Gen 1 are minimized in the Gen 2 PHE. The MS side channel width is 1.8 mm, with a lattice of slanted pin fins, tilted 45 degrees in both the flow direction and in the transverse direction to form the three-dimensional periodic flow network (see Figure 2.3(e)). Replacing the rectangular channels on the MS side in the Gen 1 design by a 3D lattice of pins improved the thermal performance of the PHE by providing additional surface area for heat transfer while increasing the residence time and mixing of the fluid in the channel. This design modification is intended to decrease the thermal resistance on the hot side of the PHE; however, the more intricate flow path in the lattice structure (see Figure 2.3(e)) is anticipated to increase pressure drop when compared to the parallel channel path in the Gen 1 design.

Table 2.1. Operating conditions corresponding to the design baseline.

T_{MS_i} (°C)	720
T_{sCO2_i} (°C)	500
P_{MS_i} (bar)	1
P_{sCO2_i} (bar)	200
$\dot{m}_{sCO2}$ (g/s)	80
$\dot{m}_{MS}$ (g/s)	120

2.3. Design Process for Gen 1 and Gen 2

Altogether, the design stages for the above-mentioned PHEs can be summarized into the flowchart shown in Figure 2.4. The design procedure starts by a by a bottom-up approach in which a detailed structural analysis of pin array is performed to determine the parameters space that will enable a structurally sound cold plate. In the top-down thermal design, a correlation-based model is developed and used to perform a parametric sweep to identify designs with high effectiveness. The overall design of the PHX is first described, followed by a discussion of the bottom-up and top-down approaches.

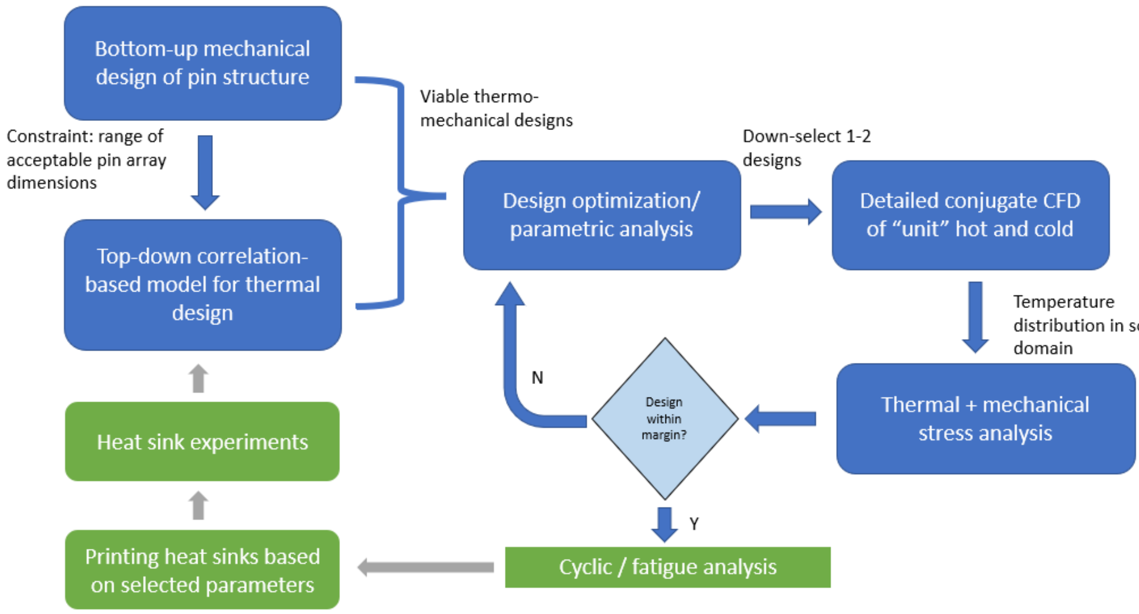

Figure 2.4. Summary of the PHEs design strategy.

Once the operational space is defined, the analysis is narrowed-down to an optimal design used for further inquiry: a detailed conjugate CFD analysis is conducted for a cold-hot unit at the end of which the temperature distribution in the solid domain of the heat exchanger is known. This temperature map then becomes an input in the thermo-mechanical analysis that evaluates the combined impact of pressure loads and temperature gradient on the structural integrity of the heat exchanger. Finally, simulations are carried out to evaluate the durability of the heat exchanger against creep and fatigue failures. Simultaneously, experiments are performed on heat sinks designed using the selected parameters ranges to incorporate the effect of surface roughness and printability on the pressure drop and heat transfer, while providing some confidence in the printability of the designed geometries.

The next two chapters will focus on the printability of the HX core and the impact on pressure drop and heat transfer, and chapter 5 and 6 will discuss the detailed design of Gen 1 and Gen 2 PHEs.

Chapter 3 Impact of Additive Manufacturing (AM) on pin array core and roughness reduction study

One of the potential issues with Laser Powder Bed Fusion (LPBF) is that the roughness, especially on down-skin features, and/or internal blockage due to incomplete powder removal can result in excessive pressure drop. To mitigate these issues, an iodine-based chemical treatment to smoothen the internal flow passages of the HE was explored. The iodine-based is a self-terminating etching process that uniformly removes material from all fluid-accessible surfaces while preserving the intricate geometrical features [54]. This chemical treatment is a two-phase process that includes an iodization followed by the dissolution of the iodized region. Adjusting parameters such as temperature and solvent composition allows to control how much material gets removed.

This chapter discusses the differences between pressure drop in design and printed pin array core of the PHE using experimental and CFD simulations. After an introduction of performance changes induced by AM, the chemical smoothening method to reduce flow restriction in internal passages is presented, and experiments are conducted on treated and non-treated pin array samples. These results are compared against CFD simulations conducted after collection of samples of the internal geometry of the tested pin array via computerized tomography (CT) scans.

3.1. Literature review on performance changes between design and printed arrays

The study of the effect of surface roughness on pressure drop and heat transfer can be traced back to Nikuradse's experiments on sand grain coated pipes [55]. His work used sand grains as a proxy for roughness and established that surface roughness not only increased the resistance to flow and promoted interlayer momentum transfer, but it also precipitated the onset of turbulent flow at lower Reynolds numbers. Subsequent studies mostly involved configurations with low relative roughness values until Kandlikar [56] suggested the concept of a constricted flow area as additional parameter in the cases of larger relative roughness as might be seen in microchannels. This new parameter allowed a better correlation in the large roughness and low Reynolds number regime where laminar flow theory appeared to systematically underestimate the friction factor. Recent studies on AM-generated roughness include various channels geometries (straight, wavy, communicating) [57-61] but also investigation of AM pin arrays [62-65]. Kirsch et al. [57] numerically optimized wavy channel geometries for given targets: maximizing the heat transfer, minimizing the pressure losses, or maximizing the combined thermo-fluidic performance. Their study revealed that some objectives could not be achieved for design reasons (wavelength of the channel) but also because of printing implications: the final channel included protrusions that were not anticipated at the design stage. In a later work by the same authors [58] involving Inconel 718 coupons fabricated through L-PBF, it was found that despite having printed channels faithful to the original model, the objective of minimizing the pressure drop could not be achieved because the manufacturing process gave rise to roughness values responsible for a friction factor almost five times that predicted by the numerical work. The same group also conducted a comparative study [63] with L-PBF cylindrical pin arrays built at a 45° angle to the build plate and demonstrated the importance of the streamwise spacing for friction factor and Nusselt number, as well as the impact of pin density on the surface roughness. The successive findings of the authors, along with other results by other research group regarding heat transfer in AM samples are collected in a review chapter [64] that reiterates the advantages of using AM for heat transfer design (namely flexibility, material efficiency and improved heat transfer performance) while highlighting the challenges involved mainly related to how surface roughness and deviation from the design geometry (strongly correlated with the build direction) alter the performance, thus suggesting the need for post-processing of the printed surfaces [64]. The Dupuis et al. [65] investigated pyramidal pin arrays and highlighted important limitations of CFD with respect to design for AM. Through micro particle image velocimetry, an increase in turbulence production in the wake region that ultimately resulted in an increase in turbulence intensity was observed. However, because of the absence of roughness in the CFD geometry, this key feature was not captured numerically. The CFD geometries modeled considered some AM deviations from design features such as tilted fins and channels, but other deviations such as the roundness of the fins features were not captured in the model. The discrepancy observed between the flow structures in the experiments (displaying a greater turbulence intensity) and the CFD could be explained by both the absence of surface roughness and by some of the deviations originating from printing.

The previous studies stress the importance of having a numerical tool or procedure allowing a better estimation of heat transfer and pressure drop of AM pin fin arrays numerically as well as refined correlations that incorporate the effect of surface roughness in the prediction of the thermofluidic performance. The current work will focus on conducting numerical simulations using CT-scans of manufactured parts in attempt to predict pressure drop and heat transfer more accurately. The effect of roughness reduction will also be captured by testing pin arrays that went through several cycles of surface smoothening treatments.

3.2. Introduction of the Self-Terminating Etching Process (STEP)

A novel Self-Terminating Etching Process (STEP) for Haynes 282 was developed by Prof. Hildreth at Colorado School of Mines. This process combines iodine-based sensitization followed by selective dissolution of iodides to uniformly remove material from all fluid-accessible surfaces while preserving elaborate geometrical features. The STEP process has been developed by Prof. Hildreth's group for post-treatment and support structure removal for various metals [54, 66-68]. This process consists in selectively sensitizing a surface by chemically changing its composition so that it can be uniformly dissolved away in a subsequent phase, without affecting the non-sensitized layers of material underneath. This chemical treatment involves two major stages: an iodization stage during which the component's surface is "sensitized" and reacts with iodine to form a layer of metal iodide salts, and a dissolution procedure during which the sensitized layer is dissolved away in mild solvents without affecting the un-iodized layer underneath. As the iodized layer thickens, the dissolution process slows down and it is possible to control how much material is removed by adjusting the temperature and allowing enough time for the iodization to become diffusion limited. These self-terminating aspects of the processes enable uniformity in material removal from all the fluid-accessible surfaces of a complex AM part.

Figure 3.1 show the scanning electron microscope images provided by Prof. Hildreth's group. After 4 hours of iodization at 450 °C, most of the powder particles attached to the pins and walls have been removed and 12 additional hours of iodization at the same temperature allow the removal of more powder, without significantly altering the pin surface. It should be noted however that the larger irregularities on the down-skin are still present at the end of the process.

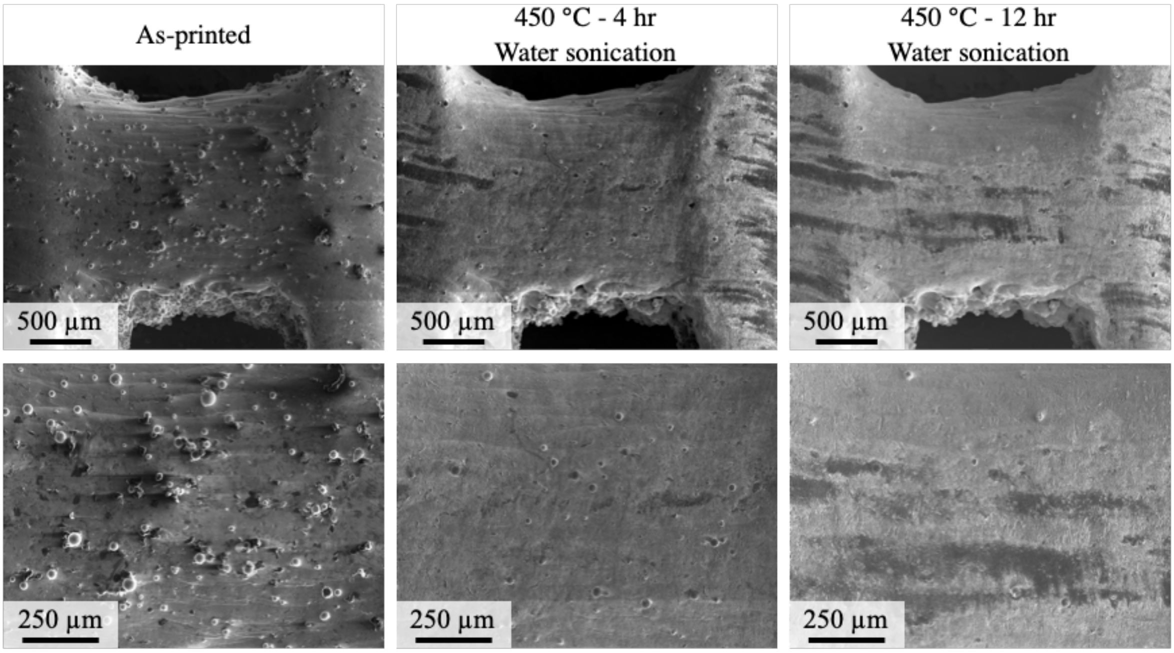

Figure 3.1. SEM images of a pin from a test coupon before and after post-processing; 4-hour iodization and 5 min sonication in water. The absence of the powder particles on the pin surface after 4-hour iodization and dissolution corroborate that the iodization duration of 4 hours successfully removes the powder particles attached to the internal surfaces. Chemical treatment and surface characterization carried out by Prof. Hildreth's group at CSM.

The process was optimized by Prof. Hildreth's group through experimental investigations of iodization temperature, duration, and surface roughness. Material removal rate typically increases with increasing temperatures, but these can sometimes lead to increased surface roughness and unwanted microstructure evolution.

3.3. Experimental study of pin arrays and open channels that underwent different levels of STEP

3.3.1. Description of the samples used in STEP

The effectiveness of STEP is demonstrated by studying the flow characteristics of heat sink samples with and without micro-pin arrays before and after STEP. Three identical pin array heat sinks and three open channel heat sinks were fabricated to assess the efficacy of the STEP treatment. The dimensions of the heat sink were tailored to be accommodated within the available furnace in the lab. The overall design and dimensions of the heat sinks are shown in Figure 3.2. Six narrow channels of length 10 cm, width 12 mm and height 1.8mm as shown in Figure 3.2 were designed to study the efficacy of chemical surface roughness smoothening. The channels are in two design variants. The first is an open channel without any flow interruption by the pin fins just to study the smoothening effect on the end walls. The other design is the same channel but with a pin array between the end walls to capture the impact on the pin walls. Three of each variant were fabricated to ensure repeatability of the baseline (no roughness treatment) measurements and to apply two different roughness treatment parametric variations and ultimately assess their impact relative to the baseline. After the pressure experiment to verify repeatability, the units were sent to Colorado School of Mines (CSM) for chemical treatment and the resulting arrays were sent back to UC Davis to assess the effects of the roughness reduction technique and finally to Carnegie Mellon University (CMU) to characterize the units via CT scanning.

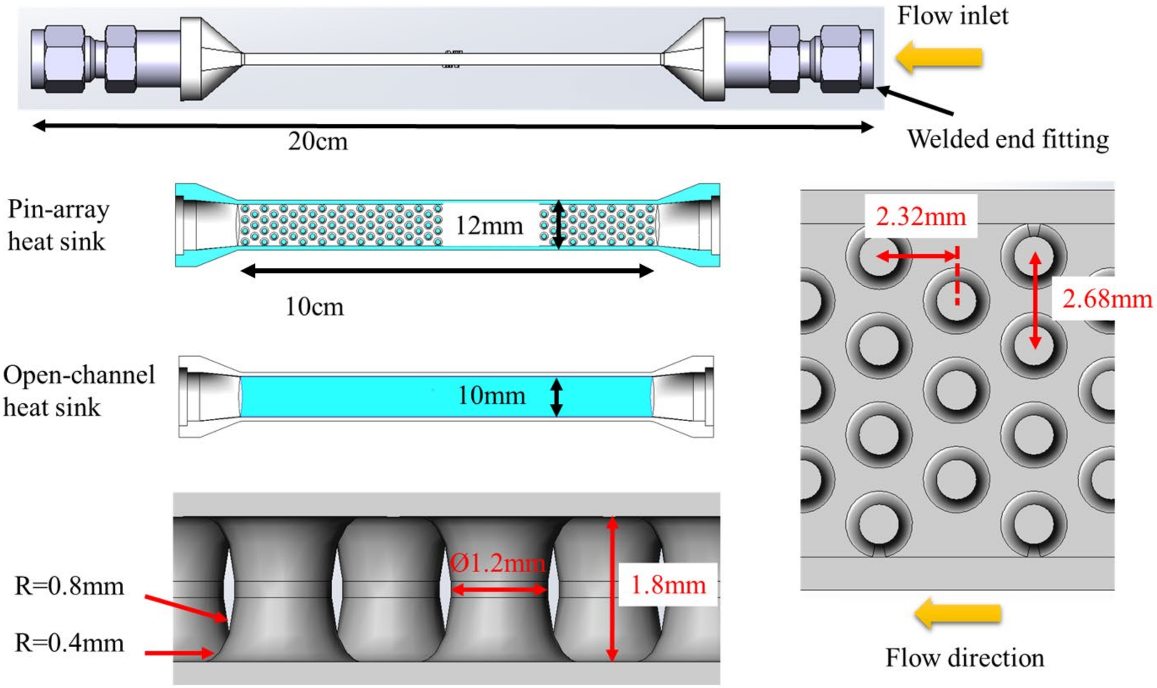

Figure 3.2. Overall dimensions of the pin-array and the open-channel heat sinks designed and fabricated to characterize the STEP process on hydraulic performance. The STEP process was performed at CSM by Subbarao Raikar.

Iodine was loaded in the channels while flowing argon into the channel, and the ends were closed with Swagelok end caps. A baseline was kept untreated for each geometry and the remaining samples were iodized for a different number of cycles. The open channels went through 1 and 4 cycles. The pin arrays went initially through 1 and 2 cycles. The 2-cycle sample was found to have an oxide layer after treatment and was not used any further for this study. After conducting experiments and collecting scans of the internal passages for the 1-cycle pin array, this sample was sent back to complete an additional 9-cycle treatment, thus creating a new 10-cycle array with the exact same geometry for a comparison free of printing variability. For each iodization cycle, the open channels and the micro-pin array channels had 350 mg and 470 mg of iodine, respectively, for a targeted equivalent nickel removal of ~5 μm. The amount of iodine is different because the internal surface area of each geometry is different. A set of channels, one open and one with micro-pin arrays, was then placed in the furnace for a cycle of iodization. Each set was iodized at 450 °C for 4 hours, and furnace cooled. The furnace was ramped up from room temperature to 450 °C at 10 °C/min. The iodide layer on the internal surfaces of the heat sink samples was dissolved by sonicating the channel in water while flowing deionized water through it using a peristaltic pump for 5 min. This was followed by circulating acetonitrile through the channel for 30 min, with the help of a peristaltic pump. The channels were rinsed with water and dried with compressed N_2. The channels were placed in a vacuum chamber for ~ 2 hours to fully dry them. Information regarding the amount of material removed by STEP will be available in an upcoming joint publication with the group of Dr. Hildreth.

3.3.2. Pressure drop experiments results on baseline and treated samples

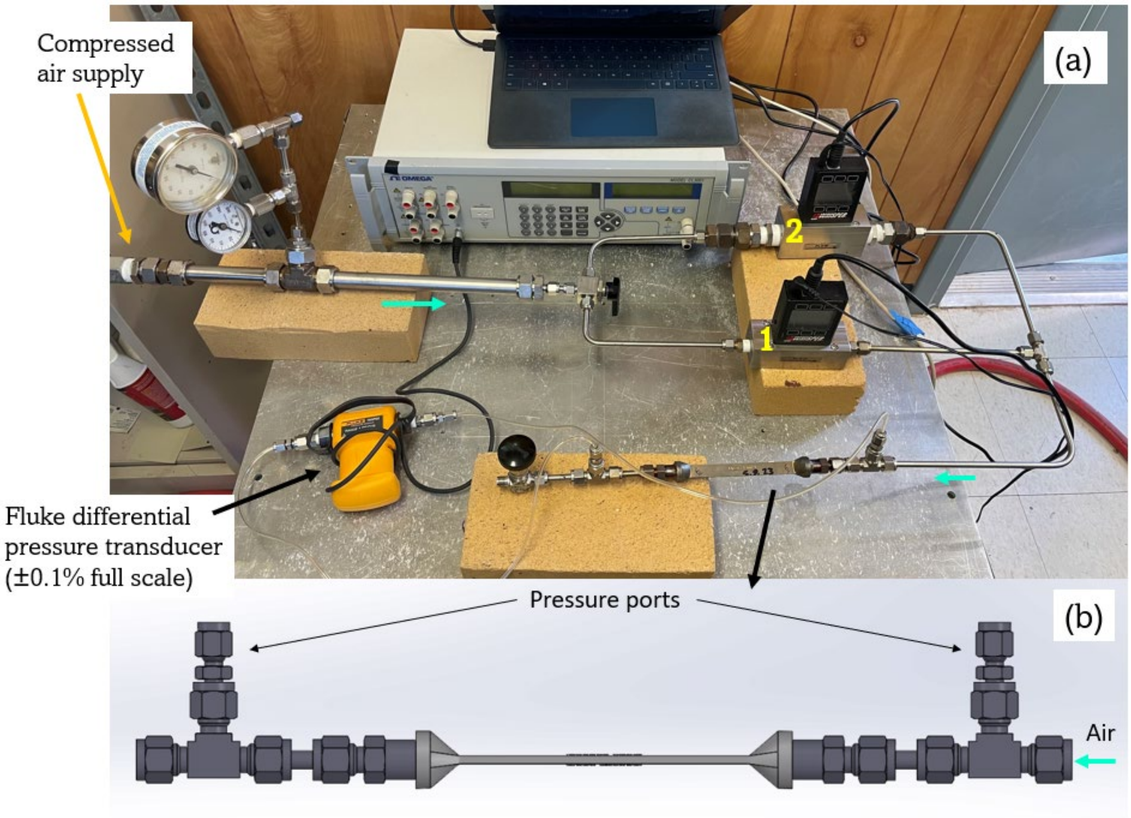

Figure 3.3. (a) Test rig used for baseline channels pressure drop, (b) section of the assembly between the pressure ports

The experimental setup shown in Figure 3.3 includes a compressor, two Alicat flow meters with different flow rate ranges to measure the mass flow rate with accuracy values tabulated in Table 3.1 (these flow meters also record the absolute pressure and the temperature of the fluid), the tested channel connected on either end via a tee fitting to a differential pressure transducer, and a needle valve at the end of the loop.

Table 3.1. Mass flow meters accuracy

	Alicat 1 (20 SLPM)	Alicat 2 (250 SLPM)
Model	MW-20SLPM-D/5M	MW-250SLPM-D/5M
Mass flow accuracy	± 0.6 % of reading or ± 0.1 % of full scale	± 0.8 % of reading or ± 0.2 % of full scale
Pressure accuracy	± 0.5 % of reading	± 0.5 % of reading
Temperature accuracy	± 0.75 °C	± 0.75 °C

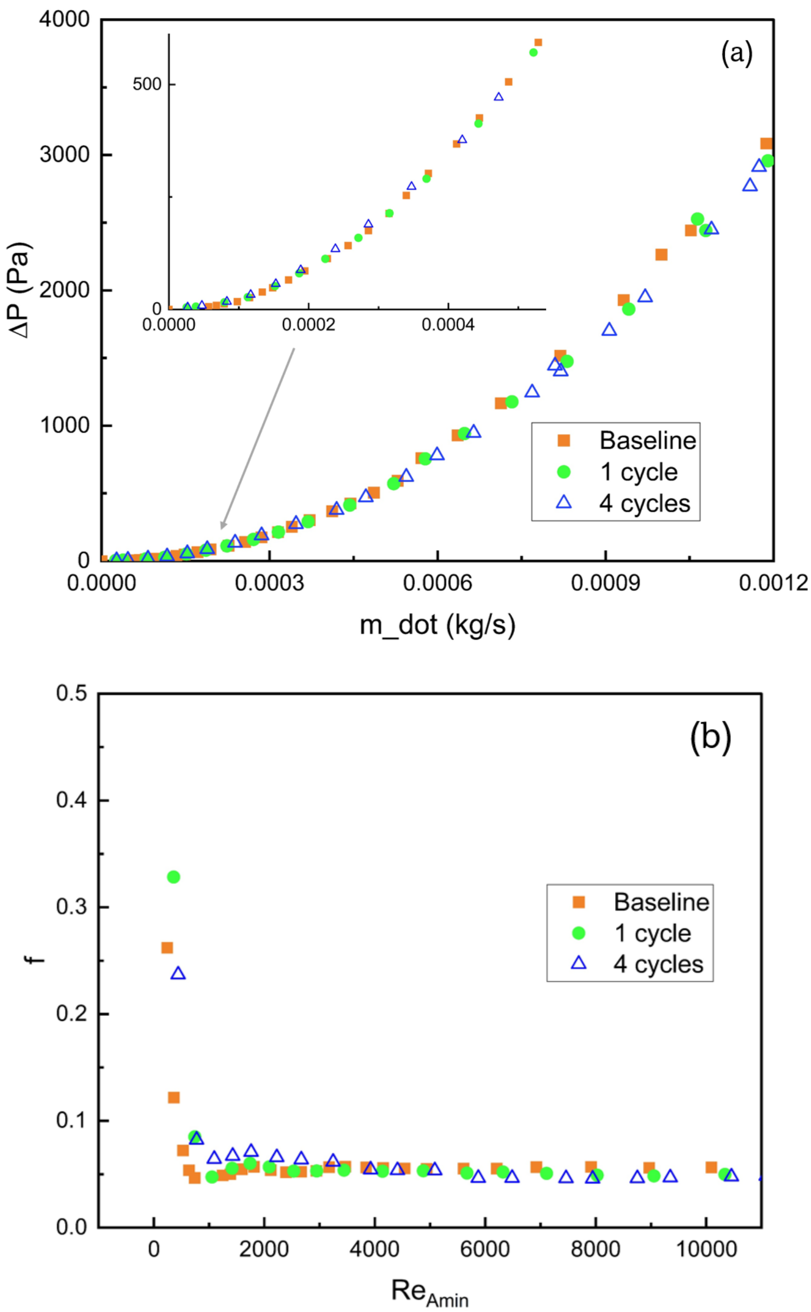

Figure 3.4. Variation of (a) pressure drop with air mass flow rate and (b) friction factor with Re_Amin in open channels that underwent 0 (Baseline), 1 and 4 STEP cycles.

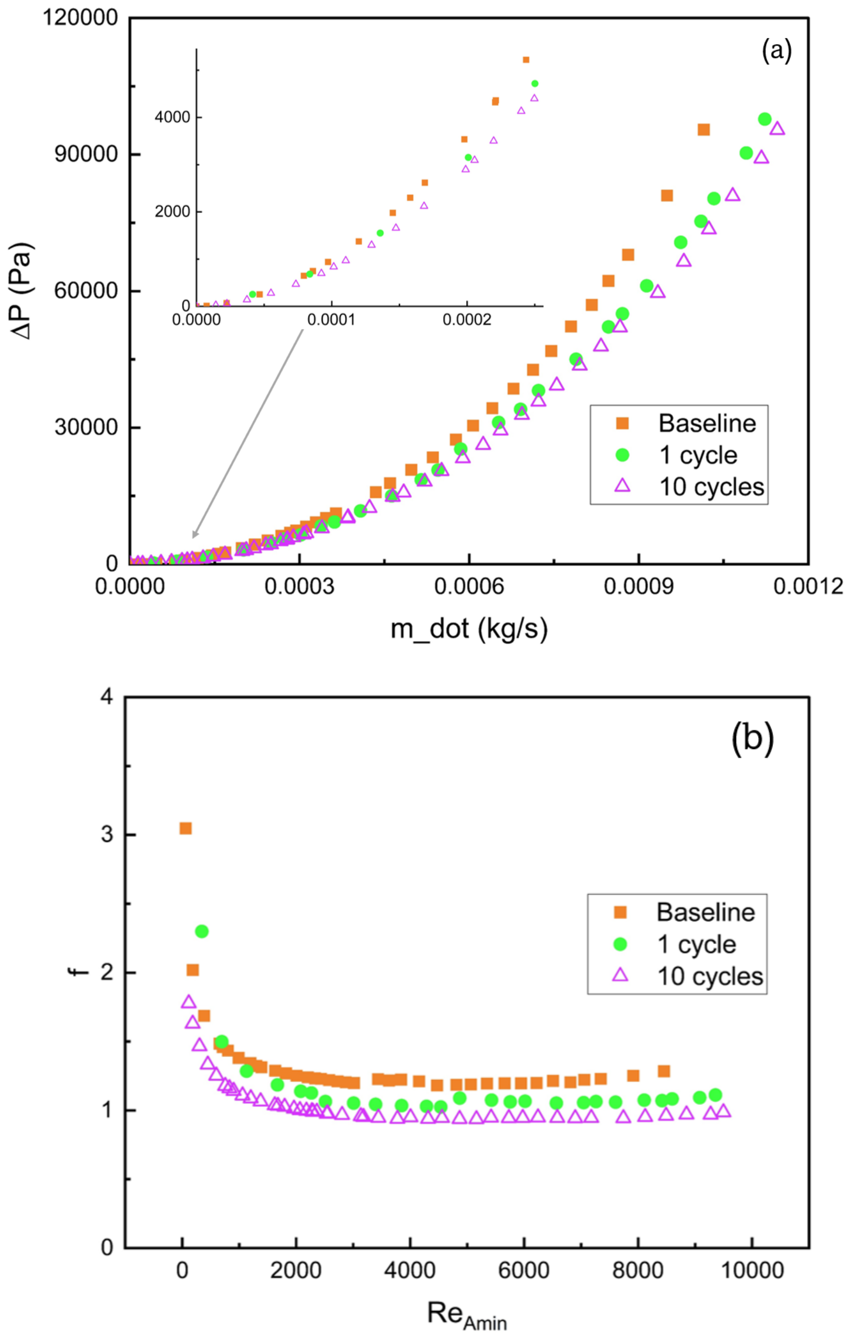

Figure 3.5. Variation of (a) pressure drop with air mass flow rate and (b) friction factor with Re_Amin in single channel pin arrays that underwent 0 (Baseline), 1 and 10 STEP cycles.

Figure 3.4(a) and Figure 3.5(a) show the plots of pressure drop at different air mass flow rates for open channels and pin array heat sinks, respectively. The dimensionless equivalent is shown in Figure 3.4(b) and Figure 3.5(b). These results were obtained after correction of the pressure drop recorded during the experiment: this original value included both the DP through the pin array and the losses in the piping and fitting that were part of the section of the assembly between the pressure ports (see Figure 3.3(d)). CFD simulations including this section of the assembly were conducted at various mass flow rates in order to evaluate the pressure drop associated with the piping and fittings.

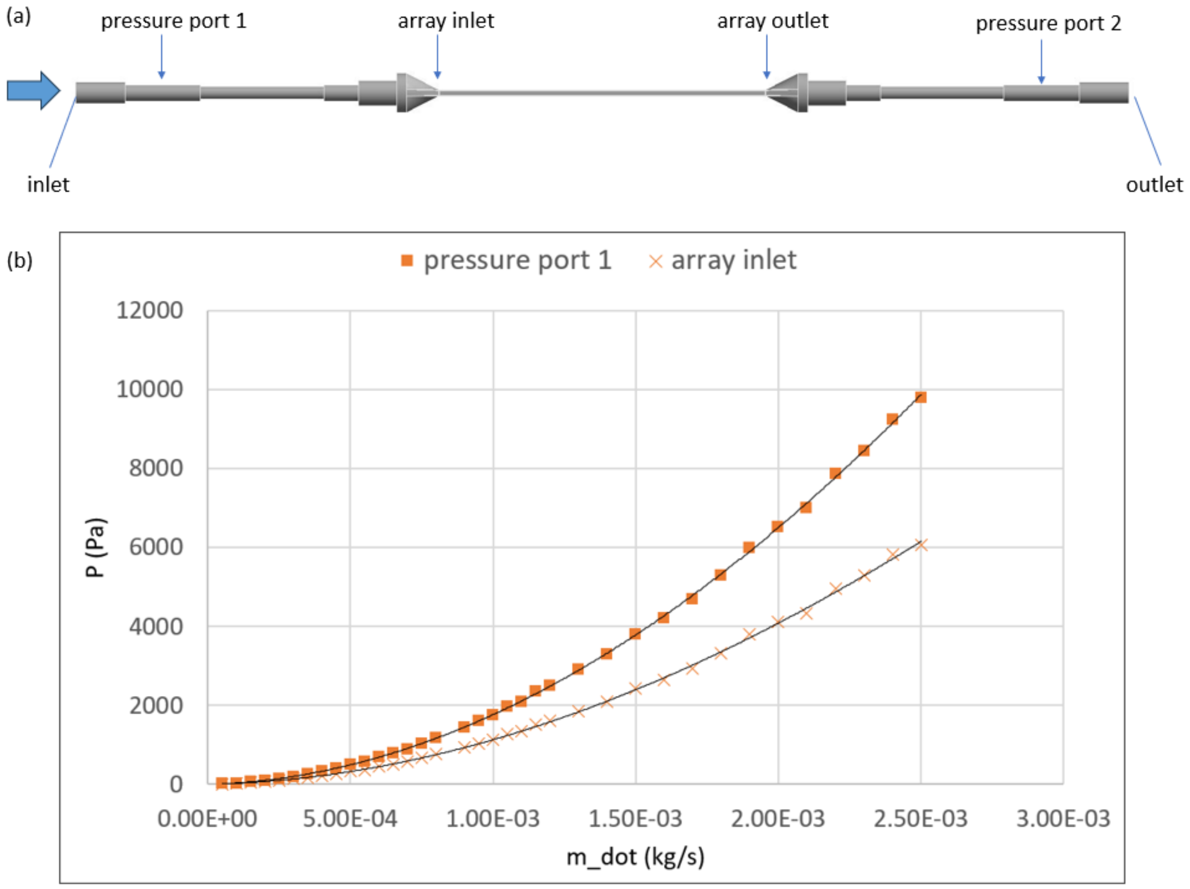

Figure 3.6. (a) Computational domain including the piping, fittings, and pin array sample, (b) static pressure as a function of mass flow rate at the location of pressure port 1 and the array inlet.

Figure 3.6 shows the computational domain used in the simulation and a plot of the static pressure results at the pressure port 1 and the inlet of the pin array, for several mass flow rates. The pressure drop between the pressure ports and the ends of the array is recorded as a function of the flow rate, and after curve-fitting, the function obtained is used to calculate the pressure losses due to the piping and fittings, which are then deducted from the losses recorded during the experiment. A decrease in pressure drop is observed between the baseline samples and the STEP samples. The pressure drop reduction after STEP is more significant in the pin array samples than the open channels. For the open channels results shown in Figure 3.4, noticeable reductions in pressure drop are seen only at higher flow rates. At the highest flow rate of 0.0012 kg/s, a 6 and 7.8% decrease in pressure drop from 3225 Pa for the baseline to 3028 and 2973 Pa, is noted for the one and four STEP cycles, respectively. At a lower flowrate of 0.0005 kg/s, the pressure losses decrease from 542 Pa for the baseline to 539 and 533 Pa for the one and four cycles, respectively (a reduction of 0.6 and 1.7%). In general, after the first cycle, the difference observed, although notable, is smaller between the first and the additional cycles.

For the pin array heat sinks (Figure 3.5), although the three cases considered display a similar pressure drop at low flow rates (below 0.0001 kg/s, see inset image in Figure 3.5), we can see a clear difference in pressure drop starting at a mass flow rate of about 0.0004 kg/s. Furthermore, the decrease in pressure losses from the baseline to one STEP cycle is more pronounced than the reduction observed from one to ten cycles. For instance, at a mass flow rate of 0.0004 kg/s the pressure drop decreases from 12900 Pa for the baseline to 11500 Pa and 10580 Pa for the one and ten cycles cases, respectively (corresponding to a 10.9 and 18% decrease from baseline). The percent reduction in pressure drop is more significant at higher flow rates. At a flowrate of 0.001 kg/s, the pressure losses decrease from 89260 Pa to 74860 and 70510 Pa, for the one and ten cycles arrays, respectively (which amounts to a 16 and 21 % reduction in pressure losses). A possible reason for pressure drop reduction at a given flow rate is that the decrease in pressure drop is mostly attributed to the removal of the powder particles attached to the pin surface, as seen in Figure 3.1. After the first cycle, the difference observed, although notable, is smaller between one and ten cycles. The marginal difference observed between one and ten cycles could be due to the lack of any noticeable change in the down-skin of the micro-pin after two STEP cycles.

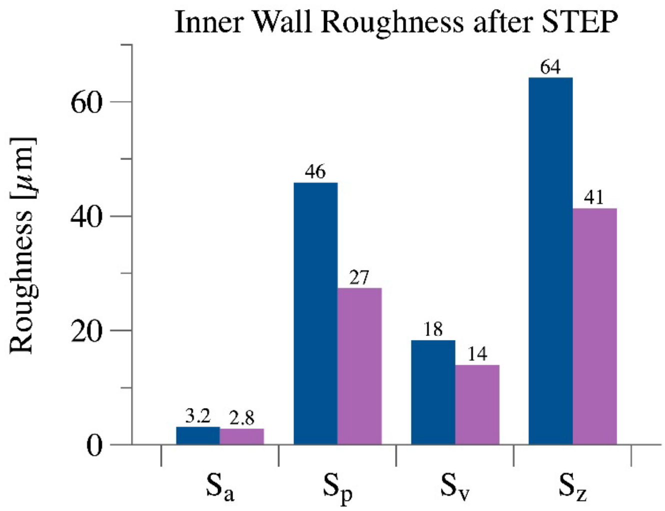

Figure 3.7. Plot comparing the roughness parameters Sa, Sp, Sv, and Sz of the inner wall of the pin array test coupon in as printed and after STEP conditions. Characterization conducted by CSM.

Surface roughness characterization was conducted at CSM. The areal surface roughness parameters average surface roughness (Sa), average minimum valley depth (Sv), average maximum peak height (Sp), and average maximum height (Sz) were measured from three 750×750 μm^2 areas with a laser scanning microscope for each sample. Figure 3.7 shows the plot of average values of the areal surface roughness parameters as-printed and STEP samples. There is no significant difference in S_a between as-printed and STEP samples (3.2±0.05 μm to 2.8±0.17 μm) as expected, since the STEP was designed to remove the powder particles without significantly changing the rest of the surface. The decrease in S_v in STEP samples compared to as-printed samples (24 % decrease from 18.3±0.68 μm to 14±3.13 μm) is likely from the large shift in the mean height of the surface due to the removal of the powder particles from the surface.

In summary, by utilizing STEP for AM Haynes 282 alloy, surface roughness parameter S_p decreased by 40% from 45.9±1.62 μm to 27.4±3.14 μm and a decrease of 16-21% in pressure drop is obtained for the pin array heat sink post treatment.

3.4. Predictability of pin array pressure drop using CFD simulations

3.4.1. Reduction of the computational domain using periodicity

The printed dimensions of the horizontally-printed pins are different than the design dimensions (more details presented in Chapter 4). Simulations of pressure drop through the pin array with design dimensions show a much lower pressure drop than from experimental measurements. There are two potential reasons for this difference- (1) surface roughness that is inherent to the LPBF process due to non-melted powder particles that are stuck to the surfaces, and (2) difference between the printed pin dimensions and design dimensions due to overprinting, especially in the down-skin regions. To assess the relative contribution of dimensional difference and roughness, the baseline and STEP treated pin array heat sinks were CT-scanned. The 3D geometry from the scans were imported into a meshing software and then into ANSYS Fluent for CFD simulations.

Performing CFD simulations on rough surfaces is computationally intensive because of small scale elements that need to be resolved and the wide range of length scales present in the model. Running simulations for a large geometry such as a pin array plate or even a reduced stripe will either not be feasible or require significant computational resources. A periodic geometry approach, where a smaller repeating section making up a larger segment is modeled and whose pressure drop results can be scaled to the extent of the actual pin array is chosen for detailed simulations. An illustration of the simulation domain is shown in Figure 3.8 where the repeating subsection along a stripe of the pin array is highlighted in blue (Figure 3.8(a)) and a more detailed description of the boundary conditions applied for the CFD simulation are shown in Figure 3.8(b)).

A periodic simulation was carried out in Fluent 2021R1 with the model shown in Figure 3.8(b) to verify that a periodic analysis on the reduced domain could be scaled up and yield a prediction of thermofluidic performance of the array within reasonable tolerance. The simulations in this section were conducted using the k-omega SST model for turbulence. Scaling up the pressure was achieved using the following equation:

$$\Delta P = dP/dx \times L \tag{3.1}$$

Where dP/dx is the main output from the periodic domain simulation and L is the length of the stripe. The results from the periodic domain of length 4.26 mm and width 2.46 mm were then compared to the pressure drop of a 100 mm stripe made up of the same repeating features as the reduced model. A strong agreement was obtained between the two methods, with a pressure drop of 12560 Pa for the small periodic geometry and 12410 Pa for the complete stripe (1.2% difference).

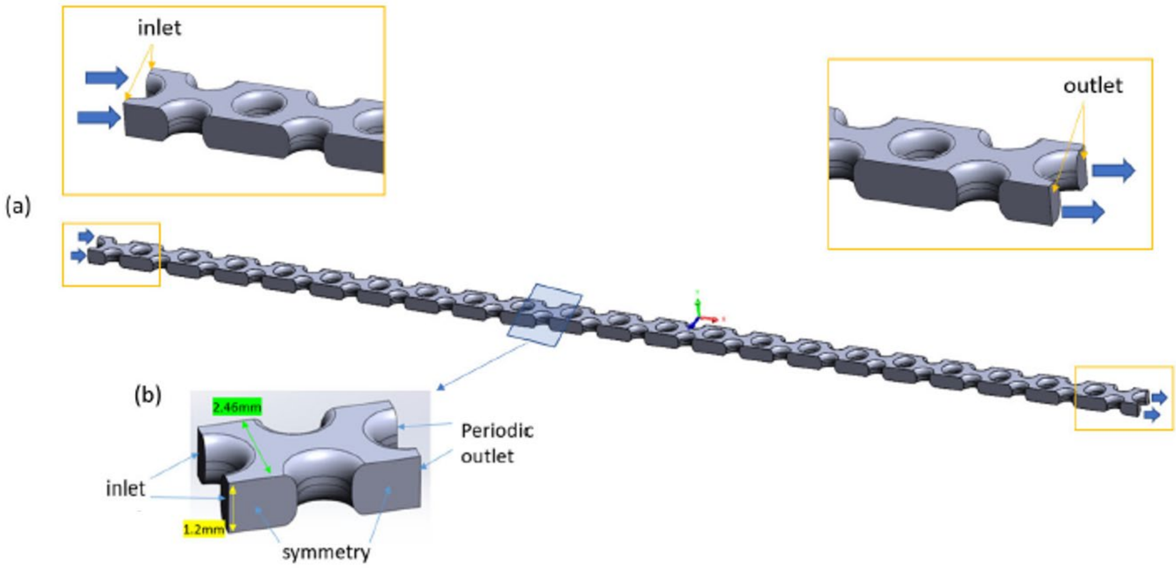

Figure 3.8. Array stripe with the periodic domain highlighted, (b) annotated CAD of the periodic domain showing the boundary conditions.

3.4.2. CFD simulations on design geometry and CT scans of printed arrays and comparison against experiments

As a reference for comparison, a periodic section of the design geometry was simulated for two flow rates corresponding to a mass flow rate of 0.15 g/s and 0.626 g/s through the pin array. The baseline pressure gradient were 7520 and 105560 Pa/m for the low and high flow rates respectively, leading to a pressure drop of 752 Pa and 10556 Pa along the 10 cm length of the pin array. The experimental pressure drop for these flow rates were 1857 Pa and 33426 Pa (see Figure 3.5), which are 2.5 times and 3.2 times larger than the design pressure drop from CFD.

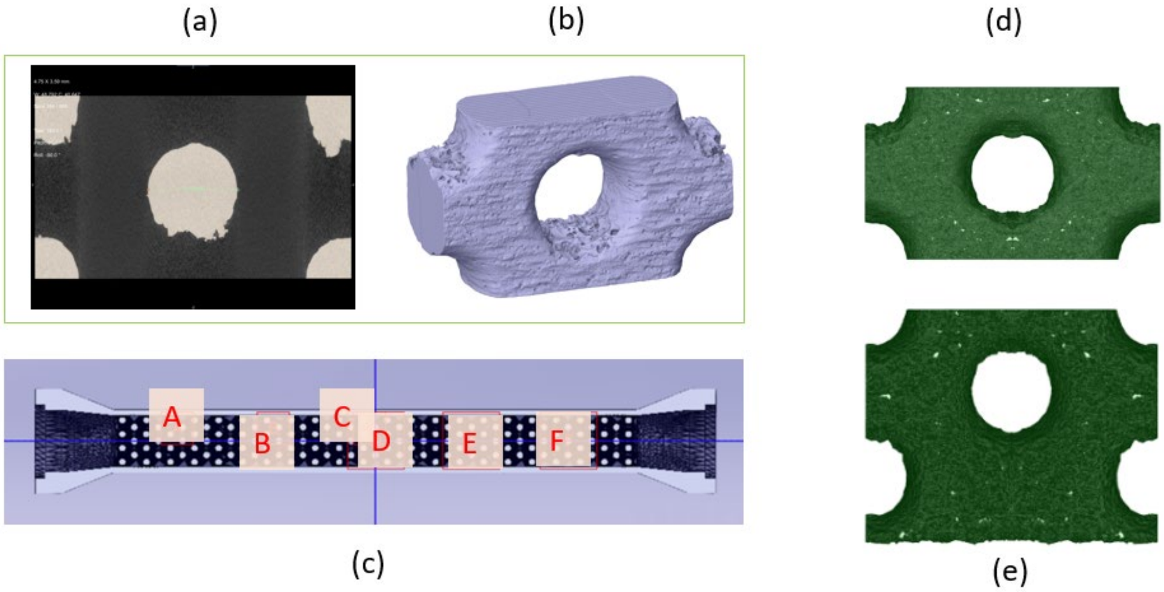

Figure 3.9. Optical image of a pin array, (b) fluid domain obtained after processing of the reconstructed scan, (c) locations of the samples collected along the pin array, (d) middle section sample, (e) wall section sample.

To obtain a 3-dimensional reconstruction of sections of the pin arrays of the printed geometry, a lab-scale CT system (ZEISS Xradia CrystalCT) at Carnegie Mellon University was used. It should be noted that the STEP-untreated pin array, denoted as baseline, was different than the one that underwent 1 cycle treatment. However, the same pin array that was processed for 1 cycle also underwent the 10-cycle treatment. Hence, the CT scans of the 1-cycle and 10-cycle pin arrays would give a true comparison of the morphology and pressure drop changes due to STEP treatment at the local scale. A voxel resolution of 4 μm was achieved and samples were collected at locations A-F of the arrays as shown in Figure 3.9. As shown in Figure 3.9(d) and (e), two types of samples were collected: samples A and C were side wall samples, and samples B, D, E and F were mid-section samples collected near the centerline and did not include any wall section.

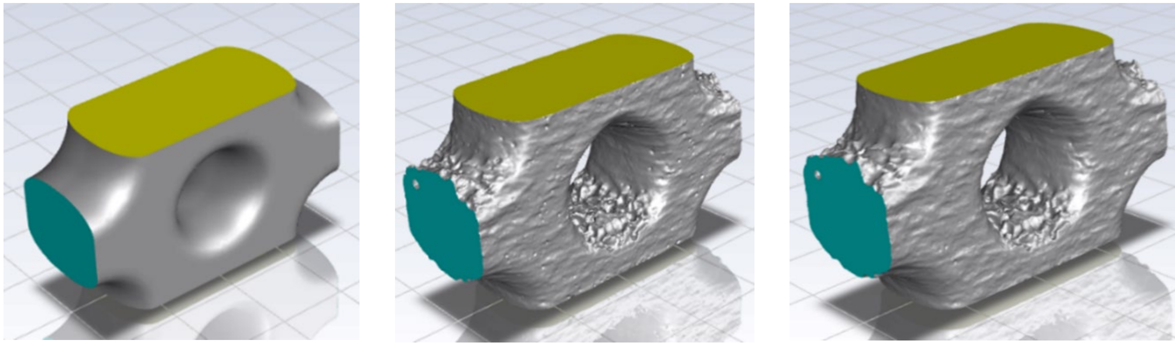

Figure 3.10. Periodic fluid domain: (from left to right) design, 1-cycle STEP treated, and 10-cycle STEP treated pin arrays.

A comparison of the domains for the design, 1-cycle and 10-cycle middle section periodic domains is shown in Figure 3.10(a)-(c) respectively. The blue face was defined as periodic inlet and its opposite face was designated as periodic outlet for the CFD simulations. The yellow face visible on top of the model and the corresponding face parallel to it but facing the bottom were defined as symmetry boundaries. It is clear that the actual geometries exhibit significant roughness on the walls, and differences in the pin shape in the down-skin regions compared to the design geometry. Moreover, a careful observation of the 1-STEP and 10-STEP geometries shows that there are fewer roughness bumps created by particles on the walls for the 10-STEP geometry. CFD simulations were performed at 6 locations shown in Figure 3.9(d) for baseline (no STEP), 1-cycle, and 10-cycle STEP-treated pin arrays at the two flow rates for which design simulations were performed. A total of 36 simulations on periodic domains were performed using the k-omega SST turbulence model.

Prior to the matrix of 36 simulations, a grid independence study was conducted to ensure stability of the results and specify the mesh parameters that would be consistently used for the mesh generation. Starting at node number of about 1.67 million, there percent difference between finer mesh results is less than 0.1%. The values specified for proximity and curvature for the mesh resulting in 1.91 million nodes were selected for the remainder of the study, as the computational expenses associated with the two coarser meshes (1.67 and 1.79 million) that yield about the same pressure results were not significantly lower.

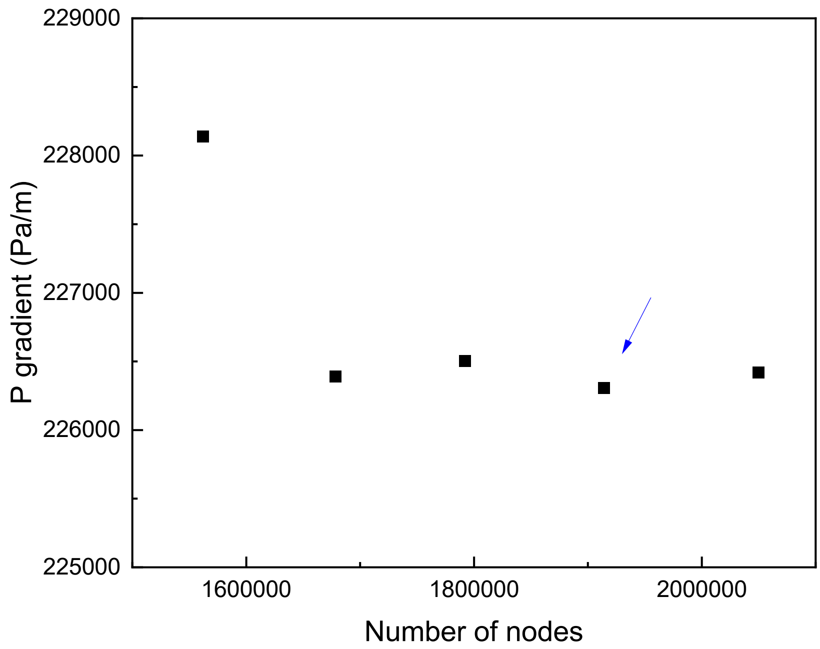

Figure 3.11. Grid independence study.

Example simulation results in the form of mid-plane velocity vectors is shown in Figure 3.12, for the design, and 1-cycle and 10-cycle STEP treatments. The 1-cycle and 10-cycle correspond to the same periodic section (location E in Figure 3.9(c)) on the same pin array. When comparing the design and the actual geometry, the pin geometries are quite different. The print direction was from bottom to top and a significant down-skin is observed in the pins in Figure 3.9(a), (b) and Figure 3.10(b) and (c).

In the design geometry, the flow impinges on the pin and accelerates as it moves around the pin to speeds as high as 18 m/s. The flow then separates around 85 degrees from the impingement line. A large wake region is located at the rear of the pin. In contrast, for the CT scanned geometries, the flow accelerates to speeds of about 28 m/s in Figure 3.12(b) and the flow separates earlier than in the design case, leading to an even larger wake and associated form pressure drop. The extent of the wake region is defined by the vertical pin dimension, i.e., the frontal diameter to the flow. Since this dimension is larger than the horizontal dimension for this non-circular pin, the velocity field suggests that this dimension should be used as the length scale in estimation of pressure drop and heat transfer rather than an equivalent pin diameter. The significant changes observed in the flow field manifests as a substantial increase in pressure drop from a baseline value of 10556 Pa to 22873 Pa for the 1-STEP treatment over the 10 cm pin array.

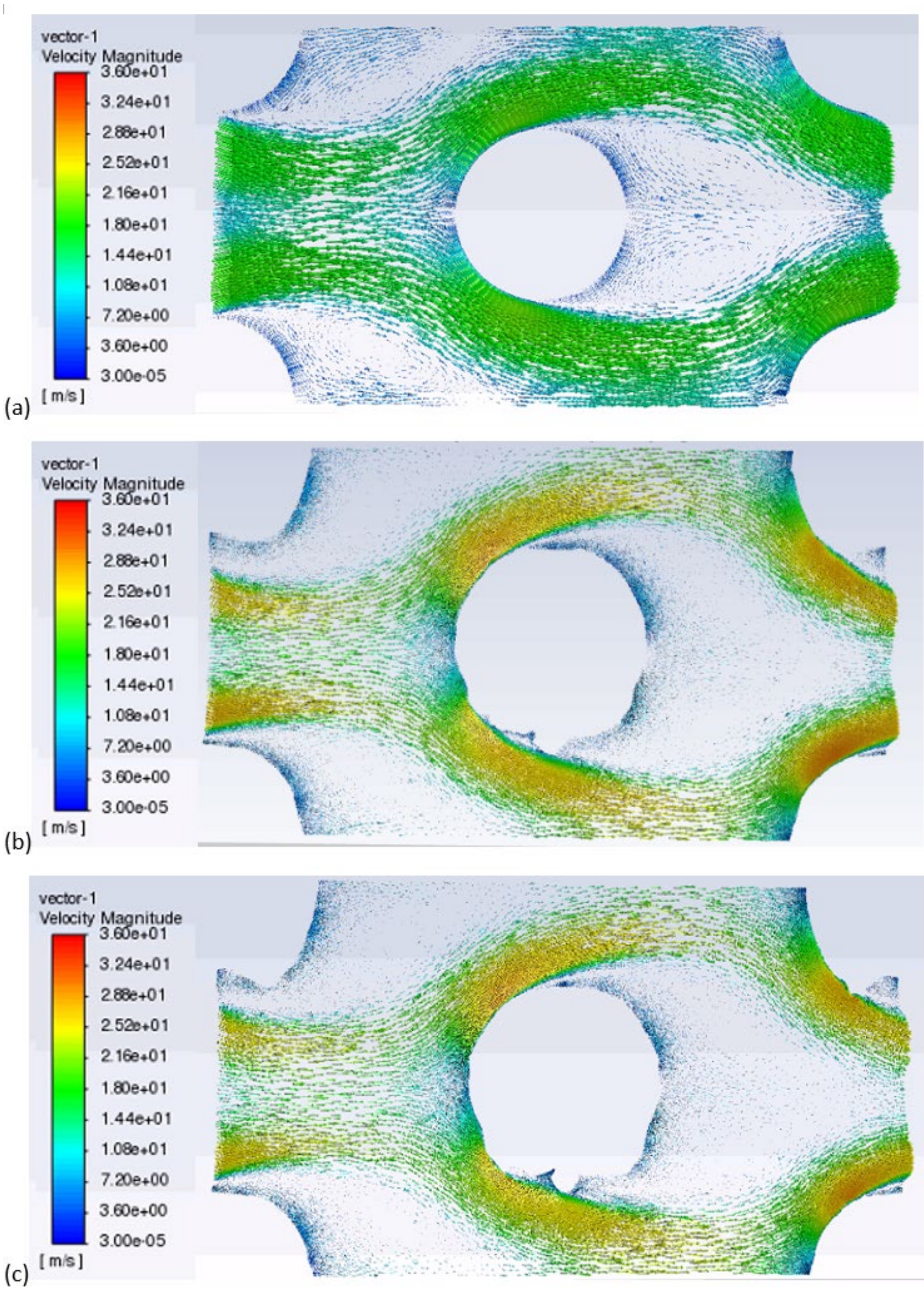

Figure 3.12. Velocity vectors in a periodic section in the middle section at location E (Figure 3.9(c)) of the pin array at the midplane of the periodic unit for (a) the design geometry, (b) 1-cycle of STEP and (c) the 10-cycle of STEP. The mass flow rate through the pin array is 0.626 g/s.

When the vector fields from the 1-STEP and 10-STEP are compared, there is a reduction in peak velocity and a slight reduction in the wake region for the latter. This change in flow field results in a corresponding 9.8 percent decrease in pressure drop from 22873 Pa (over the 10 cm length) for the 1-cycle to 20622 Pa for the 10-cycle case.

A summary of the CFD simulation results in the central sections of the pin array (locations B, D, E, and F) for the two simulated mass flow rates of 0.15 g/s and 0.626 g/s through the pin array is shown in Table 3.2. Also shown are the design pressure drop and experimentally measured pressure drop for the baseline, 1cycle and 10-cycles at the same flow rates. From Table 3.2, for both flow rates considered, the average pressure drop is observed to decrease from the baseline to the 1-cycle array and further reduction occurs with respect to the 10-cycle sample. For instance, at high flow rate and the sections B, D, E and F, the average value for the pressure drop is approximately 23.4 kPa and drops to 22.3 kPa for the 1-cycle array and about 20 kPa for the 10-cycle array. Another expected result is the decreasing variability in pressure drop results from the baseline to the treated samples.

Table 3.2.Results of the CFD simulations conducted on the scans of the pin arrays that underwent chemical smoothening for locations B, D, E and F in the center of the pin array.

m_dot = 0.15 g/s								
	B	D	E	F	dP_avg (Pa)	dP_stdev (Pa)	dP_exp (Pa)	% deviation from exp
Design	752				752	0		
Baseline	1664	1391	1577	1386	1504	139	2041	30.3
1-cycle	1474	1490	1486	1430	1470	28	1607	8.9
10-cycle	1364	1290	1348	1320	1330	33	1601	18.5
m_dot = 0.626 g/s								
	B	D	E	F	dP_avg (Pa)	dP_stdev (Pa)	dP_exp (Pa)	% deviation from exp
Design	10556				10556	0		
Baseline	25149	21695	24357	22468	23417	1607	32090	31.3
1-cycle	21958	22873	22873	21763	22367	590	27625	21.0
10-cycle	19851	19461	20622	19984	19980	482	26103	26.6

The velocity vectors in Figure 3.12 show that the shape of the pin, particularly the dimension transverse to the flow is instrumental in the overall pressure drop in these arrays. Although roughness may somewhat contribute to the pressure drop, most of the pressure losses are associated with form drag, as shown by the large wake region at the back of the pin and the early flow detachment caused by the unevenness around the pin. Since the chemical treatment of those arrays appears to mainly affect that region of the pin with partially melted powder attached due to the overhanging configuration of those pins, it makes sense that capturing the shape of the pins is enough to accurately predict variation caused by STEP. A comparison of the average pressure drop from CFD with experiments shows that the simulations underpredict the pressure drop by 9-30% for the low flow rate and by 21-31% at the high flow rate. The reason for this difference could be due to the exclusion of side wall effects. As illustrated in Figure 3.13, the printed samples were quite narrow in terms of width and most of the array was dominated by wall sections.

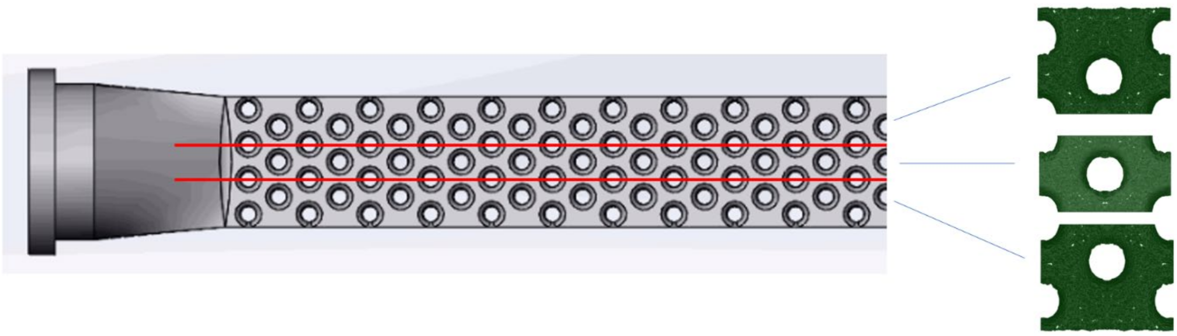

Figure 3.13. Top view of the fluid domain of a single channel pin array and a subdivision showing the relative contribution of walls and middle sections.

Hence CFD simulations were performed on X-ray CT scans obtained in locations A and C in Figure 3.9(d) that included one side wall. With a symmetry condition applied to the bottom of the computational domain shown in Figure 3.13, the influence of both side walls will be captured. A summary of the results of pressure drop for the two flow rate conditions at locations A and C is shown in Table 3.3. It is seen that the simulations predict the experimental pressure drop with much better accuracy. Three cases of percent difference lower than 5% and a maximum value of

15.6 %. This agreement gives confidence in the ability to explain the large pressure drop obtained using AM pin arrays relative to the anticipated pressure drop based on design dimensions.

Table 3.3. Results of the CFD simulations conducted on the scans of the pin arrays that underwent chemical smoothening for locations A and C that includes the wall of the pin array.

m_dot = 0.15 g/s						
	A	C	dP_avg (Pa)	dP_stdev (Pa)	dP_exp	% deviation from exp
Baseline	1891	1851	1871	28	2041	8.7
1-cycle	1926	1832	1879	67	1607	-15.6
10-cycle	1664	1679	1671	10	1601	-4.3
m_dot = 0.626 g/s						
	A	C	dP_avg (Pa)	dP_stdev (Pa)	dP_exp	% deviation from exp
Baseline	29078	28216	28647	610	32090	11.3
1-cycle	27693	27738	27716	32	27625	-0.3
10-cycle	24628	25003	24816	265	26103	5.0

In summary, detailed CFD on CT-scanned models of sections of the pin array show that the printed pins have a significant down-skin region and surface roughness. STEP treatment has been shown to reduce the surface roughness by removing the powder particles adhered to the surfaces. Velocity vector maps suggest that the 10-cycle treatment also reduces the extent of the wake region. These two effects result in a decrease in pressure drop by 20%. However, the pressure drop of the 10-cycle treated pin array is still 1.75 to 1.9 times larger than the design pressure drop for the two flow rates considered. Hence, the shape of the printed pins, which results in a significantly larger wake region is the cause for the excessive pressure drop observed in AM printed pin arrays. Since the frontal area to the flow determines the extent of the wake region, use of this diameter as the length scale for pressure drop and heat transfer correlations seems to be most appropriate.

3.5. Mechanical performance of the additively manufactured pin arrays

Surfaces resulting from L-PBF are inherently rough and this characteristic has been found to adversely impact the mechanical performance of printed parts [69-71]. The existence of local defects and surface irregularities have been linked to local stress concentration yielding a fatigue life lower than anticipated from design versions [72,73] and research is ongoing on studying roughness reduction methods to alleviate the impact on mechanical properties [74]. The objective of this section is to study how the mechanical stress varies between the design version of one of the pin array channels and the printed versions that went through different level of chemical surface treatment.

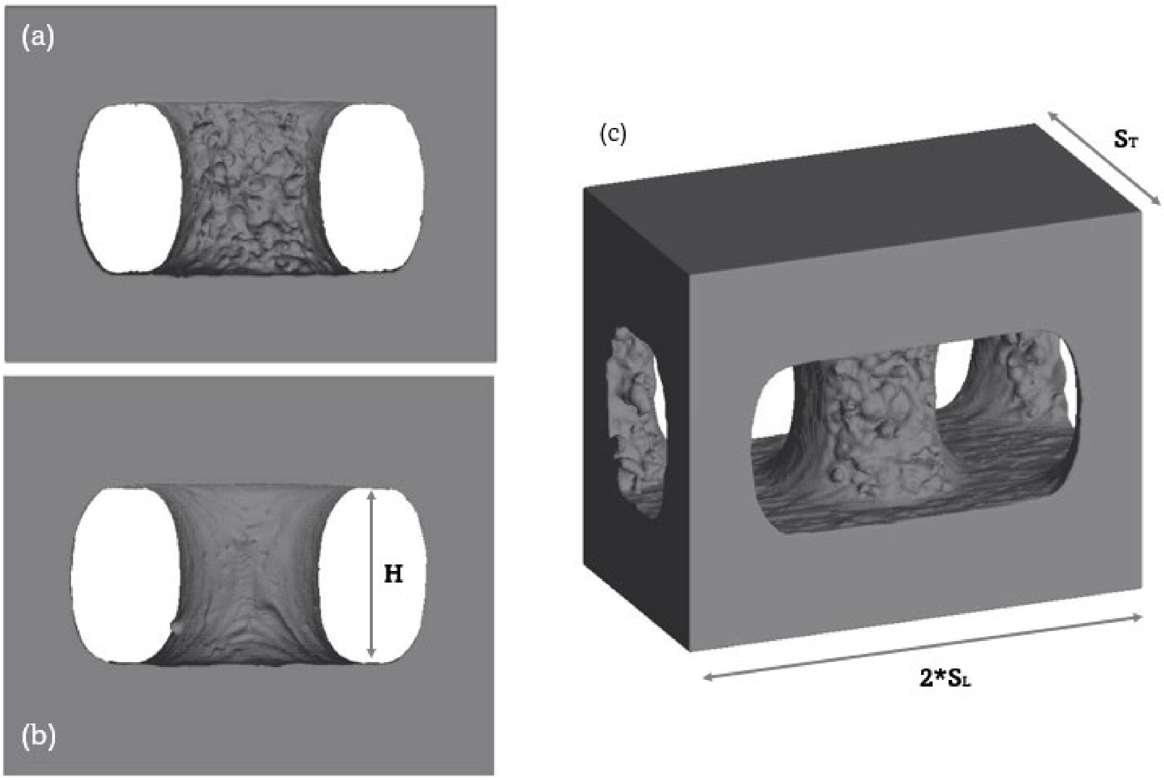

Figure 3.14. Side view of the periodic section of the solid domain showing (a) the pin downskin, (b) the top of the pin, (c) isometric view. The design dimensions of the pin array are such that H=1.8 mm, D_{pin} = 1.2 mm, S_T = 2.68 mm, S_L = 2.32 mm (image obtained from CT scanning followed by processing in Flow3d)

The model shown in Figure 3.14 is a periodic section from the 10-cycle pin array channel. It has been modeled in Ansys mechanical along with the 1-cycle, baseline, and CAD (design) version of the model in order to compare, at the level of the resolution available in Ansys mechanical, how the stress level in the model deviates from design to printed samples, as well as the changes brought about by additional rounds of surface treatment. As displayed in Figure 3.15, the computational domain was further simplified by splitting the model about the midplane using the assumption that there will be no additional insight provided by modeling the entire height of the pin, by virtue of symmetry and the absence of printed variability in the direction of the pin height (perpendicular to the build direction).

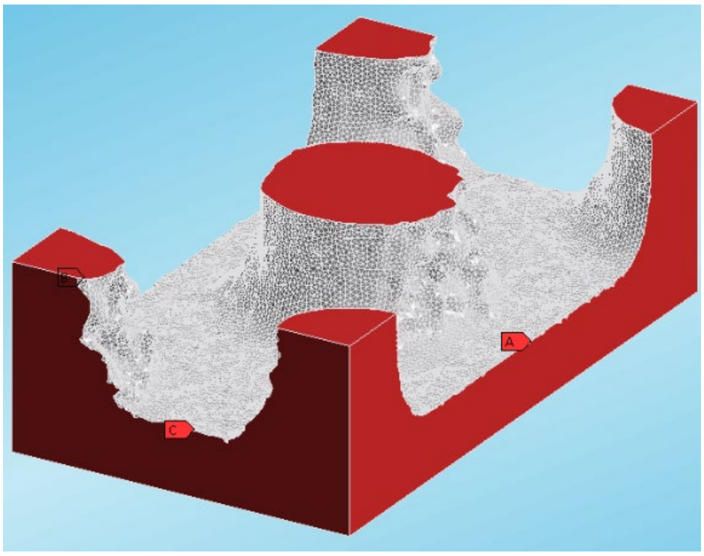

Figure 3.15. Meshed solid domain with symmetry faces highlighted in red.

Figure 3.16 and Table 3.4 show the comparison of the FEA results for the modeled geometries. While the maximum stress for the printed specimen is several times greater than that of the design, we can see that most of these high stresses are very localized and are not representative of the entire unit.

Table 3.4. Comparison of mechanical stress between the design, printed, and smoothed geometries.

	Design	Baseline	1-cycle	10-cycle
Average stress (MPa)	54.1	57.7	58.5	57
Maximum stress (MPa)	118.6	472.8	641	521.8
Surface average stress around the pins (MPa)	105.5	79.5	82.7	83.2

As shown in Table 3.4, the average stress value, despite a small increase is very close to the 54 MPa design. Comparing the baseline, 1-cycle and 10-cycle it is seen that contrary to the monotonic decrease expected from roughness reduction, the baseline case shows an average stress slightly lower than the 1-cycle and a maximum stress lower than the other two cases. This discrepancy is most likely due to variability in pin geometry: while the 10-cycle array was obtained by performing additional 9 cycles of chemical treatment on the 1 cycle case, the baseline array is a completely different geometry. A stronger case can be made by comparing the 10- and 1-cycle samples (obtained by measuring the exact same pin). We can see that albeit small, there is a reduction in the average stress existing in the model by the application of surface treatment. The surface average stress around the pins has been found to correlate better with experimental structural integrity performance as discussed later in Chapter 6. For this region dominated by the stresses in the vicinity of the pin, the design stress is actually higher than the other printed cases. This behavior is because the printed pins were on average wider than the design one (1.2 mm diameter for the design vs 1.35 mm for the printed version). The lower stress of the baseline is again most likely related to printing variability. The trend between the 1 and 10 cycle is different from the one observed for the average stress and may be explained by the fact that in this region dominated by stresses around the pin, small variations by material removal have a magnified impact more easily perceived.

The stress concentration, which are expected to relax over time, decrease by a much larger margin which attests to the ability of the STEP treatment to reduce defect/roughness-induced stresses and yield surfaces with an increased uniformity of performance.

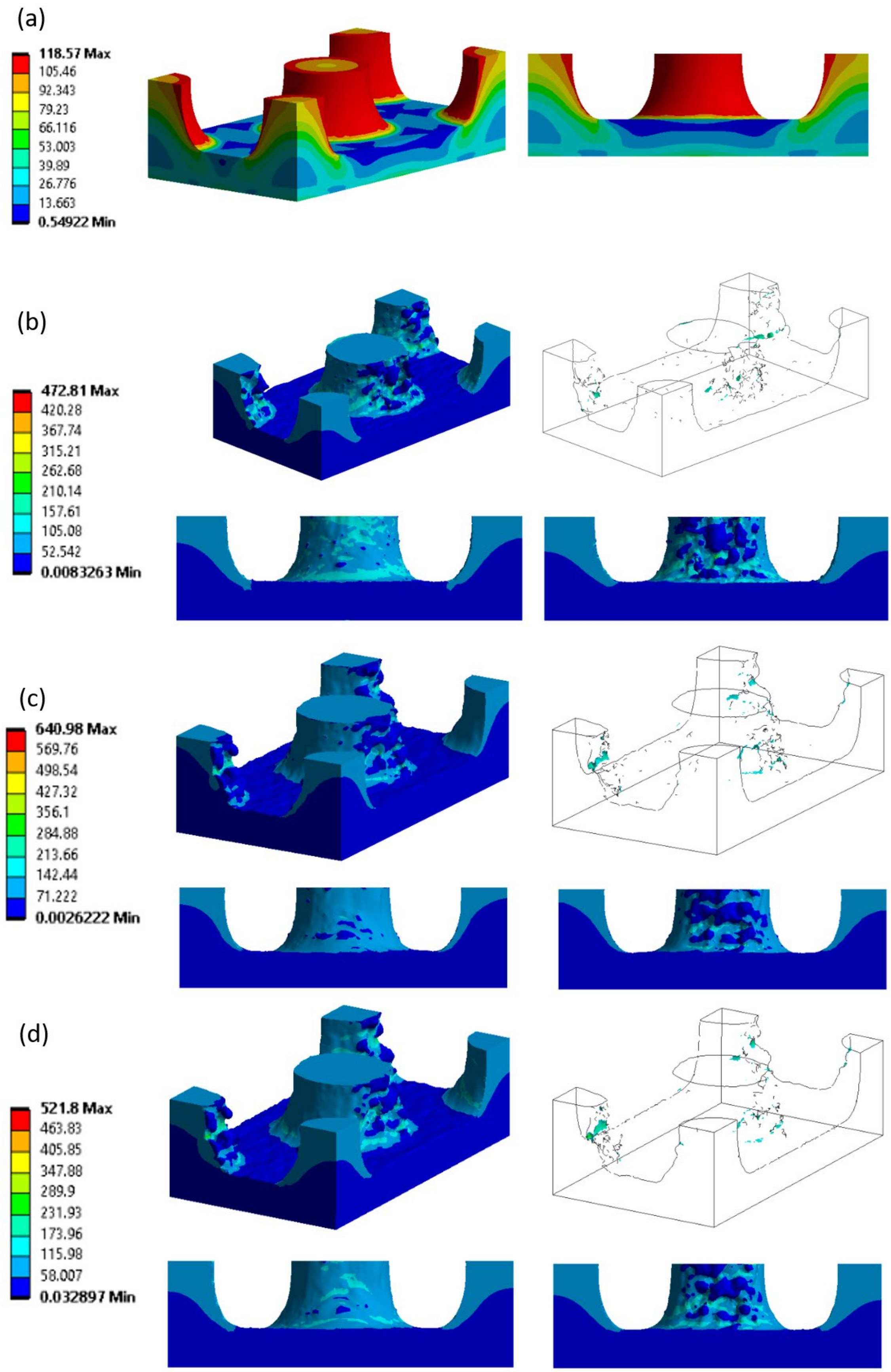

Figure 3.16. Equivalent von Mises stress for isometric and side views of (a) design geometry, (b) baseline, (c) 1-cycle and (d) 10-cycle.

Chapter 4 Pin array core – flow and heat transfer correlations

Experimental results for the development of correlations for flow through microscale pin arrays are presented in this section. Existing correlations for pin arrays are based largely on literature in thermal management and use water or dielectric fluids at Reynolds numbers below 1000. Hence, there is a need for further performance characterization of sCO_2 flows in such geometries. Different pin array models were designed to characterize heat transfer and pressure drop in additively manufactured pin arrays. Adding to this objective, the study also aims to assess the predictive capability of different correlations for various geometric configurations (pin diameter, spacing, height) in addition to flow conditions. After an overview of relevant correlations in the literature, the samples used for testing are presented and experimental results are discussed with the purpose of selecting appropriate correlations for friction factor and Nusselt numbers for the sCO_2 side with pin array. Results from CFD simulations are used to characterize the thermofluidic performance on the MS side for the gen2 design that has a 3D periodic lattice design (see Chapter 2).

4.1. Literature review and correlations summary

The ability to accurately predict heat transfer and pressure drop is an important component of heat exchanger design as it lowers the uncertainty in its design performance, in terms of power density and pressure losses that will determine the economic feasibility of a given design. Several correlations are found in the literature on friction factor and Nusselt number for flow through pin fins arrays. Several of these correlations have been considered, the relevant and most promising ones are listed in Table 4.1 along with the geometry for which they were derived and the range of Reynolds number applicability which typically does not overlap with the expected sCO_2 range for our application (Re > 2000).

Table 4.1. Literature correlations for single phase heat transfer and pressure drop in micro pin array heat sinks.

Reference	Remarks/Correlation
Prasher et al.[1] [75]	*- Micro pin fin heat sink* *- Staggered circular and square pin fin* *- Water* $40 < Re_{Dh} < 1000$ $2.48 < \alpha < 2.8$ $2.4 < \beta_T = \beta_L < 3.6$ $Nu_{Dh} = 0.132(\beta_L - 1)^{-0.256} Re_{Dh}^{0.84} \left(\frac{Pr_{test-fluid}}{Pr_{water}}\right)^{0.36}$ *if* $Re_{Dh} < 100$ $Nu_{Dh} = 0.281(\beta_L - 1)^{-0.63} Re_{Dh}^{0.73} \left(\frac{Pr_{test-fluid}}{Pr_{water}}\right)^{0.36}$ *if* $Re_{Dh} > 100$
	$40 < Re_{Dh} < 1000$ $1.3 < \alpha < 2.8$ $2.0 < \beta_T = \beta_L < 3.6$ $2.4 < \beta_L < 4.0$ $f = 4 \times 0.295(\alpha)^{1.249}(\beta_L - 1)^{-0.7}(\beta_T - 1)^{-0.36} Re^{-0.1}$ *if* $Re_{Dh} > 100$
Rasouli et al. [76]	*- Micro pin fin heat sink* *- Staggered diamond pin fin* *- LN_2 and PF-5060* $40 < Re_{Amin} < 2300$ *(validity range for no vortex shedding)* $20 < Re_{Amin} < 3000$ *(validity range for vortex shedding)* $0.7 < \alpha < 3.2$ $1.7 < \beta_T < 3.0$ $0.8 < \beta_L < 1.5$ $Nu_{Amin,no\ VS} = 0.039(\beta_T - 1)^{-0.19} Re_{Amin}^{0.837} Pr^{0.557}$ $Nu_{Amin,VS} = 0.253(\alpha)^{0.39}(\beta_L - 1)^{-0.062} Re_{Amin}^{0.747}$ *for* $\alpha > 1$, $\beta_T > 2$, $\beta_L > 1$
	$20 < Re_{Amin} < 2500$ $f = 1373.6(\beta_L - 1)^{0.16} Re_{Amin}^{-1.3}$ *if* $Re_{Amin} < 100$ $f = 9.2(\alpha)^{-0.43}(\beta_L - 1)^{0.07}(\beta_T - 1)^{0.07} Re_{Amin}^{-0.15}$ *if* $Re_{Amin} > 100$
Moores and Joshi [77]	*- Meso pin fin heat sink* *- Staggered circular pin fin* $1000 < Re_{Dh} < 10000$ $0.5 < \alpha < 1.1$ $1.3 < \beta_T < 1.36$ $1.13 < \beta_L < 1.18$ $f = 4 * 3.2(\alpha)^{-0.138} Re^{-0.42}$

Short et al.[2] [78]	*- Macro pin fin heat sink* *- Staggered circular pin fin* *- Air* $1000 < Re_{Dh} < 4500$ $1.9 < \alpha < 7.2$ $2.0 < \beta_T < 6.4$ $1.8 < \beta_L < 3.2$ $f = 4 \times 0.221(\alpha)^{0.056}(\beta_L)^{-1.4}(\beta_T)^{-0.54}Re_{Dh}^{-0.08} \times \left(\frac{L}{D_h N_{row}}\right)$
[1] The authors' correlation does not have a Pr term. However, they used a Pr correction based on Zukauskas [79], to compare their experimental data with literature. Based on the reported test conditions, water Pr was calculated at 52.5 °C. [2] The factor of $L/D_h N_{row}$ was applied because of the difference in the definition of f used by Short et al. [78] with this study.	

4.2. Description of the heat sinks geometries – design vs measured

The pin arrays in HSs were fabricated in different variants shown in Table 4.2 in order to obtain thermofluidic information on arrays with various pin parameters such as aspect ratio, and transverse and longitudinal pitch ratios. The designs were informed by Rasouli et al. [76] earlier studies where it was found that designs with aspect ratio and longitudinal pitch ratios greater than unity, and transverse pitch ratio larger than 2 yielded higher heat transfer coefficient than the denser pin arrays. Visualization studies revealed the presence of vortex shedding (VS) at the wake of the pins for such designs. Hence all heat sinks were designed to enable vortex shedding. Straight micro pin array, SM1 corresponded to the HE baseline with a transverse pitch ratio of 2.05, a pin height of 1.8 mm and circular pins. The results do not include information for SM1 which was found to have manufacturing defects. The SM2 heat sink was designed with fully circular pin shape with a diameter of 1.2 mm, height of 1.2 mm (i.e. an aspect ratio of 1), and a transverse pin ratio of 2.05. SM3 had the same geometry pitch ratio as SM2 but an aspect ratio of 1.5 and the pin shape was half-circular half-elliptic to obtain a better pin circularity (see Table 4.2). The pin in arrays SM3 to SM6 were all designed with this pin geometry of half-circle half-ellipse shape to attain more circular pin shape upon printing. SM4, 5 and 6 are variations of SM3 such that SM4 had taller pins (aspect ratio of 2.5 vs 1.5 for SM3), SM6 was an array of sparser density (β_L of 2.78 vs 1.93 for SM3) and SM5 was even sparser with the spacing increased in both transverse and longitudinal directions (β_T=3.5 of and β_L=3.03 vs 2.23 and 1.93 for SM3). It should be noted that the pin designs included significant fillets (0.8 mm radius on top and bottom) to reduce stress created by the 200-bar internal pressure. In this aspect, the pins are different from the ones for which correlations have been developed in literature.

The actual dimensions of several heat sink channels (pin diameter, height, spacing) were obtained using optical microscopy; that of SM3 is illustrated in Figure 4.1. The pin array height was lower than the design height consistently; for SM3, an average height of 1.53 mm as opposed to 1.8 mm was measured (Figure 4.1(b)). The flow frontal diameter variation of a pin in SM3 array is shown in Figure 4.1(c). The frontal diameter to the flow is 1.61 mm for SM3. Table 4.2 shows the design dimensions and the measured flow frontal diameter of the pin arrays.

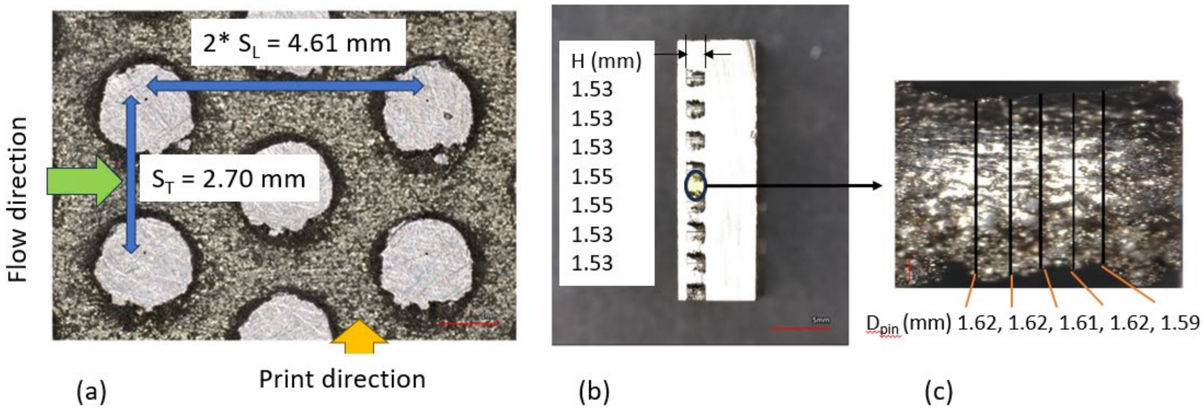

Figure 4.1. Optical micrographs of SM3 heat sink. (a) Average pin diameter in this cross-sectional view was 1.09 mm; the average transverse and longitudinal spacing was S_T = 2.7 mm and S_L = 2.31 mm respectively, (b) pin height variation (flow into the page), (c) variation in pin flow frontal diameter along the height of a pin; from this view the pin diameter is 1.61 mm.

Based on the results of CFD simulations in Chapter 3, the flow frontal diameter was chosen as the length scale for pressure drop and heat transfer. While all heat sink pin arrays were *designed* to be geometries that would enable VS, the measured dimensions, and non-dimensional parameters based on the flow frontal diameter indicate that none of the geometries would be in the VS regime per the criteria set in Rasouli et al. [76]. The SM5 and SM6 heat sinks come closest with aspect ratio being slightly under unity and pitch ratios higher than the VS criterion.

Table 4.2. Design and actual dimensions of the H230 pin arrays (for each heat sink, the first row refers to design values, the second row (purple) refers to parameter ratios estimated using measured flow frontal diameter (Figure 4.1)

Heat sink (HS)	CAD	Optical image	D_{pin} (mm)	β_T	β_L	α	VS based on Rasouli et al. [76]
SM2	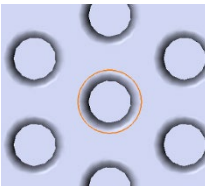	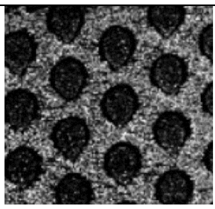	1.2	2.05	1.78	1	Y
			1.651	2.08	1.80	0.78	N
SM3	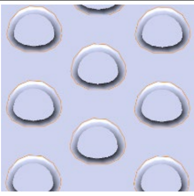	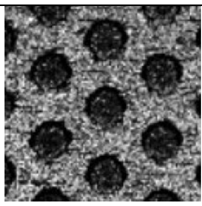	1.2	2.23	1.93	1.5	Y
			1.61	1.67	1.43	0.95	N
SM4	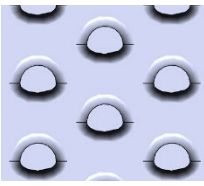	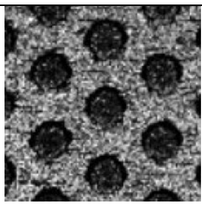	1.2	2.23	1.93	2.5	Y
			1.61	1.67	1.43	1.69	N
SM5	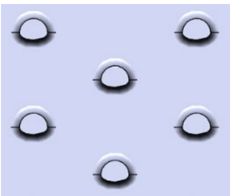	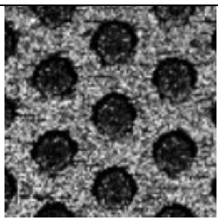	1.2	3.5	3.03	1.5	Y
			1.61	2.6	2.25	0.95	N
SM6	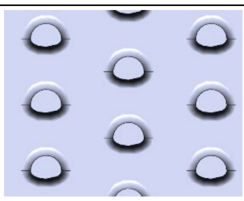	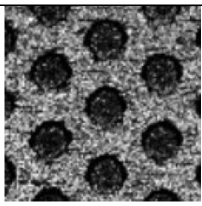	1.2	2.23	2.79	1.5	Y
			1.61	1.66	2.07	0.95	N

Figure 4.2 shows some samples and schematics of the tested heat sinks. They are comprised of two plena bringing fluid in and out of the heat sink, and an array of pin with the dimensions specified in Table 4.2. Prior to testing the manufactured heat sinks for pressure drop, high pressure

gas (nitrogen up to 1000 psi) was directed though the heat sinks (HS) to ensure that any residual powder would be removed from the array.

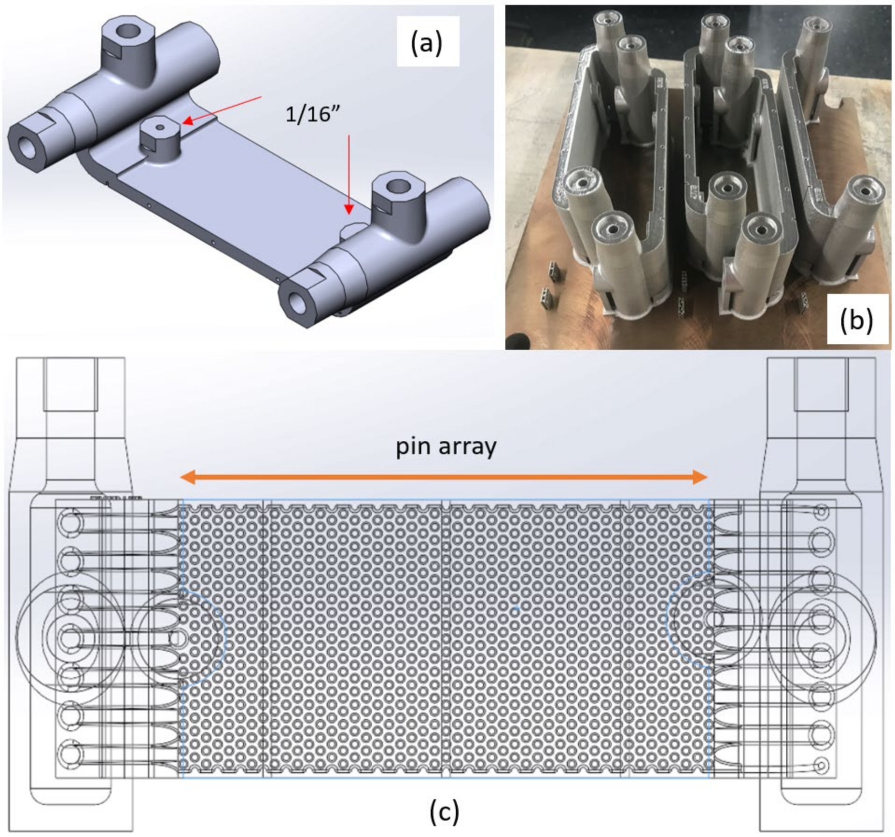

Figure 4.2. (a) Heat sink CAD isometric view, (b) Printed heat sinks attached to the build plate, (c) See-through view of the heat sink illustrating the internal features.

4.3. Description of the experimental setup and procedure

4.3.1. Pressure drop testing

Prior to testing the manufactured heat sinks for pressure drop, high pressure gas (nitrogen up to 1000 psi) was flown through the HS to ensure that any residual powder that did not get melted would not remain inside the unit. To quantify the pressure drop caused only by the pin arrays and not the headers, smaller ports (the 1/16 inch NPT ports shown in Figure 4.2(a)) were designed to connect the positive and negative sides of a precise differential pressure transducer (with bias uncertainty of ±7 Pa).

The main components of the test rig include a compressor sending 100 psi of air through the open loop, a venturi flow meter, the heat sink, a differential pressure transducer measuring the pressure losses across the pin array and a needle valve to regulate the flow. Upstream of the HS, the incoming airflow passed through a straight section shown in the inset picture in Figure 4.3 where the line pressure and temperature were recorded, and mass flow rate was measured using a venturi flow meter. The next element in the system is the heat sink itself that has pressure ports located at the start and end of the pin array, rather than the inlet and outlet headers, to solely account for pressure losses through the array. Downstream of the HS, a needle valve was placed to regulate the flow rate. All the measurements were recorded continuously throughout the experiments via a LabVIEW program.

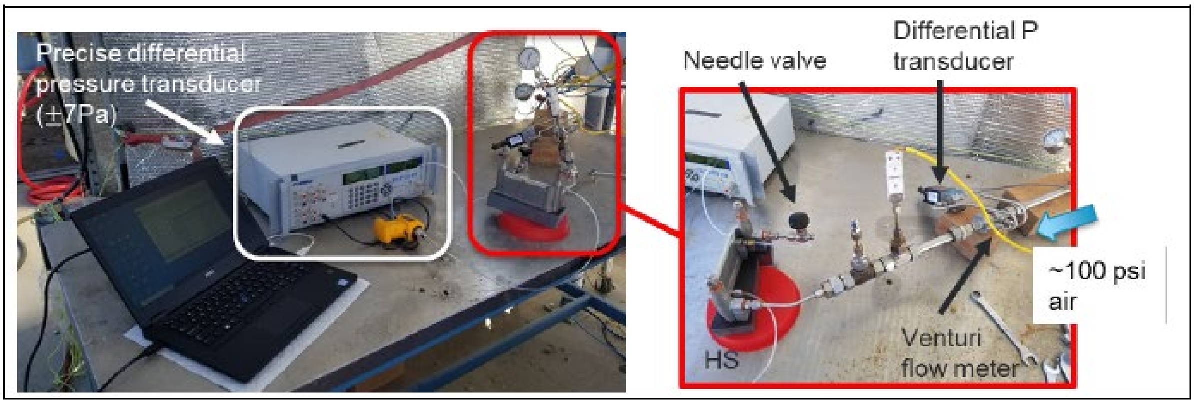

Figure 4.3. Experimental setup for pressure drop testing.

4.3.2. Heat transfer testing

Figure 4.4 shows the experimental setup for the heat transfer testing of the heat sinks. The pin array was laid out on 5 cm x 10 cm footprint area connected to plena with proper fluidic ports to measure temperature and pressure on either side. The main components of the test assembly include a tank containing liquid CO_2, a pump for high pressure CO_2 applications, and a preheater bringing the liquid CO_2 to the supercritical state. Additionally, this preheater increases the temperature of the sCO_2 to the target inlet temperature for the heat sink resting on top of the fluxmeter.

This flux meter provided heat to the test section through a set of cartridge heaters inserted at the bottom and controlled by an AC variac, see Figure 4.4(c) and (e). When the heated CO_2 exited the heat sink, it was sent to a coil heat exchanger immersed in a glycol bath and cooled by a chiller. Upon becoming a liquid, the flow was directed through a Coriolis flow meter and eventually back to the liquid CO_2 tank located upstream of the CO_2 pump. The fluxmeter and heat sink assembly were thoroughly insulated to minimize heat losses during the runs.

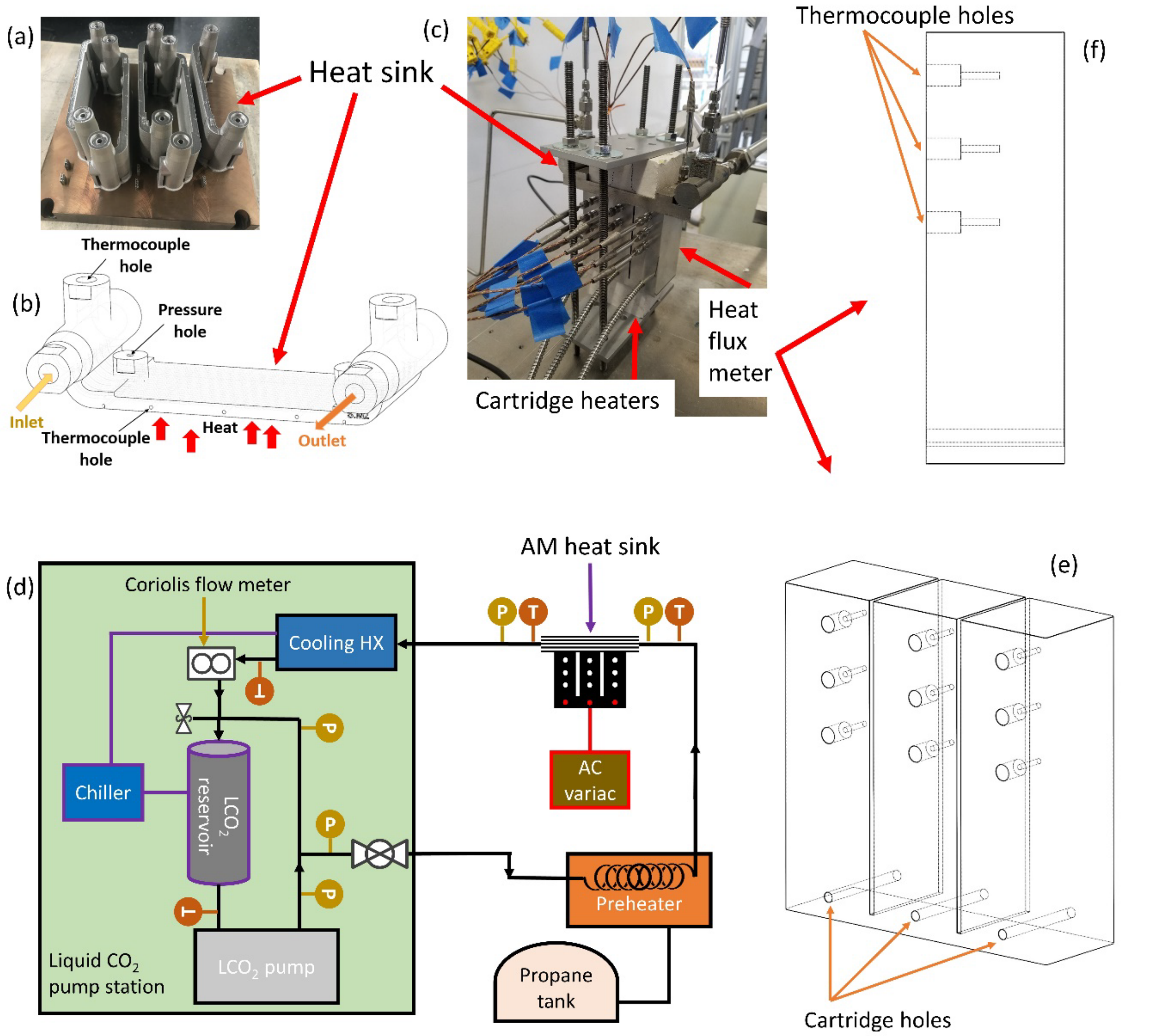

Figure 4.4. (a) AM heat sink attached to the build plate, (b) AM pin array heat sink design, (c) heat sink and fluxmeter assembly, (d) heat transfer test experimental setup line schematic, (e) isometric and (f) side view of the flux meter.

The heat flux meter was made of Aluminum (6061 with material certificate) and had three sections separated by 1.6 mm (1/16 in) gap. Three thermocouples were embedded along the height of the heat flux meter in each section distanced 16 mm apart to measure temperature gradient, calculate the heat flow toward the base of pin array heat and evaluate the uniformity of the heat flux provided by the electric cartridges. A set of thermocouples are inserted at different locations of the fluxmeter to monitor the temperatures, and from the known material conductivity, ensure that the electric cartridge supply a uniform flux to the heat sink.

Each AM pin array heat sink was designed with three thermocouple holes along the flow direction 2 mm below the base of pin array to obtain the measurement for the surface temperature after correction for the thickness of the material between the location of the holes and the actual wall. The fluid bulk temperature was monitored by thermocouples inserted into the side plena. The temperature data combined with the heat flux information were used to determine the heat transfer coefficient (h) and compare it against the correlations used in the model

$$h = \frac{q}{\Delta T\left[\left(A_{surf} - N_{pin}\pi\frac{D_{pin}^2}{4}\right) + N_{pin}\pi D_{pin}H_{pin}\eta_{pin}\right]} \tag{4.1}$$

where q is the total amount of heat quantified by the heat flux meter, ΔT is the difference between the pin array base temperature (average of three measurements along the length) and the bulk mean fluid temperature, A_{surf} is the pin array footprint area, N_{pin} is the total number of pins, D_{pin}, H_{pin} and η_{pin} are the pin fin diameter, pin fin height, and pin fin efficiency, respectively. During data reduction, the measurements from thermocouples inserted into the heat sink bottom wall were corrected to account for the heat conduction between the probe location in the wall and the surface in contact with the fluid. The corrected wall temperatures were then averaged to obtain a single value representative of the entire array. The bulk mean temperature was obtained by taking an average of the inlet and outlet fluid temperatures in the plena.

Uncertainties in measured temperatures, pressure drop, absolute pressure, and mass flow rate were based on the bias errors provided by the manufacturer. Errors were propagated to determine values such as heat transfer coefficient and Nu using the propagation of errors method [80]. To ensure reliability of experimental data, heat transfer experiments on one heat sink were replicated on three different days. The entire test section including thermocouples and insulation was dismantled, heat sink was removed from the test loop and was cleaned and reassembled. The test results indicate good repeatability within the tested Re range of $1200 < Re < 7000$, with the min., max., and average differences between the 3 replications were 0.3 %, 20 %, and 8.5 % respectively.

4.4. Testing results

4.4.1. Pressure drop results

Figure 4.5(a) shows the pressure drop results for the five heat sinks tested. The dimensionless form of the results is presented in Figure 4.5(b) in the form of friction factor as a function of Reynolds number. The Reynolds number for the pin array is based on the length scale of the hydraulic diameter evaluated at the minimum cross-sectional area of the flow, Re_{Amin}. For most heat sinks shown in Figure 4.5(b) a high friction factor is observed at the lowest values of Reynolds number and decreases exponentially up to a Re_{Amin} value of approximately 2500, after which the friction factor flattens. At a given mass flowrate, it is observed that SM2 has a pressure drop that is several times larger than all the other heat sinks tested. For instance, at a mass flow rate of 0.00125 kg/s, the pressure drop of SM2 is approximately 30 kPa meanwhile all the others have pressure losses lower than 5 kPa. This result is expected because the narrower channel of SM2 combined with the smaller pitch yield a smaller cross-sectional area open to flow, resulting in a higher flow velocity for the same mass flow rate. Moreover, the infiltration effect resulted in a SM2 pin geometry which deviated from the original model and produces pins with an equivalent diameter larger than that of the CAD. Fewer data points were collected for SM2 due to the upper limitation of the differential pressure transducer.

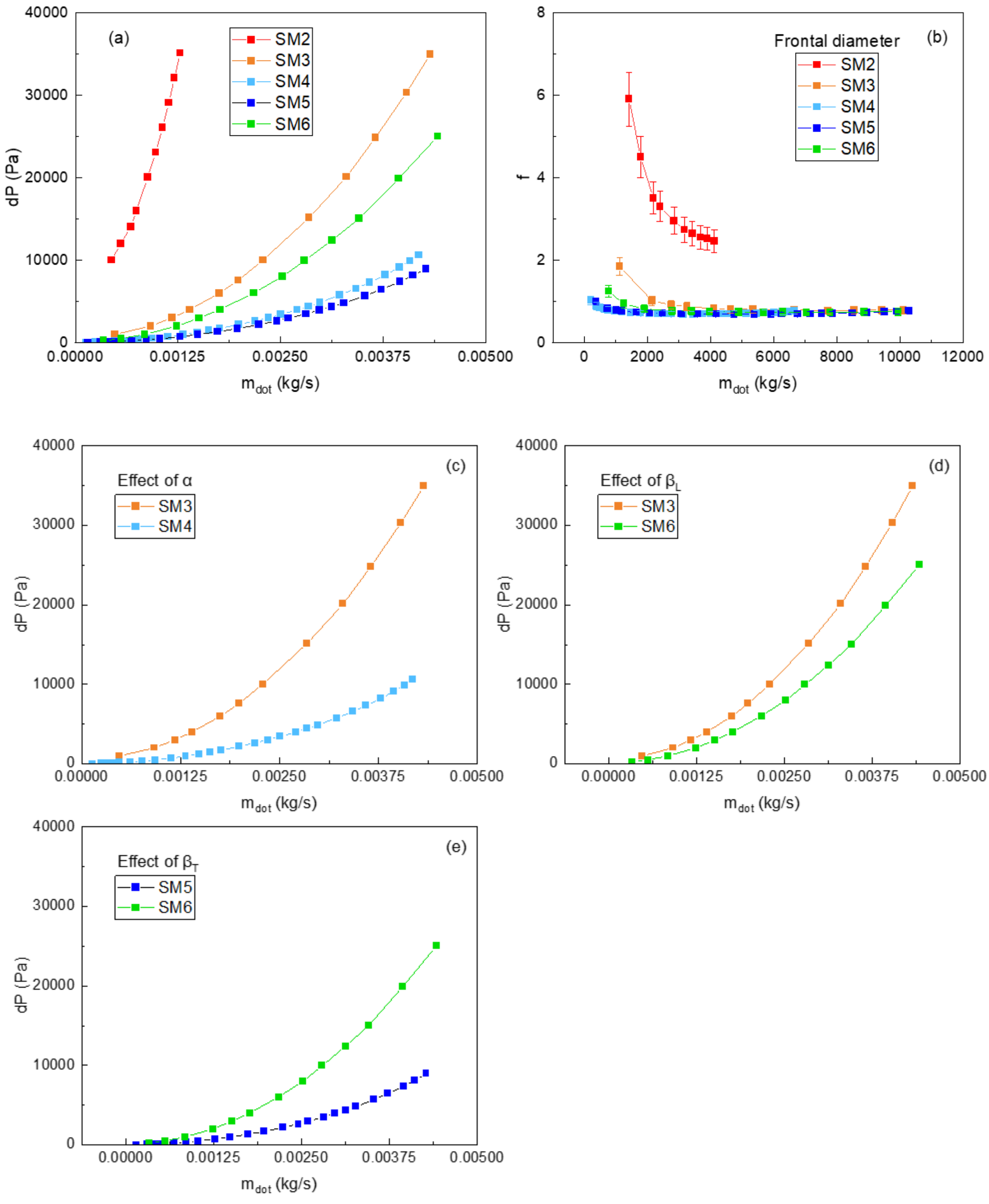

Figure 4.5. (a) Variation of pressure drop with air mass flow rate in SM2-6 pin arrays[1], (b) Variation of friction factor as a function of Re_{Amin} for SM2-6, effect of (c) aspect ratio, (d) longitudinal pitch, (e) transverse pitch on the pressure drop.

The individual effect of the aspect ratio (α), the transverse (β_T) and longitudinal pitch ratio (β_L) is illustrated in Figure 4.5(c), (d), and (e), respectively. SM3 and SM4 are identical in terms of spacing

[1] Note the errors bars for the pressure drop curves are not visible due their magnitude relative to the scale.

but differ in pin height (design aspect ratio of 1.5 for SM3 vs. 2.5 for SM4), the pressure losses are therefore higher in the case of the SM3 array due to the more restricted channel. At a flowrate of 0.0025 kg/s the pressure losses in SM3 are 11260 Pa vs 3098 Pa for SM4 or a 72.5 % decrease. The effect of the longitudinal pitch (β_L) however is less pronounced as shown in Figure 4.5(d): the design of arrays SM3 and SM6 is such that the two arrays are identical in all respects except for the longitudinal spacing β_L and this distinction is reflected in the pressure drop which amounts to 11260 Pa for SM3 vs 8790 Pa for SM6 (22 % decrease). Finally, the effect of β_T is illustrated in Figure 4.5(e): as discussed previously, the impact of β_L is rather marginal on the variation of pressure losses. Although SM5 and 6 slightly differ in terms of β_L the more significant change in pressure losses from 8790 Pa for SM6 to 2640 Pa at a flow rate of 0.025 kg/s for SM5 is mostly attributed to the β_T difference.

4.4.2. Heat transfer results

Figure 4.6 shows the results of the heat transfer testing, with the heat transfer coefficient presented in Figure 4.6(a) and the dimensionless Nusselt number (Nu) results presented in Figure 4.6(b). The individual effects of aspect ratio, and longitudinal and transverse pitch variation shown in Figure 4.6(c), (d), and (e), respectively, for a Reynolds number range from 800 to 14000. From Figure 4.6(c), it is seen that the effect of the aspect ratio on the Nusselt number is rather minimal and at a given Reynolds number. These results may be explained by the counteracting influence of increased surface area and decreased fin efficiency. In the case of β_L however, a more noticeable difference between SM3 and SM6 is observed. At a Reynolds number of approximately 7000, Nusselt values of 86 and 104 are obtained for SM3 and SM6, respectively. While the reason for this difference could be that the wider longitudinal spacing of SM6 allows for a slightly longer distance available for vortex shedding in the array. The effect of the transverse spacing (β_T) is even more pronounced as depicted in Figure 4.6(e). At a Reynolds number of 7500, SM5 has an average Nusselt number of approximately 76 while SM6 exhibits a value of about 105. Even though SM5 benefits from a shedding distance which is longer than that of SM6 by virtue of their respective longitudinal pitch (3.33 for SM5 vs 3.06 for SM6), the smaller transverse spacing of SM6 (which is still large enough to allow vortex shedding) is probably responsible for an increase in velocity at the local level, which results in an overall higher heat transfer coefficient compared to SM5.

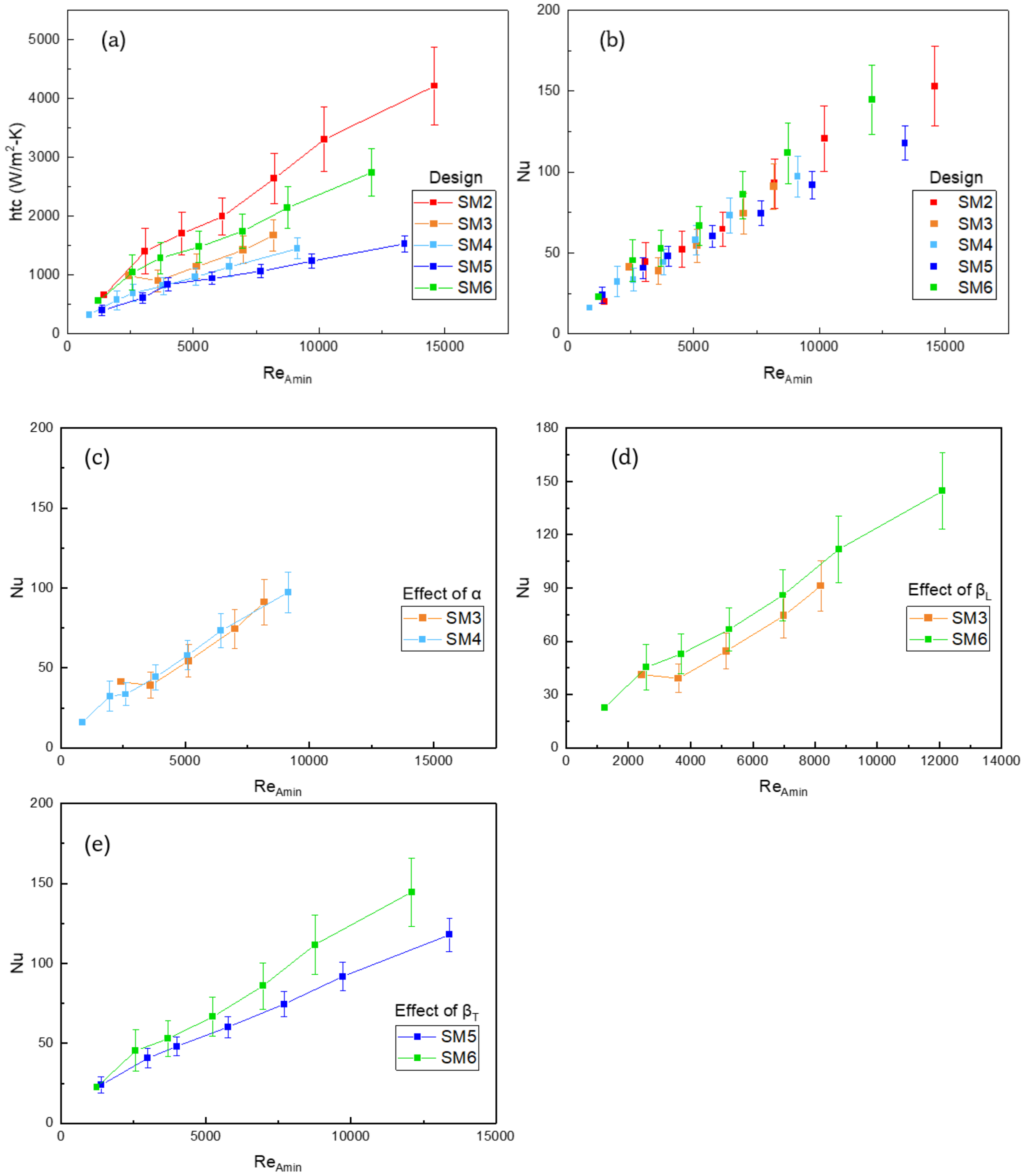

Figure 4.6. (a) Variation of the heat transfer coefficient (htc) with Re_{Amin} SM2-6 pin arrays, (b) Variation of Nusselt number as a function of Re_{Amin} for SM2-6, effect of (c) aspect ratio, (d) longitudinal pitch, (e) transverse pitch on the Nusselt number.

4.5. Correlation selection for the sCO_2 and MS sides of the HX

4.5.1. Comparison with correlations in the literature based on (1) design dimensions (2) measured dimensions.

Pressure drop results

Figure 4.7 shows the results of friction factor as a function of Reynolds number for array SM2-6, as well as a comparison against the prediction for available correlations in the literature, based on either the design dimensions or the measured one based on the flow frontal diameter of the pins. Based on the design dimension, the Rasouli et al. [76] correlation predicts the friction factor the best, even though it often yields a significant overestimate (e.g. SM5 and SM6). Considering the results based on the flow frontal diameter however, the general trend in these plots is that the Prasher et al. [75] correlation, predicts the friction factor the best. In the case of SM2, the Rasouli et al. [76] correlation gives a better prediction most likely because of the prevalence of wall effects associated with the low aspect ratio of the channel. In some instances, the Moores et Joshi [77] correlation predicts better the friction factor, but these are situations where the marginal differences with other correlations in rather small. Besides, this correlation depends only on the Reynolds number and aspect ratio, it does not capture the sensitivity of the flow condition with respect to the spacing.

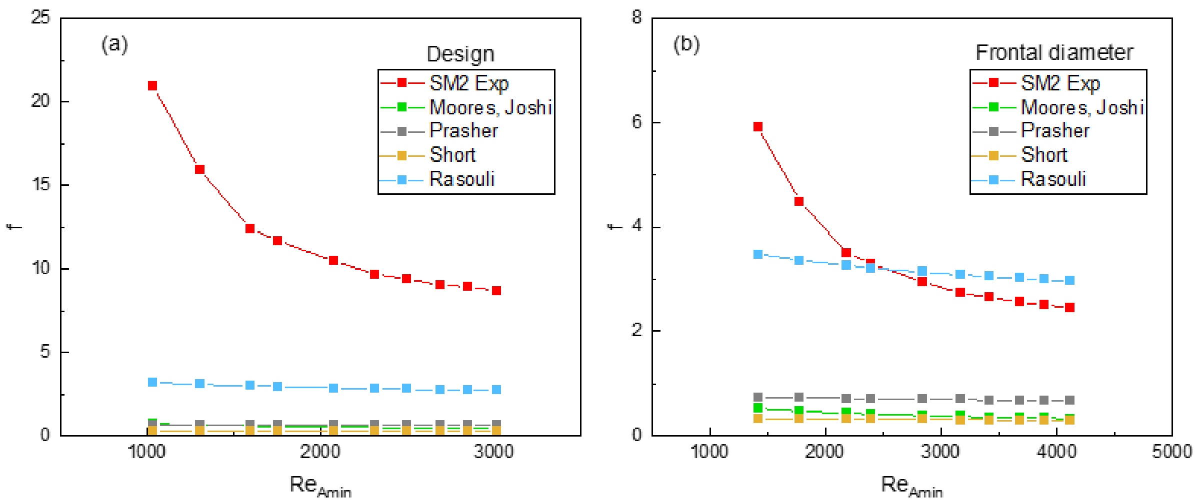

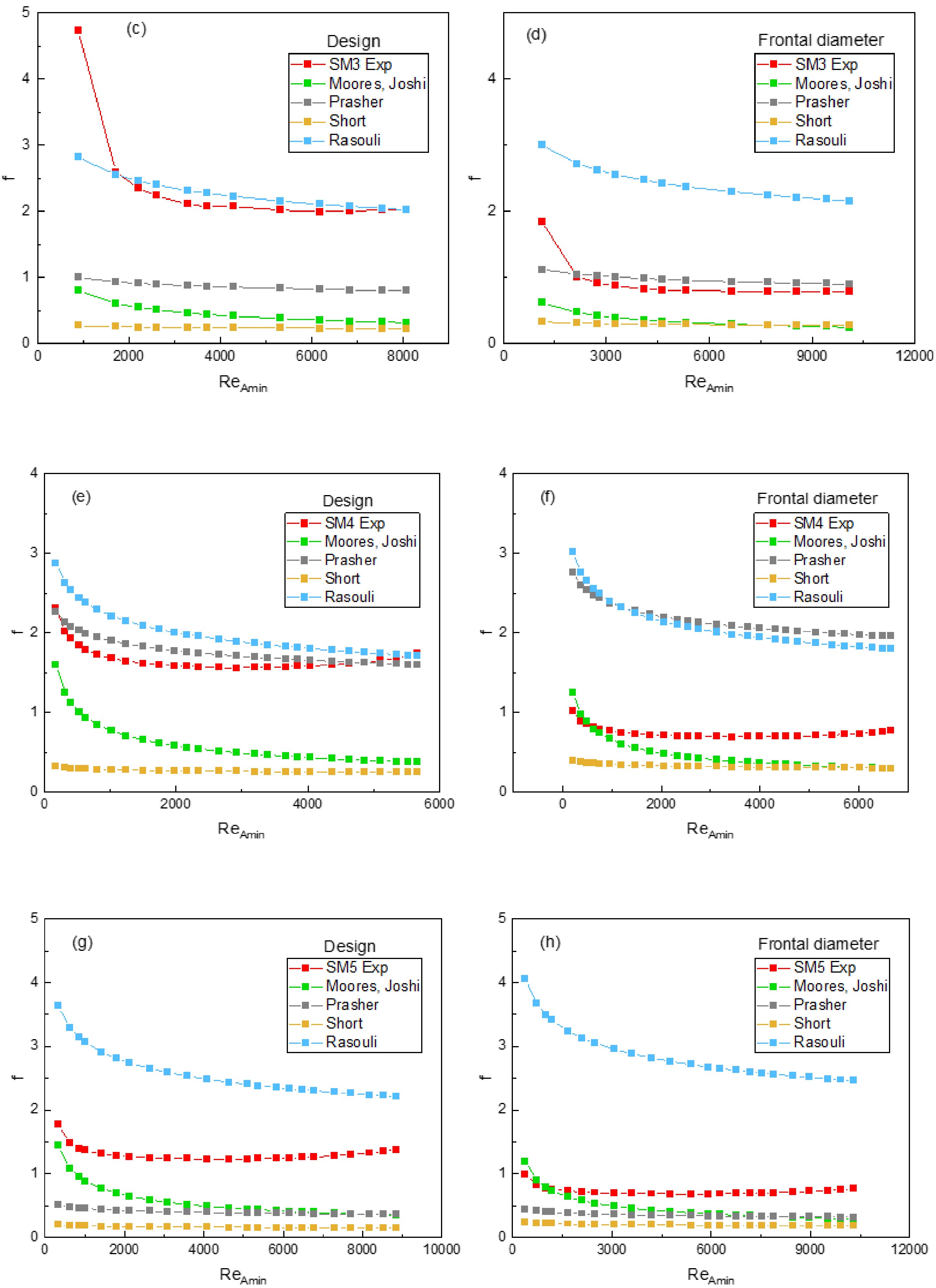
(c)
Design
SM3 Exp
Moores, Joshi
Prasher
Short
Rasouli
f
Re_Amin
(d)
Frontal diameter
SM3 Exp
Moores, Joshi
Prasher
Short
Rasouli
f
Re_Amin
(e)
Design
SM4 Exp
Moores, Joshi
Prasher
Short
Rasouli
f
Re_Amin
(f)
Frontal diameter
SM4 Exp
Moores, Joshi
Prasher
Short
Rasouli
f
Re_Amin
(g)
Design
SM5 Exp
Moores, Joshi
Prasher
Short
Rasouli
f
Re_Amin
(h)
Frontal diameter
SM5 Exp
Moores, Joshi
Prasher
Short
Rasouli
f
Re_Amin

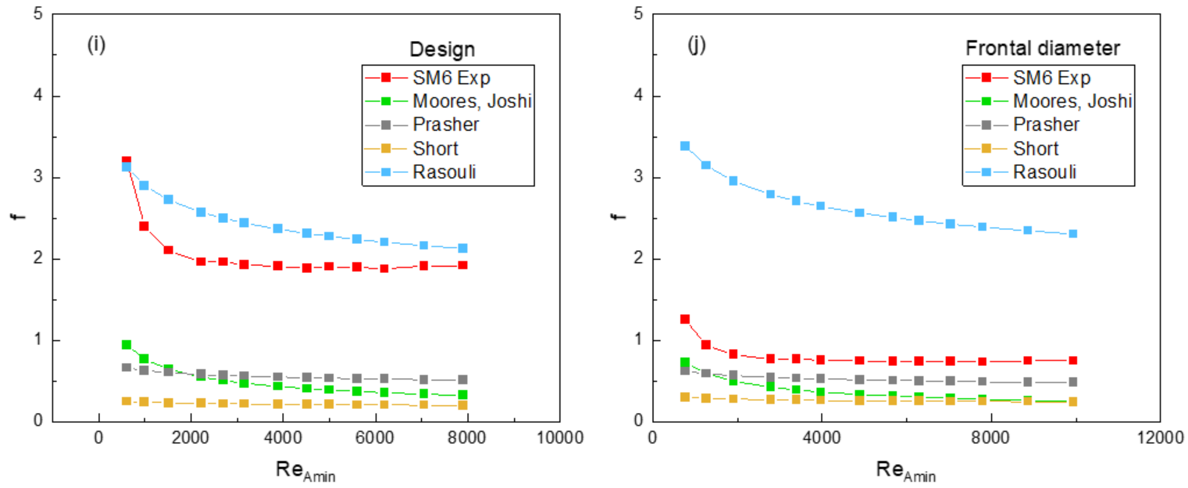

Figure 4.7. Comparison of the experimental friction factor with predictions of literature correlations for SM2 to SM6 with design diameter and flow frontal diameter as length scale.

The Mean Absolute Percentage Error (MAPE) is summarized in Table 4.3 and Table 4.4 for measured ratios based on the design and flow frontal diameter. Based on the design diameter (see Table 4.3) the Rasouli et al. [76] correlation seems to be the most accurate at predicting the friction factor for the majority of the cases considered. One case that shows a prediction that is quite off especially compared against the other correlations is that of SM5 (96.8 % MAPE) and can be explained by the fact that two out of the three geometrical parameters (these two parameters being the transverse and longitudinal spacing) are out of the range for which the correlation was originally derived for.

Table 4.3. Mean Absolute Percentage Error (MAPE) of different correlations for friction factor based on design diameter.

Correlations/pin array #	Moores & Joshi [3]	Prasher et al. [1]	Short et al. [4]	Rasouli et al. [2]
SM2	95.1	94.0	97.6	73.6
SM3	80.4	61.4	89.3	8.2
SM4	63.3	7.9	84.3	20.1
SM5	56.1	68.7	87.3	96.8
SM6	76.3	72.5	89.3	20.3

When comparing the results based on the frontal diameter (Table 4.4), the MAPE of the Prasher et al. [75] correlation seem to be the lowest among all others for SM3, 5 and 6 while the Rasouli et al. [76] correlation predicted SM2 pressure drop to within 17%. These correlations follow the qualitative trends in the experimental data as well. When comparing Rasouli et al. [76] and Prasher [75] correlations, the former predicts pressure drop of constricted pin arrays better while the latter is a better predictor of pressure drop in the other pin arrays. With the exception of the most constricted pin array, SM2, the Rasouli et al. [76] correlation generally tends to overpredict pressure drop by significant margins. The Moores and Joshi [77] and Short et al. [78] correlations tend to under-predict the experimental data consistently. The Prasher et al. [75] correlation is hence chosen for the HE model since the typical geometries for sCO_2 pin arrays closely resemble that of SM3.

Table 4.4. Mean Absolute Percentage Error (MAPE) of different correlations for friction factor based on the frontal diameter.

Correlations/pin array #	Moores & Joshi [3]	Prasher et al. [1]	Short et al. [4]	Rasouli et al. [2]
SM2	87.4	77.3	89.7	16.8
SM3	61.2	17.4	66.7	176.0
SM4	37.4	193.2	56.3	184.5
SM5	37.3	50.8	72.1	292.8
SM6	53.2	34	67.1	232.7

Heat transfer test results

Figure 4.8 shows the comparison of experiments with correlations for Nusselt number of arrays SM2-6. The MAPE values for the Prasher et al. [75] correlation and the Rasouli et al. [76] correlation with and without vortex shedding are summarized in Table 4.5 for results based on the design diameter and Table 4.6 for results based on flow frontal diameter.

Table 4.5.Mean Absolute Percentage Error (MAPE) of different correlations for Nusselt number based on design diameter.

Correlations/pin array #	Prasher et al.	Rasouli et al. (non VS)	Rasouli et al. (VS)
SM2	69	26	146.8
SM3	82.9	21.1	224.9
SM4	77.5	30	259
SM5	16.4	34.3	188.7
SM6	5.2	38.4	140.3

Based on the design dimensions, we observe again that the Rasouli et al. [76] correlation (for no vortex shedding) on average predicts Nu the best. The two cases where Prasher et al. [75] outperforms Rasouli et al. [76] is in the cases of SM5 and SM6. As mentioned previously, SM5 has geometrical features that make this array lie significantly outside the range of applicability of the correlation. Additionally, although all the heat sinks were design to exhibit vortex shedding, SM5 and SM6 were designed with a noticeably wider spacing that is more likely to comparatively display more shedding than the others. A probable explanation for the performance observed is the occurrence of vortex shedding, which is supported by the trend difference with SM5: while in all the cases considered (based on design diameter) the experimental results were bracketed by Prasher et al. [75] and Rasouli et al. [76], in the case of SM5, Nu gets large to the point were even the Prasher et al. [75] correlation yields a slight underestimate of it (see Figure 4.8).

Table 4.6.Mean Absolute Percentage Error (MAPE) of different correlations for Nusselt number based on flow frontal diameter.

Correlations/pin array #	Prasher et al.	Rasouli et al. (non VS)	Rasouli et al. (VS)
SM2	313	31.3	227.5
SM3	305.4	42.7	351.6
SM4	322.9	34.7	448.4
SM5	83.3	12.6	227.7
SM6	76.1	13.5	224.7

From Figure 4.8, the experimental values for Nu, based on the flow frontal pin diameter are always best predicted by the non-VS correlation of Rasouli et al. [76], with a MAPE that ranges from 12.6% for SM5 to 42.7% for SM3 (see Table 4.6). The VS correlation by Rasouli et al. consistently overpredicts data by a large margin. This is to be expected, since this correlation holds good for aspect ratio and longitudinal pitch ratios greater than 1 and transverse pitch ratio greater than 2. As mentioned earlier (Table 4.2), none of the heat sinks have these non-dimensional ratios when the flow frontal diameter is used as the length scale. The Prasher et al. [75] correlation also consistently over-predicts experimental data since the correlation was developed for a different range of pin geometrical parameters that are consistent with VS regime established in Rasouli et al. [76]. Both Rasouli et al. [76] and Prasher et al. [75] correlations were developed for Reynolds numbers less than 3000. However, it seems that the Rasouli et al. [76] correlation can predict, to reasonable accuracy, trends in experimental results up to Reynolds numbers as high as 15000. In light of these results, the non-VS Rasouli et al. [76] correlation was selected to predict heat transfer.

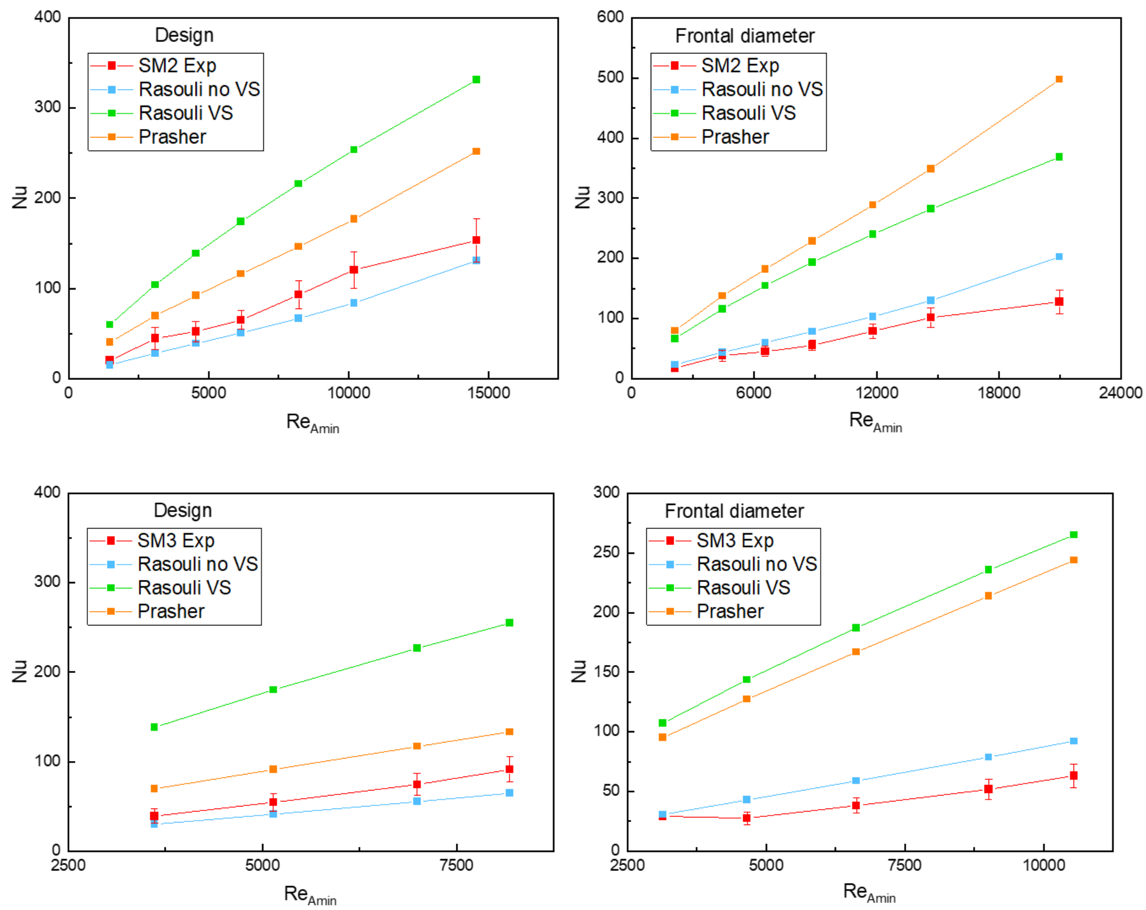

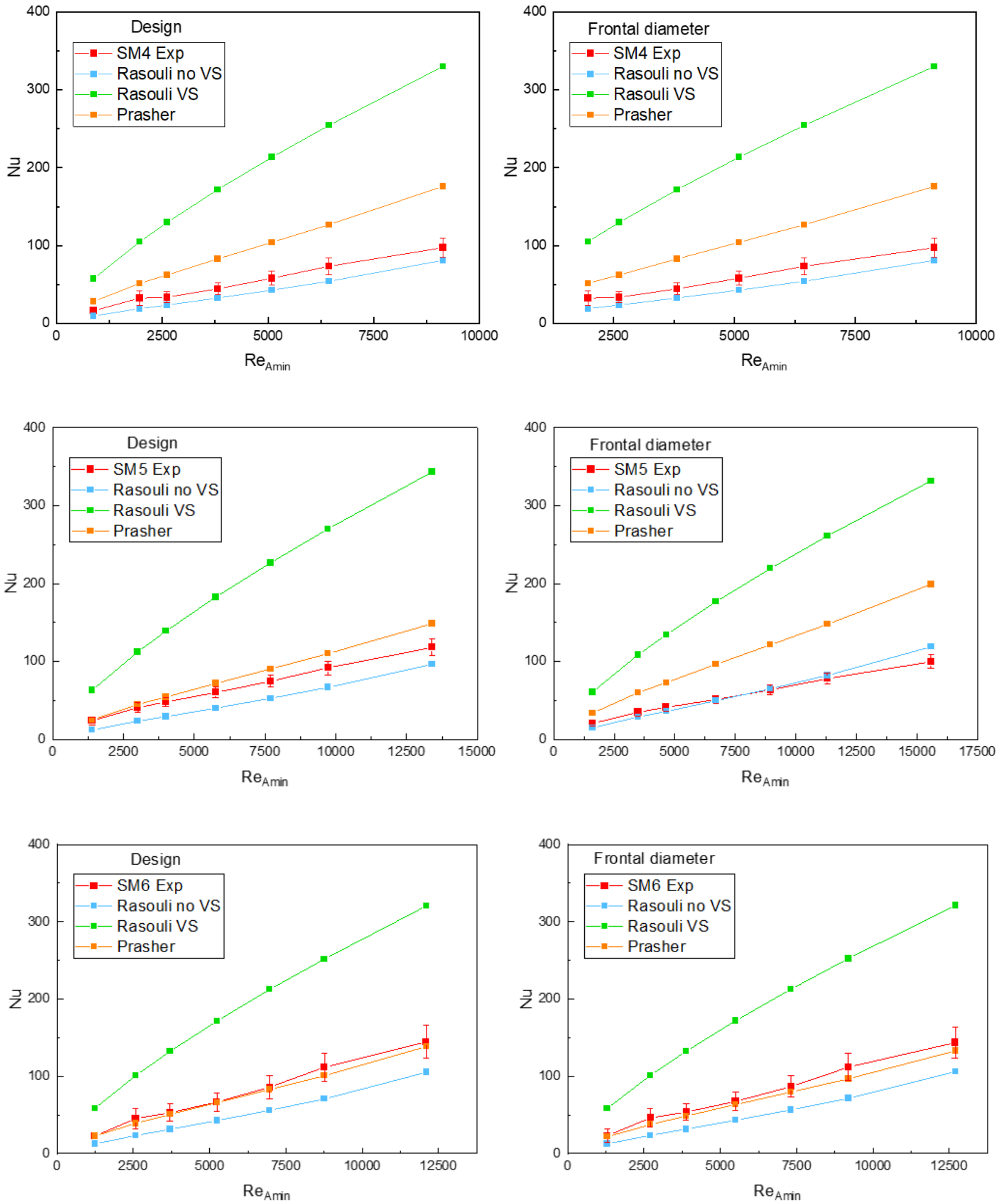

Figure 4.8. Comparison of the experimental Nusselt number with predictions of literature correlations for SM2 to SM6 based on the design diameter and the flow frontal diameter as length scales.

4.5.2. Correlation for the Gen 2 3D lattice side with MS

Due to the complex nature of the 3D lattice architecture on the hot side, CFD simulations were performed to obtain the thermal resistance for various Reynolds numbers. Figure 4.9 shows the simulation setup that consists of two computational domains- the fluid domain with MS and the solid domain of Haynes 282. A representative stripe of the array of slanted pin fins was modeled in lieu of the complete array to reduce the computational time. A constant heat flux of 40,000 W/m^2 was imposed on the top and bottom faces based on the estimated thermal rating of the full-scale PHE. The side faces were defined as symmetry boundaries. The flowrate at the inlet was varied to obtain simulation results as function of Reynolds number. The molten salt, whose temperature-dependent properties were obtained from Wang et al. [81], is a composition of 20 mol% NaCl, 40 mol% KCl and 40 mol% $MgCl_2$. The simulations were run with k-omega SST turbulence model and convergence was deemed achieved when all residuals were lower than 10^{-6} except the turbulent kinetic energy, which was of the order of 10^{-4}.

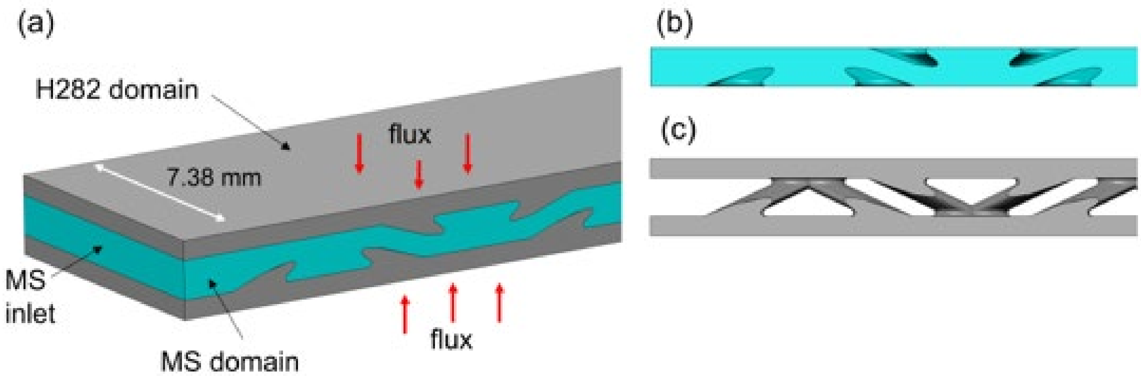

Figure 4.9. (a) CFD simulation setup, side view of (b) the molten salt and (c) H282 domains, with pin diameter of 1.2mm and channel height of 1.0mm.

The results of friction factor and thermal resistance are presented in Figure 4.10(a) and (b), respectively. Two channel heights, 1.0 and 1.8 mm were considered in the analysis. The smaller height would enhance heat transfer coefficient, while the taller channel height would ease the powder removal process and reduce pressure drop. A comparison between the two options would establish whether the heat transfer gain can justify the selection of a 1.0 mm channel. The thermal resistance R" is calculated at several locations along the length of the stripe as:

$$R_h^{"} = \frac{T_{w_{avg}} - T_f}{Q"} \tag{4.2}$$

where Tw_{avg} is the average temperature of the top and bottom walls at the location considered and T_f is average temperature of the fluid region defined by these top and bottom walls.

For the two channel heights considered, a second order polynomial was used to relate the thermal resistance to the Reynolds number, and a piecewise model was used for the friction factor as function of Reynolds number. The resulting correlations based on CFD simulations for two channel heights are listed in Table 4.7. Figure 4.10 shows that for both channel heights, the friction factor decreases sharply and linearly at low Re_{Amin} and subsequently changes at a slower rate after a Re_{Amin} of 12 and 17 for 1.8 and 1.0 mm channels, respectively. The friction factor increases by 43% from 35.7 for 1.8 mm gap to 51.2 for 1.0 mm at Re_{Amin} of 20. The percent increase drops to 32% at Re_{Amin} of 35. The thermal resistance of the 1.8 mm channel is however higher, such that going from the 1.8 to 1.0 mm channel, the value of R''_h decreases by 27% on average over all Re_{Amin}. The resistance of the 1.8 mm channel decreases more rapidly with Re_{Amin} than the other configuration such that the percent change from 1.8 mm to 1.0 mm channel is only 16% at a Reynolds number of 35.

Table 4.7. Friction factor and thermal resistance correlations for MS.

1.8 mm MS lattice core	$f_h = 146.72 - 7.76Re_{Amin}$ if $Re_{Amin} < 12$ $f_h = 86.6 - 3.47Re_{Amin} + 0.05{Re_{Amin}}^2$ otherwise	R^2=1 R^2=0.994
	$R''_h = 3.85\text{x}10^{-4} - 5.90\text{x}10^{-6}Re_{Amin} + 3.06\text{x}10^{-8}{Re_{Amin}}^2$ in K-m2/W	R^2=0.999
1.0 mm MS lattice core	$f_h = 166.7 - 6.49Re_{Amin}$ if $Re_{Amin} < 17$ $f_h = 99.7 - 3.07Re_{Amin} + 0.033{Re_{Amin}}^2$ otherwise	R^2=1 R^2=0.994
	$R''_h = 2.71\text{x}10^{-4} - 3.05\text{x}10^{-6}Re_{Amin} + 1.45\text{x}10^{-8}{Re_{Amin}}^2$ in K-m2/W	R^2=0.999

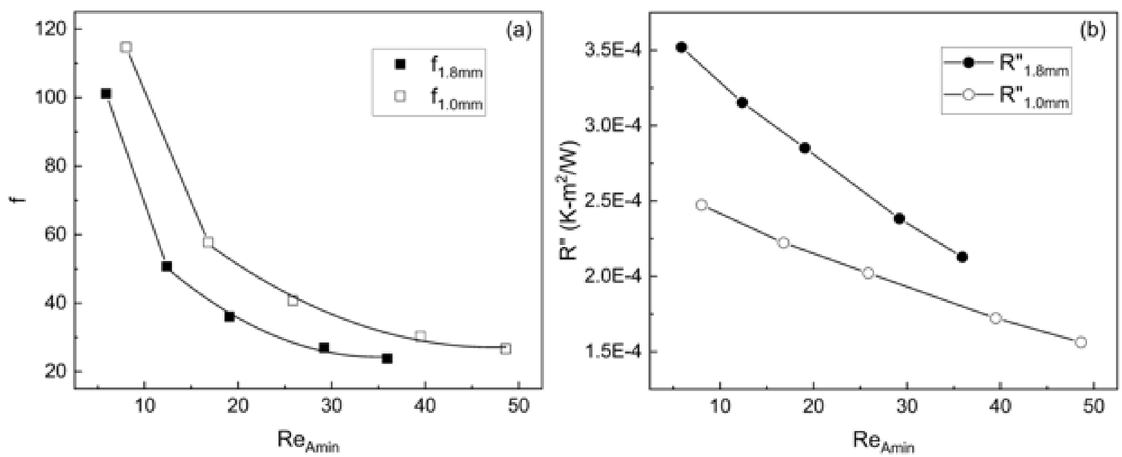

Figure 4.10. (a) Friction factor and (b) thermal resistance varying with Reynolds number for the 1.8 and 1.0 mm hot (MS) channel height. The pin diameter and wall thickness are consistent between the two arrays at values specified in Table 6.3 in Chapter 6.

Ultimately, the 1.8 mm channel was selected for manufacturing considerations and to facilitate the powder removal process.

4.5.3. Summary of correlations selected for the HE model

In summary, for heat transfer in the pin array of the HE model, the non-VS Rasouli et al. [76] correlation was adopted, while the Prasher et al. [75] correlation for pressure drop was used for friction factor. The criterion for VS was based on the flow frontal area as opposed to the equivalent diameter since the results from Chapter 3 showed that flow separation occurs based on this diameter. In 200 bar sCO_2 heat sinks, due to the high internal stresses, it is more likely that the non VS regime geometries are needed from a mechanical strength standpoint.

Some contributors to the limit in accuracy of some correlations are the variability of the pin dimensions due to the downskin region in the pins and the large fillets where the pins meet the walls which were added for mechanical stress reduction. The presence of the downskin region can be accounted for in the correlations by using the appropriate length scale for the AM pin arrays. The heat sinks used to develop correlations in literature do not have fillets; hence their ability to predict flow and heat transfer in this geometry is questionable. Nevertheless, the chosen correlations have reasonable predictability for the range of anticipated pin array geometries for this application. With additional experimental testing, it is possible to develop specific correlations for the AM pin array geometries used in the HE.

For Gen 2 MS design, simulations with design dimensions were used for pressure drop and heat transfer. Given the overprinting, it is anticipated that the experimental pressure drop will be larger than predicted by simulations. In future work, the actual geometry of the 3D lattice structure needs to be quantified, and simulations performed on the measured geometry, to determine whether the predictions match experimental results. Based on the study performed on pin arrays, we expect that the pressure drops from simulations will align closely with experiments if the actual printed dimensions are used.

Chapter 5 Gen 1 Design and Performance

The design and techno-economic performance of a compact additively manufactured (AM) molten salt-to-supercritical carbon di-oxide (sCO_2) primary heat exchanger (PHE) for solar thermal application is described. The PHE design consists of sCO_2 flow through an array of microscale pin fins while the MS flows through mm-scale rectangular channels. Constraints imposed by AM using L-PBF are considered in the design. Structural and fluid flow simulations are performed to arrive at a viable design of the core and headers. A simplified one-dimensional steady state model for the PHE is developed including the impact of surface roughness from the AM process. A process-based cost model, developed by collaborators at CMU and University of Michigan (Ziev and Vaishnav) is used to determine the tradeoff between thermofluidic design and manufacturing cost.

A parametric study is performed using the thermo-fluidic and cost models to determine the set of geometrical and flow variables that result in high power density and low cost, while restricting the pressure drop on the sCO_2 side to less than 2% of line pressure. Flow rates of MS and sCO_2 were varied over heat capacity rate ratios ranging from 0.2 to 1. Results indicate that it is possible to design a low-pressure drop AM PHE with an effectiveness of 80% and a power density of 10 MW/m^3 (including headers). Fabrication of representative nickel superalloy specimens are shown to demonstrate that low-porosity parts with the requisite dimensional tolerance of PHE core can be generated.

5.1. Gen 1 design overview

As shown in Figure 5.1, the first generation heat exchanger, henceforth referred to as Gen 1 is made of a two headers of varying cross section and a core section made of a series of hot and cold plates with a straight rectangular channel design, and a pin array design, respectively. The following sections will describe the mechanical and thermofluidic design of the heat exchanger, starting at the level of the pin and moving up to the plate and header design.

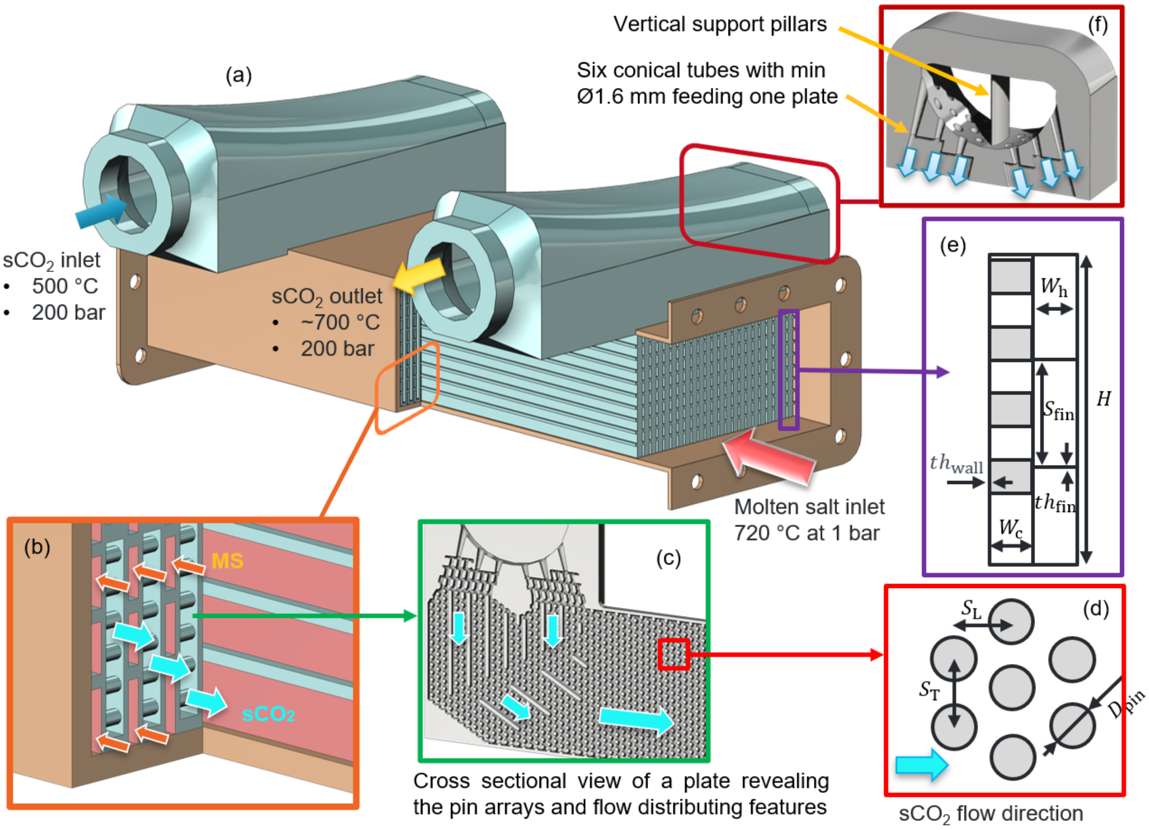

Figure 5.1. Proposed concept for AM PHE. (a) solid model of the PHE with a cut-away view of the core architecture, (b) cut-away view of the core showing the sCO$_2$ and MS passages, (c) view of the pin arrays and distributing features, (d) top view schematic of the pin array, (e) schematic of the cross-sectional view of a cold plate and adjacent hot side, (f) details of the header design with vertical support pillars and distributor tubes to direct the flow into the plates.

5.2. Bottom-up structural design

5.2.1. Design setup and criterion

The HE design was initially based on H230. The creep life of Haynes 230 components at a specified stress level and temperature, e.g., long-time rupture life at lower stress and temperature, can be extrapolated using the Larson-Miller parameter (LMP) [82]. Based on the Larson Miller approach, an upper limit of 50 MPa based on the creep rupture stress at 100,000 hours and a temperature of 720 °C was used in the design process. The spacing of the pins to withstand the

200-bar internal pressure was determined through mechanical simulations. Based on these simulations, pins needed to be of diameter 0.6 mm, with a transverse pitch of 0.8 mm for H230. Initial printing trials were performed with this core geometry but resulted in significant overprinting of the pins in the build direction, resulting in complete blockage of the flow passages through the array (see Figure 5.2(a)).

Hence, changes to the pin design were made to reduce the overprinting in the down-skin region. While the redesign alleviated the issue of complete blockage, the pins were still printed with very narrow flow gaps (see Figure 5.2(b)) which would have resulted in unrealistic designs with H230. Hence, the H230 design was abandoned and a H282 design was pursued. With H282 design, the pin spacing could be further apart due to its higher creep strength (design stress of 100 MPa).

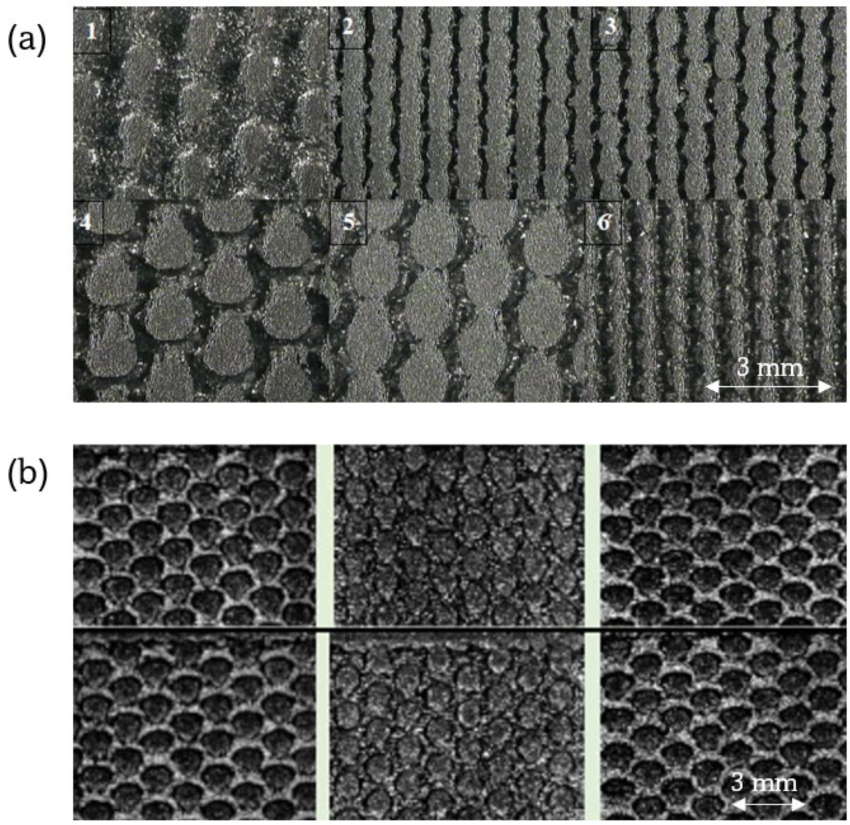

Figure 5.2. Cross sections showing (a) pin arrays with severe overprinting and (b) pin arrays redesigned to achieve better circularity. Printing of the arrays and characterization through scanning was conducted by CMU.

The design criterion used for the structural integrity analysis is based on Larson Miller Parameter calculation for a life of 100,000 hours. Using the LMP curves of Haynes 282 shown in

Figure 5.3, the allowable stress for 1% creep at the end of the desired life was 97.5 MPa. The stress value for the same life at rupture was found to be 150 MPa. A maximum von Mises stress of 100 MPa was therefore selected to design the core of the heat exchanger only subjected to the mechanical loads. This criterion provides some margin for the expected thermal stress due to the temperature gradients generated in the geometry.

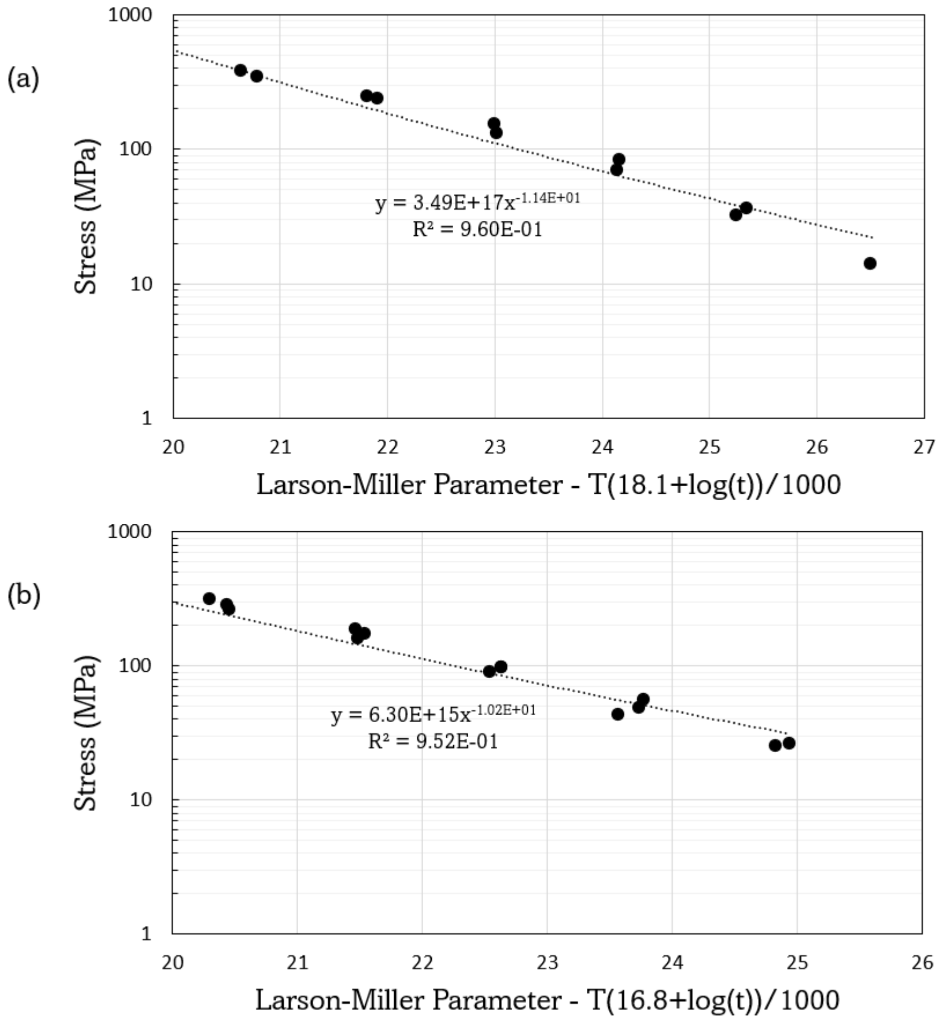

Figure 5.3. Larson-Miller Parameter of Haynes 282 at (a) 1% Creep and (b) rupture [83].

5.2.2. Core design

The pin array shown in Figure 5.4(a) is made up of repeating identical entities highlighted in blue in Figure 5.4(b) so the first stage of the design focused on a single pin in the array. Because of the symmetry of the pin, it was further sliced in two and the half pin shown in Figure 5.4(d) was used to assess the structural integrity under the expected loads. This reduced geometry was meshed, and simulations were performed using ANSYS Mechanical. The circular face obtained after defining the plane of symmetry of the pin has all its degrees of freedom left unconstrained except the displacement normal to that face by virtue of symmetry. A 200 bar pressure is imposed on the inside faces (cylindrical portion, fillets, fin base), 1 bar on the bottom of the hexagonal base and symmetry boundary conditions are specified on the 6 rectangular faces of the base.

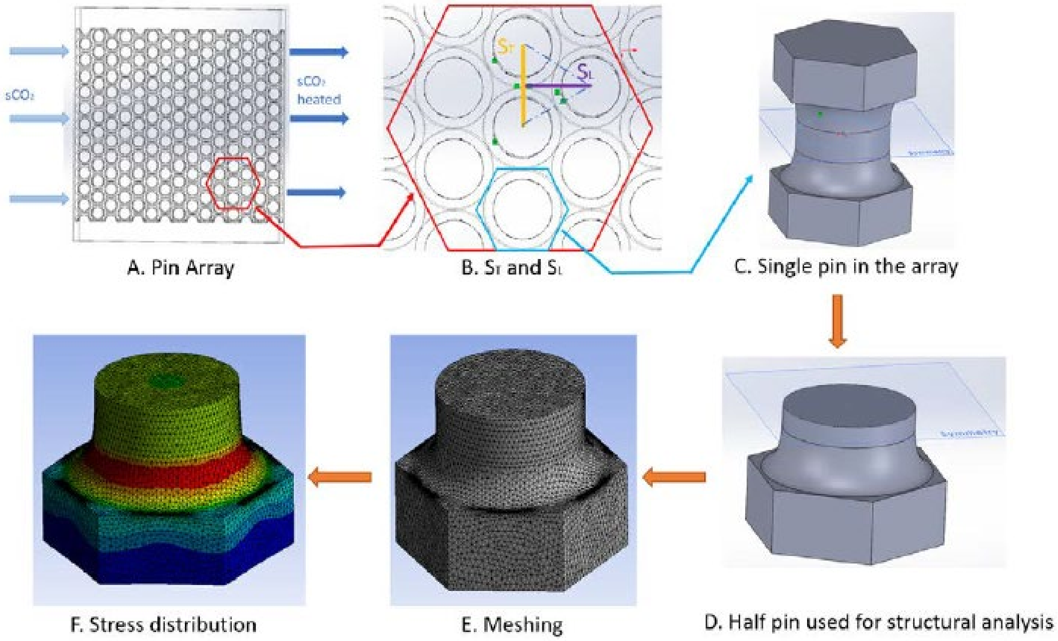

Figure 5.4. Structural integrity design flowchart

Initial simulations considered various pin architectures (elliptical, pyramidal, cylindrical, etc) for their mechanical integrity, but also their porosity (area open to flow) and their expected hydrodynamics implications. An airfoil shaped pin for example would be beneficial to minimize pressure losses but this geometry would be prohibitive for the current application because high stresses would be generated in the sharp tail area. A cylindrical pin being a blunt body in the flow would generate higher pressure losses because of recirculation zones but would be an advantageous configuration from the perspective mechanical integrity. Ultimately, a cylindrical pin was identified as the optimal geometry and was used for further parametric study.

Parametric study

Several important parameters play a role in determining the overall design of the PHE, including geometrical parameters of the core shown in Figure 5.1(d) and (e) such as the cold plate spacing, MS-side fin spacing, cold plate pin array design, and flow parameters such as hot and cold flow inlet temperatures, and mass flow rates. The stress distribution on an elemental repeating unit of the pin array was evaluated to minimize the maximum value of the von Mises equivalent stress dictated by the creep limit. A parametric study was performed in order to determine the shape of the pin that would yield the lowest stress. Various pin shapes (circular, elliptical, hourglass) were considered, with additional iterations on the pin height, wall thickness and fillet radii at the base of the pins. From the simulation results, it was observed that a circular cross-section for the pin associated with a hexagonal lattice of pins was the optimal combination to reduce the maximum stress in pin array unit cells. The final unit cell geometry, that defined the upper limit of transverse and longitudinal spacing, and the lower limit of wall thickness and pin diameter for the thermofluidic analysis, are summarized in Table 5.1.

The base case is a pin with a 1.2 mm diameter (D), 0.5 mm height, 0.5 mm top and bottom wall thickness. These dimensions were based on a prior design of waste heat recovery heat exchangers using IN 718 [84]. A staggered pin arrangement is chosen because it promotes mixing, turbulence and thus enhances the heat transfer. The pins layout is such that the transverse and longitudinal pitches (S_T and S_L) are the base and height of an equilateral triangle respectively, so updating one also affects the other dimension (see Figure 5.4(b)). A first parametric study is conducted using a pin with symmetrical fillet radius and varying the value of that fillet along with the transverse pin spacing and the pin height.

Table 5.1. Parameters for the primary sensitivity study

	ST (mm)	Fillet (mm)	Height (mm)	Max. stress (MPa)
Case 1	2.2	0.4	0.9	102.7
Case 2	2.4	0.4	0.9	125.6
Case 3	2.6	0.45	0.9	144.3

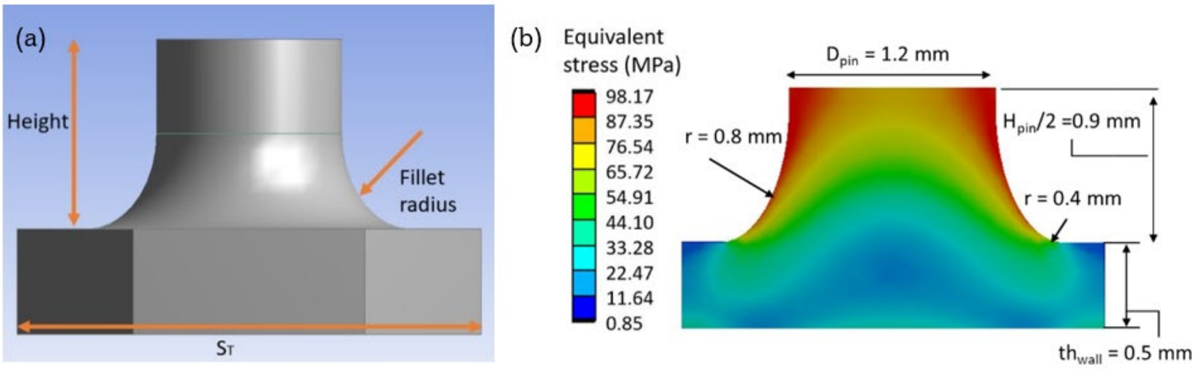

Figure 5.5. (a) Parameters varied in the sensitivity study, (b) Cross sectional stress distribution in the final design.

Table 5.1 shows a sample of the cases selected at the end of this primary study. These configurations are the ones that yielded a stress value greater than 100 MPa but within a margin (40 MPa) that could make them viable options after modifying the fillets. These cases were therefore selected for further refinement, conducting this time a parametric study on fillet asymmetry. It was observed that depending on the ratio used for the fillet radii, a stress reduction of up to 30 MPa could be obtained.

Table 5.2. Dimensions of the finalized pin design

D_{pin} (mm)	1.2
β_T	2.05
β_L	1.76
th_{wall} (mm)	0.5
H_{pin} (mm)	1.8
Fillet radii (mm)	0.8-0.4

The final pin geometry is shown in Figure 5.5(b) and its dimensions are summarized in Table 5.2. The pin section displays a maximum stress of 98 MPa with stress decreasing as we move downward towards sections with larger cross-sectional area. An independence study was conducted by varying the mesh size from 43,000 to 460,000 nodes. The maximum stress remains stable starting with the second mesh containing 71000 nodes and corresponding to an element size of 0.07mm.

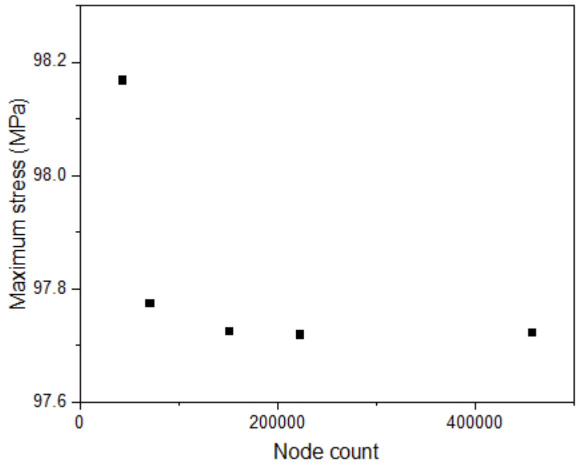

Figure 5.6. Grid independence

5.2.3. Header design and flow uniformity

The structural support features within the header to withstand 200 bar internal pressure are shown in Figure 5.1(f). Periodically located vertical pillars resulted in peak stress of 110 MPa in the pillars. Upon completion of the mechanical design, CFD simulations were performed on the header to characterize the flow distribution into the pin array plates from the header. The fluid body within the structurally designed header is shown in Figure 5.7(a) where the connection between header and each of 26 plates can be distinguished. Flow was directed into each plate from the header via six conical tubes, see in Figure 5.1(c) and in Figure 5.1(f). The fluid body was meshed and simulated in Ansys Fluent using k-epsilon turbulence model for baseline flow rate of 50 g/s. A porous media model was imposed on the region called out in red in Figure 5.7(a) to take into account the effect of pressure drop across the pin array on the flow distribution in the header. The porosity parameters for viscous and inertial terms were obtained based on pressure drop through pin array obtained by simulating a narrow strip of the core for the range of relevant flow rates. The mass flow rates discharged into each of 26 plates are plotted in Figure 5.7(b) for 50 g/s overall incoming sCO_2 flow rate entering the header (baseline flow rate in parametric study). The mass flow rate into each plate varied between 1.90 g/s and 1.93 g/s with the Mean Absolute Deviation (MAD, second ordinate in Figure 5.7(b)) among plates relative to the average of less than 1%. The low MAD indicates a viable header design for the PHE, which while intricate, can readily be fabricated using AM. The header design and flow uniformity study presented here were carried out by Dr. Rasouli, an engineer at the Western Cooling Efficiency Center of UC Davis.

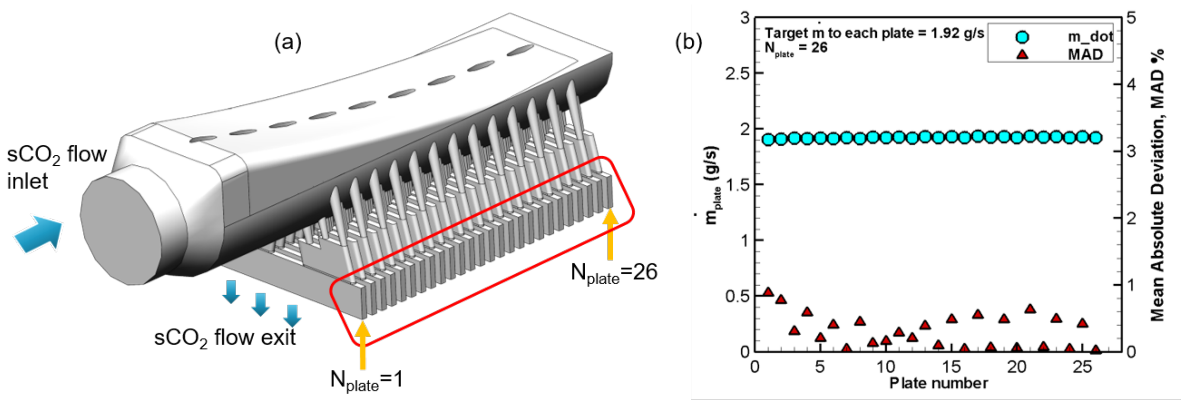

Figure 5.7. (a) View of the fluid body within the header (b) Distributed sCO_2 flow rate into each plate

The next procedure in the design was to ensure uniform flow distribution in the counter-flow region within each sCO_2 pin array plate. By virtue of symmetry, the computational domain consisted of pin array and molten salt channels with one-half thickness, as shown in Figure 5.8. In the meshing module of ANSYS, the flow domain was discretized using the method of proximity and curvature, and the near wall region was refined on both the sCO_2 and molten salt sides with inflation layers. Since the Reynolds number (Re) for the sCO_2 side was 1400, a k-ω SST turbulence model was selected for better treatment of flow separation in the wake of the pins. Prior work in literature has shown that the flow in such pin arrays transitions to turbulence at a Re of 150 [76]. The MS side was modeled as a laminar flow since the Re was about 30. Symmetry boundary conditions were defined as shown in Figure 5.8. The inlet and outlet sCO_2 faces were defined as mass flow inlet and pressure outlet, respectively. Analogous boundary conditions were applied on the side faces for the inlet and outlet faces for the salt. All other external faces (top, bottom, sides) were defined as adiabatic. Temperature dependency of the molten salt, sCO_2 and H282 properties over a range from 500 °C to 800 °C were used in the simulations. Convergence for simulations was deemed achieved when the residuals for energy, velocity, dissipation, and turbulent kinetic energy attained values of 10^{-8}, 10^{-4}, 10^{-4}, and 10^{-3}, respectively. The mass imbalance between the inlet and exit at convergence was 5.2 $*10^{-3}$ percent.

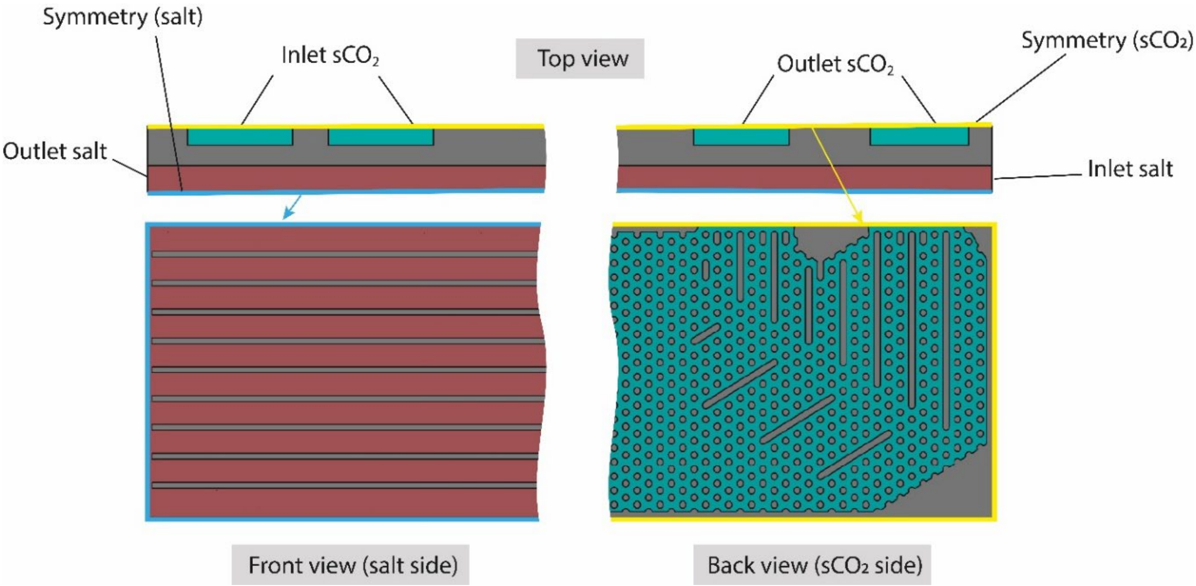

Figure 5.8. Schematic of the heat exchanger plate with one-half thickness including solid and fluid domains.

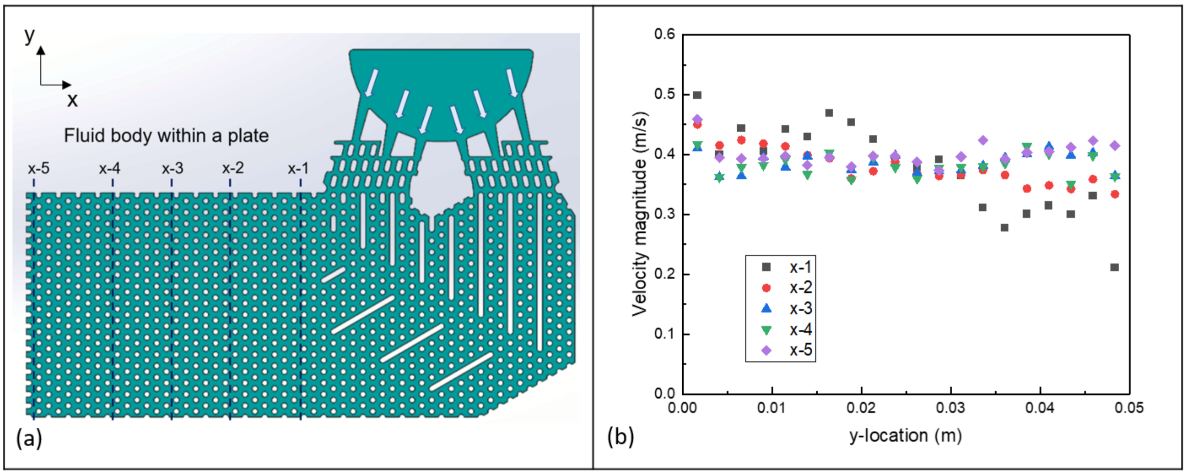

Figure 5.9. (a) Fluid body within the plate, (b) Velocity magnitude along the y-direction at different x-location in the plate.

A grid independence study with meshes varying from 15 to 21 million nodes was performed to ensure sufficient resolution to provide invariant results. The parameters altered to obtain the different meshes were the element proximity minimum size as well as the number of inflation layers. Between 15 and 21 million nodes meshes, the proximity and curvature minimum size varied from 0.15 mm to 0.122 mm and the number of inflation layers varied from 10 to 12 on the sCO_2 side and 7 to 10 on the molten salt side. A difference of less than 1 % in pressure drop on the cold side and less than 0.1 % in exit temperatures was noted from one mesh size to the next above 17 million nodes. Results from the 17 million nodes simulation are therefore used for analysis and post-processing.

To quantify the flow uniformity on the sCO_2 side, velocity magnitude along the height of the plate (y-direction) at five different locations along the flow direction (x-direction) are plotted as shown in Figure 5.9(b). The velocity magnitudes are seen to be reasonably close to one another and the largest deviation observed is at location x-1 due to its proximity to the cross flow section and the inlet of the flow domain. The mean average error of velocity magnitude at location x-1 is 16 % but the average MAD at locations x-3 – x-5 is only 3.6 %, indicating adequate flow uniformity across the height of the pin array in a majority of the counter-flow section.

5.2.4. PHE Additive Manufacturing Considerations

The design of the heat exchanger is dictated by AM constraints with an emphasis on avoiding large-scale overhanging features, i.e., a structure built directly on a powder bed without being anchored to a solid substrate. An important consideration in the design of an AM PHE was to ensure that the AM process was able to generate high density, pore-free parts. Fabrication runs were performed in an EOS M290 L-PBF machine with gas atomized H282 powder to determine the process window at a pre-heat of 200°C to produce pore-free builds. Once the process window was identified, small-scale specimens, representative of the core geometry were fabricated to determine the dimensional tolerance that could be achieved.

Table 5.3 summarizes the three laser parametric candidates within the process window and their corresponding part densities measured using the metallurgical cross-sectioning method. The higher build rate did sacrifice a little part density as the laser speed increased from 959 mm/s to 1772 mm/s when switching from S#1 to S#3, almost doubling the build rate. Yet, all three parameter sets achieved more than 99.9% in part density. Note that the EOS M290 machine has a maximum laser power of 370 W which limited the maximum applicable laser speed (and lowest part cost) with the concern of lack-of-fusion.

Table 5.3.Part densities and plate surface roughness resulting from three optimized laser parametric candidates, selected to assist the design and development of the additively built PHE using H282 gas atomized powder in an EOS M290 LPBF system.

Parameter label	Power (W)	Velocity (mm/s)	Hatch Spacing (mm)	Energy density (J/mm^3)	Density (%)	Roughness R_z (μm)
S#1	250	959	0.11	59.25	99.99	129.05
S#2	350	1366	0.11	58.23	99.96	102.06
S#3	370	1772	0.11	47.46	99.92	186.61

Table 5.4. Measured pin dimensions of micro pin array fabricated using three optimized sets of laser parameters in an EOS M290 LPBF system.

Pin diameter (mm)	Printing parameters	Measured pin dimension along x (mm)	Percentage deviation from the design along x (%)	Measured pin dimension along y (mm)	Percentage deviation from the design along y (%)
1.2	S#1: 250 W & 959 mm/s	1.310 ± 0.074	9.17 ± 6.2	1.255 ± 0.066	4.56 ± 5.5
	S#2: 350 W & 1366 mm/s	1.376 ± 0.079	14.68 ± 6.5	1.226± 0.049	2.15 ± 4.1
	S#3: 370 W & 1772 mm/s	1.327 ± 0.083	10.60 ± 6.9	1.191 ± 0.051	-0.76 ± 4.3
1.0	S#1: 250 W & 959 mm/s	1.135 ± 0.059	13.54 ± 5.9	1.069 ± 0.054	6.89 ± 5.4
	S#2: 350 W & 1366 mm/s	1.162 ± 0.074	16.24 ± 7.4	1.109 ± 0.068	10.85 ± 6.8
	S#3: 370 W & 1772 mm/s	1.100 ± 0.061	10.01 ± 6.1	1.021 ± 0.064	2.13 ± 6.4

The dimensional tolerance study aimed to identify the optimal pin design for which the as-built and the designed geometries have similar dimensions and preserve the circular pin cross-section. The primary challenge for building pins with good dimensional accuracy arises from the heat accumulation during laser melting since the pins are relatively small in size and are built as an overhanging structure. The powder bed is less thermally conductive compared with the solid [85]; especially at the bottom surface of a pin where melt tracks are only surrounded by powder, the problem of overheating can often be observed [86]. As a result, more overheated molten metal can infiltrate into the powder bed and potentially entrap partially melted particles leading to pin shape irregularity and deviation from the design dimension.

Table 5.4 summarizes pin dimensional measurements for two arrays with pin diameters of 1.2 and 1.0 mm respectively printed using three different power and speed combinations from the porosity study (Table 5.2). Every pin in a pin array was measured along the horizontal and vertical directions to derive the mean and deviation values shown in Table 5.4. The anticipated infiltration effect showed no significant impact on the bottom surfaces resulting in a less severe overprinting situation along the vertical direction compared with the horizontal direction. No clear correlation was observed between the pin dimensions printed using different parameters; however, the S#2 parameter set provided a slightly lower deviation from the design. Overall, the combinations of pin dimensions and process parameters resulted in pin dimensions within ± 8 percent of the design dimensions.

5.2.5. Thermo-mechanical analysis

Among the various failure modes which exist, fatigue and creep are two modes of importance because of the cyclic nature of the heat exchanger operation and the high temperatures expected in this design. To assess the structural integrity of the current model against these modes of failure, thermal and mechanical stresses must be calculated to determine the combined effect of temperature and pressure on the heat exchanger. The first stage of the procedure to obtain the combined thermo-mechanical stress of the heat exchanger consists in conducting a conjugate CFD analysis in Fluent with both fluid and solid domains and to solve the equations for continuity, momentum, and energy. The simulation is the same as the one of objective 1, except that this case includes the plate headers. The objective of this simulation is to obtain the temperature distribution generated in the solid section due to the heat transfer between the molten salt and the supercritical carbon dioxide. The temperature distribution is then used as an input for the following analysis which is a FEA simulation including thermal and pressure loads.

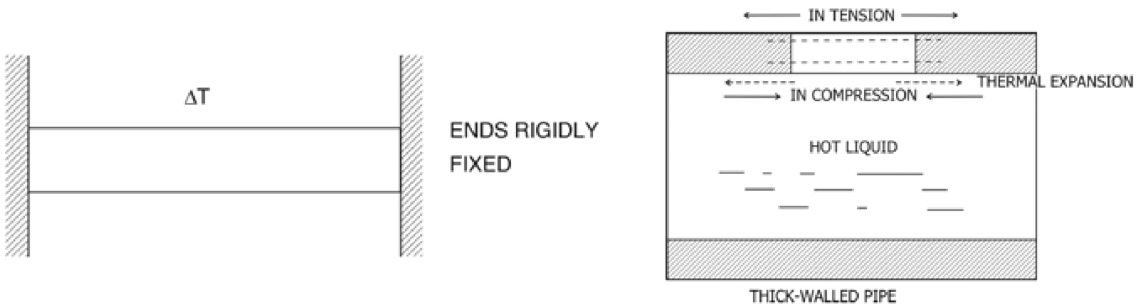

(a) (b)

Figure 5.10. (a) External constraints on a pipe between two walls, (b) Internal constraints [87]

Figure 5.10 shows the two types of constraints susceptible to induce thermal stresses [87]. Scenario (a) is shows a bar constrained on both ends and subjected to a temperature difference. As a result of this temperature change, the material expands but since the object is rigidly constrained thermal stresses are generated. Unlike scenario (a) which is an example of external constraints, scenario (b) illustrates thermal stresses induced because of internal constraints. The figure here depicts a pipe that simply rests on top of supporting structures and is free to expand and contract. If a hot fluid is circulated inside the pipe, such that the inner wall is heated while the outer wall remains at the initial temperature, thermal stresses are generated because different section of the pipe are trying to expand at different rates. The heat exchanger under consideration is expected to only be subjected to the latter constraints: the device is free to expand, and any displacement change will be translated into stress on the piping. In terms of pressure loads, the inlet and outlet sections are identical since they have the same design and are subjected to the same pressures. However, when considering the thermal load, the inlet section constitutes the bottleneck of the design because the largest temperature difference is located at the inlet. The focus of the thermo-mechanical analysis was therefore on the inlet region. After an adjustment of the coordinates, the temperature profile from the CFD simulations is mapped onto the plenum and used to evaluate the thermal stress in the design.

Three simulations are performed: a mechanical simulation with only imposed pressure, a thermal simulation with the solid body temperature, and a combined thermo-mechanical analysis which includes both pressure and thermal distribution.

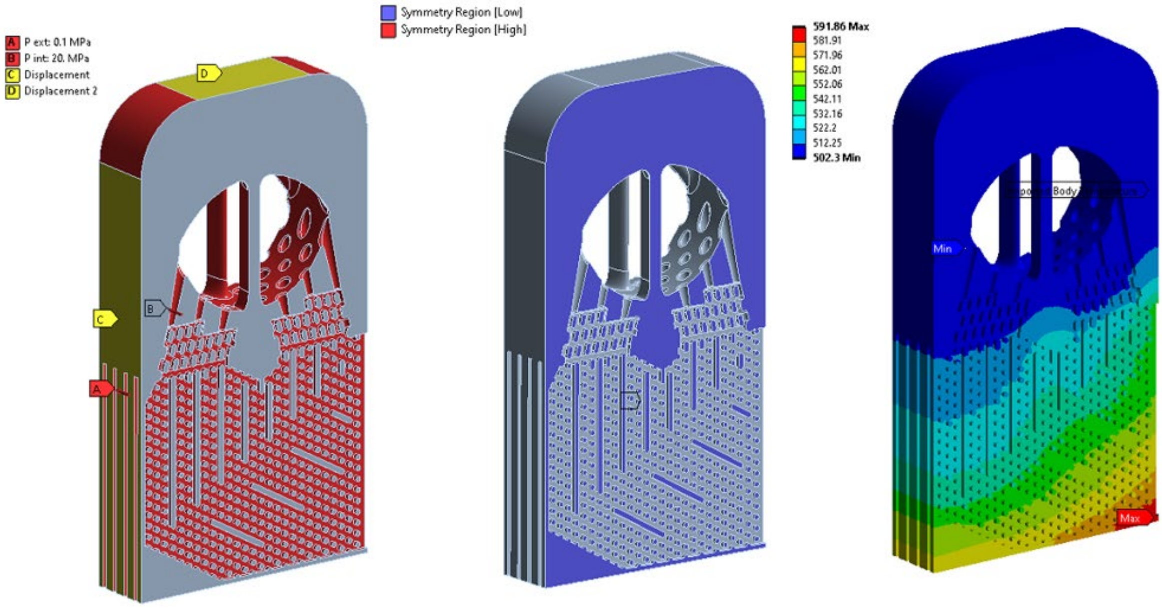

Figure 5.11. Analysis settings for a periodic section of the model.

Figure 5.11 shows the boundary conditions and loads imposed on a periodic section of the model. The yellow faces on the left picture have a zero-displacement constraint normal to them, indicating that these faces are free to move in the other two directions but can only expand and move away from the face which is normal to the direction specified in the constraint. The interior faces (red) have a 200-bar pressure imposed on them and the exterior faces (also red but located on the outer surfaces) are exposed to atmospheric pressure. In the case of the combined analysis, the temperature profile is also imposed on the model. Figure 5.12(a) illustrates the results of the thermal stress analysis. The contour on the right in Figure 5.12(a) shows regions where the thermal stress is more than 30 MPa. The header region which brings in the sCO_2 stream has a low stress profile because the fluid has a rather uniform temperature close to 500 °C. As non-uniformity and temperature changes arise in the section where the sCO_2 exchanges heat with the molten salt. Figure 5.12(b) shows the results for the mechanical-only simulation. Most of the part is subjected to stresses lower than 150 MPa. The high stress zone located at the cut region which opens on the pin array is believed to be an artifact which will not be observed in the full HX. Similar results are obtained for the combined thermo-mechanical analysis. The combined stress levels are below the 150 MPa threshold for most regions and the regions displaying some more stress compared to the pressure-only case can be traced back to the sections subject to more pronounced temperature gradients.

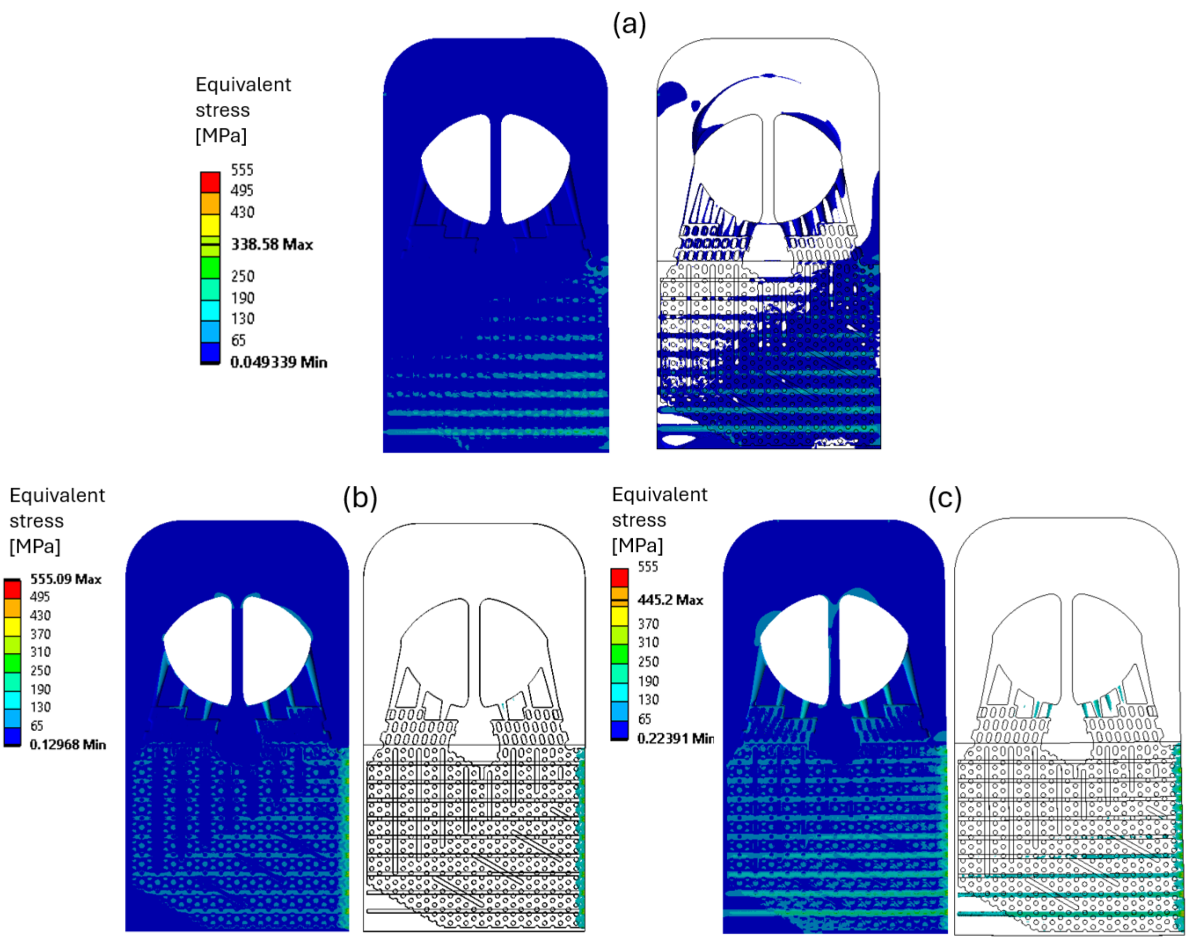

Figure 5.12. Equivalent stress and regions with stress greater than (a) 30 MPa for thermal loads only, and greater than 150 MPa for (b) mechanical only, and (c) and thermo-mechanical.

5.2.6. Creep and fatigue considerations

Creep is one of the most common modes of heat exchanger failure [88, 89] and often dictates material selection and the service life of the device. Creep is a type of deformation that usually occurs at high temperatures due to a diffusional flow of vacancies which ultimately results in a permanent change of shape [90,91]. As shown in Figure 5.13, the creeping behavior of a material can be divided into 3 stages: primary creep characterized by an initial fast rate that decreases over time, secondary creep which has a mostly constant rate, and tertiary creep where the rate keeps increasing rapidly until rupture. For this design, tertiary creep will not be analyzed and simply be associated with failure. Creep testing was conducted by CMU and it was concluded that the creep life of AM samples was comparable to that of wrought material. In addition, primary creep will be disregarded because for the selected material, this stage is brief and does not make a noteworthy contribution to the overall life of samples.

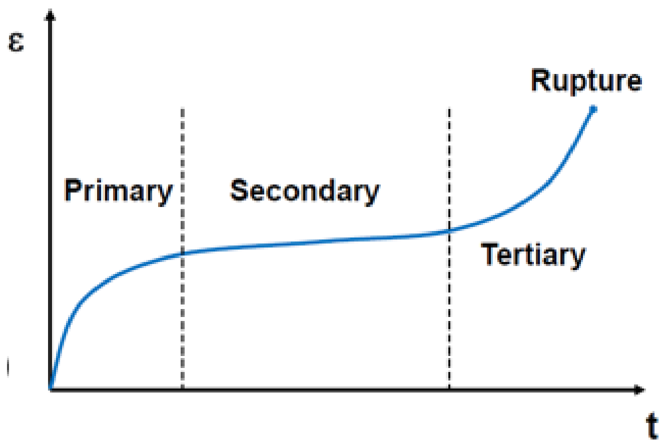

Figure 5.13. The three stages of creep.

The heat exchanger is expected to remain in the secondary creep mode for its entire lifetime. Hence the Norton's law, which is typically used to evaluate the secondary creep response of a material given the equivalent stress and the temperature, is applied to various sections of the heat exchanger under different scenarios. First, the constants of the Norton equation were derived by CMU using a least square fit for multivariate polynomial functions [91] and strain rate data for Haynes 282 at 700 °C and 750 °C for various stress levels [92]. The resulting constants defined the following law:

$$\dot{\varepsilon} = 1.898E-8\sigma^{6.805}e^{\left(\frac{-37250}{T}\right)} \tag{5.1}$$

Case 1: Single half pin with temperature and pressure cycles

The purpose of the first simulation was to obtain creep strain values for a single half pin in the array as well as to investigate the effect of results extrapolation.

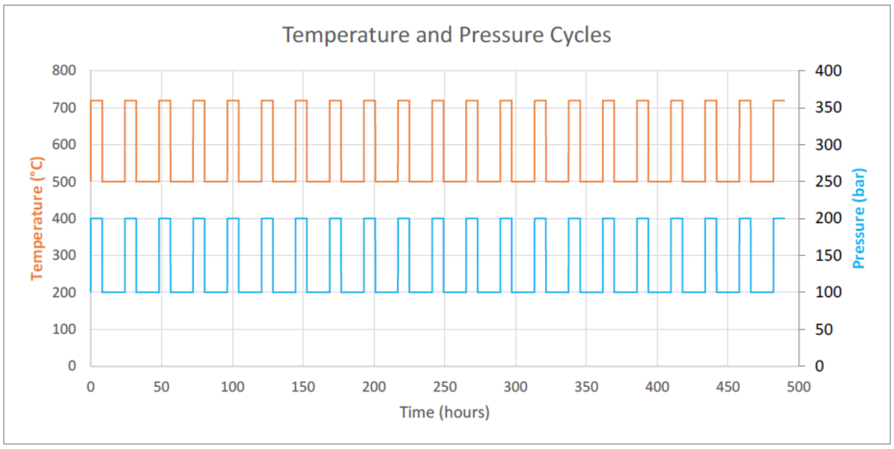

Figure 5.14. Cyclic pressure and temperature schedule proposed for creep simulations.

Plausible operation cycles for pressure and temperature are shown in Figure 5.14. The cycle starts with a 3-min ramp-up followed by 8 hours of operation at 720 °C and 200 bar, then there is a 3 min ramp-down followed by 16 hours during which the system is kept at 500 °C and 100 bar. Figure 5.15 shows the result of the simulation for 17207-hour, which corresponds to the maximum number of entries that we can specify in the solver given our cyclic profile. The green, blue and red lines on the plot correspond to the maximum, average and minimum creep strains, respectively. The maximum creep strain has a value of 3.35E-4 mm/mm and turns out to be a less conservative estimate when compared against the creep strain obtained from extrapolating a 1000-hour simulation. The trend is consistent for both the maximum and the average creep strains as shown in Table 5.5.

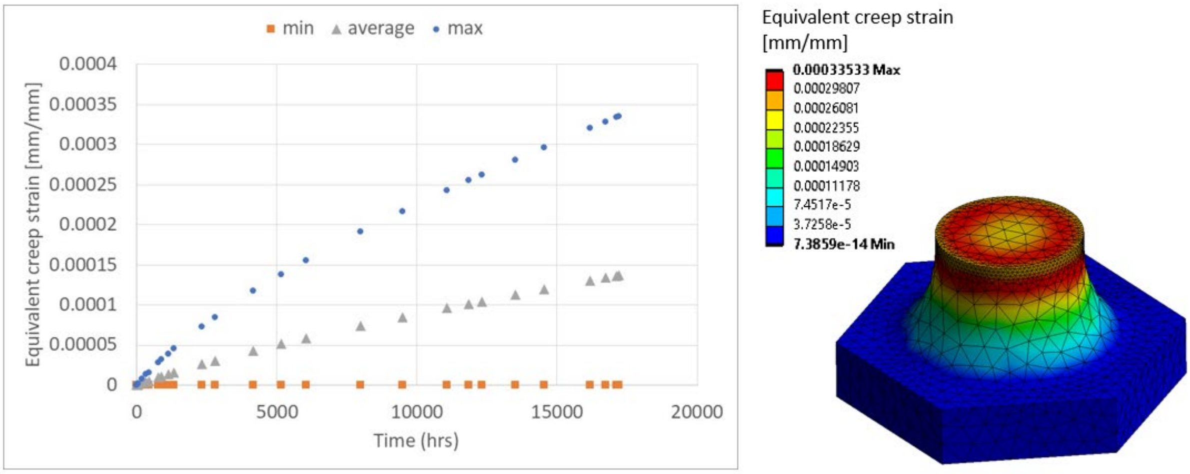

Figure 5.15. Creep strain results for 17207 hours of cyclic loading on a half pin.

Table 5.5. Comparison of creep strain values obtained from simulation and extrapolation.

Max Creep	Simulation	Extrapolation	Simulation		% diff
max over time	3.52E-05	6.05E-04	3.35E-04		57.42
time (hrs)	1000	17207	17207		
Average Creep	Simulation	Extrapolation	Simulation		% diff
max over time	1.20E-05	2.06E-04	1.37E-04		40.40
time (hrs)	1000	17207	17207		

Case 2: Single half pin with constant loads for 100,000 hours

In order to address the limitation imposed by the software, the second case focused on the creep behavior when instead of following a cyclic pattern, the load profile is simply maintained constant throughout the lifetime of the device as shown for 500 hours in Figure 5.16.

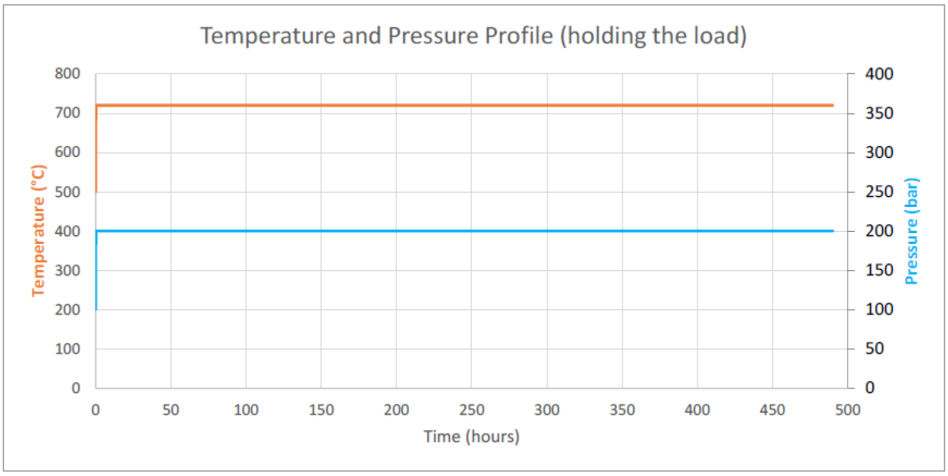

Figure 5.16. Pressure and temperature held constant for 500 hours.

This schedule is the worst scenario for the heat exchanger as shown in Figure 5.17 provided for Haynes 230 for illustration purposes.

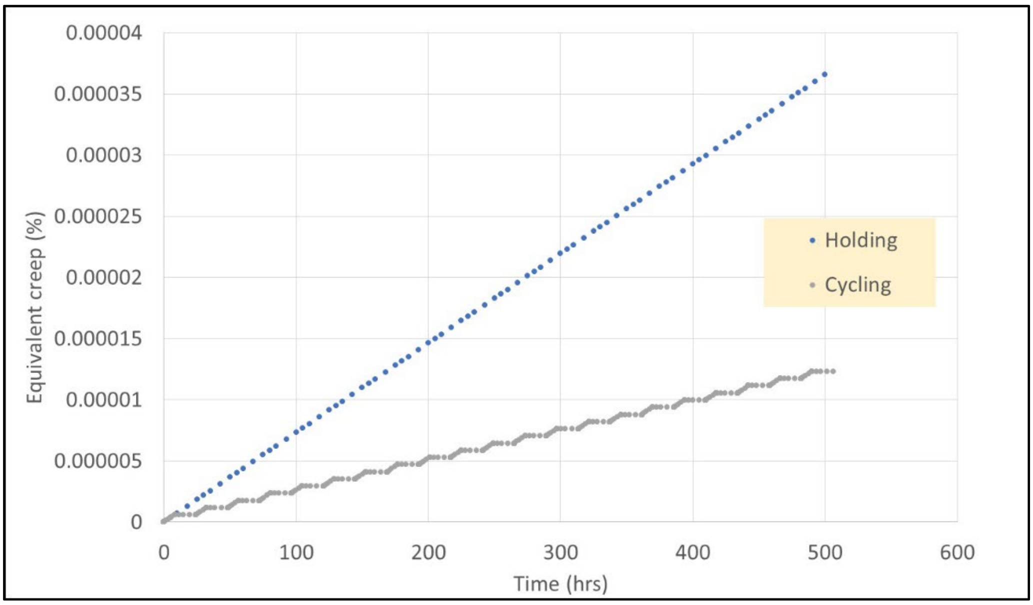

Figure 5.17. Equivalent creep resulting from cyclic operation vs constant loads for Haynes 230

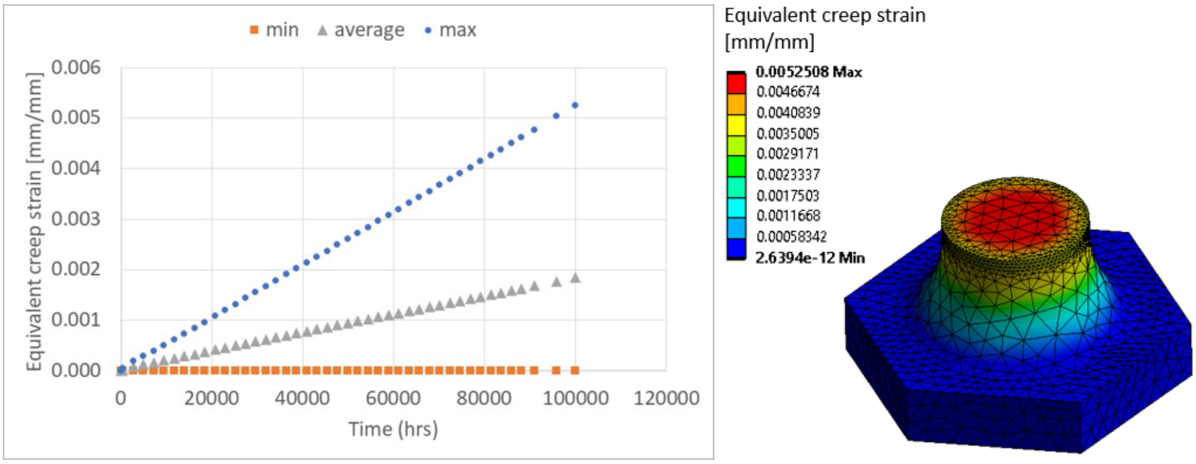

Figure 5.18. Creep strain results for 100,000hours with constant temperature and pressure loads

The maximum creep strain of the pin at the end of the 100,000 hours is about 0.5%. This result was then compared against data for Haynes 282 at 750°C [93] and it can be concluded that even for stress values higher than what we expect in our model, a 0.5% creep strain still belongs to the linear section that defines secondary creep (see Figure 5.19). Therefore, this corroborates for the pin array our earlier conclusion of the secondary creep prevailing throughout the lifetime of the heat exchanger. The aforementioned conclusion is also verified by the study of Tortorelli et al. [94] that shows that for a Haynes 282 part to survive 100,000 hours at 720 °C with respect to creep, the maximum stress tolerable is approximately 210 MPa, which is higher than our 150 MPa target.

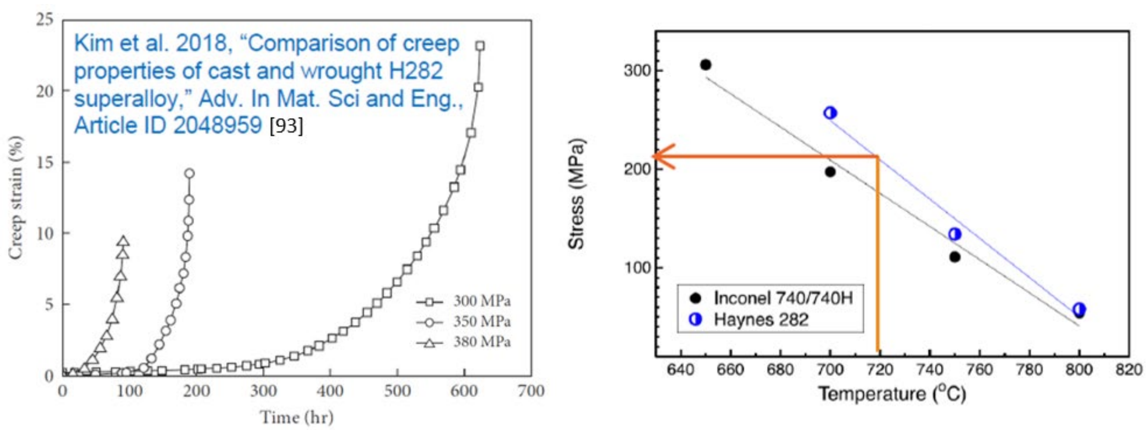

Figure 5.19. (a) Creep curves of cast Haynes 282 alloy at 750 °C [93], (b) stress for 100,000 h creep-rupture lifetime as a function of temperature predicted by applying Wilshire approach to data for aged Inconel 740/740H and Haynes 282 [94].

Case 3: Header region with a constant load for 100,000 hours

Case 2 was repeated for the header geometry and the maximum creep strain at the end of the 100,000 hours was approximately 0.4%, which is even lower than the strain reported in the pin array region. Most of the header shows creep strain values below 0.01% (see Figure 5.20).

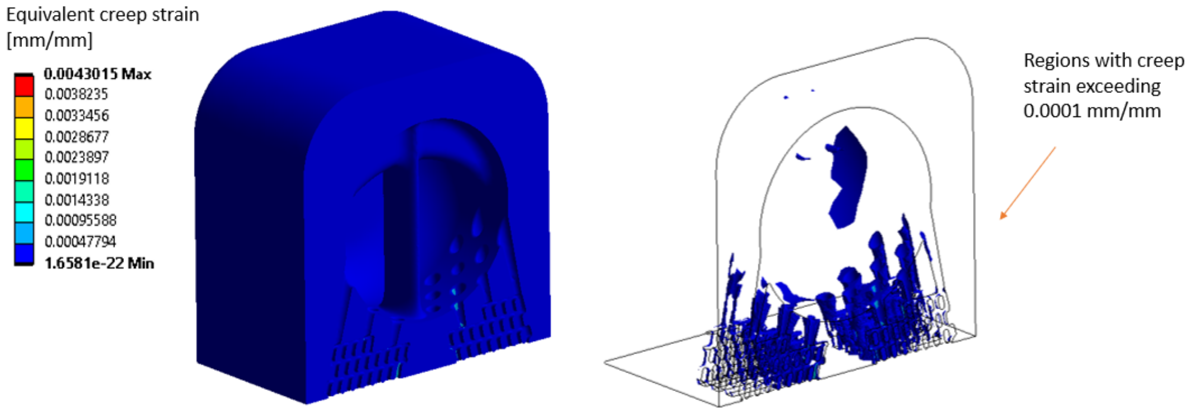

Figure 5.20. Creep strain results for 100,000 hours with constant temperature and pressure loads for the header section.

Fatigue analysis

The fatigue life estimation was performed by Jeff Gladstone, a FEA specialist collaborating on the heat exchanger design. Fatigue is a type of failure caused by cyclic loading. An estimation of fatigue life therefore requires a knowledge (in terms of stress and strain) of the different states the device under consideration will be cycling through. Two cases, “load on” and “load off”, were created to extract stress and strain information at one of the inlet tubes which is the highest stress region in the heat exchanger. Figure 5.21 shows the two cases and the stress/strain data used to define the stress/strain amplitudes necessary to evaluate fatigue life.

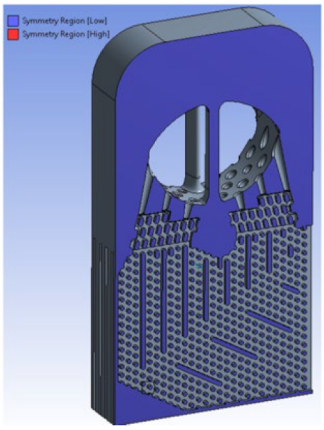

Load on (200 bar + temperature profile)

Stress (MPa)					
σ_11	σ_22	σ_33	σ_12	σ_13	σ_23
61.536	44.073	149.76	33.612	67.314	72.448

Strain(mm/mm)					
ε_11	ε_22	ε_33	ε_12	ε_13	ε_23
0.00036521	0.000046846	0.00074853	0.00047553	0.00095212	0.0010247

Load off (100 bar + 500C throughout)

Stress (MPa)					
σ_11	σ_22	σ_33	σ_12	σ_13	σ_23
9.3647	18.567	58.864	13.557	26.511	30.794

Strain(mm/mm)					
ε_11	ε_22	ε_33	ε_12	ε_13	ε_23
0.000043926	0.00003403	0.00029699	0.00019136	0.00037423	0.00043469

Figure 5.21. Component-wise stress and strain for the load on and load off cases

The total stress range computed from the FEA simulation has a value of 121 MPa. Using this stress range and the S-N curve data (see Figure 5.22) generated from strain-controlled experiments [95], it can safely be concluded that the fatigue life is more than 1,000,000 cycles.

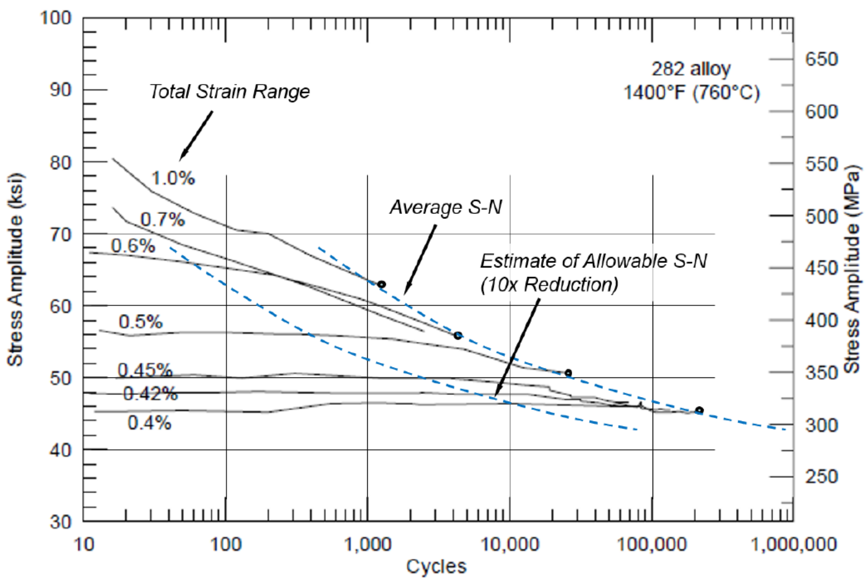

Figure 5.22. S-N curve for Haynes 282 at 760 °C and Predicted Cycle Life [95]

5.3. Simplified thermofluidic model of the PHE Core

The design of the header for mechanical integrity and flow uniformity was described in the previous section, as was the mechanical design of a unit cell of the core. In this section, a simplified model is presented to estimate the thermal performance of the PHE core. Several geometrical parameters of the core shown in Figure 5.1(e) and (f) such as the cold plate spacing, MS-side fin spacing, cold plate pin array design, and flow parameters such as hot and cold flow inlet temperatures, and mass flow rates affect the thermo-fluidic performance of the PHE.

Performing detailed CFD simulations over such a wide parameter space is infeasible; hence a simplified thermofluidic numerical model of the PHE core was developed to evaluate the performance of the heat exchanger. The inlet temperature and pressure of molten salt are $T_{H,in}$ = 720 °C and $P_{H,in}$ = 1 bar, $T_{H,in} = 720°C$ respectively. The inlet temperature and pressure of sCO_2 are $T_{C,in}$ = 500 °C and $P_{C,in}$ = 200 bar, respectively.

Figure 5.23(a) shows the simplified PHE model, which considers each cross-flow section as a unique control volume and uses the epsilon-NTU approach for heat transfer calculations. The counter-flow region, on the other hand, is divided into differential control volumes to accurately capture property variations in the fluids (Figure 5.23(b)).

The calculation process, illustrated in a flow chart in Figure 5.23(c), starts at the section labeled "Cross-flow 1" corresponding to the exit of the cold fluid and the inlet of the hot fluid. The known hot fluid inlet temperature T_{hi} is specified, and a reasonable guess for the sCO_2 outlet temperature, T_{co}, is used as input for the cold side.

The thermal behavior of the cross-flow sections is based on the lumped model assumption and a single average temperature is calculated on each side. Upon obtaining the outlet molten salt and inlet sCO_2 for this section which correspond respectively to the inlet hot and outlet cold temperatures for the counter-flow regions ($T_{hi\_counter}$, $T_{co\_counter}$), the model proceeds with the sectional counter-flow region which uses the cross-flow section temperature and pressure outputs as input conditions, and solve differential equations for each subsection of length dx. The cold inlet and hot outlet counter-flow temperatures, $T_{hi\_counter}$ and $T_{co\_counter}$, are finally passed on to the second cross-flow section that outputs cold inlet and hot outlet temperatures T_{ci} and T_{ho}. The calculated cold inlet temperature is compared to the actual known inlet temperature for the sCO_2; if the two differ significantly new guesses made, and a new iteration starts at the first cross-flow section. The process illustrated on the flowchart of Figure 5.23(c) is repeated until the two values are within 0.01 °C.

Details of the core model and correlations used for pressure drop and heat transfer coefficient are discussed in the following sections.

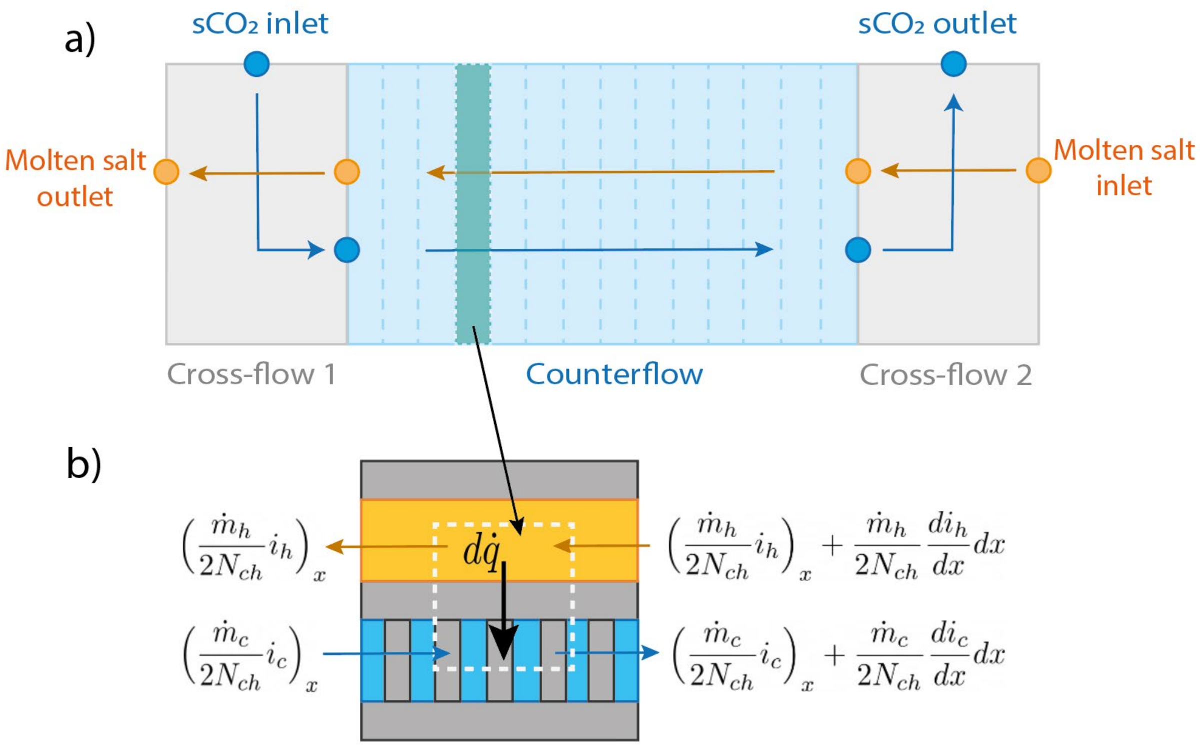

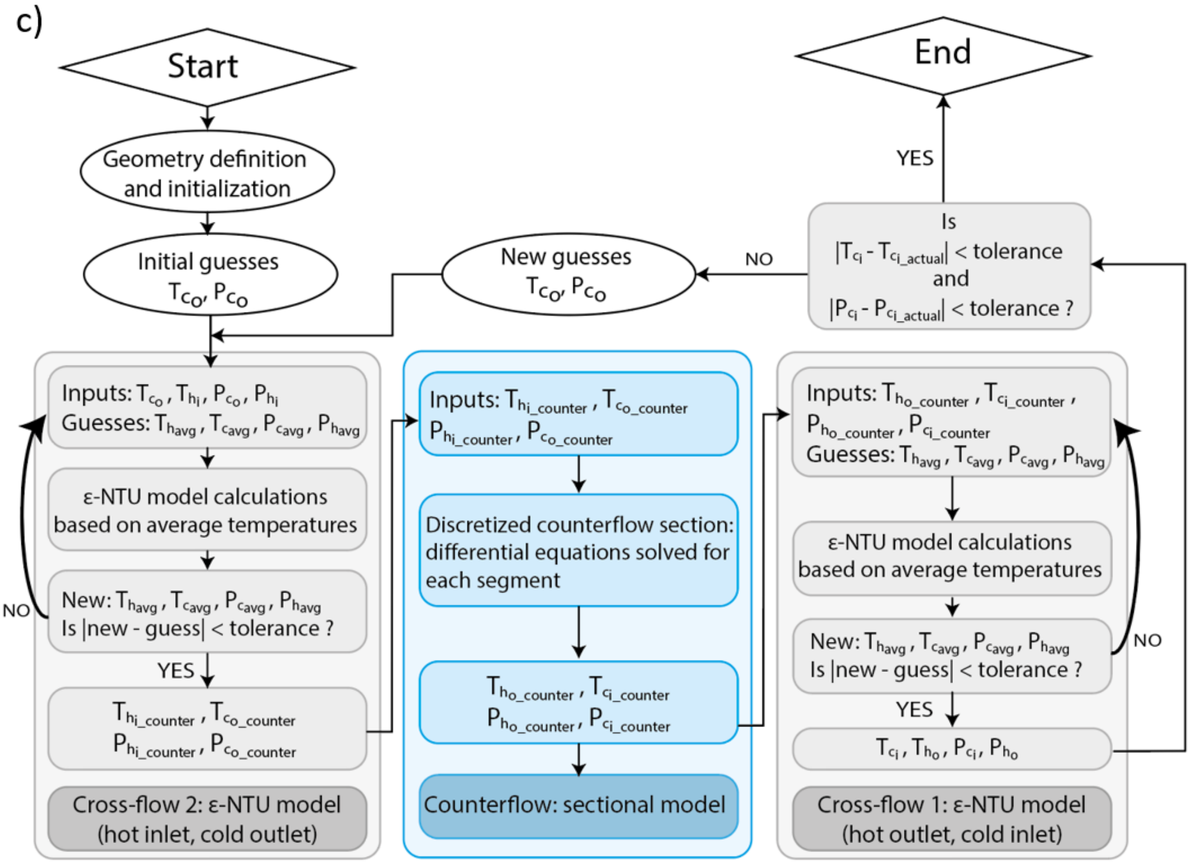

Figure 5.23 (a) Schematic of the heat exchanger, (b) Differential energy balance around half of each fluid, (c) Simplified numerical model flowchart.

5.3.1. Fluid and Material properties

The high-temperature molten salt used in this study consists of a molar ratio of 20% NaCl, 40 % KCl and 40 % $MgCl_2$. The properties of molten salt depend only on temperature because of incompressibility. The property correlations for density, specific heat capacity, thermal conductivity and viscosity are obtained from Li et al. [96]):

$$\begin{cases} \rho_H(g/cm^3) \;=\; -4.06 \times 10^{-4}\, T_H(°C) \;+\; 1.8821 \\ c_{p,H}(kJ/kg \cdot K) \;=\; -5.2799 \times 10^{-4}\, T_H(°C) \;+\; 1.3946 \\ k_H(W/m \cdot K) \;=\; -1\, x\, 10^{-4}\, T_H(°C) \;+\; 0.5082 \\ \mu_H(Pa \cdot s) \;=\; 0.3036 \times exp\left(\dfrac{2137.3}{T_H(°C) \;+\; 273.15}\right) \end{cases} \tag{5.2}$$

For sCO_2, a property table with increments of 1 K and 0.25 bar was generated in EES (F-Chart Inc). This table covers the temperature range of [753 K, 993 K] and the pressure range of [192 bar, 200 bar]. The thermal conductivity of Haynes 282 [83] can be expressed as:

$$k_{wall} = 0.019T_{wall} + 5.963 \tag{5.3}$$

5.3.2. Cross-flow section model

The cross-flow section starts with an initial guess for the outlet salt and inlet sCO_2 temperatures and pressures for this section. From these guesses, an average between the inlet and the outlet of the cross-flow section is calculated on each side. Fluid and solid properties are evaluated at these average temperatures. The cold inlet temperature, T_{ci}, is evaluated by equating the cold side energy balance with the heat rate obtained from the ε-NTU relationship,

$$\dot{q}_{cr} \ = \ C_c(T_{co} - T_{ci}) = \ Fcorr * \ \varepsilon C_{min}(T_{hi} - T_{ci}) \tag{5.4}$$

where $\dot{q}_{cr}$ is the heat transfer rate in the cross-flow region, and ε is the cross-flow effectiveness, and F_{corr} is a calibration factor to account for the actual flow configuration. The modeled geometry in the core model (Figure 5.23(a)) is a simplified version of the actual PHE geometry. Since the actual flow path from the inlet tubes feeding the flow from the header is not truly in cross-flow to the MS path, the effectiveness of this inlet section is expected to lie in between that of a counter-flow and cross flow. The calibration factor, F_{corr} (see Figure 5.24) is determined based on comparison with CFD simulations of a half-height plate (Figure 5.8).

The effectiveness is calculated using the analytical expression for cross-flow heat exchangers with one side mixed (sCO_2) and other side unmixed (MS) [97].

$$\varepsilon \ = \ \left(\frac{1}{C_r}\right)(1 \ - \ exp\{-C_r[1 \ - \ exp(-NTU_{cr})]\} \text{ for } C_{max} \text{ mixed and } C_{min} \text{ unmixed} \tag{5.5}$$

$$\varepsilon = 1 - exp\left(\frac{1 - exp[-C_r(NTU_{cr})]}{-C_r}\right) \text{ for } C_{min} \text{ mixed and } C_{max} \text{ unmixed} \quad (5.6)$$

where C_{min} is the minimum of the hot and cold heat capacity rates and C_{max} is the maximum heat capacity rate side and the heat capacity rate ratio is calculated as

$$C_r = \frac{C_{min}}{max(C_c, C_h)} \quad (5.7)$$

The number of transfer units for the cross-flow section, NTU_{cr}, in Eqs. (5.5) and (5.6) is obtained as

$$NTU_{cr} = \frac{UA_{cr}}{C_{min}} \quad (5.8)$$

where the overall heat transfer coefficient for the cross-flow region is obtained as

$$UA_{cr} = \frac{2 * N_{plates}}{\left\{\frac{1}{\eta_{oH}A_{tH}h_H} + \frac{t_w}{k_w A} + \frac{1}{\eta_{oC}A_{tC}h_C}\right\}} \quad (5.9)$$

Upon determination of the cold side inlet temperature from Eq. (5.4) the hot side energy balance, assuming no heat loss, is used to determine the hot side exit temperature, T_{ho}

$$\dot{q}_{cr} = C_h(T_{ho} - T_{hi}) \quad (5.10)$$

The determined temperatures from Eqs. (5.4) and (5.10) are compared against the original guesses and the iterative procedure continues until convergence.

5.3.3. Counterflow section model

A sectional model is used for the counter-flow region to capture property variations along the length of the PHE. A schematic of the differential control volumes used for energy balance in the counter-flow region is shown in Figure 5.23(b). The energy balance on the hot side can be written as

$$d\dot{q} + \frac{\dot{m}_H}{2N_p}\frac{di_H}{dx}dx = 0 \tag{5.11}$$

where i_H represents the local enthalpy of the hot side and N_p is the number of pairs of hot and cold channels.

Assuming that the axial pressure gradient is small relative to the temperature gradient, the enthalpy gradient can be represented as a temperature gradient,

$$d\dot{q} + \frac{\dot{m}_H}{2N_p}c_H\frac{dT_H}{dx}dx = 0 \tag{5.12}$$

The heat transfer rate from the hot to the cold stream is governed by the ratio of the local bulk temperature difference between both streams and the total thermal resistance in the path of heat flow,

$$d\dot{q} = \frac{(T_H - T_C)}{\left\{\frac{1}{\eta_{oH}dA_{tH}h_H} + \frac{th_w}{k_w dA} + \frac{1}{\eta_{oC}dA_{tC}h_C}\right\}} \tag{5.13}$$

where h_o is the overall surface efficiency, dA_t is the total area on the hot or cold side for heat transfer, dA is the differential planar based area between the two streams, th_w is the thickness of the wall separating the fluids, and h is the convective heat transfer coefficient. Combining (5.12) and (5.13), the temperature gradient on the hot side can be expressed as

$$\frac{dT_H}{dx} = \frac{2N_p}{\dot{m}_H c_H}\frac{(T_H - T_C)}{\left\{\frac{1}{\eta_{oH}dA_{tH}h_H} + \frac{th_w}{k_w dA} + \frac{1}{\eta_{oC}dA_{tC}h_C}\right\}} \tag{5.14}$$

A similar expression can be developed for the cold side temperature gradient. The heat transfer coefficient on the cold side is obtained from the Rasouli et al. [76] correlation selected after experimental testing (Chapter 4), while that on the hot side is obtained using duct flow relations. The pressure gradient on hot and cold side is obtained using

$$\left.\frac{dp}{dx}\right|_H = -\frac{f_H}{D_h}\frac{\rho_H v^2}{2} \tag{5.15}$$

$$\left.\frac{dp}{dx}\right|_C = -f_c\frac{\rho_c v^2}{2}\frac{N_L}{L} \tag{5.16}$$

where the friction factor for the hot side, f_H, is obtained from fully developed duct flow relations and for the cold side, f_c, is obtained from the Prasher et al. [75] correlation for flow through tube banks and pin arrays (described in Chapter 4).

The molten salt side is represented by straight, rectangular channels. The widely used Moody diagram [98] describes the pressure drop for flows through pipes for a relative roughness of <5%. However, the roughness of AM microchannels exceeds this limit and modified relations are needed. To take the roughness effect into account for the laminar region Kandlikar et al. [56] suggested to adjust the hydraulic diameter D_h depending on the roughness. By subtracting the peak to valley roughness, R_Z, from D_h, the reduced flow passage is represented. For the turbulent region Kandlikar et al. [56] replaced the roughness parameter with R_Z in the traditional friction factor relation [99]. In the turbulent regime, Stimpson et al. [59] developed another approach to describe rough surfaces based on a modification of the Moody relative roughness correlation. Since the flow rates on the MS side considered in the study are such that the regime will be laminar, the following correlations from Kandlikar et al. [56] are used to incorporate the roughness effect into the friction factor f in the model, for the laminar flow regime,

$$f_H = \frac{24}{Re_H}(1 - 1.355\alpha_H + 1.947\alpha_H{}^2 - 1.790\alpha_H{}^3 + 0.956\alpha_H{}^4 - 0.255\alpha_H{}^5), \tag{5.17}$$

$$Re_H < 350$$

$$f_H = \frac{1}{16}\left[ln\left(\frac{R_z}{3.7 \times D_H} + \frac{5.74}{Re_H{}^{0.9}}\right)\right]^{-2}, \quad Re_H > 350 \tag{5.18}$$

In Eq. (5.17), the aspect ratio α_H is the minimum over maximum dimension (for example width over height) of the duct. The hot side Reynolds number in Eqs. (5.17) and (5.18) was estimated as,

$$Re_H = \frac{\rho_H v_H D_{H,corr}}{\mu_H} \tag{5.19}$$

where $D_{H,corr}$ is the corrected hydraulic diameter estimated as

$$D_{H,corr} = D_H - 2 \cdot Rz \tag{5.20}$$

by subtracting the peak-to-valley roughness Rz of the channel from the nominal hydraulic diameter, D_H,

$$D_H = 2\frac{W_H H_H}{W_H + H_H} \tag{5.21}$$

The pressure drop was estimated from the friction factor as

$$\Delta P_H = 4 f_H \times \frac{L}{D_H} \times \frac{\rho_H {v_H}^2}{2} \tag{5.22}$$

For the Nusselt number of the hot side, Gnielinski's correlation and Shah's correlation are used to describe fully developed turbulent flow and laminar flow respectively [97],

$$Nu_H = \begin{cases} \dfrac{\frac{f_H}{8}(Re_H - 1000)Pr_H}{1 + 12.7\left({Pr_H}^{\frac{2}{3}} - 1\right)\sqrt{\frac{f_H}{8}}}, & 2300 < Re_H < 5 \times 10^6 \; and \; 0.5 < Pr_H < 2000 \\ 7.54(1 - 2.61\alpha_H + 4.97{\alpha_H}^2 - 5.119{\alpha_H}^3 + 2.702{\alpha_H}^4 - 0.548{\alpha_H}^5), & otherwise \end{cases} \tag{5.23}$$

5.3.4. Thermofluidic Core Model Cross-flow calibration

The actual PHE geometry includes a cross flow section, a counter-flow region, but also a hybrid zone that is neither cross nor counter-flow. In order to obtain a model which reflects this combination in the evaluated performance, a calibration stage is added to the procedure and CFD simulations for the unit-cell core consisting of half-height plate, analogous to that performed for the plate flow uniformity study is used to determine a calibration factor F_{corr} to the cross-flow effectiveness in Eq. (5.4).

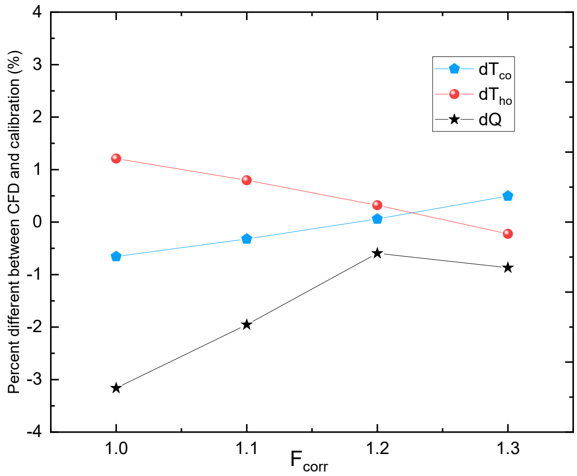

Figure 5.24. Percent difference between CFD simulation of unit-cell core and thermofluidic model predictions as a function of the calibration factor Fcorr.

Table 5.6. Correlation-based model calibration.

ε increase (%)	T_co (°C)	T_ho (°C)	% diff T_co	% diff T_ho	Q (W)	% diff Q
0	695.6	530.8	-0.656	1.209	12201	-3.162
10	698.0	528.6	-0.322	0.796	12350	-1.954
20	700.6	526.1	0.058	0.321	12519	-0.595
30	703.7	523.2	0.496	-0.224	12484	-0.870
CFD	700.2	524.4	-	-	12593	-

Table 5.6 shows the exit temperature on both sides and pressure drop on the cold side as a function of the percent increase in F_{corr} with 1 corresponding to 100% cross-flow and followed by the efficiency increasing in 10% increments. As expected, the comparison between CFD simulation and model is observed to improve with the efficiency. A F_{corr} of 1.2 was selected as final configuration and a good agreement is noted between the model and the CFD temperatures with a 0.06% and 0.32% difference between the CFD and Matlab sCO_2 and MS outlet temperatures, respectively. As shown in Figure 5.24, a F_{corr} of 1.2 minimizes the relevant parameters taken as a

whole. The difference observed even after calibration is likely due to the uniqueness of the PHE design that forces the flow to redirect at an angle.

5.4. Parametric Study

5.4.1. Process-based Cost Model

The PHE cost (in $/kW-th) is estimated for each set of geometric and flow parameters using a process-based cost model (PBCM) developed by Ziev et al. [100]. The PBCM estimates the cost to manufacture the PHE based on the costs associated with the individual stage making up the manufacturing process. The constituent costs for each process phase include equipment, material, labor, facility, utilities, consumables, and overhead. The PBCM relates constituent costs for each process stage, processing parameters, facility operating parameters, and PHE design parameters to determine the total cost. The PBCM models a four-stage manufacturing process. In the first stage, the part is formed layer-by-layer by melting metal powder via a LPBF method. In the second stage, thermal stresses built up in the part are relieved via stress-relief heat treatment. In the third stage, the baseplate on which the part is built and support structures are removed via computer numerically controlled bandsaw. In the fourth stage, an abrasive medium is forced through the PHE to clean and smooth the internal passages via abrasive flow machining. The cost estimate is provided based on the process parameter set S#2 in Table 5.4 since this parameter set resulted in relatively fast printing speeds (and hence lower cost), high part density, low surface roughness and good dimensional tolerance. Full details of the cost model are described in Ziev et al. [100].

5.4.2. Parametric Study

Several important parameters play a role in determining the overall size of the PHE; these parameters, along with their baseline values and range of variation are indicated in Figure 5.7. One parameter was varied at a time to understand the independent influence of each parameter on the PHE design, performance, and cost. The overall dimensions of the core of the PHE were kept fixed at L = 24 cm, based on the dimensions of the build plate in the EOS M290 LPBF machine. The height was fixed at 5 cm based on the ability to distribute the flow uniformly in the counter-flow section of the PHE. The upper limit on the width were also based on the dimensions of the build plate in the machine. The baseline pin diameter (D_{pin}), height (W_c or H_{pin}), and pitch ratio (β_T), were obtained from detailed mechanical stress simulations discussed in Section 5.2. The R_z roughness encompasses a range that includes process parameters S#1 and S#2 in Figure 5.7. For ease of comparison across geometric parameters, the scales of the y-axes are kept uniform for all the performance indicators except in cases that have different range or need a better resolution. While the parametric study was performed on all variables in Figure 5.7, only those that showed significant trends are reported here for brevity.

Table 5.7 . Fixed and varied parameters in PHE design

Parameters	Baseline Value	Range
L (cm)	24	--
H (cm)	5	--
W (cm) / N_{plates}	10 / 26	[10.00, 18.00] / [26, 47]
W_H (mm)	1.00	[1.00, 2.50]
W_c (mm)	1.80	[0.75, 2.50]
β_T (-)	2.05	[1.34, 2.05]
D_{pin} (mm)	1.20	[0.50, 1.50]
Th_{wall} (mm)	0.50	[0.30, 1.50]
S_{fin} (mm)	5.00	[2.00, 10.00]
Th_h (mm)	1.00	[0.3, 1.00]
R_z (μm)	60	[30.00, 150.00]
$\dot{m}_{sCO2}$ (g/s)	50	50;75
$\dot{m}_{MS}$ (g/s)	74	[64, 148]

Mass Flow Rate Variation

Figure 5.25 shows the PHE performance as a function of the heat capacity ratio, C_r, defined as the ratio of the minimum heat capacity rate, C_{min}, to the maximum heat capacity rate, C_{max}. The variation of C_r was achieved by changing the MS flow rate within the range specified in Table 5.7 for a fixed sCO_2 mass flow rate of 50g/s (Figure 5.25a-b) and 75g/s (Figure 5.25c-d). Performance indicators of interest include the outlet sCO_2 and MS temperatures, the PHE effectiveness (Figure 5.25(a), (c)), and the cost, heat duty and cold-side pressure drop (Figure 5.25(b), (d)).

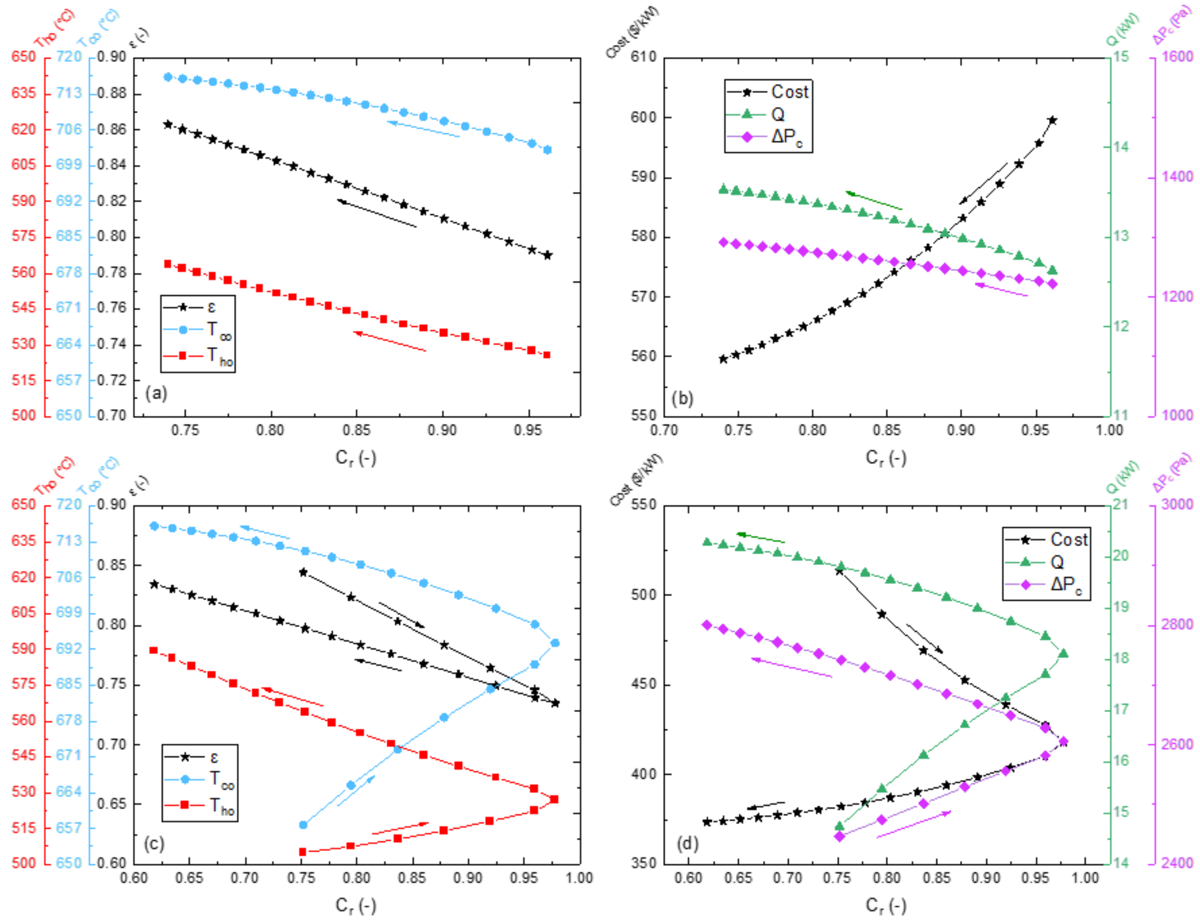

Figure 5.25. PHE performance predicted by the thermofluidic and cost models for various Cr ratios at sCO_2 flow rate of (a,b) 50g/s and (c,d) 75 g/s (as a reference, the volumetric power density at 13 kW corresponds to 6.8 MW/m^3 and at 20 kW corresponds to 10.2 MW/m^3). Arrows indicate the direction of increasing MS flow rate.

For the $\dot{m}_{sCO2}$ of 50 g/s, the C_{min} is always on the sCO_2 side, with a low C_r referring to a high MS flow rate and a high C_r corresponding to a low MS flow rate. The performance trends in Figure 5.25(a) are monotonic, with the highest effectiveness of 0.86 and outlet sCO_2 temperature 716 °C obtained for the largest MS mass flow rate (low C_r). The effectiveness increases with an decrease in C_r from a value of 0.79 at a Cr of 0.96 to a value of 0.86 at a Cr of 0.74, with a corresponding increase in thermal power rating and volumetric power density from 12.6 to 13.5 kW (Figure 5.25(b)) and 6.4 to 6.9 MW/m^3, respectively. The overall heat transfer coefficient is relatively unchanged for all C_r since the flow on the MS side is laminar. Since C_{min} is on the sCO_2 side, the NTU is also relatively constant at 10. As a reference, the effectiveness for a pure counter-flow heat exchanger at a C_r of unity and NTU of 10 is 0.91. An increase in effectiveness is related to an increase in MS flow rate (corresponding to a decrease in C_r), which causes a higher temperature differential along the PHE for heat transfer to sCO_2. The cold side exit temperature increases from 702 °C to 716 °C with a decrease in C_r over the same range, while the MS exit temperature increases by a greater amount from 526 °C to 564 °C. The pressure drop on the cold side (Figure 5.25(b)) increases slightly over the range of C_r due to increase in average temperature and a consequent increase in viscosity of sCO_2.

Performance trends for the higher sCO_2 flow rate of 75 g/s, shown in Figure 5.25(c-d), display a non-monotonic trend. For this condition as well, the UA is relatively constant due to laminar flow conditions in the MS side and the fixed flow rate on the sCO_2 side. However, with an increase in MS mass flow rate, C_{min} is on the hot side and varies with MS flow rate between 64 g/s to 84 g/s, (corresponding to C_r from 0.75 to 0.96), before switching to the cold side. This increase in C_{min} at a fixed UA causes a decrease in NTU and a corresponding decrease in effectiveness from 0.84 to 0.74. Further increase in MS flow rate beyond 84 g/s results in a fixed C_{min} value based on the cold side flow rate and causes a decrease in C_r from unity to 0.62 with increase in MS flow rate from 84 g/s to 148 g/s. In this range, the trend is similar to that seen in Figure 5.25(a) with the thermal rating and effectiveness increasing with a decrease in C_r. The exit temperatures of MS and sCO_2 increase with an increase in MS flow rate; the increase in average fluid temperature on the cold side results in a higher pressure drop (Figure 5.25(d)).

The selection of the optimal operational point is a function of several parameters with contrasting variations. The minimum sCO_2 outlet temperature for the power cycle based on DOE requirements is 700 °C (Mehos et al. [1]). However, in order to reduce parasitic losses associated with the MS loop, it is also important to exit the PHE with the lowest feasible MS temperature. It is possible to define an operational window that spans the two sCO_2 flow rates considered. A 50g/s sCO_2 flow rate associated with a C_r of 0.81 and 74 g/s of molten salt would yield a 13.3 kW power output, an outlet temperature of 713 °C for the sCO_2 and 550 °C for the molten salt, with a

sCO_2 pressure drop of 400 Pa. The same T_{ho} temperature can be achieved with a C_r of 0.83 and 75g/s of sCO_2 and 108 g/s of molten salt. The power output in this case is higher (19.4 kW) and the sCO_2 pressure drop would increase to 817 Pa. The latter configuration can be a preferred option for increased thermal power rating of the PHE; however, its effectiveness, at 0.78, is lower than the 0.84 effectiveness at the lower sCO_2 flow rate condition. Higher thermal rating and effectiveness can be obtained by increasing the MS flow rate at both sCO_2 flow rates; however, at the penalty of higher MS exit temperature. In the scenarios considered so far, the volume of the heat exchanger is kept constant so changes in PHE cost (in $/kW-th) are dictated by the thermal power rating. For the 50g/s of sCO_2 flow rate, an increase in power rating from 12.6 to 13.5 kW allows a cost reduction from $600/kW-th to approximately $560/kW-th. In the 75 g/s case, the larger variation in power output from 14.7 to 20.2 kW results in a cost reduction of $145/kW-th, from $520/kW-th to $375/kW-th.

Heat exchanger overall width (W_{max}) / N_{plates}

Figure 5.26(a-b) shows the influence of the overall width (W_{max}) on the performance parameters of the PHE. Variation in the width, with all other parameters in Table 5.7 being held constant, results in an increase in the number of hot and cold plates available for heat transfer as noted in Figure 5.26a. For a fixed flow rate of 50 g/s for sCO_2 and 74 g/s for MS, the exit temperature of the hot stream decreases while that of the cold stream increases with number of plates due to the increase in residence time for heat exchange. Consequently, the heat exchanger effectiveness increases from 0.83 to 0.88. The thermal rating of the PHE increases modestly from 13.3 kW to 13.6 kW (Figure 5.26b); however, the increase in width increases the volume of the PHE more significantly and hence the volumetric energy density decreases from 6.8 to 4.6 MW/m^3. Over the range of variation of number of plates per unit width, the cold side pressure losses decrease to almost a third of the starting value, from 1270 to 420 Pa due to the reduced mass flow rate through each plate. In this scenario, the cost is higher by almost $65/kW-th because the increase in W_{max} from 10 to 18 cm translates into an increase in material cost in the absence of significant increase in heat transfer rate.

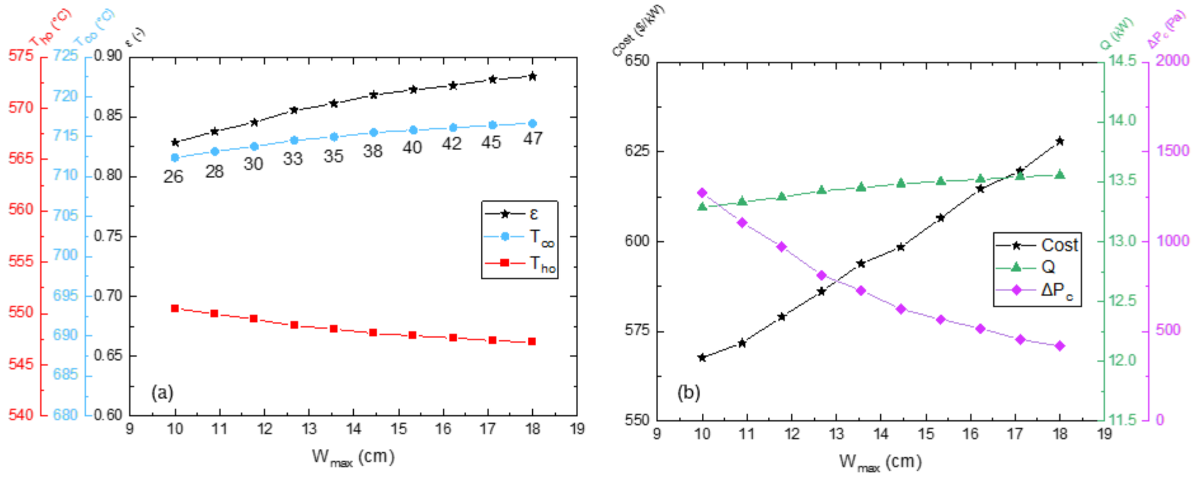

Figure 5.26. Parametric study of variation in PHE width, W_{max} varying from 10 to 18 cm: (a) T_{ho}, T_{co}, and ε variation and (b) $/kW-th, ΔP_c, and thermal rating variation with W_{max}. sCO_2 and MS flow rate of 50 and 74 g/s respectively.

Hot channel width (W_h)

Figure 5.27 shows how the hot channel width (W_h) impacts the performance of the PHE. As the hot channel width increases from 1 to 2.5 mm, the performance of the heat exchanger is adversely impacted, and the overall efficiency decreases from 0.83 to 0.63.

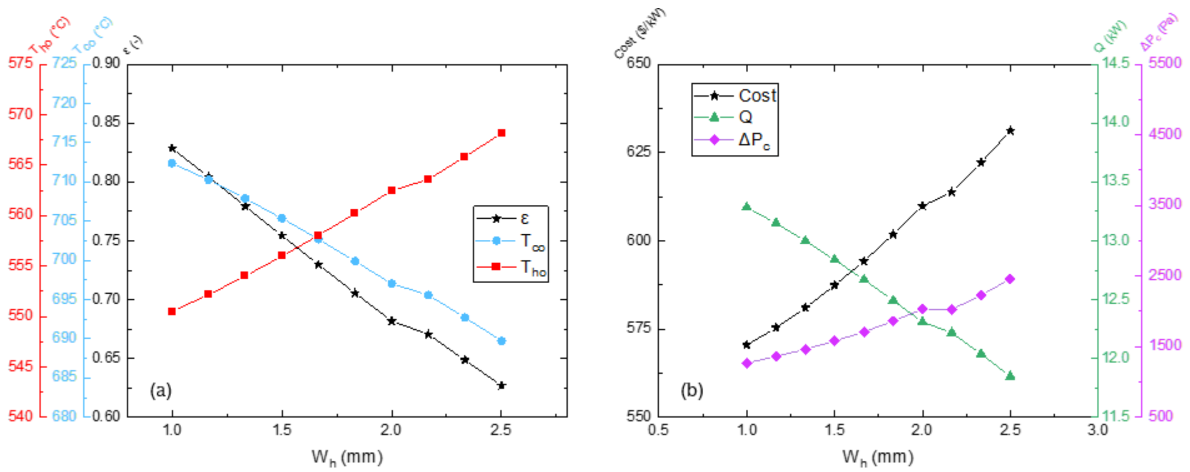

Figure 5.27. Parametric study of variation in MS channel width, W_h, varying from 1 to 2.5 mm: (a) T_{ho}, T_{co}, and ε variation and (b) $/kW-th, ΔP_c, and thermal rating variation with W_h. sCO_2 and MS flow rate of 50 and 74 g/s respectively.

This behavior is observed because fewer plates are available for heat transfer and in each plate, the residence time of the hot stream is no longer sufficient to transfer the same amount of heat to the cold side. As a result, the power output decreases from 13.3 to 11.8 kW. The total solid volume also decreases but only marginally so that the volumetric power density decreases from 6.8 to 6.0 MW/m^3. The pressure drop on the sCO_2 side increases from 351 to 653 Pa because the flow rate in each plate increases with fewer hot and cold plate pairs available. The cases with W_h of 2.0 and 2.2 mm display an almost identical pressure drop and less steep gradients for the other performance parameters because the number of plates is the same. Unlike the other cases where the increase in value of W_h is sufficient to cause the number of plates to decrease by 1, the case with W_h of 2.2 mm is a rare occurrence of N_{plate} remaining constant and induces the plateau observed between W_h values of 2.0 and 2.2mm. Similar to the volumetric power density, the increase in W_h causes a minor decrease in total volume and therefore a small reduction in material expenditure but the significant reduction in power output induces an overall increase in cost from \$570 /kW-th to \$ 630 /kW-th.

Cold channel width (W_c)

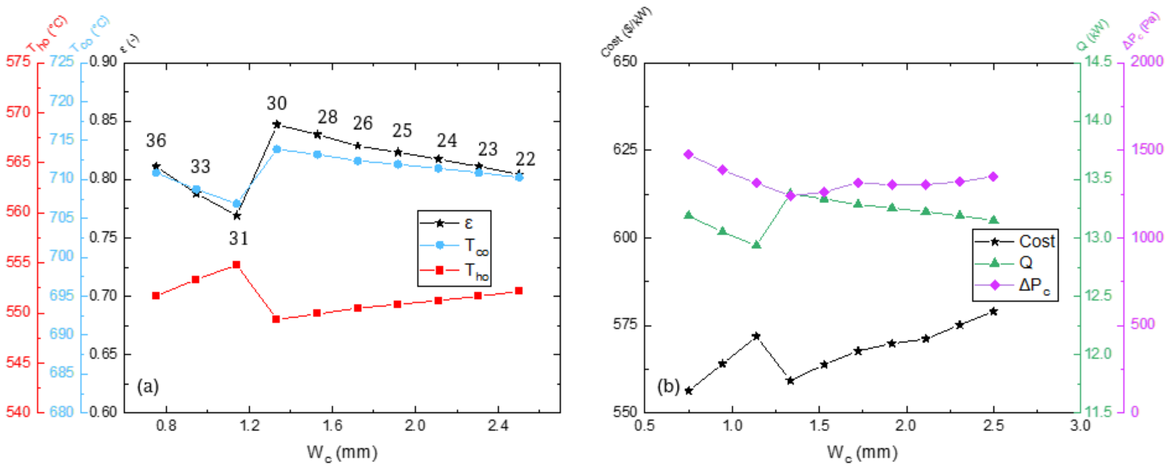

Figure 5.28. Parametric study of variation in sCO_2 channel width, Wc, varying from 0.75 mm to 2.5 mm: (a) T_{ho}, T_{co}, and ε variation and (b) \$/kW-th, ΔP_c, and thermal rating variation with W_h. sCO_2 and MS flow rate of 50 and 74 g/s respectively.

The effect of varying the sCO_2 channel width from 0.75 to 2.5 mm is illustrated in Figure 5.28. As the channel width increases, the residence time of the sCO_2 decreases due to lower number of plates, resulting in lower cold and higher hot outlet temperatures. These trends are observed in Figure 5.28 except from the case with plate number of 31 to 30, where the aspect ratio of the pin begin to assume values greater than unity, and the flow transition to a regime in which vortex shedding is expected based on the chosen correlation for heat transfer in pin arrays. Because of the performance jump observed from a W_c of 1.1 mm to 1.3 mm, the upper and lower limit of the performance markers such as efficiency, temperature and power output are not observed at the boundaries of the W_c range considered but rather at that discontinuity. At the transition, the efficiency jumps from 0.77 to 0.85 and the volumetric power density increases from 6.6 to 6.8 MW/m^3. The pressure drop varying between 1200 Pa and 1500 Pa in a non-monotonic trend is the result of the competing effect of increasing the cold channel width (decreasing velocity), and a reduced number of plates which translates into a larger volume of fluid in each plate. The cost varies between \$555 /kW-th and \$580 /kW-th with a drop when the aspect ratio exceeds unity and vortex shedding enhances the thermal performance. Changing the width of the cold channel does not impact the volume significantly and the cost trend observed in this case is determined by changes in the power output.

Discussion on parametric trends

From the results of single-effect parametric variations, one can arrive at a desired design for the AM PHE. The width (number of hot-cold core pairs) of the PHE can be scaled to increase the thermal rating. The height is kept fixed at 5 cm based on a balance between minimizing cross-flow sections at the inlet and exit and uniform flow distribution within the plate. Both the overall length and width of the PHE are constrained by the dimensions of the LPBF build plate. Given these constraints, keeping W_c at 1 mm and W_h at 1.35 mm provides the best geometrical design. This design corresponds to the peak value of effectiveness shown in Figure 5.28.

For this design and for a flow rate of 50 g/s on the sCO_2 side and 74 g/s on the MS side, an effectiveness of 0.85, a thermal rating of 13.4 kW, a power density of 6.85 MW/m^3 (11.2 MW/m^3 for core alone), can be achieved at a cost of $560 /kW-th. The heat transfer coefficient on the hot (MS) side is 2.7 times lower than that on the sCO_2 side, indicating that improvements on the MS side for heat transfer coefficient or/and surface area will result in a higher power density and lower cost. Future work on how to improve the PHE performance by a reduction of the hot side resistance is needed to further reduce cost and increase the power density.

Surface roughness has a minor effect on the thermo-fluidic performance of the PHE. With an increase in surface roughness from 30 to 150 μm, the sCO_2 pressure drop increases from 1186 to 1590 Pa and the power output marginally increases from 13.3 to 13.4 kW. Hence, from a thermo-fluidic performance standpoint, the focus of post-processing should be primarily on powder removal as opposed to reduction in surface roughness. The PHE design did not consider MS corrosion and its effect on the heat exchanger structural integrity. Studies of corrosion rates are required to assess how the heat exchanger performance would be impacted and whether the magnitude of corrosion is such that both the structural and thermofluidic aspects of the design need revision, such as increasing the thickness walls between the fluids. Based on the model, increasing the wall thickness from the baseline value of 0.5 mm to 1 mm will result in a 4.8 % decrease in effectiveness and a 1.4 % decrease in thermal rating of the PHE.

Table 5.8. Comparison of thermo-fluidic performance of PHEs with different core lengths

AM machine	PHE length (m)	$\dot{m}_{sCO2}$ (kg/s)	$\dot{m}_{MS}$ (kg/s)	C_r	q (kW)	Power density, including headers (MW/m^3)	ε	ΔP_{sCO2} (kPa)	ΔP_{MS} (kPa)	T_{ho} (°C)
EOS M290	0.24	0.050	0.075	0.80	13.4	6.86	0.85	0.54	0.56	551
GE Additive 2000R	0.80	0.19	0.288	0.80	51.2	10.8	0.90	25.3	7.1	552

The AM PHE design presented here provides high power densities while maintaining very low pressure drops on both sCO_2 and MS sides (< 1 kPa for sCO_2 and MS). The upper limit on the PHE length was restricted to 24 cm based on the dimensions of the EOS M290 LPBF machine which was used for printing and cost analysis reported in this paper. However, industrial AM machines such as the GE Additive (Concept Laser) metal X line 2000R, allow for build lengths of 80 cm and width of up to 40 cm. If the selected PHE design from the parametric study were to be 80 cm in length instead of 24 cm, with all other parameters kept the same, a significant increase thermal performance can be achieved, as shown in Table 5.8, at the expense of higher pressure drop. This pressure drop is still only 0.125 % of the line pressure of 200 bar. It should be noted that the pressure drop with the longer PHE is low when compared to designs in literature; for instance, the design sCO_2 pressure drop in Caccia et al. [53] was 100 kPa. If the number of hot/cold plates were scaled up to the 40 cm width of the X line 2000R, the resulting PHE would have a thermal rating of 205 kW. Further scaling up to MW-scale PHE can be obtained by numbering up such 205 kW modules by welding header tubes.

In summary, the design of an additively manufactured (AM) nickel superalloy molten salt (MS)-to-supercritical carbon di-oxide (sCO_2) primary heat exchanger (PHE) was described. The PHE design was based on pressurized pin array plates through which sCO_2 flows, separated by straight channels through which MS flows. Details of structural design and flow distribution in the pin array and headers were discussed. Correlation-based thermofluidic, and a process-based cost model (by Ziev et al. [100]) were developed to evaluate the performance and assess the cost implications of MS-sCO_2 AM PHEs for concentrated solar power applications. An increase in the length of the core from 24 cm to 80 cm results in a 6 % increase in effectiveness, from 0.85 to 0.90, and a 58 % increase in power density, from 6.86 MW/m^3 to 10.8 MW/m^3. The pressure drop for the 80 cm-long PHE is only 0.125 % of the line pressure on the cold side.

The AM fabrication costs are based on a single-laser EOS machine, typically used in a research environment. Further reductions in cost can be achieved through use of multi-laser machines, process refinements (e.g., laser beam shaping or dithering) that allow for higher printing speeds, and industrial engineering improvements that either reduce material handling or allow it to take place outside the AM machine.

Chapter 6 Gen 2 design and comparative performance

The Gen 1 design discussed in Chapter 5 consisted of multiple pairs of mm-scale pin arrays on the sCO_2 (cold) side and parallel channels on the MS side. The sCO_2 headers were located outside the MS path, resulting in a significant cross-flow region for sCO_2 flow at the entrance and exit of the core, and a counterflow region in the rest of the core. Results indicated that designs with an effectiveness of 90% and power densities of 10.8 MW/m^3, including headers, can be obtained for an exit hot side temperature of 550 °C. Because of the low flow rates on the MS side (Re < 50) and low heat transfer coefficient on this side, the PHE design was heat transfer limited on the MS side, requiring core lengths of 80 cm to obtain effectiveness of 0.90 and a high power density of 11.4 MW/m^3. Scalability was possible in the lateral direction by increasing the number of pairs of hot and cold flow paths; however, scalability was not possible in the vertical direction of the build due to the location of the sCO_2 headers. This chapter discusses the second generation (Gen 2) heat exchanger and the changes that were introduced to address the limitations of the Gen 1 model. It starts with the motivations behind the switch from Gen 1 to Gen 2 and introduces the major changes in the geometry. Thermofluidic and mechanical design details are presented and experiments are conducted to substantiate findings relating to the structural integrity of the HE. The chapter concludes with an update of the simplified thermofluidic model and performance predictions.

6.1. Limitations of Gen 1 and objectives of Gen 2

The objective of modifying the Gen 1 HE architecture is to obtain a design that is more scalable and compact by innovations in the header design and the MS channel flow path. The overall PHE design is first presented highlighting its unique attributes, followed by a description of the details of the header design. One of the key advantages of AM is that it permits an integrated header-core design that enables compact designs and elimination of failure at the joint. Integrity of the header-core interface is demonstrated by pressure tests on a sub-scale PHE. A simplified thermofluidic model is used to assess the performance of the PHE core using correlations developed from experiments and computational fluid dynamics (CFD) simulations. The cost model developed by Ziev et al. [100], is used to assess the variation in cost based on these parameter variations. The PHE performance is discussed over a range of flow and geometric parameter variations. The impact of AM machine features and design on cost is assessed.

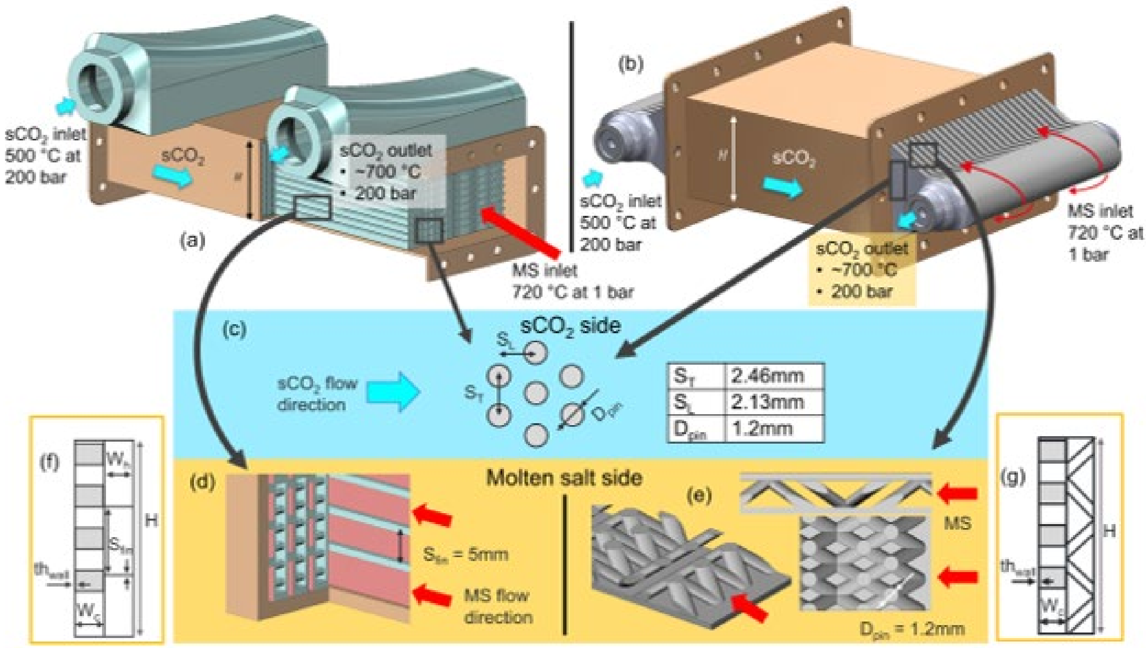

Figure 6.1. Overview of (a) the AM PHE design proposed by Tano et al. [101] (Gen 1 design, with rectangular channels on the Molten Salt side (MS)) and (b) the Gen 2 design with a lattice of slanted pins on the molten salt side, (c) schematic of the pin fin array on the sCO_2 side, (d) cut-away view of the Gen 1 design with rectangular channels on the MS side, (e) lattice of slanted pins on the MS side in the Gen 2 design, schematic of the cross-section of (f) Gen 1 and (g) Gen 2 designs.

A comparative view of the two designs is presented in Figure 6.1 with the Gen 1 and 2 PHEs in Figure 6.1(a) and (b), respectively. Both models are designed with nominal dimensions to fit the base plate of an EOS M290 laser powder bed fusion printer. Details of the sCO_2 and MS flows in the core are shown in Figure 6.2. The modifications relative to the Gen 1 design shown in Figure 6.1 and Figure 6.2 address the low heat transfer rate on the MS side, which hinders compactness of the PHE, and the scalability of the design in the vertical build direction. As shown in Figure

6.1(d) and (e), the rectangular channels on the MS side in the Gen 1 design were replaced by a 3D lattice of pins that provide additional surface area for heat transfer while increasing the residence time and mixing of the fluid in the channel. This design modification is intended to decrease the thermal resistance on the hot side of the PHE; however, the more intricate flow path in the lattice structure (see Figure 6.2(e)) is anticipated to increase pressure drop when compared to the parallel channel path in the Gen 1 design shown in Figure 6.1(d).

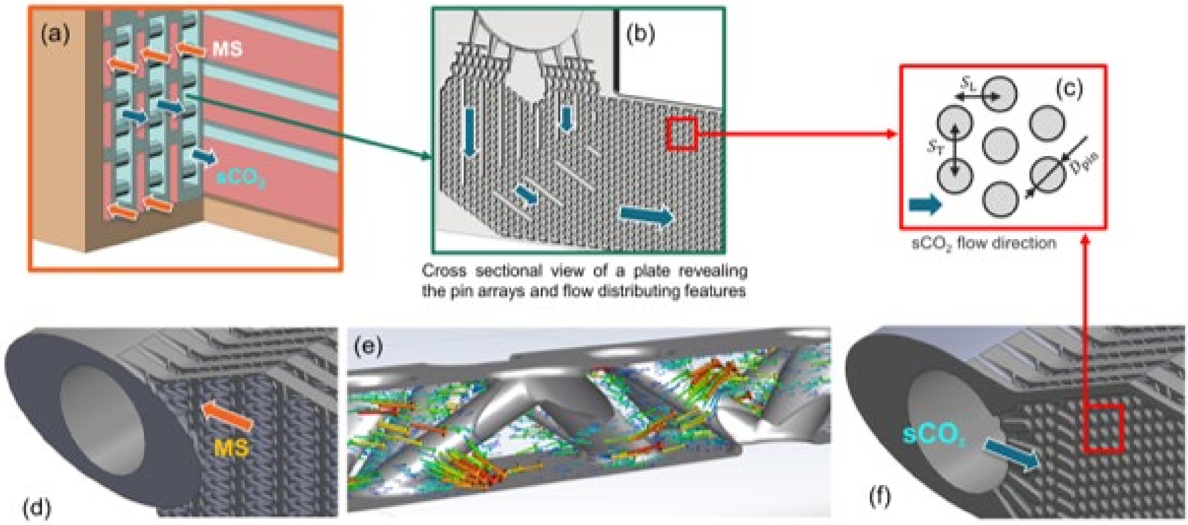

Figure 6.2. Gen 1 PHE design features (a) MS flow in rectangular channels, (b) sCO_2 flow in pin array plate with cross flow region at the entrance, (c) pin array schematic; Gen 2 design features (d) MS flow in 3D lattice, (e) velocity vectors illustrating flow path in the MS lattice, (f) cross view of sCO_2 flow passages.

To substantiate and quantify these claims in the initial stages of the Gen 2 design, conjugate CFD simulations were performed on a unit strip of hot and cold sections of the Gen 2 PHX core (see Figure 6.3) in order to characterize its thermal performance. This comparison of unit strips captures the enhancement due to the MS side improvement, the additional improvement due to the elimination of the cross-flow sections is not captured at this stage of the analysis. The Gen 1 design was simulated at identical inlet conditions of fluid temperature and mass flow rate of sCO_2 and MS.

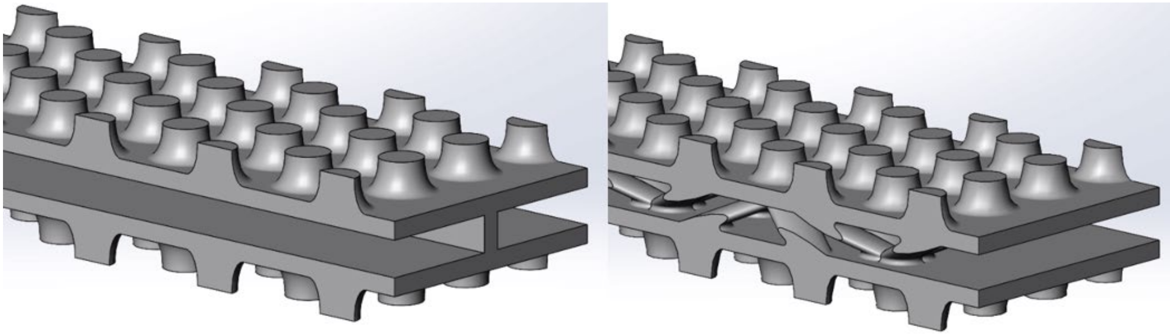

Figure 6.3. Solid domain of the stripes used for the conjugate CFD analysis showing the two half-channels of CO_2 and the MS channel in between for the Gen 1 (left) and Gen 2 (right) design.

Table 6.1. Thermofluidic performance of Gen 1 and Gen 2 designs.

Design	L (cm)	T_{in} (°C)		Mass flow rate (g/s)		T_{out} (°C)		dP (Pa)		Q_{stripe} (W)	ε
		sCO_2	MS	sCO_2	MS	sCO_2	MS	sCO_2	MS	-	-
Gen 1	10.2	500	720	0.283	0.344	665.8	556.5	255	117	59.4	0.763
Gen 2	10.2	500	720	0.283	0.344	673.4	547.6	259	2000	62.7	0.806
Gen 2*[2]	10.2	500	720	0.283	0.378	683.6	557.4	262	2191	64.9	0.834

Keeping the same flowrate between Gen 1 and Gen 2 designs (top two rows in Table 6.1), an improvement in the thermal performance is observed with a 16.5 °C increase in temperature difference between the hot and cold outlets. The 3D lattice of slanted pin fins on the salt side provide additional surface area for heat transfer and the arrangement of these pins is such that the flow is highly mixed. However, the pressure losses are consequently increased from 117 to 2000 Pa. The effectiveness increases from 76.3% to 83.4% for this design and the heat transfer rate is increased by 5.7 percent in Gen 2 compared to Gen 1.

Another way to evaluate the performance improvement while incorporating some flow parameter constraints is to determine how much more heat can be transferred for the same hot outlet temperature (first and third rows in Table 6.1). The case Gen 2* was run with this objective in mind: using the same geometry, temperatures and sCO_2 flow rate, simulations for various molten

[2] The Gen 2* uses the same geometry as the baseline of Gen 2, the inlet temperatures of sCO_2 and MS are kept the same, but the MS flow rate is adjusted so that the outlet MS temperature would match that of Gen 1.

salt flow rates were carried out until the outlet temperature of the molten salt of Gen 1 and Gen 2 v2 were reasonably close. The total heat transferred for this stripe based on the enthalpy and the flow rate yielded a value of 64.9 W for Gen 2 v2 versus 59.3 W in the case of Gen 1, which is a 9.41% improvement.

The second design change pertained to the headers, which are different in shape but also in location. As illustrated in Figure 6.1(b) as well as Figure 6.4(a) and (e), the new sCO_2 headers were aerodynamically shaped and integrated into the MS flow passages. By comparing Figure 6.2(b) with Figure 6.2(f), the less efficient cross flow zones observed in Gen 1 are minimized in the Gen 2 PHE. Furthermore, the integration of the headers in the flow path allows for scalability of the unit as shown in Figure 6.4(e). The Gen 1 design (Figure 6.1(a)) can only be scaled up by adding more plates in the depth (horizontal scalability) but with the Gen 2 architecture, it is now possible to achieve vertical scalability by building the stacks one on top of the other. The overall length of a single Gen 2 stack, which conforms to the dimensions of the EOS M290 build plate, is 24 cm, including the headers. The sCO_2 pin array plates are 18 cm in total length and include 2.3 cm long diverging and converging sections near the headers followed by a 13.4 cm long rectangular section that is 5 cm tall. Twenty-six such pin array plates are assembled in the width to make up the stack with a nominal rating of 20.7 kW under the current design conditions. The MS side channel width is 1.8 mm, with a lattice of slanted pin fins, tilted 45 degrees in both the flow direction and in the transverse direction to form the three-dimensional periodic flow network (see Figure 6.2(e)).

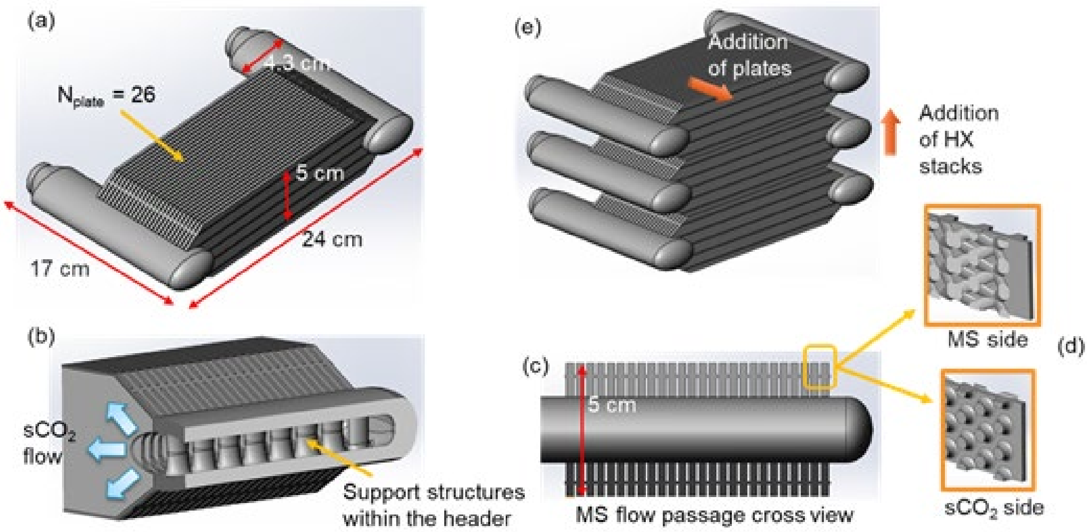

Figure 6.4. SETO Gen 2 HX (a) Overall look of the HX model, (b) support structures within the sCO_2 header, (c) MS flow passage cross view, (d) samples of pin arrays on MS and sCO_2 sides, (e) scaling up approach.

6.2. Second Generation (Gen 2) HX design

Figure 6.5 shows a summary of the design methodology which includes structural, thermofluidic and cost considerations. A unit cell of the core was used for mechanical simulations, while a correlation-based model was used for fluid flow and heat transfer. Headers for the sCO_2 side were designed to ensure uniform flow distribution across each pin array and between the pin arrays, while also satisfying structural integrity. A process-based cost model was used to assess the impact of variables on cost (see Ziev et al. [100]).

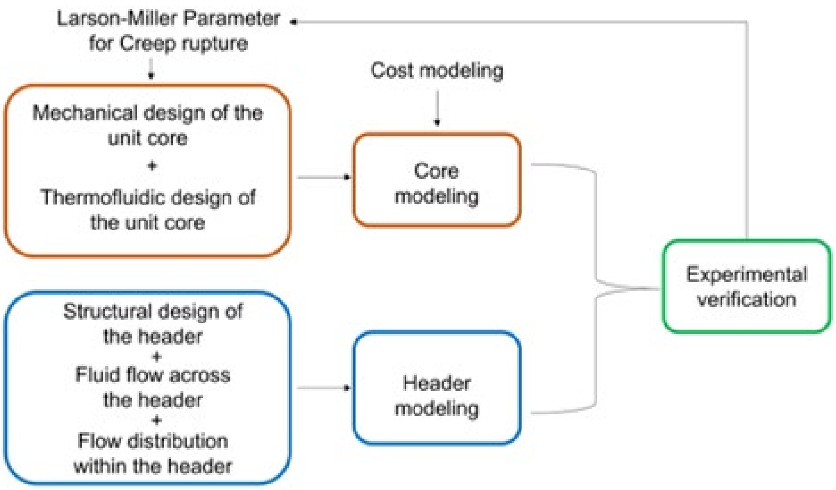

Figure 6.5. Summary of the design methodology.

For the header design to be viable, the sCO_2 headers would have to be made as compact as possible and of aerodynamic shape to reduce pressure drop on the MS side. The challenge with compactness of the sCO_2 header are threefold: 1) there needs to be sufficient wall thickness to withstand the 200-bar internal pressure, (2) the flow distribution among multiple sCO_2 pin arrays needs to be uniform, and (3) the flow must be distributed uniformly across the lateral height within each pin array. Iterative simulations were performed between structural and fluid flow to determine the geometry of the header that would meet these requirements. The allowable stress in the design was restricted to a value of about 150 MPa, based on creep-rupture considerations using Haynes 282 [83] and the Larson Miller parameter approach [102] with a maximum temperature of 720 °C and a lifetime of 100,000 hours. After conducting a static structural simulation of the header using linear periodic boundary conditions and applying the expected 200 bar pressure on the internal walls of the model, the final stress distribution showed a maximum equivalent stress of 168 MPa with most of the header subjected to stresses lower than 100 MPa.

6.2.1. Header mechanical design

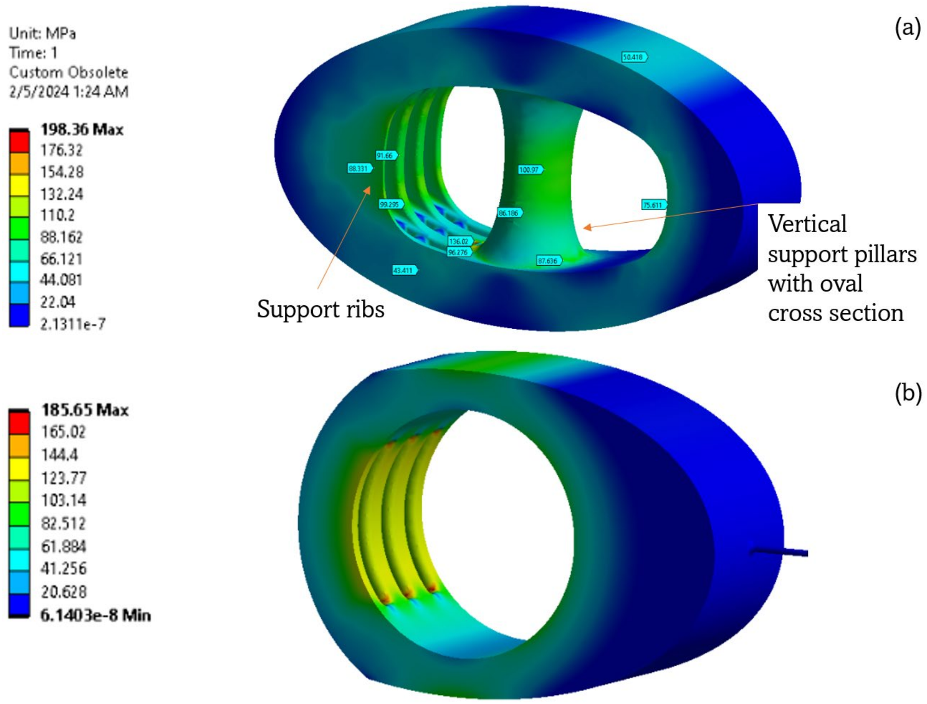

Figure 6.6. Comparison between (a) the original design and (b) the revised version.

In the first iteration of the Gen 2 PHE design (see Figure 6.6(a)), the headers were designed with pillars and ribs to mitigate the mechanical stress concentration near the entrance region and obtain a design within the limits of the mechanical strength of the material (H282). However, these added features had an adverse effect on the flow distribution uniformity between the sCO_2 pin array plates because zones of recirculations were created in the wake region of the pillars. The header was therefore redesigned and after several iterations, the model shown on Figure 6.6(b) was obtained (please refer to Appendix A for intermediate versions of the header). The outer height of the header was kept the same to avoid impacting the MS flow distribution, and the following changes were made: (1) the internal cross section of the header was changed from elliptical to circular, leading to lower stresses and (2) the ribs were eliminated. As seen from Figure 6.6 the average stress profile looks similar but the peak stress value decreases from 198 MPa to 185 MPa.

6.2.2. Header and core flow distribution

Fluid flow simulations were performed in Ansys Fluent to ensure a uniform flow distribution from the sCO_2 header into each pin array. The modeled geometry is shown in Figure 6.7(a). To manage the computational complexity of incorporating multiple pin array flow paths of the PHE core into the header flow distribution analysis, a porous media approach was employed, wherein the pressure drop in the core was modeled using inertial and viscous terms based on CFD simulations of the pin array. The red boxed area in Figure 6.7(a) identifies the region of the model defined as porous media. CFD simulations were run for different flow rates on a representative stripe of the pin array plate. A correlation between velocity and pressure drop was obtained. From this analysis, it was possible to derive the inertial and viscous parameters establishing an equivalence between the fluid flow in the pin array plate and in a section of porous media [101]. Due to the presence of bends and recirculation regions in the wake of the flow distribution features at the entrance of each pin array (see Figure 6.2(f)), the k-omega SST turbulence model was used. Figure 6.7(b) shows the flow uniformity in terms of mass flow rate in each plate (primary ordinate) and percent difference between the local and average mass flow rates (secondary ordinate) for total incoming flow rates of 50, 75 and 100 g/s. For reference, the 50 g/s incoming flow rate corresponds to a Reynolds number of 86,160 based on the inlet diameter and a Reynolds number based on pin diameter of 1,314 for the pin array. For all the flow rates considered, the mass flow rate into all pin arrays of the core was within 5% except into the one closest to the inlet, for which it was about 6 percent lower than average.

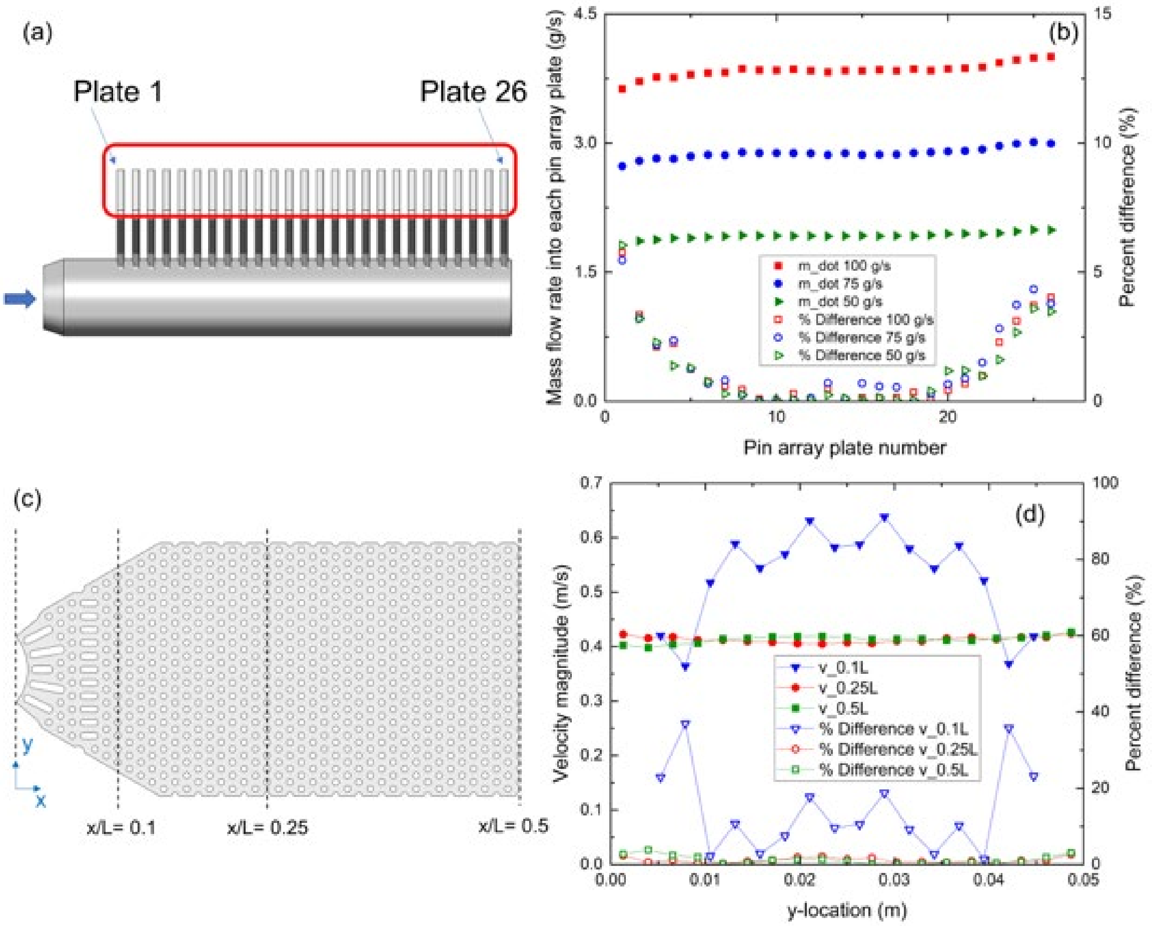

Figure 6.7. (a) Fluid domain for the study of flow distribution within the header, (b) flow distribution in the PHE plates for varied flow rates, (c) flow domain showing location of velocity sampling, (d) flow distribution across the height of the core section in terms of total velocity vector magnitude (array dimensions such as pin diameter and spacing are constant at the baseline values in Table 6.3).

Upon verification of uniform flow into each sCO_2 pin array, the design of each pin array for flow uniformity across its width was performed. The final iteration of the design that ensured structural integrity and uniform flow distribution is shown in Figure 6.7(c). Elongated ribs near the entrance of the pin array were added to ensure uniform flow distribution across the width. The streamwise velocity magnitude across the width of the pin array is plotted in Figure 6.7(d) at three different axial locations corresponding to $x/L = 0.1$, 0.25 and 0.5. The percent difference relative to the mean velocity at the respective location is shown in the secondary ordinate in Figure 6.7(d). In the diverging section near the inlet, at location $x/L = 0.1$, some flow non-uniformity is observed, with regions of higher velocity in the center of the pin array. However, once the flow enters the straight rectangular section of the pin array plate, the uniformity in flow distribution improves significantly at all locations across the plate height such that the highest value percent difference drops to below 3 % (see $x/L = 0.25$ and 0.5 locations), indicating uniform flow distribution exists for a majority of the core.

6.2.3. Thermo-mechanical analysis

After completing the flow uniformity study, a conjugate heat transfer analysis of the Gen 2 model was carried out to obtain the temperature profile in the solid domain, due to the heat transfer between the hot and cold streams. With these results, three simulations were conducted: a mechanical only simulation in which pressures are the only loads, a thermal simulation isolating the effects of the temperature gradients, and a thermo-mechanical simulation that evaluates the combined effect of temperature variations and pressure.

Figure 6.8 shows the setup of the thermo-mechanical simulation which focused on a representative section of the heat exchanger. The analysis was conducted using the temperature distribution at the inlet because the largest temperature difference, and thus the greatest thermal stresses, are expected at the inlet region.

The periodic nature of the PHE plates allowed us to reduce the computational domain to the model shown in Figure 6.8. The temperature map was imposed onto this model and pressures of 200 and 1 bar were applied on the internal and external faces, respectively. The faces at the midplane (x-z plane) were defined as zero displacement boundary conditions because the heat exchanger is symmetric with respect to that x-z plane. One assumption of the simulation is that the stress result is independent of the number of plates considered: the modelling of the outmost plate and a few internal plates is expected to be representative of the stress states in the design. Another symmetry plane was therefore defined and all the faces in yellow normal to the z-axis have a zero displacement boundary condition. This setup can also be thought of as the plane of symmetry of a heat exchanfer made of 5 plates. Finally, a zero displacement condition was specified on the faces normal to the x-axis, at the location were the pin array was truncated. The idea behind this simplification is that the inlet region already incorporate the most extreme condition, and extending the pin array all the way to the actual symmetry plane (normal to the x-axis) should not provide any essential information.

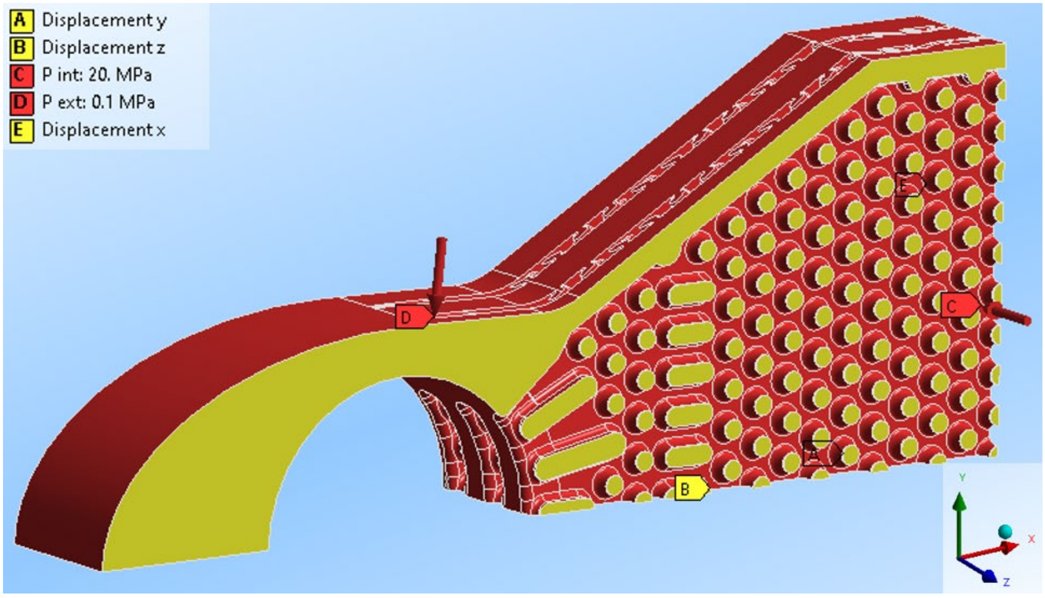

Figure 6.8. Pressure and boundary conditions for the thermo-mechanical analysis of the header-pin array assembly.

Figure 6.9 shows the stress results for the three simulations. The stress caused by temperature gradients are rather low and most of the geometry shows stress levels lower than 70 MPa. From Figure 6.9 (a-c), it appears that the mechanical stress contributes the most to the combined stress quantitatively but also qualitatively, because the peak stress regions between (a) and (c) overlap. The maximum von Mises stress has a value of 307 MPa and happens at the fillets of the entrance region of the pin array. However if we apply a stress filter and display only the portions of the heat exchanger with stress values greater than 150 MPa (Figure 6.9(d)), we observe that most of the heat exchanger is within the design criterion. The stress concentration highlighted in Figure 6.9(d) will lessen in intensity with stress relaxation, not considered in this analysis but captured in the creep simulations presented in the next section.

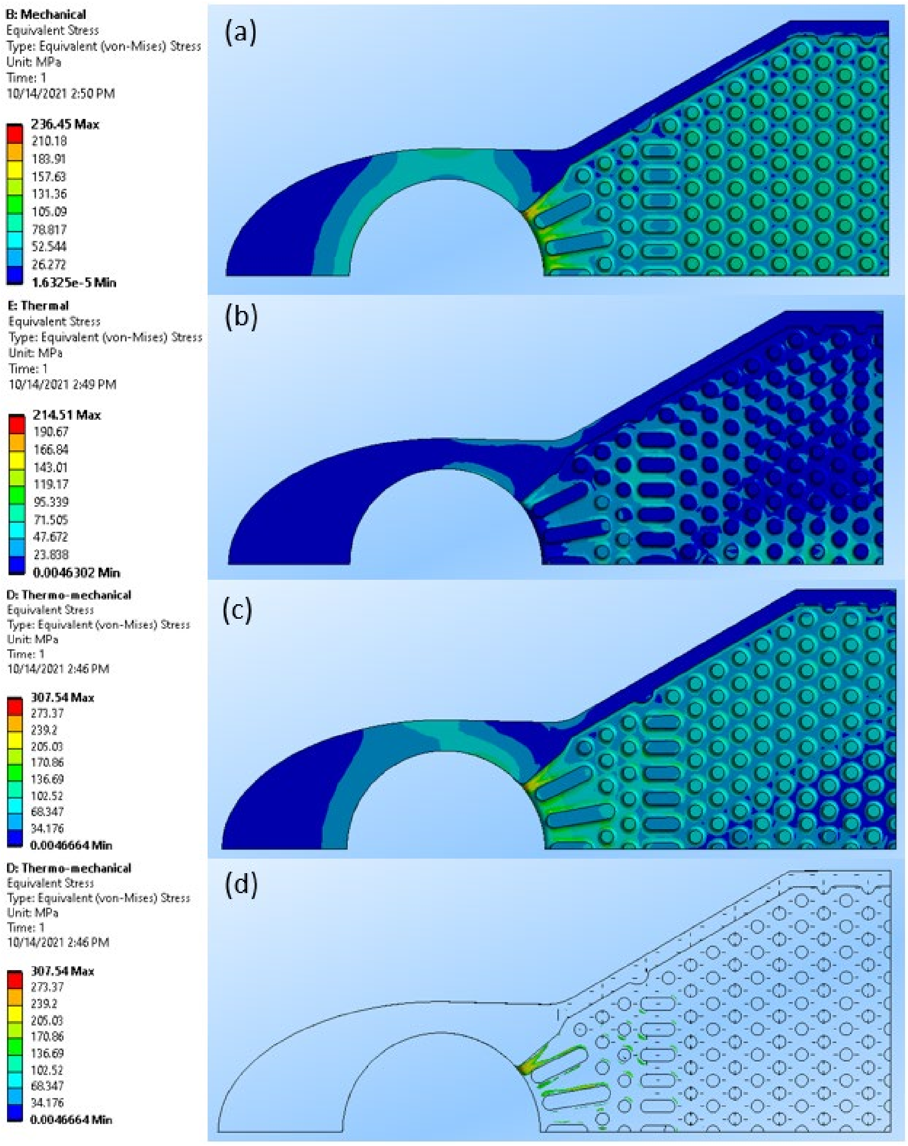

Figure 6.9. Von Mises equivalent stress for (a) mechanical only stress, (b) thermal stress, (c) combined thermo-mechanical stress, (d) combined thermo-mechanical stress with high stress regions (>150 MPa) highlighted.

6.2.4. Creep modeling

Creep simulations for the Gen 2 design are conducted in ANSYS Mechanical 2021R1 using the Norton model for secondary creep developed during previous quarters. The geometry presented in the thermo-mechanical section is used again for two creep simulations which correspond to the extreme loading conditions of the heat exchanger is likely to experience. The first case is a mechanical only stress that maximizes the creep strain rate, and the second combines thermal and pressure loads.

Case 1: 100,000 hours creep simulation with uniform body temperature of 720 °C

In this simulation, the thermal stresses are neglected since the temperature is kept uniform, but from the viewpoint of creep strain, this is the worst scenario given the relation between creep strain rate and temperature for Haynes 282:

$$\dot{\varepsilon} = 1.898 \times 10^{-8} \sigma^{6.805} e^{\left(\frac{-37250}{T}\right)}$$

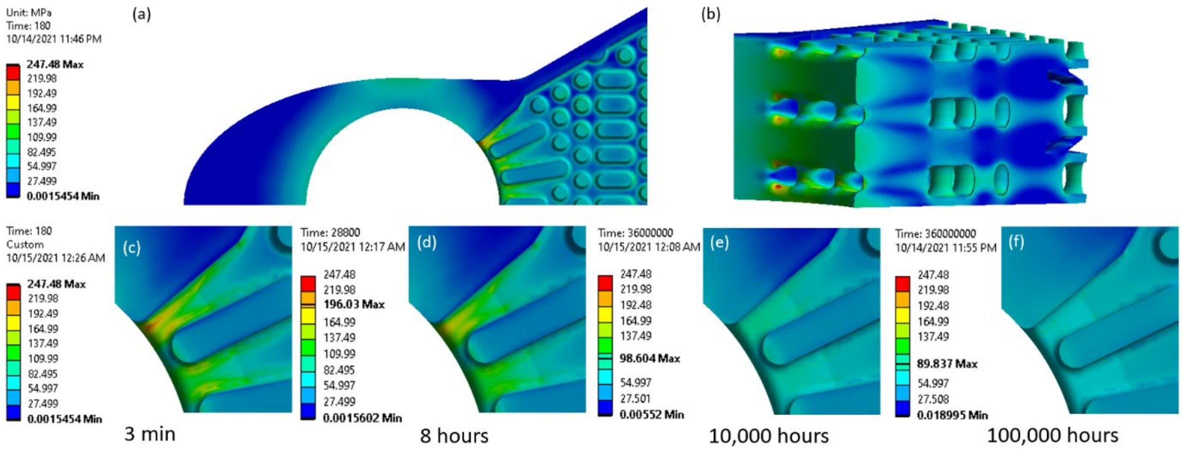

Figure 6.10. Mechanical stress distribution in the heat exchanger (a) cross-section at t=3 min, (b) side-view showing 3 plates at t=3 min, stress concentration at (c) t=3 min, (d) t=8 hours, (e) t = 10,000 hours, (f) t = 100,000 hours.

Figure 6.10 shows the stress distribution at the end of 100,000 hours of operation, starting with a 3 min ramp-up of the applied pressure from 100 to 200 bar, and the temperature from 500 to 720 °C. Figure 6.10 shows that the peak stress is maximum at 3 min. An examination of the stress profile reveals that both the header and pin array display stress values lower than 130 MPa, and the high stresses are concentrated at the fillets near the entrance of the pin array, with a maximum von Mises stress of 247.5 MPa. The pattern is consistent throughout the model and is also observed in the adjacent plates (Figure 6.10(b)), but this high stress decreases rapidly: from the peak value of 247.5 MPa at 3 min, stress relaxation allows the material to deform so that the stress decreases to 196 MPa after 8 hours of operation and ultimately to 90 MPa after 100,000 hours, which is a 63 % reduction compared to the starting peak stress value.

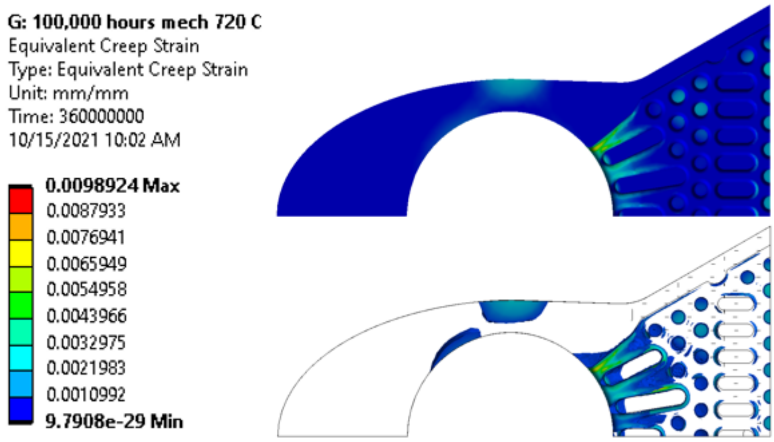

Figure 6.11. (a) Creep strain results for 100,000 hours with constant temperature and pressure loads, (b) location with strain exceeding 0.1 %.

Figure 6.11 shows the creep results corresponding to this simulation setup. The maximum creep strain is located at the fillets of the entrance region, which is expected since this is the location of high stress concentration. The largest creep strain of 0.99 % is a worst-case scenario since in practice, the model will not be subject to a temperature of 720 °C for the entire lifetime of the PHE. For the most part, the strain values are rather low, and the model mostly shows creep strain lower than 0.1 % (Figure 6.11(b)).

Case 2: 100,000 hours creep simulation with temperature distribution during regular operation.

In this case, the stress relaxation effect on the combined thermo-mechanical stress distribution is studied. The stress is expected to be higher because under this configuration, the effects of thermal gradients are included. In terms of creep however, this situation will be less extreme than the previous case because the temperatures at the inlet (with larger thermal gradients) are lower in magnitude compared to the outlet region.

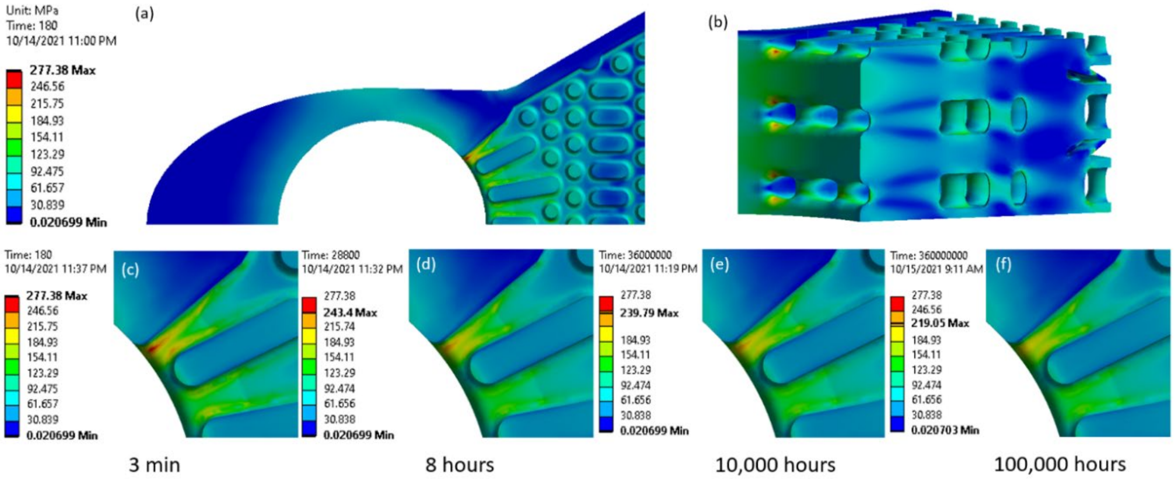

Figure 6.12. Thermo-mechanical stress distribution in the heat exchanger, (a) cross-section at t=3 min, (b) side-view showing 3 plates at t=3 min, stress concentration at (c) t=3 min, (d) t=8 hours, (e) t = 10,000 hours, (f) t = 100,000 hours.

The resulting stress distribution is presented in Figure 6.12. The stress map is consistent with the results obtained in case 1, with the maximum stress at the entrance fillets and the stress magnitude decreasing over time. The stress reduction however is not as significant as before, with the maximum stress decreasing from 277.4 to 219 MPa, which corresponds to a 21 % reduction.

In terms of creep strain, this setup exhibits creep strain values even lower than the first case because even though the temperature gradients at the inlet are greater -and the thermal stresses are larger- these temperatures are lower in magnitude compared to the outlet with a maximum temperature of 570 °C.

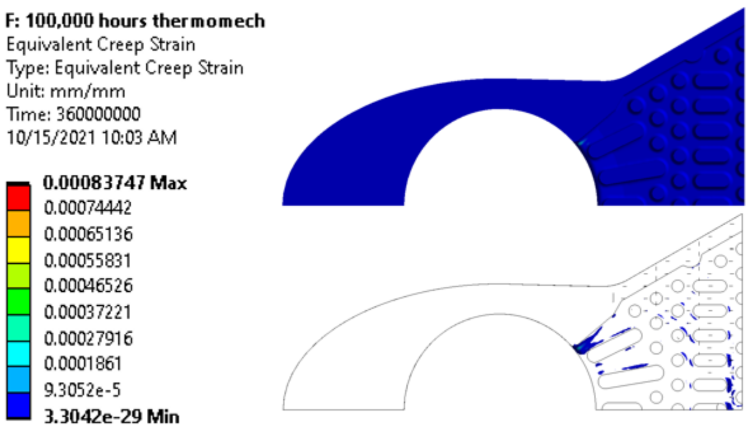

Figure 6.13. (a) Creep strain results for 100,000 hours with constant pressure and inlet temperature profile applied, (b) locations with strain exceeding 0.001%.

The two cases considered are two worst scenarios of the expected operational schedule, maximizing the creep deformation and the stress respectively. In practice, the PHE is expected to have stress and creep strain profile which are a mix of the extreme cases considered in this section.

6.3. Header-Core mechanical integrity verification

One of the stated advantages of AM is the ability to design and fabricate integral header and core architectures for heat exchangers. In traditionally manufactured heat exchangers such as PCHE, the core is welded or brazed to the headers, and this could lead to potential failure locations at the header-core location, in addition to inefficient heat exchange in cross flow sections. To experimentally verify the mechanical integrity of the integrated header-core architecture of the AM PHE, sub-scale PHEs specimens, with 3 pairs of hot and cold plates and headers, were designed and fabricated for accelerated testing at temperature. Additively manufactured 316L SS was used instead of H282 in order to accelerate time to failure and obtain results in a timely manner. Since the Larson-Miller analysis is an accurate description of the material behavior of metallic systems, the choice of material was dictated by testing expediency and powder availability. The design was intentionally weakened in the core to determine whether failure would occur at this weakened region or at the header-core intersection. Both location and time to failure were of interest. If the failure occurred at the weakened section in the core rather than in the header-core section, it would corroborate the FEA model and confirm that the PHE can be designed for the appropriate life considering the high-stress regions. If the time to failure at operating temperature matched the predicted lifetime based on a Larson Miller approach, confidence in the printing parameters and AM approach would be obtained.

6.3.1. Design and modeling of the units for integrity testing

Two different models of the sub-scale PHE were designed with varying degrees of weakened core regions. The first sub-scale PHE model for structural analysis, along with the imposed boundary conditions, is shown in Figure 6.15(a) and the second design is shown in Figure 6.15(d). For the first model, an entire row of pins was removed from the core (see Figure 6.14(d) and Figure 6.15(a)), while for the second design, every other pin in the same row was removed (see Figure 6.14(e) and Figure 6.15(d)). For both designs, a symmetry boundary was imposed on the top half pin plate and a 200 bar internal pressure was imposed on the sCO_2 pin arrays while atmospheric pressure was imposed on the MS side.

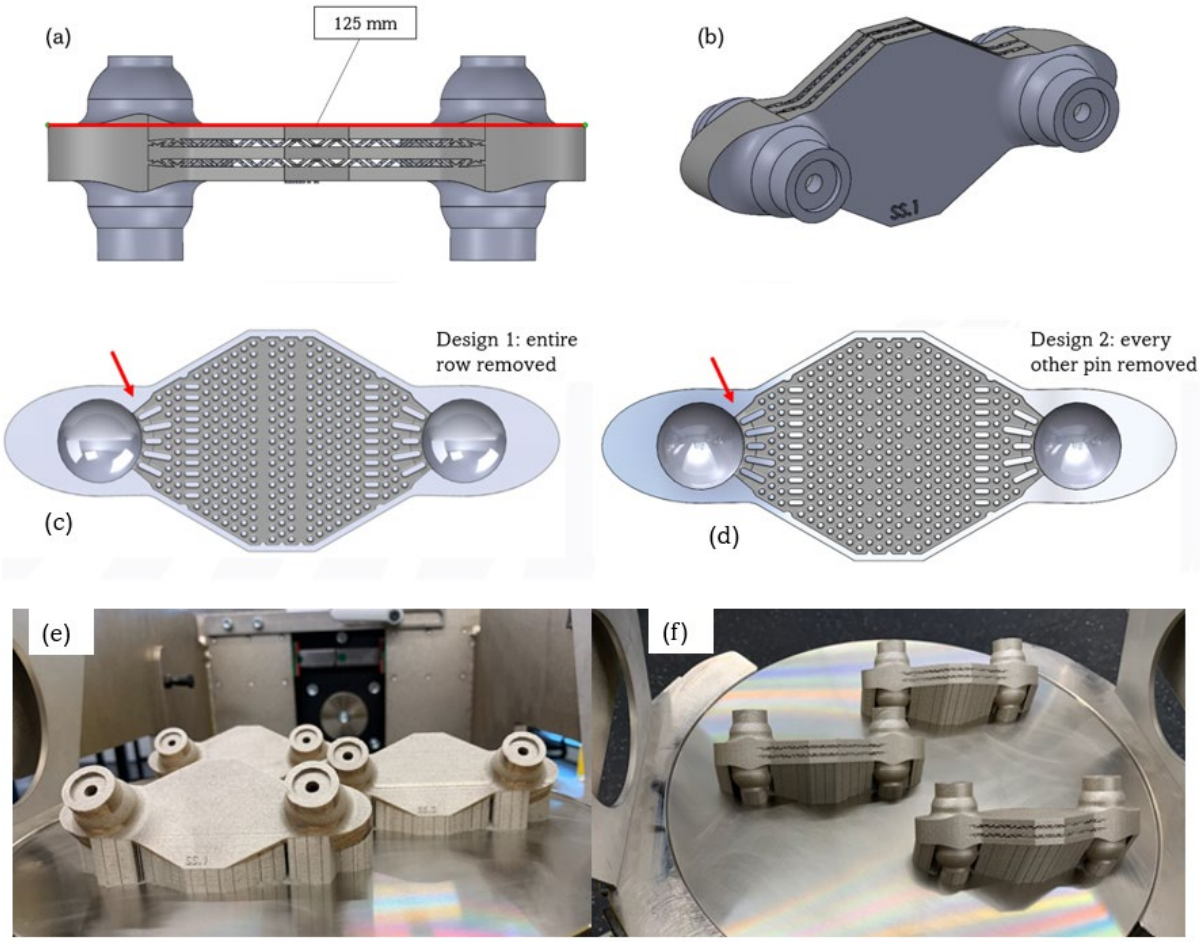

Figure 6.14. Sub-scaled 3-plate HX design from (a) the top view, (b) tilted front view, and cross-sectional view of (c) design with an entire row of pins removed, (d) design with some pins missing, (e) front, and (f) top views of the sub-scaled units on the build plate. The red arrow indicates the header-core junction whose integrity is being tested.

In order to determine the time to failure, the creep-rupture data of printed SS316 generated by Li et al. [102] were used to generate a relationship between rupture stress, time to failure, and temperature using the Larson-Miller Parameter (LMP) approach:

$$\sigma_{\text{rupture}} = -0.0586 * T * (17 + \log_{10}(t)) + 1400 \quad (6.1)$$

where T is in Kelvin and the time t in seconds.

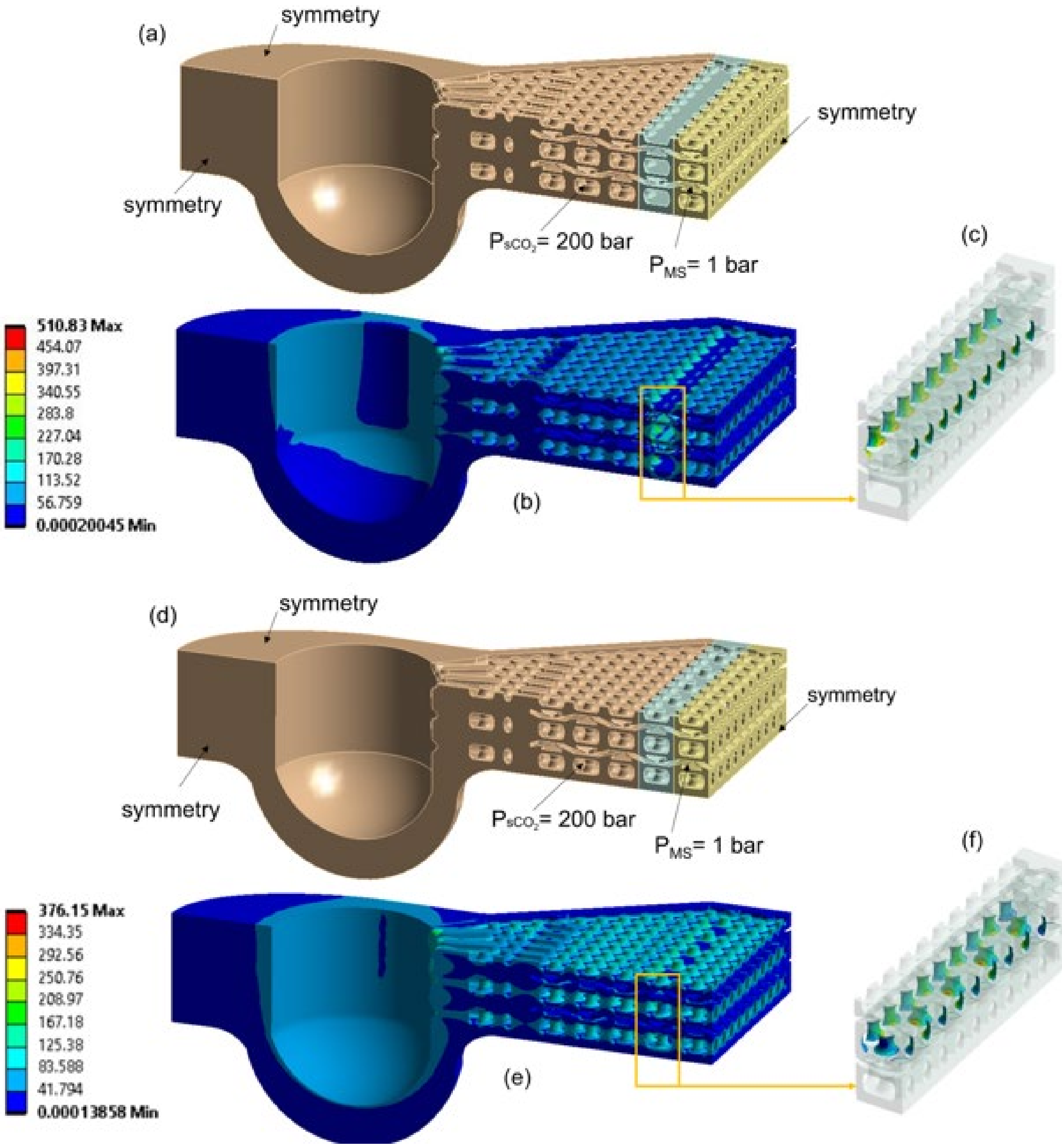

Figure 6.15. Setup and boundary conditions for (a) Design 1 and (d) Design 2, stress distribution for (b) Design 1 and (e) Design 2, high-stress region for (c) Design 1 and (f) Design 2.

The results of the structural simulations in ANSYS Mechanical for the first design are shown in Figure 6.15(b) and (c) and life estimations at different locations of Design 1 and 2 are summarized in Table 6.2. For the first design, the peak and average stresses in the unit are approximately 510 and 48 MPa, respectively, and it is seen that regions of higher stress in the 170 MPa range (and peak of 220 MPa) exist at the entrance of the pin array in between the elongated flow distribution structures (see Figure 6.15(b)). The stress in the region of the core with the removed row of pins is also similarly high; the regions of high stress are located in the surrounding pins facing the open row of pins. The high-stress regions in the pins surrounding the open core region are shown in Figure 6.15(c). Based on the peak stress of 510 MPa in the design, the expected time for failure for a pressure of 200 bar and a temperature of 743 °C (highest operational temperature recorded during the experiment) was estimated to be less than 0.1 s, while the estimate based on the global average stress yield a rupture time of 8471 min (141 hours). Since the high stresses observed in the simulation will relax in practice during the experiment, it was expected that the correct metric to predict the time to rupture of the unit should be a value bracketed by the 48 and 510 MPa stress estimates. To further this analysis, the average surface stress in the missing row region of each plate was calculated to estimate the expected life.

Table 6.2. Estimated rupture time at different locations of Design 1 and 2.

		Design 1		Design 2	
#	Stress cases	Failure stress (MPa)	Life (minutes)	Failure stress (MPa)	Life (minutes)
1	Maximum	510	0.00015	376	0.026265
2	Global average	48	8471	42	10684
3	Average in the weakened region (3 plates)	77	2760	54	6717
4	Average surface stress - top plate	150	164	113	686
5	Average surface stress - middle plate	177	58	115	635
6	Average surface stress - bottom plate	167	85	112	713

The average stress in row #3 of Table 6.2 was calculated as the average equivalent stress in the weakened region. It includes both the stress at the surface of the pins and in the solid. As another measure of the local stress, the surface stress at the surface of the pins in the top, middle and bottom pin arrays in the weakened regions are reported in rows 4-6 of Table 6.2. The average stress in this region was 77 MPa with local surface-averaged values of 150, 177 and 167 MPa for the stress concentration region in the top, middle and bottom plates, respectively. Given the location of the absolute maximum stress and the local peak in each plate, the expectation of failure for this design was in the core region with the missing row of pins. Among the three local results considered, the average surface stress in the middle and bottom plates gave the most realistic estimate of time to rupture of 58 and 85 minutes, which compare well with the experimental results described in the following section.

The stress distribution in the second design is shown in Figure 6.15(e). As with the first design, it is seen that there are regions of high stress near the entrance to the pin array in between the elongated flow distribution structures and the peak stress in this region is similar to that in the first design. The high-stress regions in the core row with every other pin removed is shown in Figure 6.15(f). As with the first design, the high-stress zones are in the pins surrounding the regions where pins have been removed. The peak stress in this region is 376 MPa with an average of 115 MPa in the middle plate. Compared to the first design, the second design exhibits less stress variation from one plate to an adjacent one. Based on the average surface stresses in this region, the time to failure for a pressure of 200 bar and temperature of 743 °C was estimated to be 10.6 hours.

The two designs were printed at CMU using SS316 in a Trumpf TruPrint 3000 laser powder bed fusion printer. The majority of the volume was printed with laser power, scanning velocity, hatch spacing, and layer thickness of 220 W, 700.0 mm/s, 150 μm, and 30 μm, respectively, with additional contour, up-skin, and down-skin laser scans. A porous, net-like structure was printed below the specimens to support the bottom surface of the specimens during printing. Since the units were not stress-relieved, they were left attached to the build plate to avoid damage due to residual stresses.

6.3.2. Facility description

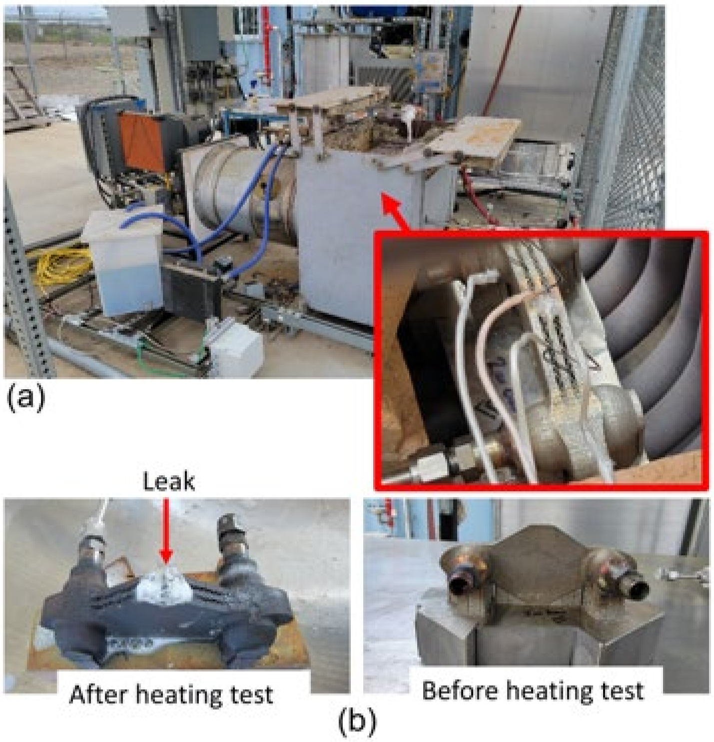

Figure 6.16. (a) Experimental facility, (b) AM stainless steel unit before and after testing.

A picture of the pressure and temperature test facility is shown in Figure 6.16. The facility consisted of a 500,000 BTU/hr (165 kW) Maxon® burner that was connected to a test chamber using 21-inch circular stainless-steel ducting lined with high temperature rigid insulation. The circular duct wall was equipped with an active cooling scheme consisting of water-cooled copper coils integrated around the ducting, a water pump and a small air-cooled radiator to dissipate the heat from the water. The test chamber was 3ft x 3 ft x 2 ft (Width x Height x Depth) and was made with ¼” wall thickness steel plate with high temperature insulation lining the inner walls. The chamber was mounted on a strut channel frame with locking castors. The back and top walls were adjustable to permit placement of the test article to be tested and for exhausting of the combustion gases, respectively. The test article to be pressure tested was placed within the chamber and it was connected to a high-pressure nitrogen source with high-pressure-rated tubing integrated with an electronically-controlled pressure regulator and an electronically-controlled three-way solenoid valve assembly. The solenoid valve assembly could be used to isolate the test article from the nitrogen cylinder upon application of pressure. Furthermore, it could be used to relieve pressure and re-pressurize the test article during cyclic pressure testing. A PID controller on the burner was wired to the control station located in adjacent office space container where the experiments were monitored remotely. The burner controller enabled the adjustment of the fuel-air ratio and hence the test chamber set temperature.

The experiments started by pressurizing the units at ambient temperature with a hold time at each set pressure. During the hold time, the unit was isolated from the pressure source to monitor the pressure for any decay indicative of a leak. All the above units passed pressure test at ambient with 30 minutes hold time at the max pressure of 200 bar.

6.3.3. Results

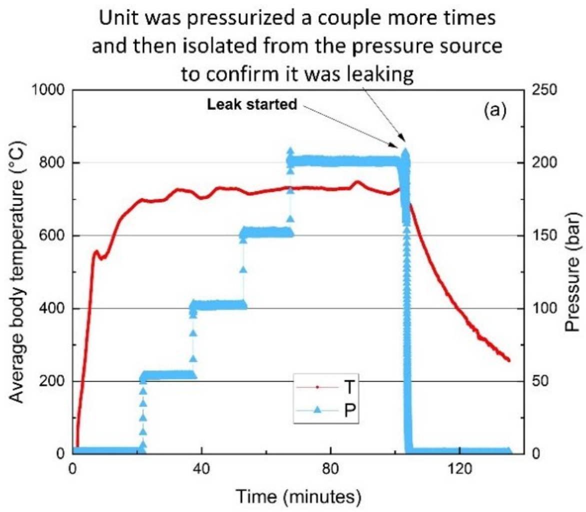

Figure 6.17. (a) Time series of weakened unit (Design 1) body temperature and internal pressure throughout the test, (b) weakened sub-scale unit showing leak in the middle section after testing at high temperature and pressure. The internal features dimensions are kept at the baseline values in Table 6.3.

The elevated temperature testing started out with the weakest design (Design 1), and a target temperature and pressure of 720 °C and 200 bar, respectively. The Design 1 unit was placed in the burner chamber and five k-type thermocouples were inserted at different locations of the unit (as shown on the inset figure of Figure 6.16(a)). The time series of this unit body temperature (the average of all five thermocouples) and the unit internal pressure throughout the first round of testing are plotted in Figure 6.17(a), and Figure 6.17(b) shows a picture of the failed (Design 1) unit. First, the unit was heated up to the target temperature of 720 ^{0}C at atmospheric pressure. The unit was then pressurized in increments of 50 bar and 15 minutes hold time until the target value of 200 bar was achieved. The test proceeded until any potential failure sign could be noticed.

The first unit withstood a cumulative testing time of around 150 minutes before failing, with the last 35 minutes being at the highest pressure of 200 bar. Failure was characterized by an abrupt decay in the pressure observed while the unit was still at the target temperature, which is an indication of a leak. The test was stopped and after the cool down process, the unit was removed from the chamber for inspection. No visible sign of defect was observed on the external walls, but after pressurizing the unit with compressed air (100 psi), applying soapy water, the approximate location of the leak was revealed to be adjacent to the location of the missing rows at the center of the part and between the sCO_2 plates (see Figure 6.17(b)). The test was conducted a second time with a second identically printed sub-scale unit to ensure repeatability of the experiment. The unit failed after about 57 minutes at the highest temperature and pressure. Leak test revealed that this unit failed at the core region and away from the header core. The second sub-scale design (Design 2) with alternate pins missing in two rows (Figure 6.15(d)) was also pressure tested at temperature. Over a span of two days, the unit was under 200 bar pressure at 730 °C for over 11 hours without any loss of pressure, at which point the test was concluded.

When compared with the simulation results, these experimental results reveal the following: (i) The prediction of failure location for the first design is consistent between the simulation and experiments, (ii) the predicted lifetime using the LMP approach using the maximum stress is an underestimate of the actual failure time while using the average stress is an overestimate. A local average of the surface stresses near the weakened location from the mechanical simulations seems to be the most accurate metric to predict the time to rupture. The experimental results also established confidence in the printing parameters and process.

6.4. Modification of the correlation-based model

The correlation-based thermo-fluidic model presented in Chapter 5 for the core design was modified to reflect the changes made to the design in the PHE core. The objective of this simplified numerical model was to evaluate the thermofluidic performance of the heat exchanger over a wide design space efficiently. The inlet temperature and pressure of the fluid streams were kept fixed at 720 °C and pressure of 1 bar for the molten salt, and 500 °C and 200 bar for the sCO_2. As shown in Figure 6.18 the PHE was made up of a single counterflow region to reflect the new architecture of the HX. The main counterflow section was further discretized to incorporate the effect of temperature dependent properties.

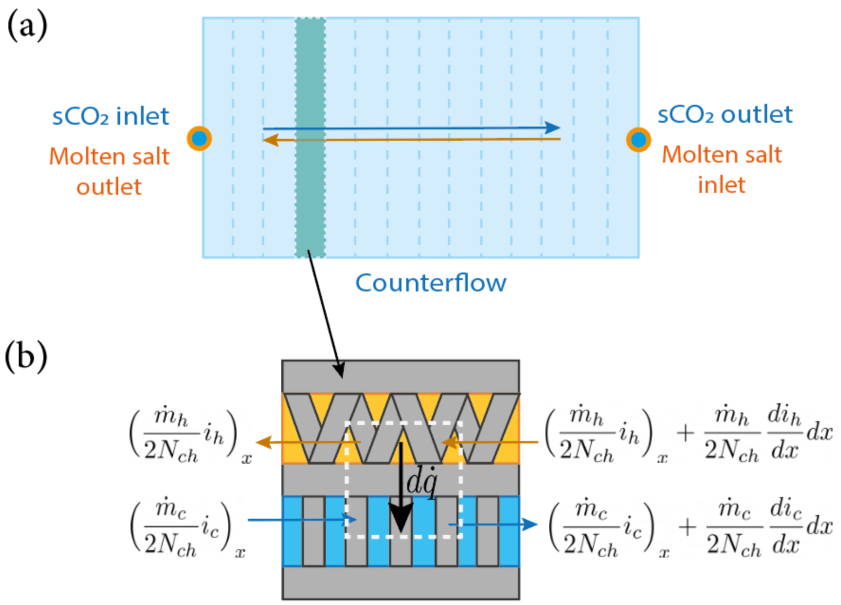

Figure 6.18. (a) Schematic of the Gen 2 PHE, (b) differential energy balance for a control volume with half control volume on each side.

The modeling process is very similar to the one presented in Chapter 5 for the Gen 1 HX, hence for the sake of brevity, details will not be repeated in this section.

Due to the complex geometry of the lattice structure on the MS side, the thermal resistance on this side was written in terms of a thermal resistance rather than a heat transfer coefficient (as presented in Chapter 4). An analogous modification is implemented in the counterflow section and with the assumption of incompressible flow, the specific enthalpy (i) in Figure 6.18 can be expressed in terms of the specific heat at constant pressure such that the temperature gradient on the hot side is given by

$$\frac{dT_h}{dx} = \frac{-2N_{plates}}{\dot{m}_h c_{p_h} dx} \frac{(T_h - T_c)}{\left\{\frac{R_h''}{A_{ctr}} + \frac{t_w}{k_w A_{ctr}} + \frac{1}{(\eta_{pin,c} N_{pin} A_{pin,c} + A_w) h_c}\right\}} \tag{6.2}$$

A similar equation can be written for the cold side. The thermal resistance to heat flux on the hot side, R_h", and the heat transfer coefficient on the cold side, obtained from CFD and experiments, respectively, will be discussed in the next section. The local temperatures on the hot and cold side are obtained through an iterative process. First, a guess is made on the outlet sCO_2 temperature and a differential equation solver in MATLAB is used to obtain the temperature distribution in each control volume of the counterflow region. At the end of this process, the inlet sCO_2 temperature is obtained and this result is compared to the known inlet temperature. The iterative process stops when the two values are within the specified tolerance of 0.1 °C.

6.5. Gen 2 performance and comparison with Gen 1

Based on the thermofluidic model described earlier and the cost model available in Ziev et al. [100], a parametric study was conducted on the geometrical and flow parameters of the PHE to identify tradeoffs and design geometries that would lead to high power densities. The parameters were varied sequentially, holding all others at a baseline value, to isolate their impact on the performance. The varied parameters and their baseline values are summarized in Table 6.3. The baseline values for the hot and cold channel width (W_c and W_h) are the result of a compromise between the fin efficiency and the channel gap that will minimize manufacturing-induced flow obstruction. The pin diameter (D_{pin}), transverse pitch ratio (β_T) and wall thickness (t_w) were set from simulations on mechanical stress. The range of surface roughness was based on measurements of as-printed parts (upper limit) and potential for reduction in roughness with surface treatments such as abrasive flow machining or other chemical treatments (lower limit). While all parameters were varied, only results for the parameters with the most impact on performance are presented in this section.

Table 6.3. Fixed and varied parameters in PHE optimization.

Parameters	Baseline Value	Range
L_{HX} (cm)	18	[16.00, 35.00]
N_{plates}	26	[21, 39]
W_{max} (cm)	12	[10.00, 18.00]
H (cm)	5	[5.00, 6.00]
W_h (mm)	1.80	1.00, 1.80
W_c (mm)	1.80	[0.75, 2.50]
β_T (-)	2.05	[1.34, 2.05]
D_{pin_c} (mm)	1.20	[0.50, 1.50]
D_{pin_h} (mm)	1.20	[-]
t_w (mm)	0.50	[0.30, 1.50]
R_z (μm)	60	[30.00, 250.00]
$\dot{m}_{sCO_2}$ (g/s)	80 (Re_{Amin} = 2480) C_{min} on this side at MS baseline flowrates	[-]
$\dot{m}_{MS}$ (g/s)	115 (Re_{Amin} = 23)	[97, 119] (Re_{Amin} = [18, 25])

6.5.1. Flow rates variation

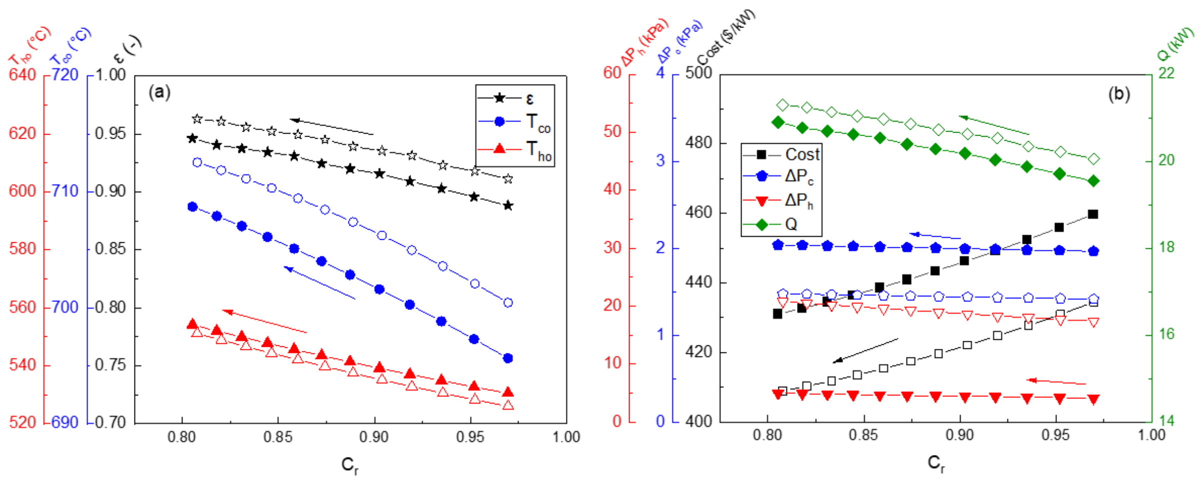

Figure 6.19. PHE performance prediction as a function of C_r, the filled and hollow symbols represent a hot channel width of 1.8 mm and 1.0 mm, respectively (for reference, the volumetric power density at 20 kW corresponds to 16.3 MW/m^3 for the 1.8 mm case). The arrows indicate the direction of increasing MS flow rate and all the parameters are constant at their baseline value specified in Table 6.3.

Figure 6.19 shows the impact of varying the flow rate of the MS (hot) stream relative to the sCO_2 (cold) stream, represented as heat capacity rate ratio, C_r, on the performance of the PHE with the baseline geometry indicated in Table 6.3. The impact of varying C_r on exit fluid temperatures and effectiveness is shown in Figure 6.19(a), while the pressure drop and cost (in $/kW) are shown in Figure 6.19(b). The sCO_2 flowrate is kept at 80 g/s and the arrows in Figure 6.19 show the direction of increasing MS flowrate. The PHE with 1.8 mm channel gap width on the hot side is represented by the filled symbols, and the 1.0 mm gap width PHE is depicted with hollow symbols. At an equal overall width of the PHE, the 1.0 mm gap will result in more plates and an increased heat transfer surface area compared to the 1.8 mm gap configuration. The PHEs with the two different channel gap widths show a similar trends in terms of effectiveness and outlet temperatures (Figure 6.19(a)), and thermal rating (Figure 6.19(b)). The 1.0 mm channel PHE has an effectiveness that varies from 0.91 to 0.96 compared to 0.89 to 0.95 for the 1.8 mm channel case. The better thermal performance of the 1.0 mm channel PHE is observed in the form of higher thermal rating (Figure 6.19(b)) and power density. For example, at a C_r ratio of 0.93, the thermal rating and power density are 20.3 kW and 21.8 MW/m^3 compared to 19.9 kW and 16.1 MW/m^3, for the 1.0 and 1.8 mm cases, respectively. This trend can be explained by the higher fin efficiency on the hot side for the 1.0 mm channel and the increased local velocity in the PHE with narrower MS channels. Figure 6.19(a) shows that an increase in MS flow rate is accompanied by an increase in T_{co} because the thermal resistance on the hot side decreases (as discussed in Chapter 4). However, the increased velocity results in a decrease in residence time, which results in an increase in T_{ho}. A tradeoff exists between a high effectiveness and a lower T_{ho}, which is a desired feature to minimize parasitic losses in the system.

The two PHE designs are comparable in terms of pressure drop on the cold side (Figure 6.19 (b)); the difference observed (1964 Pa for 1.8 mm hot side channel vs 1413 Pa for 1.0 mm at a C_r of 0.97) results from the counteracting effects of lower flow per plate in the 1.0 mm PHE and a higher temperature and thus viscosity on the sCO_2 side. The pressure drop on the hot side, however, is several times greater for the narrower channel. For example, at a C_r of 0.93, the pressure drop through the 1.0 mm gap width is 18 kPa compared to 4.3 kPa for the 1.8 mm gap width. At a constant hot channel gap width, the volume of the heat exchanger remains unchanged; hence the trends in cost (in $/kW-th) reflect the power rating variations. As the MS mass flowrate increases from 97 to 119 g/s, the power rating increase from 19.5 to 20.9 kW translates into a cost reduction from $460/kW-th to $430/kW-th for the 1.8 mm hot channel PHE. In the 1.0 mm case, a cost reduction from $434/kW-th to approximately $408/kW-th is achieved with a power rating enhancement from 20 to 21.3 kW.

Since powder removal is a key concern associated with AM of complex structures with internal pathways, the 1.8 mm design was selected to finalize the design.

6.5.2. HX length.

Figure 6.20 shows the PHE performance as a function of L_{HX}, the total length of the PHE core. The exit temperatures of the streams and effectiveness trends with core length are shown in Figure 6.20(a) while the pressure drops, thermal rating and cost (in $/kW-th) are shown in Figure 6.20(b). As the length increases, there is more surface area and residence time for heat exchange between the two streams as shown by the increase in temperature difference with T_{ho} decreasing from 552 to 542 °C and T_{co} increasing from 704 to 717 °C. The effectiveness increases 7% from 0.92 to 0.98 with core length. Although the thermal rating increases from 20.5 to 21.7 kW as L_{HX} changes from 16 to 35 cm, the volumetric power density decreases from 18.3 to 9.8 MW/m^3 due to the increase in core volume from 1.11 to 2.21 dm^3. The pressure drop follows a linear increase from 4315 to 9210 Pa on the hot side and 1800 to 4072 Pa on the cold side. The non-monotonic trend in cost can be explained in terms of the different growth rates of the power rating and PHE volume with L_{HX}. As the length increases, so does the heat exchanger volume and the expenses related to material cost, and the other processing parameters. The additional cost is justified by the associated increase in power rating, as evidenced by the initial decrease in cost per kW. However, a point is reached at L_{HX} of 20 cm, where the power rating gain comes with a larger increase in material volume, thereby causing a rise in $/kW-th cost beyond L_{HX} of 20 cm from $433/kW-th for L_{HX} of 20 cm to $445/kW-th for L_{HX} of 36 cm.

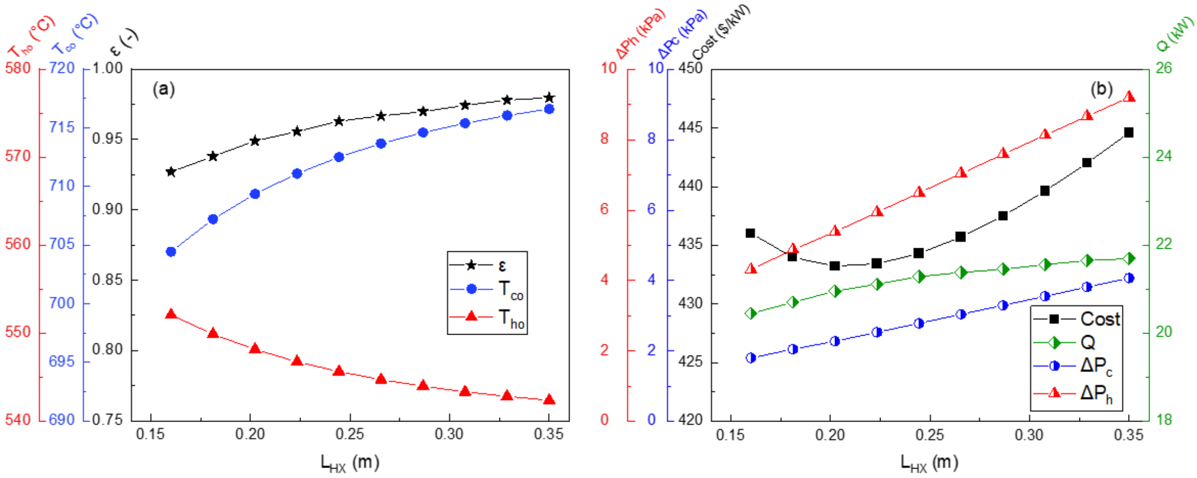

Figure 6.20. PHE performance varying with the total length of the heat exchanger from 16 to 35 cm: (a) ε, T_{co}, and T_{ho} variation and (b) $/kW-th, ΔP_c, ΔP_h, and thermal rating variation with L_{HX}. sCO_2 and MS flowrates of 80 and 115 g/s, respectively. All other parameters are constant at their respective baseline value specified in Table 6.3.

6.5.3. Total width of the PHE.

The impact of the overall width (number of plates) on the PHE performance is shown in Figure 6.21. The exit temperatures of the streams and effectiveness trends with core width are shown in Figure 6.21(a) while the pressure drop, thermal rating and cost (in $/kW) are shown in Figure 6.21(b). The residence time increases with the number of plates in the PHE, since the total flowrate gets subdivided into more streams, and the PHE effectiveness increases from 0.93 to 0.95. The thermal rating improves from 20.5 to 21 kW, but the additional pairs of hot and cold streams translates into a volume increase, which causes a drop in power density from 19.8 to 11.6 MW/m^3. The pressure drop decreases on both hot and cold sides due to a decrease in mass flow rate through each plate in the core with an increase the overall width while keeping the total MS and sCO_2 flowrates constant. A cost reduction from $439/kW-th to $427/kW-th is observed because the increase in material cost associated with adding more plates is lower than the increase in power rating.

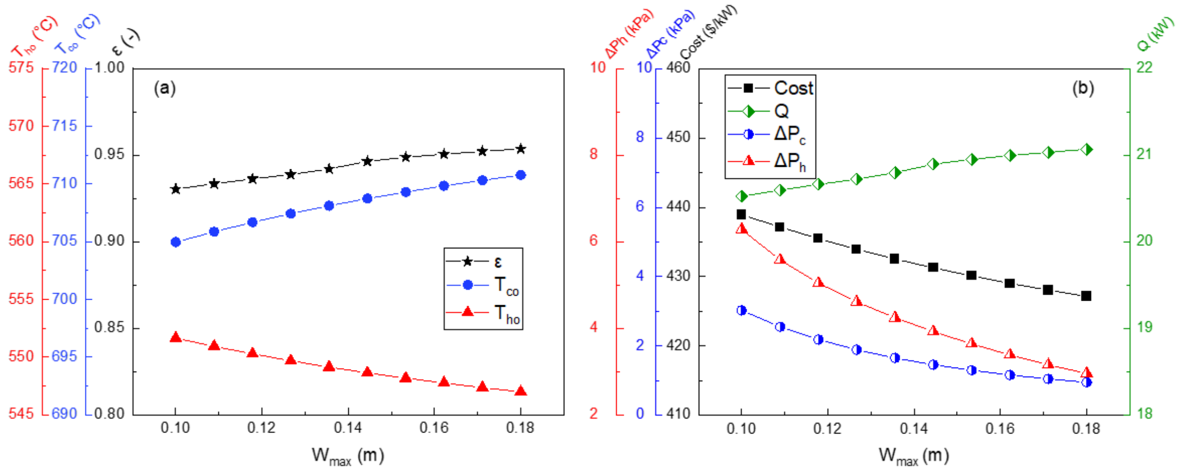

Figure 6.21. PHE performance varying with the total width of the heat exchanger from 10 to 18 cm: (a) ε, T_{co}, and T_{ho} variation and (b) \$/kW-th, ΔP_c, ΔP_h, and thermal rating variation with W_{max}. sCO_2 and MS flowrates of 80 and 115 g/s, respectively. All other parameters are constant at their respective baseline value specified in Table 6.3.

6.5.4. Roughness (Rz)

Figure 6.22 illustrates the influence of the peak-to-valley roughness Rz on the thermal performance of the heat exchanger. The Rz range was selected to span the values obtained from sample measurements on the sCO_2 side, before and after abrasive flow machining, and was modeled so that Rz effectively results in a reduction in the height of the pin array on the cold side. It should however be noted that in practice, Rz alone does not capture the entirety of how roughness impacts the surface, as the surface structure could vary significantly in the other two dimensions. Due to the complex nature of the flow path through the 3D lattice on the MS side, the impact of surface roughness was not modeled on this side. The reduction in the minimum cross-sectional flow area A_{min} due to the channel constriction by surface roughness appears to have a prominent effect on the thermal performance by increasing the heat transfer coefficient on the cold side and reducing the thermal resistance. As a result, the effectiveness increases from 0.94 to 0.96 and the rating from 20.6 to 21.1 kW. The pressure drop on the cold side, however, increases from 1.9 kPa to 3.4 kPa due to the constriction in the open channel area.

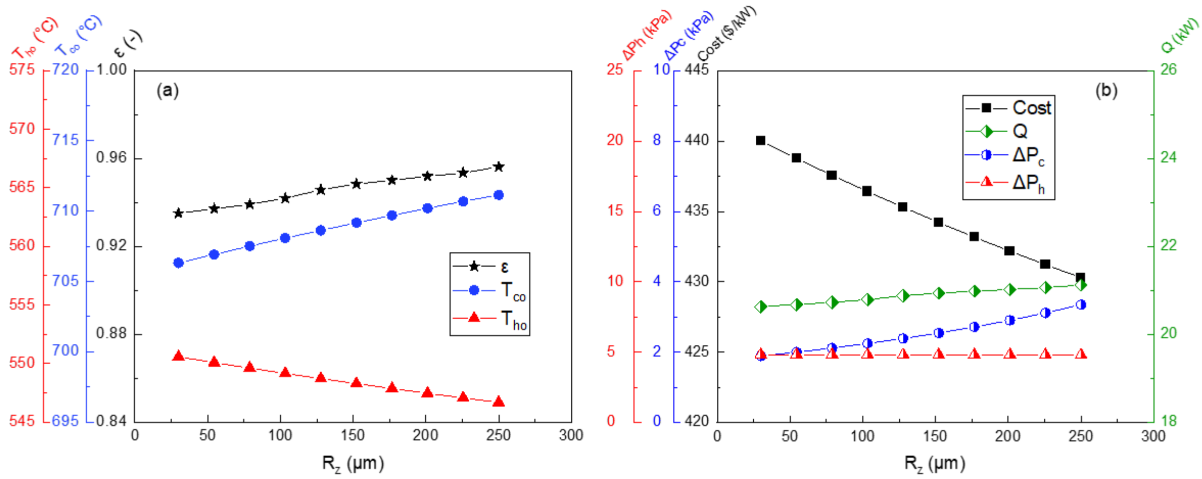

Figure 6.22. PHE performance varying with the cold side roughness from 30 to 250 µm: (a) ε, T_{co}, and T_{ho} variation and (b) $/kW-th, ΔP_c, ΔP_h, and thermal rating variation with. sCO_2 and MS flowrates of 80 and 115 g/s, respectively. All other parameters are constant at their respective baseline value specified in Table 6.3.

The effect of various parameter was considered in this study and based on the previous findings, it can be suggested that the most effective way to combine the advantages of high power density, low pressure drop and high effectiveness is by increasing the number of plates in the model (larger W_{max}). Increasing the length of the PHE does increase the thermal performance of the PHE and lower the cost but only up to the point when the increase in material volume and associated manufacturing costs match the gain in thermal performance, after which there is only a marginal increase in thermal rating and the trend in cost (in $/kW-th) reverses. The effect of increasing the flow length in the PHE has the adverse effect of increasing the pressure drop whereas an increase in number of plates, at constant mass flowrate lowers the pressure losses. The effect of surface roughness is less straightforward to incorporate at the design stage because roughness is not a parameter that can easily be monitored and predicted before printing. Further study is required to formulate accurate design guidelines, but a reasonable operation window can be specified based on the average size of the powder and available surface smoothing methods.

6.6. Pathway to cost reduction and comparison between Gen 1 and 2

In this section, we explore the impact of changing PHE design and printing process parameters on cost. The cost in $/kW-th presented in the parametric study is based on the conservative set of parameters and a single-laser machine (print speed of 700 mm/s). However, high part density is obtained at higher print speeds and laser powers. A porosity map was generated from a build using H282 with various speeds and laser powers by CMU with the motivation of operating within a 'process window' for which low porosity is maintained regardless of small variations in local process conditions. Fourteen cube specimens printed with various speeds and laser powers were cross-sectioned, and around 20 to 50 optical micrographs were each taken from different parts of the cubes and key results are summarized in Table 6.4.

Table 6.4. Porosity as a function of laser power and speed for H282 test cubes.

	Sample 1	Sample 2	Sample 3
Speed (mm/s)	700	959	1366
Power (W)	300	350	350
Porosity (%)	0.03	0.04	0.03

It is seen that very low porosities of 0.03%, obtained at the conservative printing speed of 700 mm/s can also be obtained at higher speeds of 959 mm/s and 1366 mm/s. Figure 6.23 shows a cost comparison between Gen 1 and Gen 2 PHEs for two printing speeds (959 and 1366 mm/s) and three commercially available machines: the EOS M290 which is a single laser machine currently used for the printing of the articles tested in this study, the EOS M400-4 machine with four lasers, and the SLMNGXII600 twelve laser machine equipped with a system that reduces the set-up/teardown and heat-up/cool-down time.

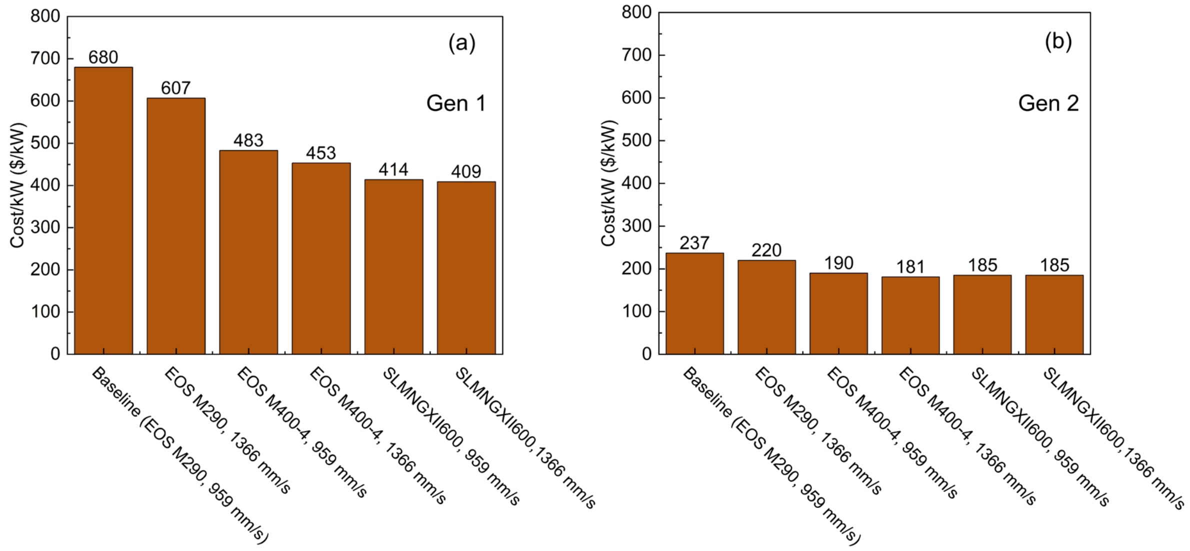

Figure 6.23. Cost in $/kW for (a) Gen 1 and (b) Gen 2 on three different machines and two printing speeds, 959 and 1366 mm/s, based on an annual production volume of 1500 units.

The results reveal that switching to the Gen 2 PHE design results in more than twofold cost reduction for all the printers investigated. The cost reductions are primarily driven by reduced material used per kW and reduced printing costs per kW. The reduced printing costs per kW are related to the reduced material used because melting less material requires less time. Additionally, printing at higher speeds and with more advanced printers that have more lasers reduce printing costs by reducing the time required to melt the material. These reductions in cost show diminishing returns with respect to printing speed because the print time-related costs only account for a portion of the total cost. Costs associated with machine set up, pre-heating, cooldown and part removal time and post-processing costs are not affected by the reducing in printing time. It is seen that the Gen 2 design reduces the PHE cost by 2.8 times for the baseline print speed of 959 mm/s. A further 22 percent decrease in cost, to $185/kW-th, can be obtained by using the twelve-laser machine.

Analogous results are presented in Table 6.5 which compares Gen 1 and 2 performances at constant Cr ratio (left and middle columns) and at constant outlet temperatures on the hot side (left and right columns). Although the mass flow rates differ, we conclude that the performance enhancement from Gen 1 to 2 boils down to a more efficient architecture combining a more compact HX (volume reduction by 40%) with better heat transfer design.

Table 6.5. Comparison between Gen 1 and Gen 2.

	Gen 1 EOS M290	Gen 2 EOS M290	Gen 2 EOS M290
Length (m)	0.24	0.24	0.24
Width (m)	0.12	0.12	0.12
Core height (cm)	5	5	5
S_T (mm)	2.46	2.46	2.46
S_L (mm)	2.13	2.13	2.13
D_pin_c (mm)	1.2	1.2	1.2
H_pin_c (mm)	1.8	1.8	1.8
m_dot_sCO2 (kg/s)	0.05	0.08	0.08
m_dot_MS (kg/s)	0.075	0.119	0.115
Cr	0.803	0.805	0.83
T_sCO2_out (C)	713.7	708.7	707
T_MS_out (C)	551.6	554.1	550
Effectiveness	0.84	0.95	0.94
Q (kW)	13.4	20.9	20.7
dP_sCO2 (Pa)	1275	2038	2027
dP_MS (Pa)	630	4973	4827
Power density (MW/m3)	6.8	17	16.8
Volume (m3)	2.00E-03	1.20E-03	1.20E-03

In summary, design of a compact, scalable additively manufactured (AM) primary heat exchanger for solar thermal applications was presented. The new design is compared against the Gen 1. The key design novelties include (a) a lattice structure in the MS flow, which increases the heat transfer rate on the side with the largest thermal resistance, and (b) incorporation of sCO_2 headers within the MS path. The latter results in a near-counter flow arrangement for the PHE and a design that can be scaled in two dimensions.

The structural integrity of the header-core junction was assessed and validated by conducting experiments at a pressure of 200 bar and a temperature of 730-743 ^{0}C on AM 316 stainless steel printed sub-scale specimens. A comparison between the structural simulations and the experimental results revealed that the maximum stress used as design parameter is quite conservative. A more realistic value to consider is an average surface stress localized around a stress-concentration zone.

Thermofluidic and process-based cost models were used to determine the impact of variation of geometric and flow parameters on the performance and cost of the PHE. The results show that a factor of 2.8 times reduction in cost can be achieved by the Gen 2 design, with power densities as high as 16.8 MW/m^3 (including headers) for an effectiveness of 0.94 for the HX with 1.8 mm MS channels, and an effectiveness of 0.96 with power densities of 22.7 MW/m^3 for the 1.0 mm MS channels HX.

Pathways to cost reduction by increase in print speed and industrial-scale AM machines were presented. The largest cost reduction is achieved by the design changes, followed by increase in print speed from 700 mm/s to 959 mm/s. While the presented design was for MS to sCO_2, the design can be readily adapted for solid particle medium to sCO_2 heat exchangers, with particles flowing through the lattice channels.

Chapter 7 Experimental validation of the HX model

In this section, experimental testing of a prototype heat exchanger is carried out and the results are compared against the HX model introduced in Chapter 6 for the Gen 2 PHE and based on correlations selected after heat sinks characterization in Chapter 4. The finalized model is later used to provide a design for a scaled-up 1 MW PHE. A sensitivity study is performed on this scaled-up PHE to analyze how variation in operating parameters such as mass flow rate and inlet temperatures would affect its performance.

The heat transfer and mechanical integrity experiments mentioned in this chapter were performed by Erfan Rasouli and Aref Aboud, two engineers at the Western Cooling Efficiency Center at UC Davis. The results from these experiments will be used to validate the HX model.

7.1. HE Fabrication

The Gen 2 HE was fabricated in Haynes 282, in an EOS M290 system at the Next Manufacturing Center at Carnegie Mellon University. The single-laser EOS M290 machine has square build plate of sides 25 cm which constrain the maximum dimensions of the HX that could be printed using this system. Although the PHE unit was designed to exchange heat between sCO_2 on the cold side and chloride MS as the hot flow, the testing was performed with heated air as a surrogate for MS on the hot side due to the lack of test facilities with chloride salt loops. One major benefit of the Gen 2 design is that it allows for vertical scalability of the units by stacking them one on top of the other. In order to practically demonstrate this, four PHE units, each consisting of five hot-cold pairs of plates, were AM fabricated.

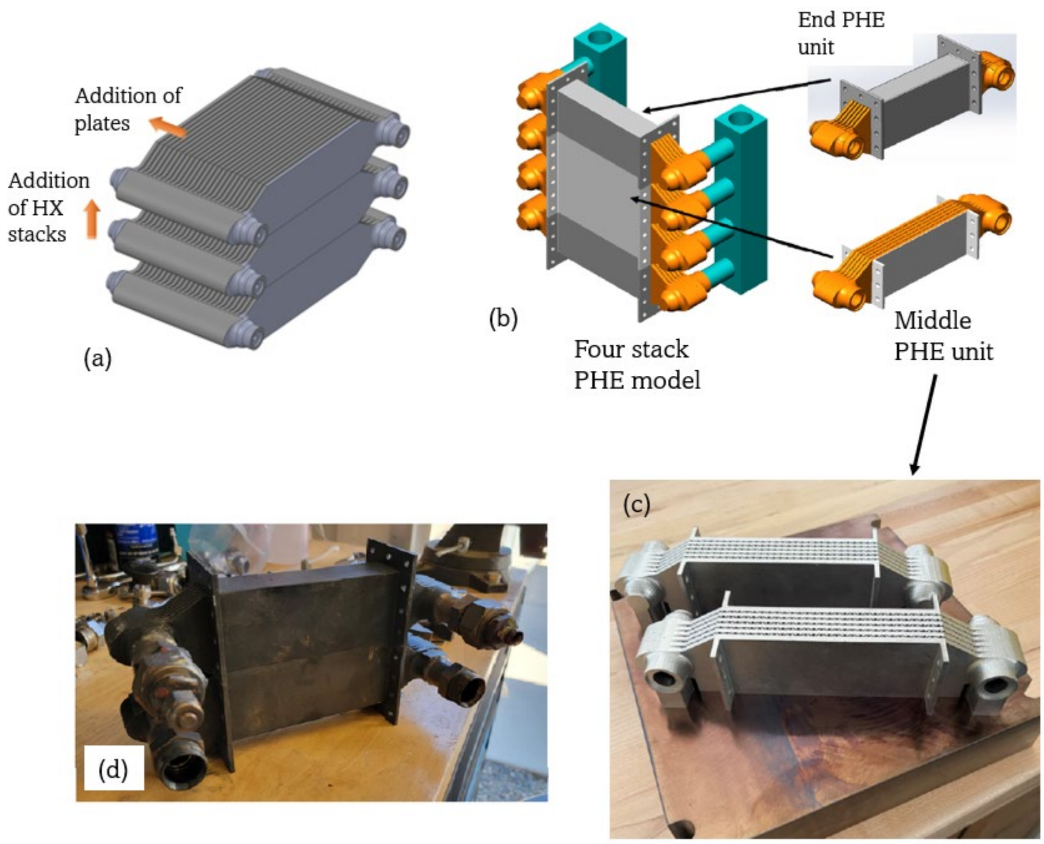

Figure 7.1. (a) Stack of 26-plate HX, (b) stack of four 5-plate HX with two middle and two end PHE units, (c) printed middle PHE units attached to the build plate, (d) stack of end PHE units after mechanical integrity test at high temperature.

The concept of scalability is illustrated in Figure 7.1(a). The model of the actual stack design for testing is illustrated in Figure 7.1(b) with a manifold bringing the CO_2 flow in and out of each HX unit of the stack. The units were similar, with the only distinction being the integrated surrounding flange. Following printing, the units shown in Figure 7.1(c) were heat treated and any support structures needed for the build were cut using wire EDM. Structural integrity testing, up to application pressure and temperature (200 bar and 720 °C), was conducted on each HE unit to ensure leak-free and structurally sound units. After completing mechanical tests, the units were ready to be stacked and welded together, incorporating appropriate side headers for the hot air stream.

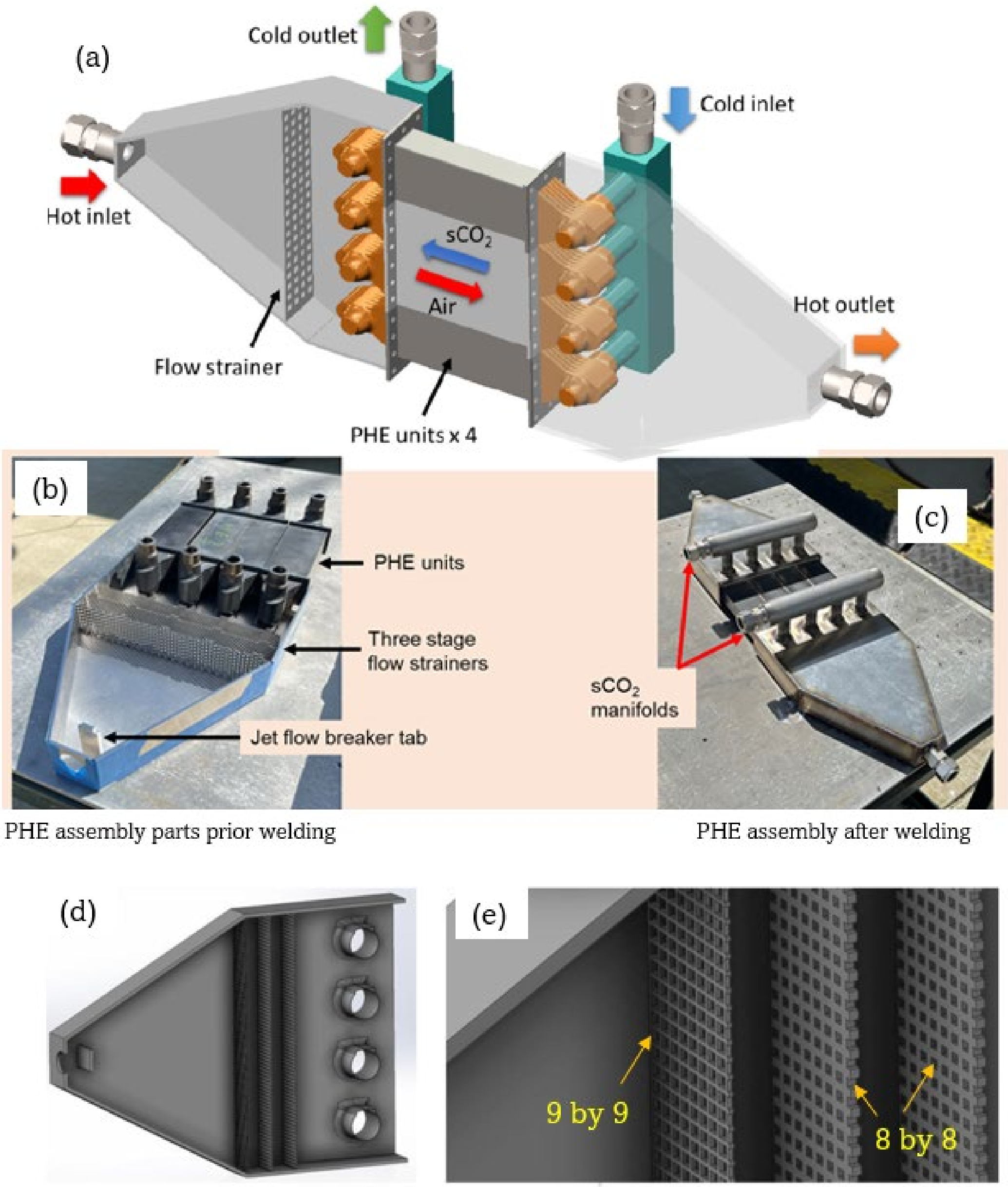

Figure 7.2. HE assembly: (a) Overview of the four-stack HE with side headers to carry the hot air stream in and out of the unit, (b) PHE assembly parts prior to welding showing the slow straighteners, (c) PHE assembly after welding the hot air headers and the sCO_2 manifolds, (d) CAD of the air header, (e) close-up view on the meshes used to straighten the flow.

The air-side headers, as depicted in Figure 7.2, were in the direction of the hot side flow. Since the inlet piping was from a smaller diameter, a diffuser section was used to expand the flow to the rectangular cross-sectional area of the PHE core. Figure 7.2(e) shows that flow straightener meshes of progressively finer size, 9 by 9 (0.079" opening size) followed by two 8 by 8 (0.062" opening size), were placed in the diffuser section to provide a uniform velocity into the core. The hot air header was designed using iterative mechanical and computational fluid dynamics (CFD) simulations to determine parameters such as wall thickness, the number of flow straighteners, and pore dimensions required for uniform flow distribution. Figure 7.3 shows the velocity vectors as well as the velocity contour at the location were the air enters the HX unit on the 3D lattice side.

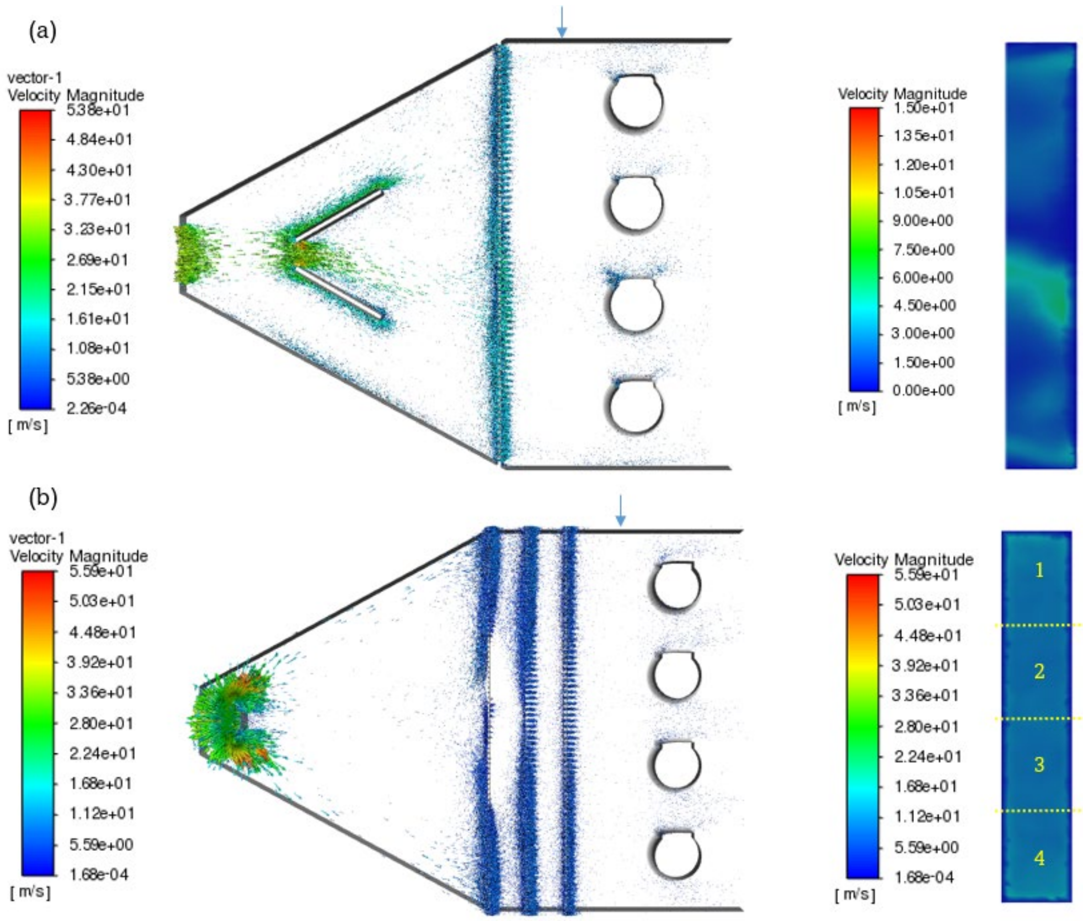

Figure 7.3. Velocity vectors and velocity contour at the HX entrance on the MS side for (a) one of the intermediate iterations, (b) the finalized design. The arrow indicates the location of the cross-section sampling.

Figure 7.3(a) shows an intermediate iteration that used diverting structures and a single mesh in an attempt to uniformly distribute the air. While Figure 7.3(a) shows some clear locations of higher velocity compared to the rest of the cross-section, Figure 7.3(b) which shows the final design using 3 meshes, exhibits a higher degree of flow uniformity along the entire height of the plenum. The plenum cross-section was divided into four quarters (as illustrated on Figure 7.3) and the velocity in each section was outputted. For comparison, the model shown in (a) has velocity magnitudes varying from 1.6 to 2.4 m/s while model (b) has velocity magnitude varying from 1.10 to 1.24 m/s. Details of velocity variations are summarized in Table 7.1.

Table 7.1. Velocity variation across the plenum height.

	Model (a)		Model (b)	
Sections	Velocity (m/s)	Percent diff (%)	Velocity (m/s)	Percent diff (%)
Quarter 1	2.22	7.12	1.24	5.99
Quarter 2	3.38	34.76	1.11	5.14
Quarter 3	1.61	38.49	1.10	5.98
Quarter 4	2.38	0.03	1.22	4.53
Plane average	2.38	-	1.17	-

The final components to be welded together are illustrated in Figure 7.2(b), where the header plates were water jet cut to size from 1/8" thick SS304. The assembled PHE, including the hot air header and sCO_2 manifolds, is presented in Figure 7.2(c), ready to be connected to the heat transfer test loop.

7.2. Experimental facility

The components of the closed loop sCO_2 test facility are detailed in Rasouli et al. [103]. Figure 7.4(a) presents a simplified line schematic of the facility in the PHE test mode configuration. Air flow was directed through the PHE in an open loop while sCO_2 was circulated in a closed loop. The test facility consisted of a liquid CO_2 pumping station, a station for preheating sCO_2 and compressed air flows, the PHE contained within a powder-filled insulation box, and finally, a three-stage heat rejection station to cool down sCO_2 and condense it before reaching the liquid CO_2 reservoir at the CO_2 pumping station. The air supply was provided by an air compressor capable of delivering a flow rate of 0.0168 m3/s (35.6 cfm) at 6.2 bar (90 psi). The tube coil assembly used as an air preheater within the preheating chamber could heat up 20 g/s of air (36 cfm) to 800 °C.

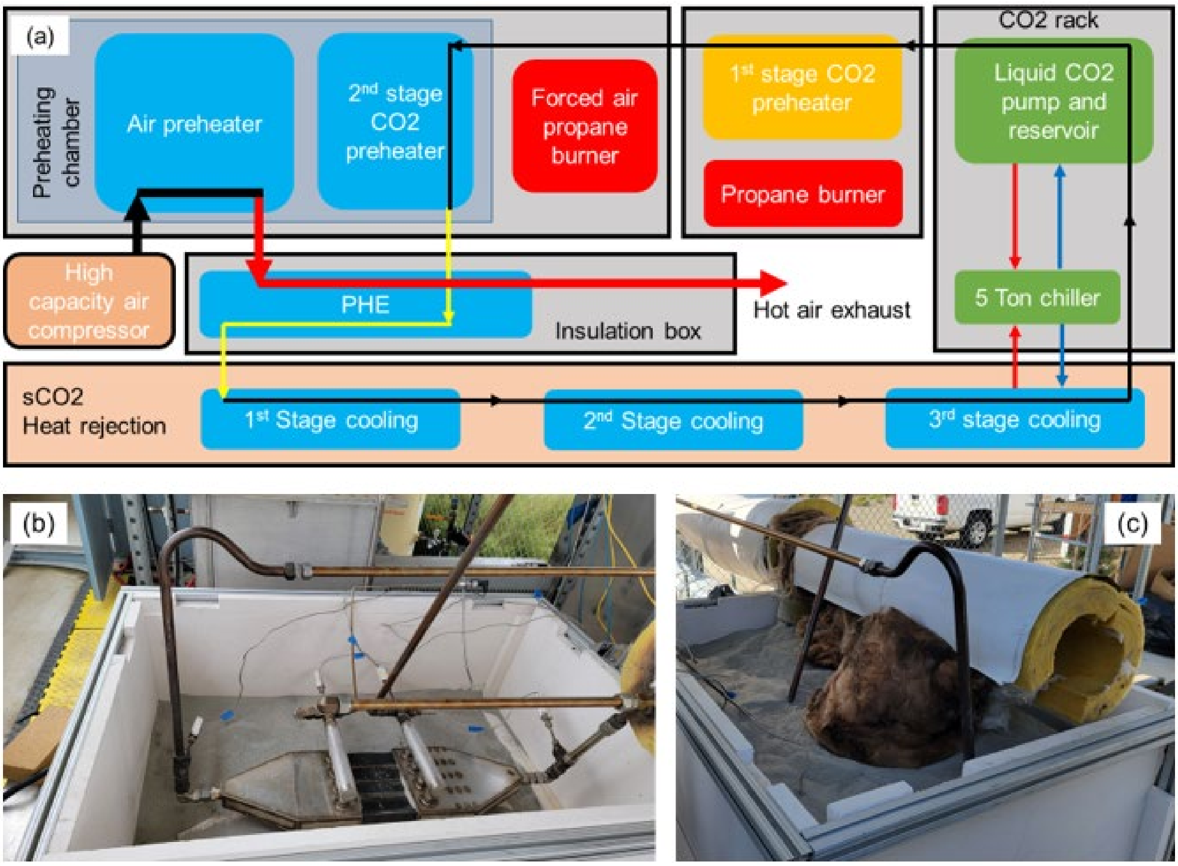

Figure 7.4 (a) Simplified schematic of the sCO_2 facility in PHE test mode, (b) PHE assembly instrumented within the insulation box, (c) insulation box filled with powder insulation and incoming tubing covered with layers of insulation.

The PHE assembly, instrumented within the insulation box, is depicted in Figure 7.4(b). Type K thermocouples were mounted at the inlet and exit of both hot and cold streams, along with absolute pressure transducers for the sCO_2, enabling the determination of sCO_2 enthalpy at the inlet and exit ports. A Coriolis flowmeter (Micromotion CMF010H) was used to measure the CO_2 mass flow rate, and a laminar flow element mass flow meter (Alicat M-1000SLPM with factory calibration) measured the air flow rate. The PHE assembly's air outlet port was plumbed such that the exhaust air stream was vented to the ambient. The insulation box containing the PHE assembly was filled with pyrogenic silica, FREEFLOW®, a pourable microporous powder rated for 1000 °C with a thermal conductivity of 0.07 W/m-K at 800 °C (Figure 7.4(c)).

7.3. Results

7.3.1. Mechanical integrity tests

The PHE units underwent testing for leak and mechanical integrity once fluidic fittings were welded at their ports. The unit was mounted into the test chamber of the pressure (P) and temperature (T) test facility, as seen in Figure 7.5(a), and connected to the pressure source line (nitrogen gas), with the other end capped off (see inset picture in Figure 7.5(a). After pressurizing the unit to the desired level, it was isolated from the source pressure line using a solenoid valve assembly. The pressure time series of one of the tested PHE units is plotted in Figure 7.5(b); as seen, the unit could withstand 200 bar pressure at ambient temperature without leaks, with a hold time at maximum pressure of approximately 30 minutes.

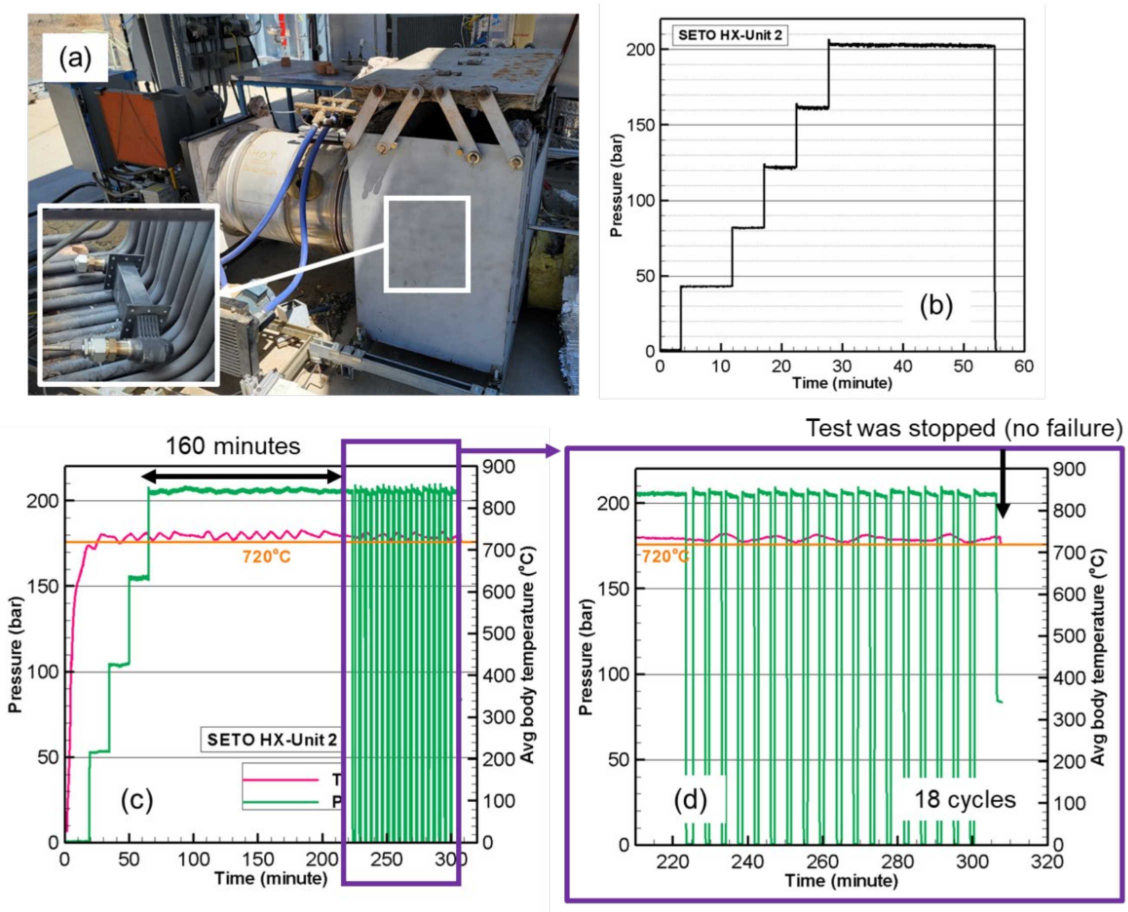

Figure 7.5. Mechanical integrity testing of the PHE units. (a) P&T test facility- inset picture shows a PHE unit mounted within the test chamber, (b) time series of unit pressure during testing of the PHE unit #2, (c) pressure and temperature time series during static and cyclic pressure testing of the PHE unit #2 at temperature ~720 °C, (d) zoomed-in P&T variation trends while cycling the P at the elevated T.

The pressure test was then repeated at elevated temperature (~720 °C). The PHE unit was instrumented with five Type K thermocouples (TC), placed into the cavities between the sCO_2 plates. The burner set temperature was adjusted so that the average of five TCs stayed above 720 °C throughout the tests. Once the average body temperature of the PHE unit exceeded 700 °C, just like the pressurization at ambient temperature tests, the PHE unit was pressurized stepwise (with 50 bar increments), and the unit was kept at max pressure for more than two hours while being isolated from the pressure source. Elevated temperature pressure tests included a few cyclic pressure tests. The number of cycles was limited due to the restricted supply of propane to the test facility and the overall duration of the P&T tests. The pressure cycle consisted of purging the line pressure to the ambient (with a 1-minute hold time) and abruptly pressurizing it back to 200 bar (with a 3-minute hold time). As seen in Figure 7.5(c,) the PHE unit #2 withstood 200 bar pressure for 160 minutes at T > 720 °C and was leak-free after 18 cycles of pressure. Similar tests were repeated for the other three PHE units.

7.3.2. Pressure drop tests

The pressure drop measured on the pin array side was compared against the model results. Results of friction factor as a function of Reynolds number based on minimum hydraulic diameter through the pin array, D_{Amin}, is shown in Figure 7.6. The Reynolds numbers for the heat transfer tests ranged from 680 – 2500. Two replications of pressure drop measurements were performed, yielding very similar results. The Prasher et al. [75] and Rasouli et al. [76] used in the model predicts the trends of the experimental pressure drop trend well beyond a Re of about 400. Above a Re of 400, the Prasher et al. [75] correlation underpredicts the measured pressure drop with a MAPE of 43.3% while the Rasouli et al. [76] correlation over-predicts the data by a MAPE of 52.6%. It should be noted that the measurement location of the pressure drop in the HE experiment was outside the HE, while the measured pressure drop in the heat sinks in Chapter 4 was across the pin array. Hence, additional pressure losses through the sCO_2 plenum and entrance and exit pathways is included in the HE testing, which would contribute to the increased MAPE relative to the Prasher et al. [75] correlation.

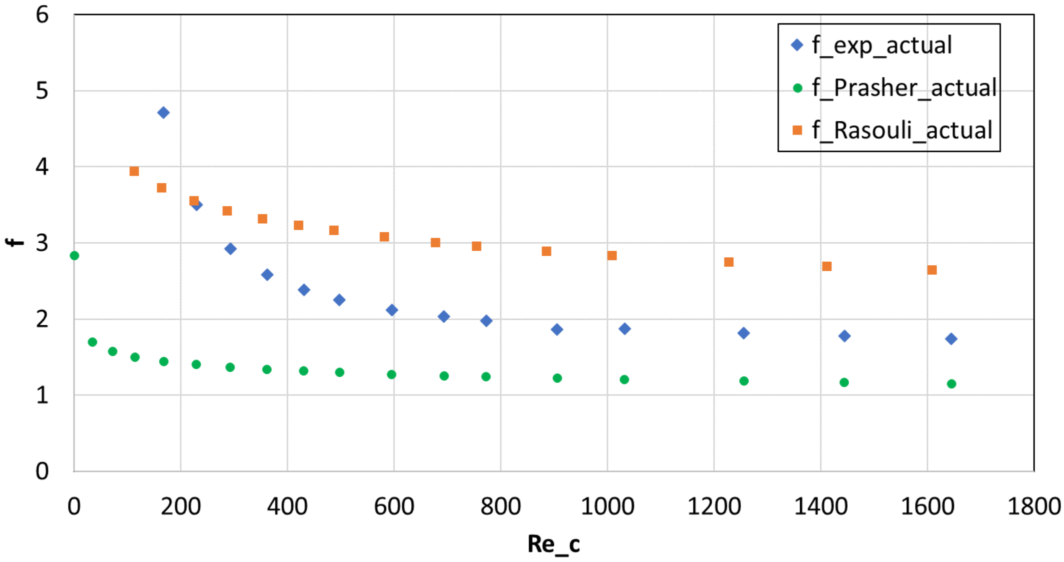

Figure 7.6. Comparison of experimental and correlation non-dimensional pressure drop in the pin array (cold side) as a function of non-dimensional flow rate.

For the molten salt side, the experimental friction factor obtained from experimental testing of the heat exchanger is shown in Figure 7.7 along with results from CFD simulations of the molten salt side. The Reynolds numbers for the heat transfer tests on the hot side ranged from 270 to 530. The CFD result significantly underestimates the actual fluidic performance of the heat exchanger. As seen in Figure 7.7, at a Reynolds number of approximately 320, the experimental friction factor has a value of 25 while the CFD results show a value of 9. In terms of trend however, at Reynolds number values of 100 and above, there is an agreement in terms of the shape of the friction factor curves. There are additional pressure losses due to expansion, contraction, and flow straighteners in the experiments that is not captured by the CFD simulations of the MS side of the HE, and could account for some of the observed difference.

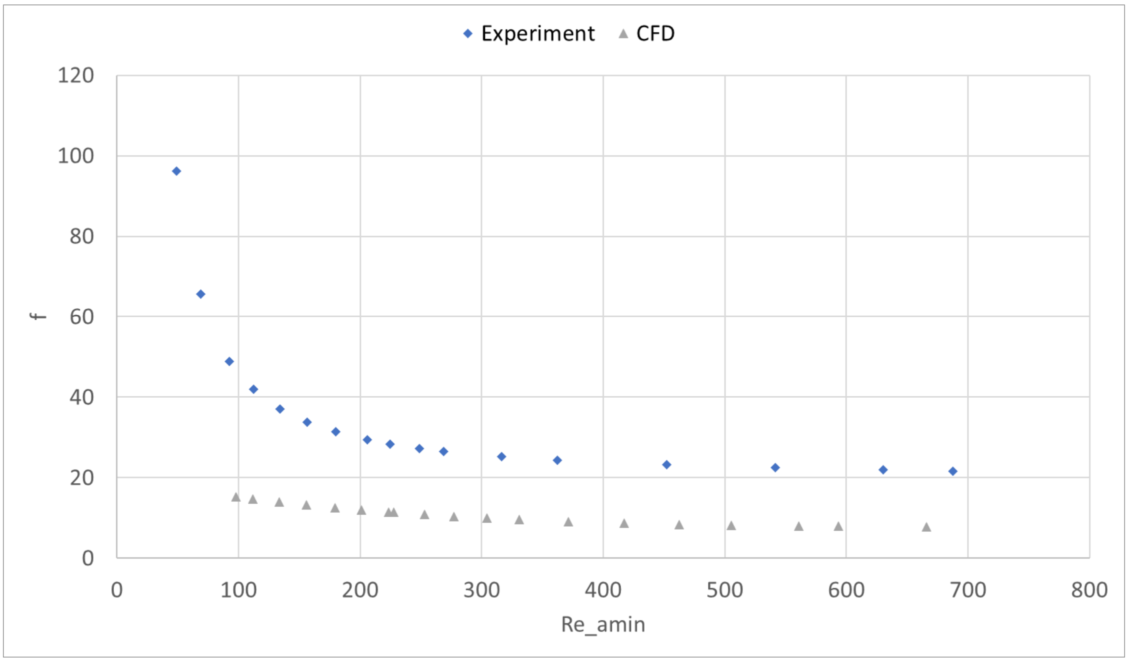

Figure 7.7. Comparison of the friction factor variation with Reynolds number in the experiment and CFD for the hot side of the exchanger.

7.3.3. Heat transfer experiments

The PHE assembly was integrated into the sCO_2 test loop and underwent three days of heat transfer testing. Experiments were conducted by maintaining a constant flow rate for one stream while varying the flow rate of the other stream. The design target for inlet temperature and pressure, as well as the conditions achieved during the testing campaign, are shown in Table 7.2. The tested conditions covered the targeted sCO_2 inlet temperature and pressure. The highest hot air inlet temperature reached was 706 °C, which was close to the design temperature for the chloride MS of 720 °C. As illustrated in Figure 7.4, the air and 2nd stage CO_2 preheater coils are within one heating chamber, and the heated fluids were carried in tubing that were bundled together and covered in layers of insulation (see Figure 7.4(c)); thus, changing the mass flow rate in one stream would impact the inlet temperature of both streams, as the incoming tubing outer walls were in touch with each other and heat exchange between two fluids was possible.

Table 7.2. PHE test conditions

Metric	sCO_2	Air (surrogate fluid for MS)
Inlet temperature, T_{in} (°C) (target value)	225 - 620 (500)*	545 - 706 (720)
Line pressure, P (bar) (target value)	84 - 208 (200)	3 - 4.8
Mass flow rate, $\dot{m}$ (g/s)	12 - 40.2	13.4 - 20.8

*target conditions for application are noted in parentheses

Representative uncertainties in measured and derived quantities are provided in Table 7.3. Uncertainty in temperatures and mass flow rates are based on manufacturer specified bias errors as well as variations in process conditions at steady state. Uncertainties in derived quantities are obtained using a propagation of errors method [80].

Table 7.3. Uncertainties in measured and derived quantities in HE experiments

Measured or derived quantity	Range of measured values	Average uncertainty (%), Maximum uncertainty (%)
$T_{SCO2\ in}$ (°C)	225 - 620	1.85 (0.44%), 3.29 (1.0%)
$T_{SCO2\ out}$ (°C)	400 - 686	2.34 (0.41%), 3.12 (0.68%)
$T_{air\ in}$ (°C)	530 - 706	2.65 (0.4%), 3.01 (0.57%)
$T_{air\ out}$ (°C)	230 - 652	1.8 (0.42%), 2.61 (0.78%)
m_{sCO2} (g/s)	6 – 40	0.12 (0.56%), 0.22 (0.56%)
m_{air} (g/s)	12 - 19	0.19 (1.0%), 0.24 (1.2%)
q_{sCO2} (W)	1300 - 8500	78.84 (2.44%), 148.9 (1.76%)
q_{air} (W)	1700 - 8400	81.1 (2.54%), 106.1 (1.26%)
ε	0 - 1	0.023 (2.5%), 0.024 (3.13%)

Since both streams were instrumented, the HE thermal load could be calculated using either air or sCO_2 side measurement. The parity plot between Q_{co2} and Q_{air} is shown in Figure 7.8. It is seen that a heat rate greater than 8 kW was achieved for the highest tested sCO_2 mass flow rate (40.2 g/s). As seen from the trend, a higher imbalance between the hot and cold stream heat rates was observed for low values, which corresponded to low mass flow rates. The imbalance percentile increases up to 18% for the lower q values that corresponds to lower flow rates. For the range of tested mass flow rates, based on the q_{sCO2}, the PHE assembly could demonstrate core volumetric and gravimetric power densities (resulting from heat exchange between sCO_2 and air, excluding the hot air headers and CO_2 manifolds) of 2.4 – 7.1 MW/m^3 and 0.52 – 0.94 kW/kg, respectively. Using sCO_2 and MS flow rates of 80 and 115 g/s would yield volumetric and gravimetric power densities of 16.7 MW/m^3 and 4.3 kW/kg, respectively.

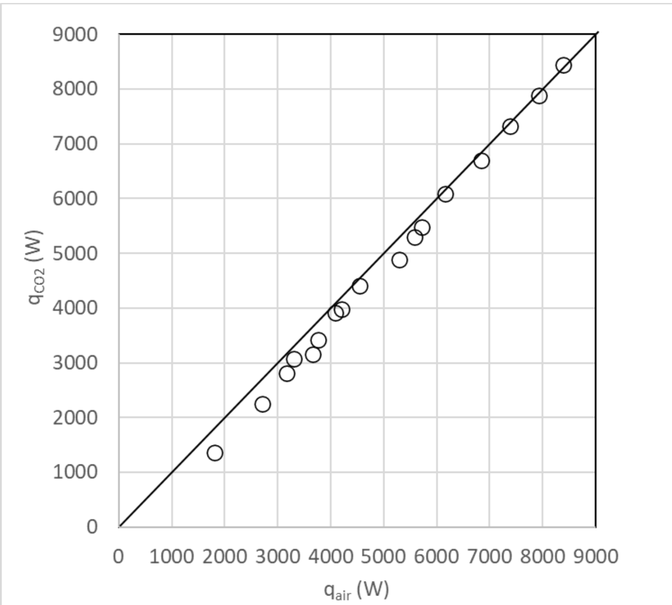

Figure 7.8. Parity between heat rate on hot and cold sides

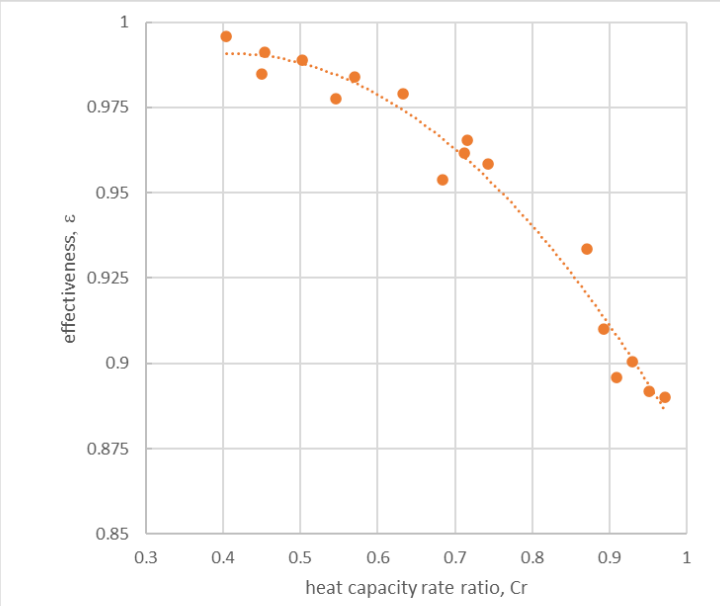

Figure 7.9. Variation of PHE assembly effectiveness against the heat capacity rate ratio, C_r

In Figure 7.9, the variation of PHE effectiveness is plotted against the heat capacity rate ratio, C_r. The C_r is defined as the ratio of the minimum heat capacity rate stream to the maximum heat capacity rate stream in the heat exchanger. The observed trend indicates an increasing effectiveness with decreasing C_r, aligning with anticipated trends in heat exchanger performance. In a heat exchanger, the maximum and minimum effectiveness values are theoretically associated with C_r values of ~0 and 1, respectively. Lower C_r values can be achieved by increasing the flow rate of either the hot or the cold stream.

7.4. Model validation with experimental results

The experimental conditions of mass flow rate of air and sCO_2, system pressure, and inlet temperatures of the fluid streams were provided as inputs to the sectional correlation-based model. Table 7.4 shows the dimensions of the pin array that were taken from the CT scan of sample specimens of the same design dimensions as the HE.

Table 7.4. Design and printed dimensions of the pin.

	Design	Actual
D_{pin} (mm)	1.2	1.35
W_C (mm)	1.8	1.65
S_T (mm)	2.46	2.45
S_L (mm)	2.13	2.12

The parity plots of predicted heat transfer rate, air exit temperature, and sCO_2 exit temperature against experimental results are shown in Figure 7.10(a), Figure 7.10(b) and Figure 7.10(c) respectively. As seen from the trends, the model can provide an excellent prediction of the experimental results. The average difference between the predicted and experimentally determined values of heat transfer rate, and hot side and cold side exit temperatures are respectively 0.8%, 1.5%, and 0.97%, respectively. The larger differences are observed at lower flow rates, and heat transfer rates, where the experimental heat losses tend to be a higher fraction of the heat transfer rate.

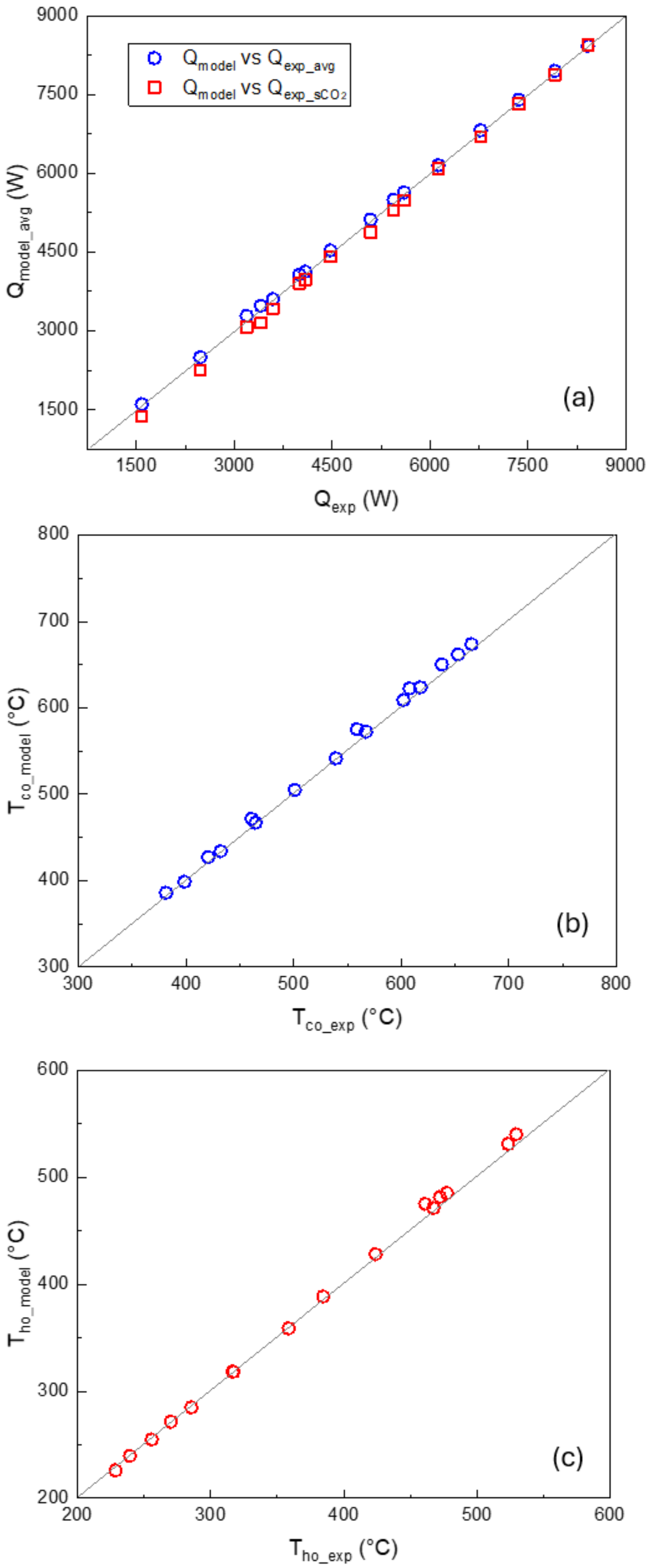

Figure 7.10. Parity plots between correlation-based model and experimental results of (a) heat transfer rate, (b) sCO_2 outlet temperature, and (c) air outlet temperature

7.5. Scaling to 1 MW PHE using validated model

In this section, the validated Gen 2 HE model was used to predict the size and performance of a larger scale MS-sCO_2 PHE. The geometry of the core is the same as the one experimentally validated in the prior section (baseline values in Table 7.5). To increase the capacity of the HE, the number of pairs of hot and cold arrays is scaled in the depth and height. The mass flow rate per unit arrays (stack of 24 cm by 24 cm by 20 cm) of the core on the MS and sCO_2 sides were selected based on the modeling results presented in Chapter 6 and are summarized in Table 7.5.

Table 7.5. Summary of the thermofluidic conditions for the baseline HE of 167.5 kW rating.

	m_{sCO2} per array (g/s)	m_{MS} per array (g/s)	Heat capacity rate ratio C_r	$T_{MS, in}$ (°C)	$T_{sCO2, in}$ (°C)
Baseline	640	960	0.8 (C_{min} on cold side)	720	500
Range	560-720	800-1040		670-770	450-550

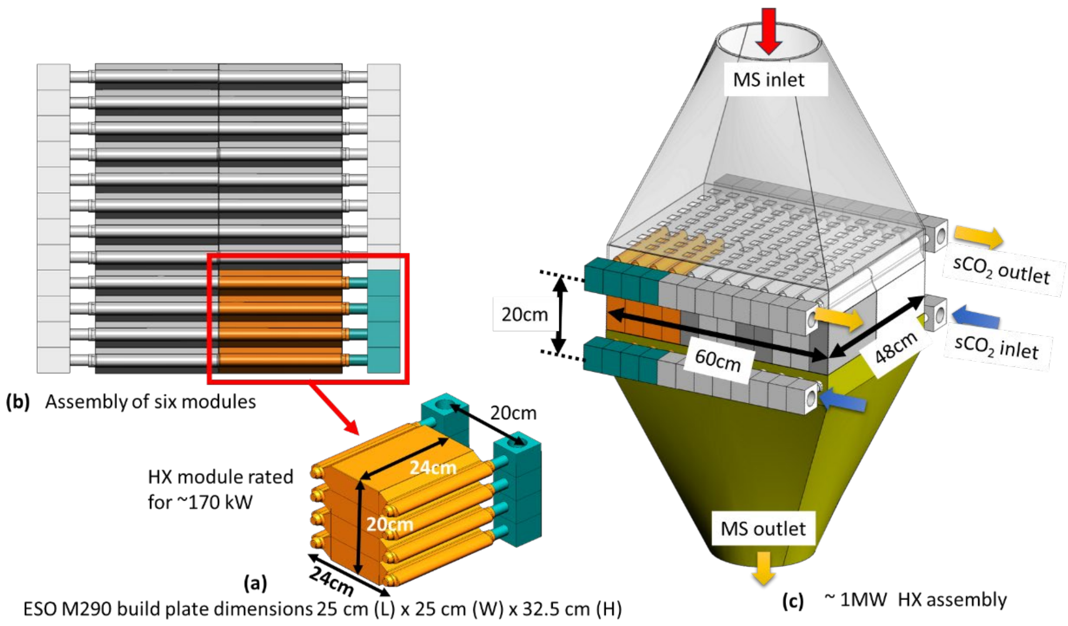

Figure 7.11. Schematic of a multi-module 1 MW HE (a) dimension of the HE module that can be built in a EOS M290 machine, (b) cross-sectional view of a 6 module HE, and (c) isometric view of the multi-module HE.

As part of another project, Carnegie Mellon University demonstrated that builds as tall as 25 cm can be built without any impact on porosity and distortion. Hence, it is reasonable to assume that a stack of 4 Gen 2 HEs can be built vertically totaling 20 cm in height. If the entire width of the build plate is filled with hot and cold pairs in the core, a HE with a build volume of 24 cm (L) x 24 cm (W) and 20 cm (H) can be printed in an EOS M290 single laser machine (Figure 7.11(a)). At the baseline conditions, the capacity of this HE would be 167.5 kW. With six such builds a 1 MW HE can be assembled. Figure 7.11(b) shows the cross-sectional view of the multi-module assembly and Figure 7.11(c) shows the HE with a MS header. The 48 cm wide, 60 cm tall and 20 cm wide HE core with integrated sCO_2 headers would have a capacity of ~ 1MW.

The impact of variations in system operating temperatures from the baseline shown in Table 7.5 were analyzed next for fixed mass flow rates on the MS and sCO_2 sides. It was assumed that with variations in solar insolation, the inlet temperature to the HE could vary by the hour and day of the year. Similarly, the impact of variation in sCO_2 and MS inlet temperature and flow rates to the HE was analyzed. Table 7.5 shows the range of variation of m_{dot_sCO2}, m_{dot_MS}, $T_{MS,in}$ and $T_{sCO2,in}$ in the study.

Contour maps of HE performance with variations in MS (hot) and sCO_2 (cold) inlet temperatures are shown in Figure 7.12 and variations with MS and sCO_2 flow rates are shown in Figure 7.13. Contours of the hot outlet temperature, cold outlet temperature, thermal rating of the HE, and effectiveness of the HE are shown in Figure 7.12(a-d), respectively. The HE rating is given for 1 module as shown in Figure 7.12(a). The anticipated performance of the HE can be determined using these maps. For example, at the baseline T_{hi} of 720 °C and T_{ci} of 500 °C, the T_{ho}, T_{co}, Q and ε are 555.2 °C, 709.1 °C, 167.5 kW and 0.948, respectively. If the MS inlet temperature decreases to 670 °C, the T_{co} would drop to 662 °C and the thermal rating would decrease by 22.8% to 129.3 kW. On the contrary, an increase in MS inlet temperature from 720 °C to 770 °C would cause an increase in T_{co} to 756 °C, and Q increase by 32.7% percent to 222.4 kW. The contours also illustrate tradeoffs to arrive at an operating condition for the HE. A high effectiveness can be obtained with increased T_{hi} and T_{ci} (top right side of the plots); however the MS outlet temperature would also increase, thereby decreasing thermal capacity rating.

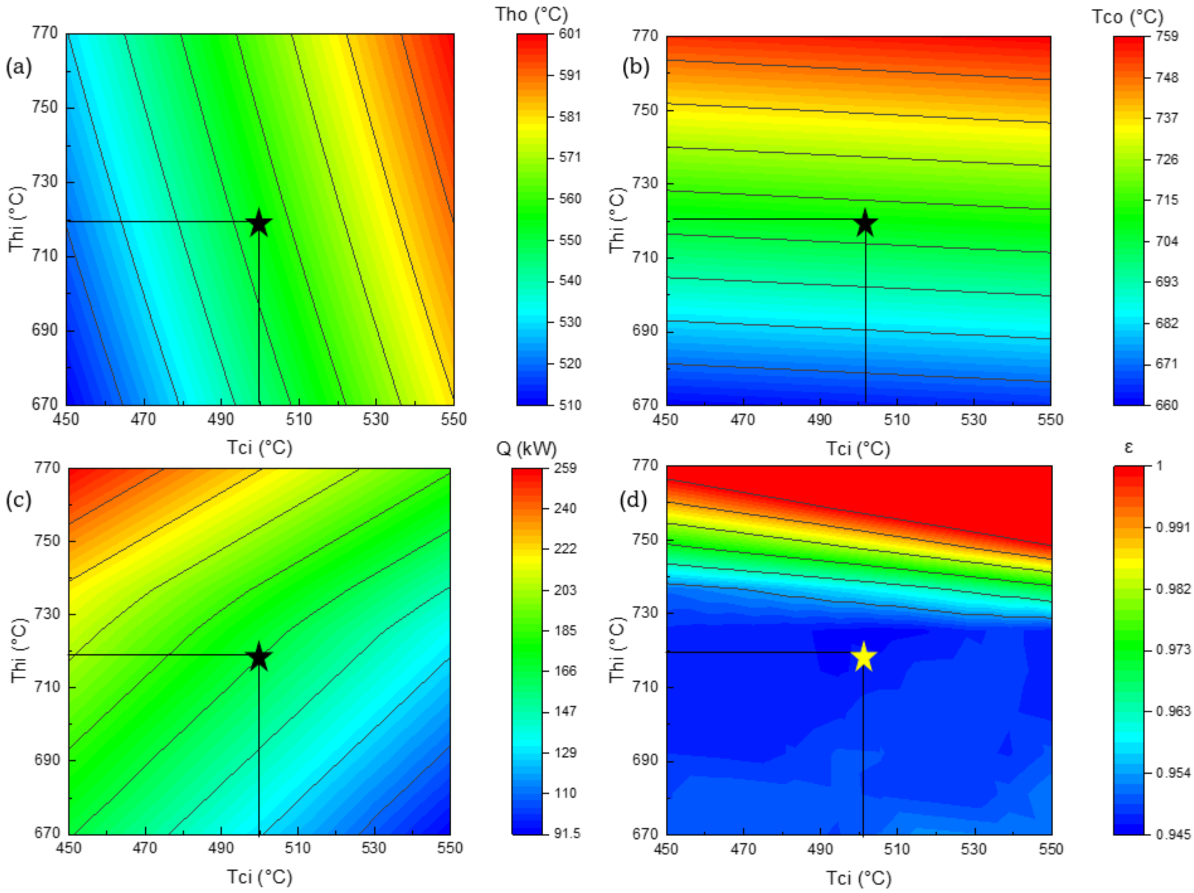

Figure 7.12. Impact of variation in operating conditions (inlet temperatures) on the HE performance: (a) MS exit temperature, (b) sCO_2 exit temperature, (c) thermal rating (kW), and (d) effectiveness.

From Figure 7.13(c) we can see that increasing the sCO_2 flow rate is more influential in achieving a higher thermal rating than increasing the MS flow rate. For instance, increasing the sCO_2 flow rate from 0.6 to 0.7 kg/s at a MS flow rate maintained constant at 1.04 kg/s causes a Q increase from 159.8 kW to 182.1 kW, which is a 14% increase compared to a 2% increase from 156.7 to 159.9 kW for MS flow rates increasing from 0.9 to 1.04 kg/s at sCO_2 flow rate of 0.6 kg/s. This trend is also observed on the other thermal performance indicators, a smaller temperature change of 4 degrees is observed from changing the MS flow rate by about 0.1 kg/s from 0.9 kg/s (T_{co} of 710.4 °C) to 1.04 kg/s (T_{co} of 714.8 °C) than from altering the sCO_2 value from 0.6 kg/s (T_{co} of 714.8 °C) to 0.7 kg/s (T_{co} of 707.7 °C).

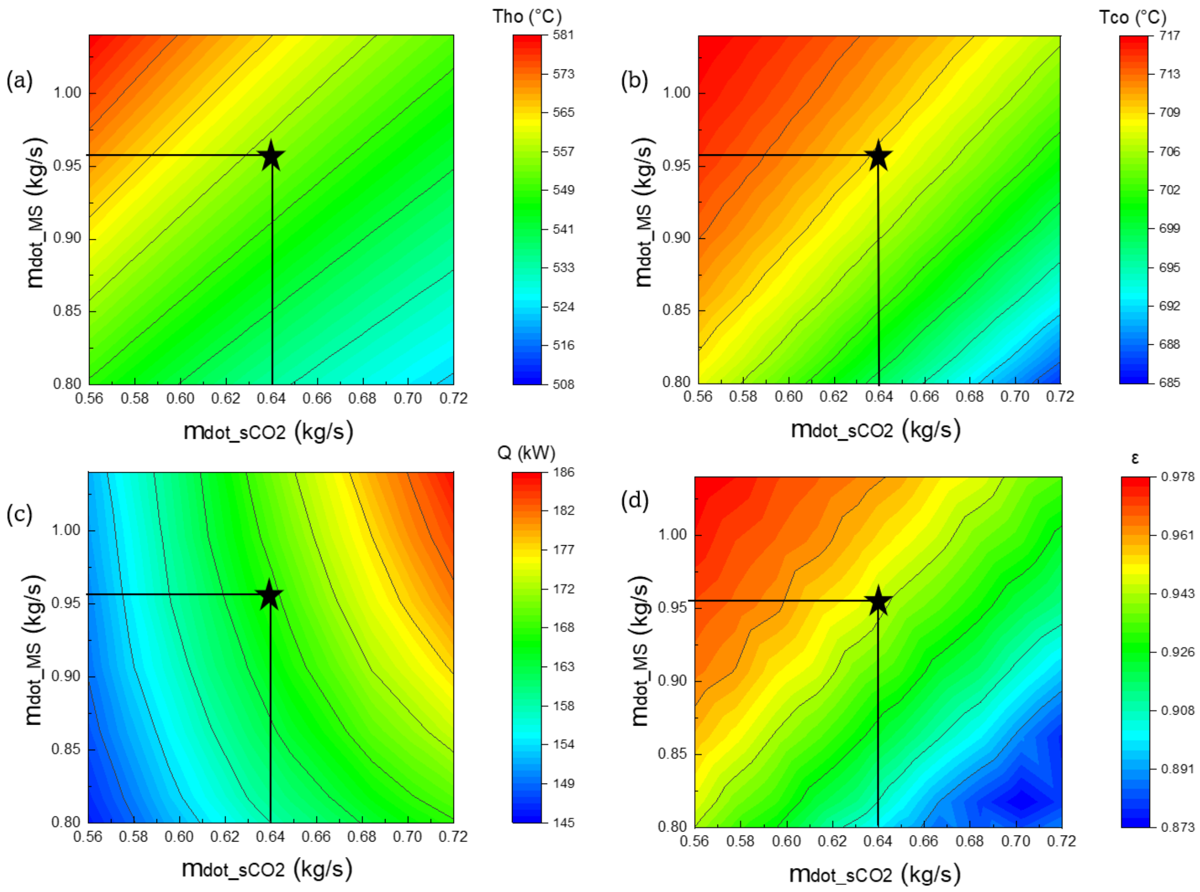

Figure 7.13. Impact of variation in operating conditions (CO_2 and MS flow rates) on the HE performance: (a) MS exit temperature, (b) sCO_2 exit temperature, (c) thermal rating (kW), and (d) effectiveness.

In summary, a scaled-up design of the HE is presented in this section. The validated HE model is used to predict the performance of the HE with variations in operating temperatures that would be anticipated in the system. Similar maps can be developed for variations in mass flow rate of the hot and cold streams. Together, the results will aid in development of controls schemes and an operational window in which the component level performance can be optimized relative to the system level variations.

Chapter 8 Conclusions and Recommendations for Future Work

A scalable heat exchanger for the liquid pathway of a molten chloride salt (MS)-to-supercritical carbon dioxide (sCO_2) has been demonstrated. Fabrication was performed using the laser powder bed fusion (LPBF) additive manufacturing (AM). Two Nickel-based superalloys were considered - Haynes 230 (H230) and Haynes 282 (H282). Process windows for LPBF AM were established to provide a dense, low porosity part for both alloys.

Two designs (generation 1 and 2) of the heat exchanger were developed by co-design effort considering mechanical stresses, thermal and fluidic performance, and AM fabrication constraints such as overhangs, powder removal, and build dimensions. The designs consist of a pin array on the sCO_2 side and either straight or 3D periodic lattice on the MS side of the core. Additional design considerations included creep, fatigue, and thermal stresses. The second-generation design resulted in a higher effectiveness, more compact, and lower cost HE with a volumetric power density of 16.8 MW/m^3, including the sCO_2 header volume, for an effectiveness greater than 94% at a heat capacity rate ratio of 0.8.

One of the key issues with LPBF is the roughness of the surfaces that can result in excessive pressure drop. To reduce pressure drop, a novel iodine-based chemical treatment was applied [68]. The iodine-based is a Self-Terminating Etching Process (STEP) to uniformly remove material from all fluid-accessible surfaces while preserving the intricate geometrical features. Scanning electron microscope images show removal of the powder particles attached to the pins and walls after one cycle of the chemical treatment. Detailed CFD simulations of fluid flow was performed by importing the CT scan images of the baseline, and STEP-treated pin array samples into the fluid solver. These simulations confirmed that the pressure drop predicted was within 15% percent of the measured pressure drop. Pressure drop reductions of up to 21% were measured between the baseline and chemically treated pin array. While the reductions in pressure drop were significant, the treatment could not significantly smoothen the rough down-skin surface of the pins that are oriented horizontal to the print direction- the cause for much of the pressure losses.

A simplified thermo-fluidic model was developed for design and analysis of the HE performance. The sectional model was based on correlations developed for pin arrays in open literature. To determine whether these correlations would reasonably predict flow and heat transfer in printed pin arrays, heat sinks with varied pin array geometries were fabricated and characterized. The measured pressure drop in AM pin arrays was found to be significantly higher than that predicted by correlations in literature or by computational fluid dynamics simulations when using the design geometry. Detailed X-ray computed tomography reconstruction of the printed pin array revealed that the down-skin of the pins increased the frontal area of the pins to the flow. With account for this flow frontal area, it is possible to get reasonable predictions for heat transfer using the Rasouli et al. [76] correlation for the designs experimentally characterized in this study. The Prasher et al. [75] correlation provided the best fit to experimental pressure drop data.

To experimentally demonstrate the performance of the HE, four second-generation HE cores, each with 5 pairs of hot and cold channels were printed. The cores were assembled to form a 20 pair HE and characterized for heat transfer. Heated air was used as a surrogate to the chloride salt on the hot side and sCO_2 in the 100-200 bar range was used on the cold side. Heat transfer rates varied between 3.0 and 8.4 kW for air-sCO_2 (20 kW at the baseline considered for the MS-sCO_2 case). The results of exit temperatures and heat transfer rate were compared against the model. The model was able to predict experimental results to within 1.00% percent for heat transfer rate, 1.26% percent for exit sCO_2 temperature and 1.01% percent for exit air temperature.

The validated HE model was used to determine the performance of a scaled-up design. With a 20 cm tall build that covers 24 cm x 24 cm of the build plate, a 167.5 kW HE can be built in a single laser machine with a bed size of 25 cm x 25 cm. The impact of system-level variations in inlet temperature and flow rates on the performance of this HE was established.

In summary, it has been demonstrated throughout this work that it is feasible to design and fabricate, using metal AM, compact primary HEs that meet the performance targets at the stringent operating conditions encountered in the liquid pathway for Gen3 CSP power plants. The validated model can be used to design MS-sCO_2 HEs as well as analyze its steady-state performance. It can further be incorporated into a system model to determine the tradeoffs between cycle efficiency, and HE size and cost. Overall, the viability of AM heat exchangers for high temperature CSP devices was established and its benefits highlighted.

To further this work, a full-scale 167.5 kW HE could be built, and its dimensional tolerance, structural integrity, and performance characterized. There is also potential to apply this design for particle-to-sCO_2 HEs.

In addition, Haynes 282 heat sink units should be printed and experimentally characterized in order to improve the confidence level in the comparison between experimental and available correlations in the literature. Indeed, the heat sinks used in this study were fabricated with Haynes 230 which turned out to yield parts that could deviate significantly from the design, whereas Haynes 282, which is the alloy used for the full scale HE built displays a much better dimensional fidelity to the design and would impose less variability on the printed array.

Finally studying how the thermofluidic performance and mechanical integrity would vary over time under the effect of corrosion would be useful in characterizing more comprehensively the useful life of this heat exchanger.

References

[1] Mehos, M., Turchi, C., Vidal, J., Wagner, M., Ma, Z., Ho, C., Kolb, W., Andraka, C., & Kruizenga, A. (2017). Concentrating Solar Power Gen 3 Demonstration Roadmap (Technical Report No. NREL/TP-5500-67464).

[2] Achkari, O., & El Fadar, A. (2020). Latest Developments on TES and CSP Technologies—Energy and Environmental Issues, Applications and Research Trends. Applied Thermal Engineering, 167.

[3] Smith, R., Inomata, H., & Peters, C. (2013). Introduction to Supercritical Fluids: A Spreadsheet-Based Approach. Elsevier.

[4] Feher, E. (1968). The Supercritical Thermodynamic Power Cycle. Energy Conversion, 8, 85-90.

[5] White, M. (2021). Review of supercritical CO2 technologies and systems for power generation. Applied Thermal Engineering.

[6] Pandey, V., Kumar, P., & Dutta, P. (2020). Thermo-hydraulic analysis of compact heat exchanger for a simple recuperated sCO2 Brayton cycle. Renewable and Sustainable Energy Reviews, 134.

[7] Zhang, H., Guo, J., Huai, X., Cheng, K., & Cui, X. (2019). Studies on the thermal-hydraulic performance of zigzag channel with supercritical pressure CO2. The Journal of Supercritical Fluids, 148.

[8] Saeed, M., & Kim, M.-H. (2019). Thermal-hydraulic analysis of sinusoidal fin-based printed circuit heat exchangers for supercritical CO2 Brayton cycle. Energy Conversion and Management, 193, 124-139.

[9] Jing, Q., Xie, Y., & Zhang, D. (2020). Thermal hydraulic performance of printed circuit heat exchanger with various channel configurations and arc ribs for SCO2 Brayton cycle. International Journal of Heat and Mass Transfer, 150.

[10] Wang, W.-Q., Qiu, Y., He, Y.-L., & Shi, H.-Y. (2019). Experimental study on the heat transfer performance of a molten-salt printed circuit heat exchanger with airfoil fins for concentrating solar power. International Journal of Heat and Mass Transfer, 135, 837-846.

[11] Khalesi, J., & Sarunac, N. (2019). Numerical analysis of flow and conjugate heat transfer for supercritical CO2 and liquid sodium in square microchannels. International Journal of Heat and Mass Transfer, 132, 1187-1199.

[12] Shi, H.-Y., Li, M.-J., Wang, W.-Q., Qiu, Y., & Tao, W.-Q. (2020). Heat transfer and friction of molten salt and supercritical CO2 flowing in an airfoil channel of a printed circuit heat exchanger. International Journal of Heat and Mass Transfer, 150.

[13] Chu, W.-X., Bennett, K., Cheng, J., Chen, Y.-T., & Wang, Q.-W. (2020). Thermo-Hydraulic Performance of Printed Circuit Heat Exchanger With Different Cambered Airfoil Fins. Heat Transfer Engineering, 41.

[14] Katz, A., Aakre, S., Anderson, M., & Ranjan, D. (2021). Experimental investigation of pressure drop and heat transfer in high temperature supercritical CO2 and helium in a printed-circuit heat exchanger. International Journal of Heat and Mass Transfer, 171.

[15] Wang, W.-Q., Qiu, Y., He, Y.-L., & Shi, H.-Y. (2019). Experimental study on the heat transfer performance of a molten-salt printed circuit heat exchanger with airfoil fins for concentrating solar power. International Journal of Heat and Mass Transfer, 135, 837-846.

[16] Kruizenga, A., Li, H., Anderson, M., & Corradini, M. (2012). Supercritical Carbon Dioxide Heat Transfer in Horizontal Semicircular Channels. ASME Journal of Heat Transfer, 134(18).

[17] Ren, Z., Zhao, C.-R., Jiang, P.-X., & Bo, H.-L. (2019). Investigation on local convection heat transfer of supercritical CO2 during cooling in horizontal semicircular channels of printed circuit heat exchanger. Applied Thermal Engineering, 157.

[18] Jin, F., Yuan, D., Chen, D., Hu, L., Huang, Y., & Bu, S. (2023). Experimental study on cooling heat transfer performance of supercritical CO2 in zigzag printed circuit heat exchanger. International Journal of Heat and Mass Transfer, 215.

[19] Safari, Y., Abdollahi, S. A., Mahmoudi, M., Safaei, M., Taghinia, F., Pasha, P., & Ganji, D. D. (2023). Numerical study of heat transfer of wavy channel supercritical CO2 PCHE with various channel geometries. International Journal of Thermofluids, 18.

[20] Su, X.-K., Li, X.-W., Chen, Q.-J., Shi, Q.-W., Qiu, J., & Gu, L. (2023). Numerical study on conjugate heat transfer characteristics of liquid lead-bismuth eutectic and supercritical carbon dioxide in a PCHE straight channel.

[21] Liu, S.-h., Huang, Y.-p., Wang, J.-f., Liu, R.-l., & Zang, J.-g. (2020). Experimental study of thermal-hydraulic performance of a printed circuit heat exchanger with straight channels. International Journal of Heat and Mass Transfer, 160.

[22] Cheng, K., Zhou, J., Zhang, H., Huai, X., & Guo, J. (2020). Experimental investigation of thermal-hydraulic characteristics of a printed circuit heat exchanger used as a pre-cooler for the supercritical CO2 Brayton cycle. Applied Thermal Engineering, 171.

[23] Chai, L., & Tassou, S. A. (2019). Numerical study of the thermohydraulic performance of printed circuit heat exchangers for supercritical CO2 Brayton cycle applications. Energy Procedia, 161, 480-488.

[24] Chu, W.-x., Li, X.-h., Ma, T., Chen, Y.-t., & Wang, Q.-w. (2017). Experimental investigation on SCO2-water heat transfer characteristics in a printed circuit heat exchanger with straight channels.

[25] Han, Z., Guo, J., Chen, J., & Huai, X. (2023). Experimental and numerical investigations on thermal-hydraulic characteristics of supercritical CO2 flows in printed circuit heat exchangers. International Journal of Thermal Sciences, 194.

[26] Jin, F., Chen, D., Hu, L., Huang, Y., & Bu, S. (2022). Optimization of zigzag parameters in printed circuit heat exchanger for supercritical CO2 Brayton cycle based on multi-objective genetic algorithm. Energy Conversion and Management, 270.

[27] Liu, S., Gao, C., Liu, M., Chen, Y., Tang, J., Huang, Y., ... Xing, T. (2023). An improved zigzag-type printed circuit heat exchanger for supercritical CO2 Brayton cycles. Annals of Nuclear Energy, 183.

[28] Wang, J., Yan, X.-p., Boersma, B. J., Lu, M.-j., & Liu, X. (2023). Numerical investigation on the Thermal-hydraulic performance of the modified channel supercritical CO2 printed circuit heat exchanger. Applied Thermal Engineering, 221.

[29] Han, Z., Guo, J., Zhang, H., Chen, J., Huai, X., & Cui, X. (2021). Experimental and numerical studies on novel airfoil fins heat exchanger in flue gas heat recovery system. Applied Thermal Engineering, 192.

[30] Wu, J., & Xiao, J. (2023). Numerical study of crossed airfoil fins in a printed circuit heat exchanger. Applied Thermal Engineering, 230(Part A).

[31] Han, Z., Guo, J., Liao, H., Zhang, Z., & Huai, X. (2022). Numerical investigation on the thermal-hydraulic performance of supercritical CO2 in a modified airfoil fins heat exchanger. The Journal of Supercritical Fluids, 187.

[32] Zhang, H., Guo, J., Cui, X., Zhou, J., Huai, X., Zhang, H., Cheng, K., & Han, Z. (2021). Experimental and numerical investigations of thermal-hydraulic characteristics in a novel airfoil fin heat exchanger. International Journal of Heat and Mass Transfer, 175.

[33] Chang, H., Han, Z., Li, X., Ma, T., & Wang, Q. (2022). Experimental study on heat transfer performance of sCO2 near pseudo-critical point in airfoil-fin PCHE from viewpoint of average thermal-resistance ratio. International Journal of Heat and Mass Transfer, 196.

[34] Kapoor, M., Doğan, Ö., Rozman, K., Hawk, J., Wilson, A., L'Estrange, T., & Narayanan, V. (2016). Diffusion bonding of H230 Ni-superalloy for application in microchannel. In The 5th International Symposium - Supercritical CO2 Power Cycles (pp. March 28-31, San Antonio, Texas, USA).

[35] Pilagatti, A. N., Piscopo, G., Atzeni, E., Iuliano, L., & Salmi, A. (2021). Design of additive manufactured passive heat sinks for electronics. Journal of Manufacturing Processes, 64, 878-888.

[36] Cormier, Y., Dupuis, P., Farjam, A., Corbeil, A., & Jodoin, B. (2014). Additive manufacturing of pyramidal pin fins: Height and fin density effects under forced convection. International Journal of Heat and Mass Transfer, 75, 235-244.

[37] Dupuis, P., Cormier, Y., Fenech, M., Corbeil, A., & Jodoin, B. (2016). Flow structure identification and analysis in fin arrays produced by cold spray additive manufacturing. International Journal of Heat and Mass Transfer, 93, 301-313.

[38] Kong, D., Jung, E., Kim, Y., Manepalli, V. V., Rah, K. J., Kim, H. S., ... Lee, H. (2023). An additively manufactured manifold-microchannel heat sink for high-heat flux cooling. International Journal of Mechanical Sciences, 248.

[39] Schleifer, S. L., & Regev, O. (2023). Additive manufacturing of anisotropic graphene-based composites for thermal management applications. Additive Manufacturing, 70.

[40] Lad, A. A., Hoque, M. J., Christian, S., Zhao, Y., Balda, J. C., King, W. P., & Miljkovic, N. (2023). High power density thermal management of discrete semiconductor packages enabled by additively manufactured hybrid polymer-metal coolers. Applied Thermal Engineering, 220.

[41] Yun, M., Hsu, W.-T., Shim, D., Nam, J., Heo, J. H., Song, J.-Y., ... Cho, H. H. (2024). Design and fabrication of heat pipes using additive manufacturing for thermal management. Applied Thermal Engineering, 230(Part B).

[42] Greiciunas, E., Borman, D., Summers, J., & Smith, S. (2019). A numerical evaluation of next generation additive layer manufactured inter-layer channel heat exchanger. Applied Thermal Engineering, 162.

[43] Greiciunas, E., Borman, D., Summers, J., & Smith, S. (2021). Experimental and numerical study of the additive layer manufactured inter-layer channel heat exchanger. Applied Thermal Engineering, 188.

[44] Ning, J., Wang, X., Sun, Y., Zheng, C., Zhang, S., Zhao, X., ... Yan, W. (2022). Experimental and numerical investigation of additively manufactured novel compact plate-fin heat exchanger. International Journal of Heat and Mass Transfer, 190.

[45] Ferster, K., Kirsch, K., & Thole, K. (2017). Effects of Geometry, Spacing, and Number of Pin Fins in Additively Manufactured Microchannel Pin Fin Arrays. ASME. J. Turbomach., 140(11).

[46] Li, W., Yu, G., & Yu, Z. (2020). Bioinspired heat exchangers based on triply periodic minimal surfaces for supercritical CO2 cycles. Applied Thermal Engineering, 179.

[47] Kelly, J., Finkenauer, L., Roy, P., Stolaroff, J., Nguyen, D., Ross, M., ... Haslam, J. (2022). Binder jet additive manufacturing of ceramic heat exchangers for concentrating solar power applications with thermal energy storage in molten chlorides. Additive Manufacturing, 56.

[48] Alteneiji, M., Ali, M. H., Khan, K., & Al-Rub, R. A. (2022). Heat transfer effectiveness characteristics maps for additively manufactured TPMS compact heat exchangers. Energy Storage and Saving, 1(13).

[49] Singh, D., Yu, W., France, D., Allred, T., Liu, I.-H., Du, W., ... Messner, M. (2020). One piece ceramic heat exchanger for concentrating solar power electric plants. Renewable Energy, 160, 1308-1315.

[50] Du, W., Yu, W., France, D., Singh, M., & Singh, D. (2022). Additive manufacturing and testing of a ceramic heat exchanger for high-temperature and high-pressure applications for concentrating solar power. Solar Energy, 236, 654-665.

[51] Zhang, X., Tiwari, R., Shooshtari, A., & Ohadi, M. (2018). An additively manufactured metallic manifold-microchannel heat exchanger for high temperature applications. Applied Thermal Engineering, 143, 899-908.

[52] Zilio, G., Teixeira, M., Mortean, M., Brandão, F., Pontin, T., Oliveira, J., & Paiva, K. (2022). Structural analysis of compact heat exchanger samples fabricated by additive manufacturing. International Journal of Pressure Vessels and Piping, 199.

[53] Caccia, M., Tabandeh-Khorshid, M., Itskos, G., Strayer, A., Caldwell, A., Pidaparti, S., ... Sandhage, K. (2018). Ceramic–metal composites for heat exchangers in concentrated solar power plants. Nature, 562.

[54] Hildreth, O. J., Nassar, A. R., Chasse, K. R., & Simpson, T. W. (2016). Dissolvable Metal Supports for 3D Direct Metal Printing. 3D Printing and Additive Manufacturing, 3, 90-97.

[55] Nikuradse, J. (1950). Laws for flow in rough pipes. NACA TM 1292.

[56] Kandlikar, S. G., Schmitt, D., Carrano, A. L., & Taylor, J. B. (2005). Characterization of surface roughness effects on pressure drop in single-phase flow in minichannels. Physics of Fluids, 17(10), 100606.

[57] Kirsch, K.L., Thole, K.A. (2018). Numerical optimization, characterization, and experimental investigation of additively manufactured communicating microchannels. J. Turbomach., 140(11), Article 111003.

[58] Kirsch, K.L., Thole, K.A. (2017). Experimental investigation of numerically optimized wavy microchannels created through additive manufacturing. J. Turbomach., 140(2), p. 021002.

[59] Stimpson, C.K., Snyder, J.C., Thole, K.A., Mongillo, D. (2017). Scaling roughness effects on pressure loss and heat transfer of additively manufactured channels. Journal of Turbomachinery, 139(2), 021003.

[60] Kirsch, K.L., Thole, K.A. (2017). Heat transfer and pressure loss measurements in additively manufactured wavy microchannels. J. Turbomach., 139, Article 11007.

[61] Stimpson, C.K., Snyder, J.C., Thole, K.A., Mongillo, D. (2016). Roughness effects on flow and heat transfer for additively manufactured channels. J Turbomach, 138.

[62] Ferster, K.K., Kirsch, K.L., Thole, K.A. (2018). Effects of geometry and spacing in additively manufactured microchannel pin fin arrays. ASME J. Turbomach., 140.

[63] Kirsch, K.L., Thole, K.A. (2017). Pressure loss and heat transfer performance for additively and conventionally manufactured pin fin arrays. Int. J. Heat Mass. Tran., 108, 2502-2513.

[64] Thole, K.A., Lynch, S.P., Wildgoose, A.J. (2021). Review of advances in convective heat transfer developed through additive manufacturing. In J.P. Abraham, J.M. Gorman, & W. Minkowycz (Eds.), Advances in Heat Transfer (Vol. 53, pp. 249-325). Elsevier.

[65] Dupuis, P., Cormier, Y., Fenech, M., Corbeil, A., & Jodoin, B. (2016). Flow structure identification and analysis in fin arrays produced by cold spray additive manufacturing. Int. J. Heat Mass Transf., 93, 301-313.

[66] Lefky, C. S., Zucker, B., Wright, D., Nassar, A. R., Simpson, T. W., & Hildreth, O. J. (2017). Dissolvable Supports in Powder Bed Fusion-Printed Stainless Steel. 3D Printing and Additive Manufacturing, 4, 3-11.

[67] Yazdanparast, S., Raikar, S., Heilig, M., & Hildreth, O. J. (2022). Iodine-Based Sensitization of Copper Alloys to Enable Self-Terminating Etching for Support Removal and Surface Improvements of Additively Manufactured Components. 3D Printing and Additive Manufacturing, 4(1), 3-11.

[68] Raikar, S., Heilig, M., Mamidanna, A., & Hildreth, O. J. (2021). Self-terminating etching process for automated support removal and surface finishing of additively manufactured Ti-6Al-4 V. Additive Manufacturing, 37.

[69] Kethamukkala, K., Meng, C., Chen, J., & Liu, Y. (2023). Crack growth-based life prediction for additively manufactured metallic materials considering surface roughness. International Journal of Fatigue, 176, 107914.

[70] Maleki, E., Bagherifard, S., Guagliano, M., (2023). Correlation of residual stress, hardness and surface roughness with crack initiation and fatigue strength of surface treated additive manufactured AlSi10Mg: Experimental and machine learning approaches. Journal of Materials Research and Technology, 24, 3265-3283.

[71] Muhammad, W., Kang, J., Inal, K. (2023). The competing role of defects and surface roughness on the fatigue behavior of additively manufactured AlSi10Mg alloy. International Journal of Fatigue, 177, 107965.

[72] Brandl, E., Heckenberger, U., Holzinger, V., & Buchbinder, D. (2012). Additive manufactured AlSi10Mg samples using Selective Laser Melting (SLM): Microstructure, high cycle fatigue, and fracture behavior. Materials Design, 34, 159–69.

[73] Nasab, M. H., Giussani, A., Gastaldi, D., Tirelli, V., & Vedani, M. (2019). Effect of surface and subsurface defects on fatigue behavior of AlSi10Mg alloy processed by laser powder bed fusion (L-PBF). Metals (Basel), 9(10), 1063. https://doi.org/10.3390/met9101063.

[74] Behjat, A., Lannunziata, E., Gadalińska, E., Iuliano, L., & Saboori, A. (2023). Improving the surface quality and mechanical properties of additively manufactured AISI 316L stainless steel by different surface post-treatment. Procedia CIRP, 118, 771-776. https://doi.org/10.1016/j.procir.2023.06.132.

[75] Prasher, R. S., Dirner, J., Chang, J. Y., Myers, A., Chau, D., He, D., & Prstic, S. (2007). Nusselt Number and Friction Factor of Staggered Arrays of Low Aspect Micropin–fins under Cross Flow for Water as Fluid. ASME Journal of Heat Transfer, 129(2), 141-153.

[76] Rasouli, E., Naderi, C., & Narayanan, V. (2018). Pitch and Aspect Ratios Effects on Single-Phase Heat Transfer through Microscale Pin Fin Heat Sinks. International Journal of Heat and Mass Transfer, 118, 416-428. https://doi.org/10.1016/j.ijheatmasstransfer.2017.10.105.

[77] Moores, K. A., & Joshi, Y. K. (2003). Effect of Tip Clearance on the Thermal and Hydrodynamic Performance of a Shrouded Pin Fin Array. ASME Journal of Heat Transfer, 125(6), 999-1006. https://doi.org/10.1115/1.1621897.

[78] Short, B. E., Raad, P. E., & Price, D. C. (2002). Performance of Pin Fin Cast Aluminum Cold Walls, Part. 1: Friction Factor Correlations. Journal of Thermophysics and Heat Transfer, 16(3), 389-396. https://arc.aiaa.org/doi/pdf/10.2514/2.6692.

[79] Zukauskas, A. (1972). Heat Transfer from Tubes in Crossflow. Advances in Heat Transfer, 8, 93-160. https://doi.org/10.1016/S0065-2717(08)70038-8.

[80] Taylor, B. N., & Kuyatt, C. E. (1994). Guidelines for evaluating and expressing the uncertainty of NIST measurement results (NIST Technical Note 1297). NIST, Gaithersburg, MD.

[81] Wang, X., Del Rincon, J., Li, P., Zhao, Y., & Vidal, J. (2021). Thermophysical Properties Experimentally Tested for NaCl-KCl-MgCl2 Eutectic Molten Salt as Next-Generation High-Temperature Heat Transfer Fluids in Concentrated Solar Power Systems. ASME Journal of Solar Energy Engineering, 143(4), 041005. https://doi.org/10.1115/1.4049253.

[82] Jiang, R., Mostafaei, A., Pauza, J., Kantzos, C., & Rollett, A. D. (2019). Varied heat treatments and properties of laser powder bed printed Inconel 718. Material Science and Engineering A, 170-180.

[83] HAYNES 282 alloy. (2020). Haynes International. Retrieved from http://haynesintl.com/docs/default-source/pdfs/new-alloy-brochures/high-temperature-alloys/brochures/282-brochure.pdf?sfvrsn=20.

[84] Rasouli, E., Davis, C. A., Subedi, S., Montgomery, C., Mande, C. W., Western Cooling Efficiency Center, & Narayanan, V. (2018). Design and performance characterization of an additively manufactured primary heat exchanger for sCO2 Waste Heat Recovery Cycles. Proceedings of the 6th International Symposium on Supercritical CO2 Power Cycles.

[85] Wei, L. C., Ehrlich, L. E., Powell-Palm, M. J., Montgomery, C., Beuth, J., & Malen, J. A. (2018). Thermal conductivity of metal powders for powder bed additive manufacturing. Additive Manufacturing, 21, 201-208. https://doi.org/10.1016/j.addma.2018.02.002.

[86] Wu, Z., Sneha, P. N., & Rollett, A. D. (2020). Exploring the fabrication limits of thin-wall structures in a laser powder bed fusion process. The International Journal of Advanced Manufacturing Technology, 110(1), 191-207.

[87] Barron, R. F., & Barron, B. R. (2012). Design for Thermal Stresses. John Wiley & Sons.

[88] Ali, M., Ul-Hamid, A., Alhems, M., et al. (2020). Review of common failures in heat exchangers – Part I: Mechanical and elevated temperature failures. Engineering Failure Analysis, 109, Article 104396.

[89] Jones, D. R. H. (2004). Creep failures of overheated boiler, superheater and reformer tubes. Engineering Failure Analysis, 11, 873-893.

[90] Dowling, N. E. (2013). Mechanical Behaviour of Materials: Engineering Materials for Deformation, Fracture, and Fatigue (4th ed.). Pearson.

[91] Asraff, A. K., et al. (2013). Comparison of Creep Properties of Four Copper Alloys and Creep Based Stress Analysis of a Rocket Engine Combustion Chamber. Procedia Engineering, 55, 45–50. https://doi.org/10.1016/j.proeng.2013.03.217.

[92] Song, X., et al. (2016). Micro-Mechanism during Long-Term Creep of a Precipitation-Strengthened Ni-Based Superalloy. Journal of Materials Science, 52(8), 4587–4598. https://doi.org/10.1007/s10853-016-0703-0.

[93] Kim, et al. (2018). Comparison of Creep Properties of cast and wrought Haynes 282 superalloy. Advances in Materials Science and Engineering, Article ID 2048959.

[94] Tortorelli, P. F., et al. (2014). Long-Term Creep-Rupture Behavior of Inconel® 740 and Haynes® 282. ASME 2014 Symposium on Elevated Temperature Application of Materials for Fossil, Nuclear, and Petrochemical Industries. https://doi.org/10.1115/etam2014-1003.

[95] Pike, L. M. (2007). Low-Cycle Fatigue Behavior of HAYNES® 282® Alloy and Other Wrought Gamma-Prime Strengthened Alloys. Volume 5: Turbo Expo 2007. https://doi.org/10.1115/gt2007-28267.

[96] Li, Y., Xu, X., Wang, X., Li, P., Hao, Q., & Xiao, B. (2017). Survey and evaluation of equations for thermophysical properties of binary/ternary eutectic salts from NaCl, KCl, MgCl2, CaCl2, ZnCl2 for heat transfer and thermal storage fluids in CSP. Solar Energy, 152, 57-79.

[97] Nellis, G., & Klein, S. (2009). Heat Transfer. Cambridge.

[98] Moody, L. F. (1944). Friction factors for pipe flow. Trans. ASME, 66, 671–684.

[99] Miller, R. W. (1996). Flow Measurement Engineering Handbook (3rd ed.). McGraw-Hill.

[100] Ziev, T. L., Rasouli, E., Tano, I.-N., Wu, Z., Yarasi, S. R., Lamprinakos, N., Narayanan, V., Rollett, A. D., & Vaishnav, P. (2021). Cost of Using Laser Powder Bed Fusion to Fabricate a Molten Salt-to-Supercritial Carbon Dioxide Heat Exchanger for Concentrating Solar Power. 3D Printing and Additive Manufacturing Journal, 10(3). http://doi.org/10.1089/3dp.2022.0188.

[101] Tano, I.-N., Rasouli, E., Ziev, T., Wu, Z., Lamprinakos, N., Seo, J., Schulze Balhorn, L., Vaishnav, P., Rollett, A., & Narayanan, V. (2021). An Additively-Manufactured Molten Salt-to-Supercritical Carbon Dioxide Primary Heat Exchanger for Solar Thermal Power Generation – Design And Techno-Economic Performance. Solar Energy, 234, 152-169. https://doi.org/10.1016/j.solener.2022.01.056.

[102] Li, M., Zhang, X., Chen, W.-Y., & Heidet, F. (2020). Progress Report on the Assessment of the Material Performance for TCR Applications (ANL/NSE-20/42).

[103] Rasouli, E., Mande, C. W., Stevens, M. M., & Narayanan, V. (2019). On-Sun Characterization of Microchannel Supercritical Carbon Dioxide Solar Thermal Receivers: Preliminary Findings. ASME Energy Sustainability Conference.

Appendix A

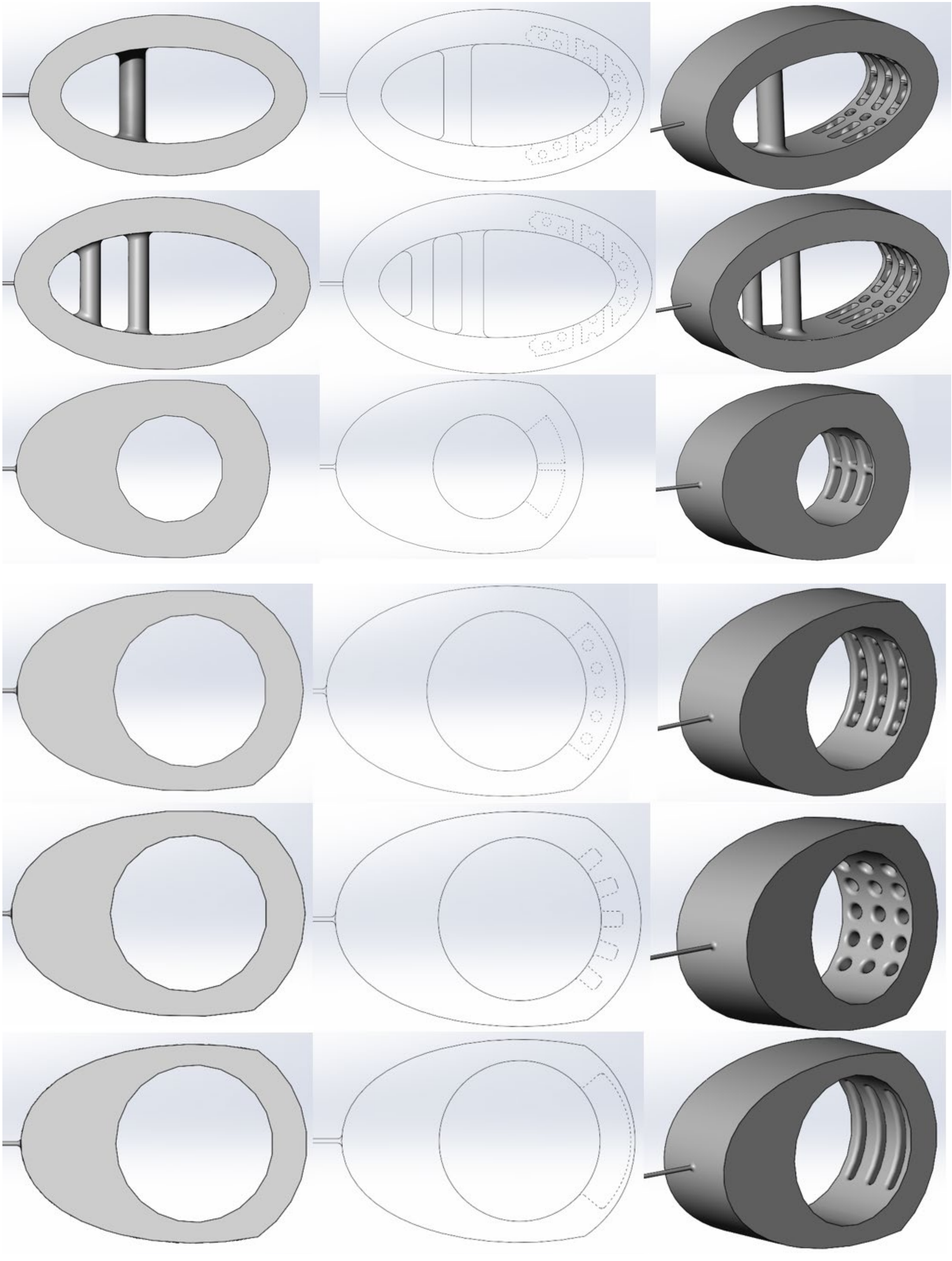

Figure A.1. Main iterations of the header design of the Gen 2 heat exchanger.